THE DEVELOPMENT OF A NOVEL TECHNIQUE IN MEASURING HUMAN SKIN DEFORMATION *IN VIVO* TO DETERMINE ITS MECHANICAL PROPERTIES

JAMALUDDIN MAHMUD, B. Eng (Hons), M.Sc.

PhD THESIS

2009

INSTITUTE OF MEDICAL ENGINERING AND MEDICAL PHYSICS

SCHOOL OF ENGINEERING

CARDIFF UNIVERSITY

ABSTRACT

Skin is the largest organ of the human body with a complicated multi-layered structure. Its mechanical properties are important in many applications but not well understood. The complex behaviour of skin makes it challenging, yet interesting, when measuring and quantifying its mechanical properties. Accepting this challenge the current study aims to develop an experimental protocol to measure *in vivo* the deformation of human skin; which ultimately lead to quantifying its mechanical properties. This thesis divides the work into four main areas of research:

A novel experimental protocol was developed to measure human skin deformation *in vivo* employing the motion analysis (MA) techniques. The non-invasive protocol was found repeatable, reliable and accurate. The data generated was found useful and ready for input into an inverse finite element analysis (FEA) implementation. The results for five subjects show that the overall mean ± standard deviation (SD) for the axial displacement, u_0 and u_{90}, was found to be 11.7 ±1.6 mm and 12.3 ± 3.3 when 1N load was applied in the X=0° and X=90° directions respectively. The ratio of axial displacements, (u_{90}/u_0), ranges from 0.63 to 1.45 with a mean ± SD of 0.982 ±0.34 and 0.982 ±0.32 for left and right arms respectively.

Finite element (FE) models were developed using Abaqus to simulate skin deformation based on the information gained from the experiments. Systematic case studies were built up to study the effect of element types, mesh sizes, loading types. Material parameters for human skin were estimated. The Ogden material parameters for Subject 1, were estimated to be close to $\mu = 10$ Pa and $\alpha = 110$. However, the result was not in good agreement with previous works. This indicates the need for a reliable inverse FE programme with an optimisation procedure.

The approach to perform FE simulation with an optimisation procedure (using Matlab) had been demonstrated to be useful when combined with the digital image correlation (DIC) techniques and therefore adapted for the current study. The experimental data generated by the MA techniques was used to determine the Ogden's material parameters of skin using the adapted approach. For five subjects, the mean ± SD set of material parameters (including prestretch, λ_p) are $\mu = 9.5 \pm 2.4$ Pa, $\alpha = 26.5 \pm 3.6$, $\lambda_p = 0.26 \pm 0.1$; and $\mu = 9.6 \pm 2.5$ Pa, $\alpha = 22.3 \pm 8.1$, $\lambda_p = 0.4 \pm 0.3$ for X=0° and X=90° respectively. In general, the results are found close to the skin properties proposed by other researchers.

As an alternative approach, the DIC technique was used to replicate the experimental protocol. Employing the same procedure as before, the experimental data was used to determine the material parameters of skin. The results for the same subjects were found to be close to the previous work.

A general comparison was made between the experimental and computational approaches and recommendations for further work have been suggested.

Keywords: Skin, *in vivo*, motion analysis, inverse FEA, optimisation, digital image correlation, Abaqus.

To my beloved parents
Hjh Jimah
My eternal source of inspiration and courage
You raised me up... to more than I can be
In loving memory of my dad, Mahmud (1929-1980)
You're always in my heart

To my dearest wife
Aija
Thank you for loving me
Without you, my life is incomplete

To my loving children
Hazim, Iman & Izzah
My pride and joy
Your births are great blessings

To my beloved parents in law
Hj Hamid & Hjh Latifah
With endless prayer

To my beloved siblings
Bang Chup, Bang Man, Kak Yah, Bang Mei,
Bang Nai, Kak Ijan, Kak Ita, Kak Ina,
You nurtured my soul and enriched my life

ACKNOWLEDGEMENTS

CONTENTS

CHAPTER 1

INTRODUCTION AND LITERATURE REVIEW

CHAPTER 2

A NOVEL METHOD TO MEASURE SKIN DEFORMATION *IN VIVO* EMPLOYING MOTION ANALYSIS TECHNIQUES

CHAPTER 3

THE DEVELOPMENT OF FINITE ELEMENT MODELS TO SIMULATE SKIN DEFORMATION

CHAPTER 4

MEASURING THE MECHANICAL PROPERTIES OF HUMAN SKIN

CHAPTER 5

MEASURING SKIN PROPERTIES USING DIGITAL IMAGE CORRELATION TECHNIQUES

CHAPTER 6

DISCUSSIONS

CHAPTER 7

CONCLUSIONS AND FURTHER WORK

REFERENCES

APPENDICES

ABBREVIATIONS

2D   2-dimension

3D   3-dimension

Ave   Average

B   Best

DIC   Digital Image Correlation

Expt   Experiment

F   Female

FE   Finite Element

FEA   Finite Element Analysis

FEM   Finite Element Method

GAG   Glycosoaminoglycans

M   Male

MA   Motion Analysis

Opt   Optimum

pp   page

QTM   Qualisys Track Manager

rms   Root mean square

S1   Subject 1

S2   Subject 2

S3   Subject 3

SD   Standard deviation

NOTATION

<	lower than
>	greater than
=	equal
%	percent
α	Ogden's material exponent
a	Ogden's material exponent (for graphs' legend)
C	Cauchy stress tensor
C_{10}, C_{11}	Mooney-Rivlin constants
cm	centimetre
Δ	difference
E	Young's Modulus
E	Lagrangian Green strain tensor
F	Deformation gradient
G	Shear Modulus
Hz	Hertz
J	Volume ratio
λ	Principal Stretch
L1	Marker L1
L5	Marker L5 (load point)
kg	kilogram
kPa	kiloPascal

μ	Ogden's material coefficient
m	metre
mm	millimetre
μm	micrometre
mV	milliVolt
N	Newton
N	The order of Ogden's function
p	Prestretch (for graphs' legend)
p	Hydrostatic pressure
P	First Piola-Kirchoff (nominal) stress
Pa	Pascal
p.s.i	Pound per square inch
S	Second Piola-Kirchoff stress
SO	Stochastic optimisation
σ_E	Engineering stress
σ	stress
u	Axial displacement
UDL	Uniformly distributed load
u_{90}/u_0	Axial displacement ratio
u_{max}	Maximum axial displacement
v	Lateral displacement
V	Voltage
W	Strain energy function

CHAPTER 1

INTRODUCTION AND LITERATURE REVIEW

1.1 Introduction

Skin is the largest organ of the human body with a complicated multi-layered structure (Payne, 1991) and many studies have been undertaken to assess its functions and properties for cosmetic and clinical applications. These include prediction of wrinkle-formation, cosmetic product design and evaluation, wound healing, scarring, ageing and surgery. From an engineering standpoint, the mechanical behaviour of skin is of wide interest and the mechanical properties of skin are important, e.g., Bader and Bowker (1983) pointed out that the mechanical properties of skin is important to the production of mechanically compatible soft tissue replacements. Sanders et al (1997) revealed that the response of skin to mechanical stress is an important issue in the quality of life of persons with disabilities. Lafrance et al (1998) stated that knowledge of the mechanical functions of cutaneous grafts, such as novel tissue engineered skins, is essential in the cutaneous reconstruction of severe burns or in the treatment of ulcers for persons suffering from locomotor impairment. Jemec et al (2001) remarked that the mechanical properties of human skin are important to its normal functions and that objective measurement of skin mechanics is a relevant experimental (and possibly clinical) measure in the examination of human skin. He used the mechanical properties of skin to verify sclerosis, scar tissue evolution, moisturiser effects and many other aspects of skin biology. Hendriks et al (2003) confirmed that knowledge about the mechanical behaviour of the skin *in vivo* is of

importance for cosmetic and clinical applications. Evans et al (2007) stated that accurate prediction of the deformation and wrinkling of skin would be invaluable in many applications such as the planning of plastic surgery, the design of devices such as razors or car seats that interact with the skin and in the animation industry. Tran et al (2007) reported that in a clinical domain, surgeons and physicians require an evaluation of the mechanical behaviour of human skin to deal with skin diseases, skin aging assessments, monitoring the remedial effects of drugs in curing diseases and stretch ability for wound healing studies in plastic surgery.

This review justifies the importance of new research to enhance the depth of knowledge already pertaining to the mechanical properties of skin. Undoubtedly, the complex behaviour of skin makes it challenging, yet interesting, to quantify its mechanical properties. Many attempts have been made to produce a formulation or numerical values that can describe skin behaviour accurately and none have been accepted as a sole solution. Accepting that challenge, the current study aimed to explore the biomechanics of skin that will ultimately lead to determining quantitative values that can describe the mechanical properties of skin accurately. In order to achieve this six key objectives have been paramount and discussed in Section 1.2.

At the initial stage, the current study assessed several potential experimental and computational techniques to explore the possibilities of developing innovative approaches to fulfilling its objectives. Ideally, *in vivo* testing is preferred over *in vitro* as it is more realistic and thus provides higher validity. Nevertheless, for *in vivo* testing, the main consideration is to establish an experimental procedure that is non-invasive and repeatable. Another issue related to *in vivo* testing (except suction test) is to define clearly the boundary conditions. Experimentation employing motion analysis (MA) techniques has been identified as having high potential to fulfil this objective.

Moreover, they are practical and relatively simple to operate (Mahmud et al 2008). However, it is not possible to determine the mechanical properties by the data produced from such an experimental method alone. A numerical technique that could relate the experimental data and skin properties is required. For this purpose, the finite element method (FEM) was employed. FEM is a numerical method used to solve mathematical physics and engineering problems (Fagan 1992). The easiest way to develop a finite element (FE) model and simulate skin deformation is to use a commercially available FEM software such as Abaqus (Dassault Systemes Simulia Corp, Providence, RI, USA). To support the simulation results, a FE programme (using Matlab, The MathWorks, Inc.) that incorporated an optimisation procedure was used as an alternative approach to quantifying and determining skin properties from the experiment data. It was also desired to use an alternative experimental technique that could support the outcomes of the current study and hence, due to its potential, digital image correlation (DIC), a full-field measurement technique was employed. The integration of experimental-computational techniques (MA-Abaqus-FE-DIC) is novel and provides a comprehensive and powerful tool in exploring the biomechanics of skin. As a consequence, several novel outputs of this study were achieved including the development of new *in vivo* experimental method and FE models that could simulate skin deformation accurately.

This thesis is written for the reader with a background understanding of motion analysis techniques, digital image correlation techniques, finite element methods, general engineering and basic knowledge of skin. A glossary is provided in Appendix A to explain some technical terms which in particular might be unfamiliar to the reader.

1.2 Aim and objectives of the study

The ultimate aim of this study and thesis has been to determine the mechanical properties of human skin. A MA technique was employed as the primary experimental procedure to measure skin deformation *in vivo*. Abaqus was used to model and simulate skin behaviour during the tests. A Matlab FE programme with an optimisation procedure was used to determine the mechanical properties of skin and DIC technique was employed as an alternative tool to support the findings.

In order to achieve these aims, the studies described in this thesis were undertaken to explore the following key objectives. The outcomes will eventually contribute to adding knowledge about the behaviour of human skin. The key objectives were:

1. Development of a novel technique in measuring skin deformation *in vivo* employing MA

To determine the mechanical properties of skin accurately, precise data of skin deformation are needed. This can be achieved by developing a reliable experimental procedure. Consequently, on starting this study, great effort went towards developing a novel technique. This will be a major contribution for the current study and adding to the knowledge on measuring human skin *in vivo*.

2. Development of FE models to simulate skin deformation

A basic approach to determine the mechanical properties of skin is by simulating skin behaviour using a FE software. A simple but robust FE model that could simulate skin deformation reasonably accurate is ultimately desired to prevent researchers from conducting unnecessary experiments. Therefore, the current study attempts to develop such a model based on the information provided and data generated by an experimental procedure developed to measure skin deformation *in vivo*. Except for

material parameters, the inputs for the model were extracted directly from the experiments, i.e. load, boundary condition and geometrical data. Using a trial and error approach and systematic case studies, the results were compared to the experiments to identify the material parameters. The FE modelling and simulation of nonlinear hyperelastic material introduces many challenges; therefore the experience and knowledge gained from this work would be invaluable.

3. Adaptation of a FE programme with an optimisation procedure to determine skin material parameters

A FE programme with an optimisation procedure has been developed by Evans (2009) to determine skin material parameters based on the experimental data generated using the DIC technique. Therefore, the current study attempts to adapt the approach by using the experimental data from the previous experiment (MA techniques). The experimental output was different from the DIC output thus requiring several new subroutines. The current study provided a basic understanding of inverse FE implementation. It also demonstrates that the integration between experiment (MA techniques) and FE modelling is a useful tool in determining skin properties.

4. Using the DIC techniques to measure skin deformation *in vivo*

An alternative experimental procedure that could generate comparable results to MA technique provides a means of supporting the findings of this study. The experimental data could also be used to overcome any deficiency using the MA techniques. Therefore, the current study attempts to measure skin deformation *in vivo* using the DIC techniques. The experimental data was used to determine skin properties.

5. Investigation of skin deformation and properties for all subjects

The tests were conducted on five subjects, therefore, an investigation were carried to observe skin behaviour for these subjects. The results portray the initial findings on skin behaviour and might stimulate other researchers' interest in investigating further on this matter. The typical values of human skin properties found in the current study would be a useful data for skin study.

6. Comparison of experimental and computational techniques employed in the current study

As the current study employed two experimental and two computational techniques in fulfilling its aim, these techniques were compared to one another to explore the advantages and limitations of each technique. This is a significant contribution to the community as the discussions might provide useful information for other researchers who intend to adapt similar techniques for their research.

1.3 Literature review

Although the approach of the current study seems to be straight forward, the main challenge was to integrate them and produce comparable results (have common features). For this purpose, a comprehensive literature survey has been conducted to understand previous studies, the diversity of the approaches and the advantages and limitations in the application of measuring skin properties. A considerable amount of literature was examined because of the multidisciplinary nature of the study. The outcome of this survey determined the context and scope of work for this research that ultimately will lead to the introduction of novel methods that make a significant contribution to enhancing knowledge about the biomechanics of human skin. The next section of this chapter seeks to present a comprehensive description of the current and previous methods used in studying skin properties.

There are many publications on studying the properties and functions of skin, however, in this section the key publications related to the current study are selected. Due to the diversity and multidisciplinary nature of the current study, the review is segregated into several sub-sections to highlight the following:

- The structure and functions of skin
- The biomechanical properties of human skin, described in historical research
- Characterising skin properties using experimental methods
- Previous works employing analytical approach
- Constitutive equations to describe skin behaviour
- Simulating skin behaviour using FEM
- DIC technique, described in historical research
- Previous works related to the MA techniques

1.3.1 Skin structure

"Macroscopically, skin is a dual-layer organ consisting of the dermis and epidermis. The dermis owing to its collagen component; is mostly responsible for the structural integrity of the skin" (Enderle et al 2005). A cross-sectional sketch of normal human skin is shown Figure 1.1.

Stratum Corneum
(thickness 0.010-0.020 mm)

Living Epidermis
(thickness 0.030-0.130 mm)

Dermis
(thickness 1.1 mm)

Subcutaneous Fat
(thickness 1.2 mm)
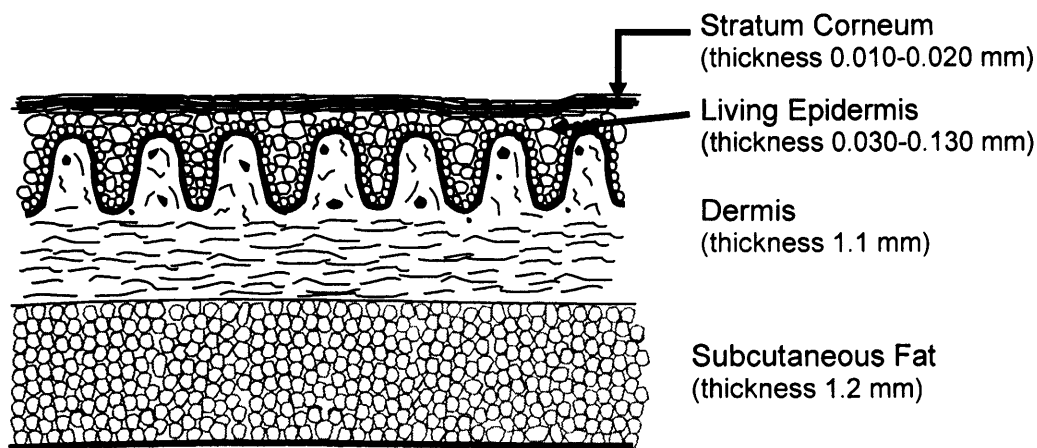
Figure 1.1: Skin anatomy (Trans et al 2007).

1.3.1.1 Epidermis

"The epidermis is the outermost layer of epithelial tissue, which contains no blood vessel and most of it is so thin except at the palms of the hands and the soles of the feet. In parts of the body other than the palms and soles, only the layer of stratum corneum and stratum germinativum are regularly present. The Stratum corneum is a flat, relatively thick layer of dead cells arranged in parallel rows. This keratinised layer of the epidermis consists of soft keratin (as compared with the hard keratin in fingernails and toenails), which helps keep the skin elastic. The Stratum germinativum consists of stratum spinasom and stratum basale, which generate new cells. The stratum basale rests on the basement membrane next to dermis. It consists of a single layer of columnar or cuboidal cells. Like the stratum spinosum, it undergoes cell division, producing new cells to replace those being shed in the exposed superficial

layer. The stratum spinosum is composed of several polyhedral cells". (Carola et al 1992)

1.3.1.2 Dermis

"Most of the skin is composed of dermis ("true skin"), a strong flexible connective tissue meshwork of collagenous, reticular and elastic fibres. Collagenous fibres, which are formed from the protein collagen, are very thick and give the skin much of its toughness (The thickest dermis is located on the back, thighs and abdomen). Although reticular fibres are thinner, they provide a supporting network. Elastic fibres give the skin flexibility. The cells of the dermis are mostly fibroblasts, fat cells and macrophages, which digest foreign substances. Situated between the dermis and epidermis is an uneven junction called the papillary layer. This structure is filled with capillaries which nourish both the dermis and the stratum germinativum" (Carola et al 1992).

1.3.1.3 Hypodermis

"The hypodermis is a subcutaneous fatty tissue layer situated below the dermis. The main function of this structure is to connect the dermis to the underlying tissue; it also stores excess nutrients within fatty deposits. The adipose layer also reduces heat loss from the body and increases padding. The boundary between the epidermis and dermis is distinct; that between the dermis and hypodermis is not" (Carola et al 1992).

1.3.1.4 Major skin molecules

Skin is a tissue, made of groups of cells which mostly composed of organic compounds and water. The approximate chemical composition of the skin is water (70.0%) protein (25.5%), lipids (2.0%), trace minerals (0.5%) and other substances (Enderle et al 2005). The protein comprises of four main types; which are collagen,

elastin, Glycosoaminoglycans (GAG) and proteoglycans. Collagen and elastin forms the connective tissue in the dermis (Section 1.3.1.2). GAG and proteoglycans are very similar to mucus proteins, which hold water and moisturises the skin. Collagen is the most abundant protein in the body forms the structural network of skin. It is one of the strongest proteins in nature and gives skin its strength and durability. Through aging, collagen deteriorates and causes the skin to become thinner and eventually sag (Bader and Bowker 1983). Elastin is similar to collagen but is a more stretchable protein that maintains the skin's elasticity (Carola et al 1992). It provides the matrix that holds individual skin cells in place. Elastin also contains two unique amino acids, namely desmosine and isodesmonsine. The two proteins together permit the skin to stretch and then regain its original shape. With age, the skin's elastin breaks down and causes wrinkles. GAG contains special sugar substances that have high water-holding properties. Proteoglycans are larger molecules with many attached GAG. Hydrated GAG and proteoglycans cushion and provide mechanical support to tissues.

1.3.2 Skin functions

"Based on its anatomy, skin functions very well to cover and protect the inner organs. In addition, it acts as a stretchable protective shield that prevents harmful micro-organisms and foreign material from entering the body. It also helps in regulating the body temperature, excretion, synthesis and sensory reception" (Carola et al 1992). Unquestionably, it forms the aesthetic envelop for human face and body.

1.3.3 The biomechanical properties of skin

"Skin is indeed multifunctional and has consequently an extremely complex structure. It is multilayered with convoluted and often indistinct interlayer boundaries, and its properties are different in different directions (anisotropic). Its structure and

appropriate function vary with body site. The properties of skin also vary with the rate of application of stress and the length of time over which the stress is maintained (viscoelastic), and are very sensitive to ambient conditions, age and recent handling" (Edwards and Marks 1995). In 1870, Langer demonstrated the anisotropy of skin, when he noted that after having excised a circular patch of skin from a corpse, the shape changed into an oval (Langer 1978). By describing this behaviour due to the internal stress and elastic modulus, he established the existence of what became known as the Langer lines. For the human arm, the Langer lines are shown in Figure 1.2.

Figure 1.2: The Langer lines for human arm
(extracted from Langer (1978), page 105)

Therefore, many attempts have been made to study the distinct properties skin. Properties can be broadly classified as physical and mechanical. Physical properties are density, electrical conductivity, resistivity etc. Mechanical properties of a material describe the behaviour of a material when subject to a force (Green and Nokes 1988).

Even though initially, a clinical approach was most popular method used to study the properties and functions of skin by dermatologists, pathologists and skin biologists, subsequently, with the involvement of physical scientists and engineers, several new approaches have been developed and employed to determine the properties of human skin. Generally, they can be classified into three approaches: experiments (*in vitro* and *in vivo*), analytical and FE simulation. Therefore, in this section, previous

studies are described separately according to the three approaches. Further sections describe the previous research employing the DIC and MA techniques.

1.3.4 Experimentation approach

Experimentation has been the most common and widely used approach to determining the mechanical properties of skin. For more than forty years, various techniques and procedures have been developed to study human skin properties. Early studies involved *in vitro* tests on cadaveric skin. Recent advances in technology and equipment have enabled researchers to develop and conduct *in vivo* tests; such as suction, torsion, indentation, traction and tensile tests, on human skin. Each of these is employed to establish the associated mechanical properties of the skin.

Tensile tests are used to determine the elastic modulus of a material under uniaxial loading. Based on the mechanics of materials, this relatively simple approach has been widely applied to measure skin properties *in vitro*. Skin samples, either human or animal, are prepared by separating the skin from subcutaneous fat and then making measurements under controlled humidity and temperature. By careful control *in vitro* tests could produce reliable and reproducible results. *In vitro* tests were conducted on skin to determine the associated strength values (e.g. breaking strain), time-dependent values (e.g. creep and relaxation) and non-time dependant values (e.g. elasticity) (Edwards and Marks 1995). Therefore, it is unquestionable that *in vitro* tests have provided considerable knowledge of the response of skin to applied mechanical forces. However, for human skin, recently, *in vivo* testing has always been the desired approach expected to explain the mechanical properties accurately. This is because *in vitro* tests isolate skin from its complex interactions of surrounding tissues, blood flow and oxygen diffusing from air. Moreover, the specimens can be used only once

and could not be further modulated *in vivo* (Edwards and Marks 1995). Thus, time series measurements must use different sites, which mean more samples are required for adequate interpretation of results. By contrast, *in vivo* tests provide real time and in situ information about the human skin properties. However, because only the top boundary of skin is accessible to an *in vivo* test method, there is no chance of designing a "pure" or direct measurement of any single property of the dermal fibrous connective tissue. Therefore, investigators have devised many tests that apply such stresses as would normally be experienced, and measures some force, distance, or time parameter (or some combination of these). In this way empirical data can be gathered. However, the main issue raised for these *in vivo* test methods is the lack of control at the test area boundaries. Other than suction tests (Hendriks 2003), the *in vivo* test proposed by the current study could clearly define its boundary conditions. Moreover, the information at a specific point in the test area is also accessible.

The study of skin structure using tensile test has been reported as early as in 1966, where Ridge and Wright constructed an extensometer, utilising a constant rate of extension system. At that time, they managed to come up with an empirical equation which characterises the stress-strain curve of skin. Chapuis and Agache (1992) developed a technique allowing the determination of the stress-strain characteristics of the collagen lattice through the calculation of its stiffness modulus, which they claimed would be useful to cosmetologists and dermatologists for their routine screening. However, both tests were conducted *in vitro* and calculated the linear elastic modulus for the specimens. Therefore, their results do not really explain skin behaviour and not useful to the current study.

Attempts have also been made to conduct tensile test on human skin *in vivo*. For example, Wan Abas and Barbenel (1982) used a uniaxial tension test of human skin *in vivo* to investigate strain distribution at the abdomen. A subsequent similar study was conducted using biaxial tension test (Wan Abas 1994). Nevertheless, only the strains were investigated and skin properties were not determined in either study. Khatyr et al (2004) claimed that the single-axis extension test is relatively little used to study the mechanical properties of human skin *in vivo*. Therefore, a series of tests were carried out with an original device developed in their laboratory. Their results were used to develop a viscoelastic model. The calculated elastic modulus helped them to determine the main directions of anisotropy on the forearm. Although credit should be given to them for attempting to characterise the anisotropic behaviour of human skin, using the elastic modulus limits the usefulness of the data as skin is highly nonlinearly elastic.

Prete et al (2004) used uniaxial stretching to measure the viscoelastic properties of skin samples, prepared from three types of mouse skin. This is done *in vitro* which would not be of interest to the current study. More recent developments involve a new extensometer to measure *in vivo* uniaxial properties of pig skin (Lim et al 2008). However, the study focused on the deformation of skin rather than determining the properties of skin.

Other reported works employing the tensile tests to characterise human skin include Dunn et al (1985) and Raposio and Nordstrom (1998) for uniaxial and Gibson et al (1969), Lanir and Fung (1974), Cook et al (1977), Alexander and Cook (1977) and Lafrance et al (1998) for biaxial tensile.

The suction test is a method used to achieve biaxial measurements of skin properties. According to Khatyr et al (2006), currently, the suction test is the only real test that is in use in both research laboratories and dermatology departments. This is mainly because of the availability on the market of perfectly operational apparatus. The suction test is an adaptation of the plate inflation test long used in traditional mechanics to characterise thin sheet metal. In general, the results analysed solely concern the amplitude of the maximum elevation of the dome of skin which is obtained as a result of the negative pressure applied i.e. suction. They determined the Young's modulus by using FE simulation and the results were compared with analytical method: geometrical model and Timoshenko equation. The discrepancy in results proved that the mechanical properties determined are not reliable. Moreover, they only investigate the linear behaviour of skin.

Small et al (2006) have used the cutometers for mechanical property assessment, where the aims of their research were to determine the influence of dermal thickness, tissue composition, and age on the biomechanical properties of the skin at three body sites. A cutometer (Figure 1.3) is a non-invasive, *in vivo* suction skin elasticity meter which uses simple measuring principle (Dobrev 2000). When its testing probe is slightly pressed on the skin, it results a temporary vacuum. Therefore, the skin is lifted, stretched and released. These deflections are optically recorded and evaluated. They measured the biomechanical properties skin for 30 subjects using two devices: Cutometer and Biomechanical Tissue Characterisation system. Using statistical analysis, they compared several parameters including elasticity, elastic deformation and elastic recovery. Though they claimed that both results correlate, no elasticity (Young's Modulus) parameters for skin were reported.
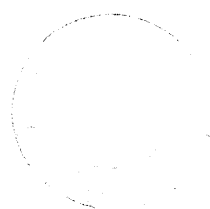
Figure 1.3: The image of **Cutometer**®SEM 575
(extracted from www.derma.uni-jena.de)

Other studies involving the use of suction test are summarised. Earlier in 1997, Pierard et al performed a study to evaluate the rheological properties of anetoderma using a non-invasive *in vivo* suction method. In 1998, Diridollou et al claimed that they had developed a new and original device which they called the "echorheometer", comprising a suction system with an ultrasound scanner (A-mode, TM-mode and B-mode) that enables the simultaneous visualization and measurement of the deformation of skin structures *in vivo*. Figure 1.4 shows the diagram of the "echorheometer". Jemec (2001) enhanced the suction tests by combining a ballistometer in his research. A study of skin mechanical properties by means of cutometer has been reported by Dobrev (2002) where he discussed some aspects of the biological informativeness and interpretation of the results obtained studying skin mechanical properties with cutometer. The suction test has also been used by Schlangen et al (2003) in his attempt to study the time-dependent mechanical behaviour of the skin. The work of Hendriks et al (2003, 2004) is of interest to the current study. Combining the suction test and FE simulation, they determined the mechanical properties of human skin. Their work is discussed further in Section 1.2.7. Another similar study was conducted by Delalleau et al (2008) and also discussed in the same section.
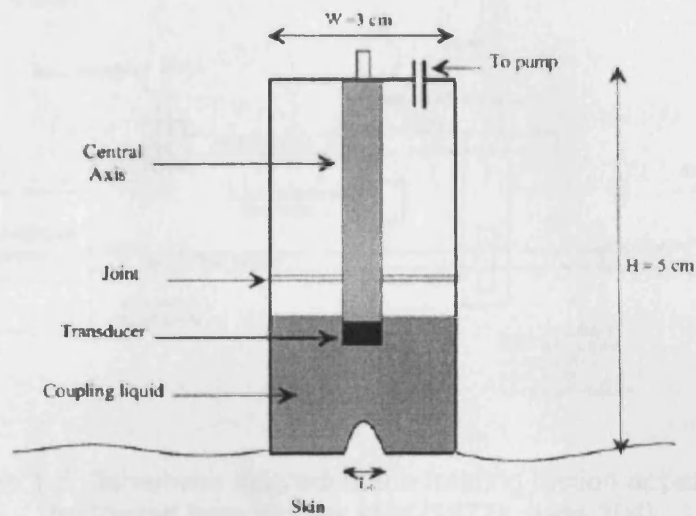
Figure 1.4: Diagram of the "echorheometer"
(extracted from Diridollou et al (1998), page 215)

Another type of test, which is commonly used in materials science and has been adapted into the study of skin properties, is the torsion test. This test is developed to determine the torsion coefficient, shear stress. The work done utilising this test has been reported as early as in 1977 by Highley et al in their attempt to study the frictional properties of human skin. The schematic presentation of the friction apparatus is shown in Figure 1.5. The system consisted of a motor-driven nylon wheel which generated a lateral force during rotation on the skin surface. The load exerted by the wheel (force normal to the contact point with skin) was applied via a spring connection (Highley et al 1977). Sanders et al (1997) criticised the work saying that the load applicators performed adequately for the purposes but were inappropriate for the investigation of skin available as the load applicator could not control the normal and shear load applied.
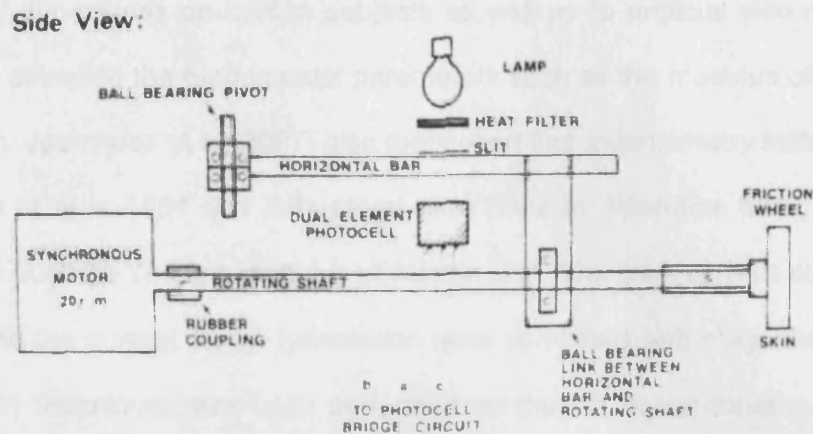
Figure 1.5: Schematic diagram of the rotating friction apparatus.
(extracted from Highley et al (1977), page 304)

Another early research team who were very keen in employing this test was Agache et al (1980). They reported their methods to study the mechanical properties and determining the Young's modulus of human skin *in vivo*. The mechanical properties of the *in vivo* dermis were measured by means of a torque applied to the skin. They employed the same method to study the influence of ageing on human skin. The tests were carried on 141 subjects aged 3-89 years, using the torsional device (Leveque 1980).

Indentation tests are originally used to determine the hardness of a material. However, they have also been used to determine the elastic property of material. Various shapes of indentor have been used by researchers to characterise the behaviour of skin (Payne 1981). Bader and Bowker (1983) developed an experimental indentation system to *in vivo* characterise the mechanical properties of human skin and underlying tissues. The work stemmed from the need for producing soft tissue replacement that is mechanically compatible to the host tissue. The stiffness moduli were determined to compare between young and old tissue. Jachowicz et al (2007) performed indentation, also called indentometry, using spherical probes with various

geometrical dimensions on human subjects as well as to artificial skin models. The aim was to calculate the fundamental parameters such as the modulus of elasticity of human skin. Jachowicz et al (2007) also mentioned that indentometry tests were used by Dikstein et al in 1984 and Zahuani et al in 2002 to determine basic mechanical parameters such as Young's modulus of human skin. The work of Tran et al (2007) is of interest to the current study. Indentation tests combined with magnetic resonance image (MRI) technique have been performed on the left dorsal forearm of a young man in order to reveal the mechanical behaviour of all skin layers. The mechanical parameters were determined using inverse FEA. The computational work is discussed further in Section 1.3.7.

Traction tests are used to determine the deflection of skin and coefficient of friction (i.e. material properties and roughness). Traction refers to the friction between an object and the surface it moves upon, where the friction is used to provide motion. In 2005, Topliss et al (2005) described their early experience with skin traction for the closure of open wounds associated with fracture. They demonstrated the stretch of skin, however, no material parameters reported. In 2001, Retel et al used a skin incision test in their study to determine the nonlinear properties of human skin. They performed computational simulation with reference to the incision. The nonlinear material effect was not clearly shown as they used the Young Modulus to simulate skin behaviour.

Other than the classical test methods described earlier, advanced mechanical tests have also been used to characterise the properties of skin. Jacobi et al (2004) utilised the surface roughness test, which is commonly used to evaluate metal surfaces, on human skin. They claimed that *in vivo* evaluation of human skin surface topography is of great interest for dermatological research because this type of topography

represents the three-dimensional (3D) organization of the dermis and the subcutaneous tissue. They reported that the surface topography can be considered to be a mirror of the functional status of the skin and it is an expression for the possibility of the skin to respond to mechanical stimuli and threats.

Dobrev (2005) performed fatigue tests on skin, claiming that skin fatigue can successfully be evaluated with a suction skin elasticity meter (Cutometer SEM 474), using measurements with several repetitions of the measuring cycle. The aim of his study was to compare the informativeness of Cutometer standard R-parameters with new area-parameters regarding age-related changes in human skin fatigue. The results show that after multiple deformations at one and the same region, adult skin shows larger fatigue than young skin. The skin progressively loses the capability to restore its initial position and each subsequent curve has lower amplitude and lower elastic retraction.

Another interesting innovative attempt was to utilise bending tests to study soft tissue. Nicosia (2007) presented a theoretical framework to analyze bending tests for soft tissue, which can be extended to study the properties of human skin.

Despite numerous experimental methods that have been employed using stretching, torsion, indentation and suction; lack of standardisation, qualitatively and quantitatively, makes comparison of results difficult. Thus, since the abundance of methods and technical devices that are found in the literature creates a wide diversity in experimental conditions (skin sites, nature and amplitude of the deformations), there is minimal *in vivo* data available on the biomechanical properties of human skin (Raposio and Nordstrom 1998). It was also found that not all studies led to quantifying the mechanical behaviour of skin (e.g. Topliss et al 2005). Some of the

experimentations (particularly developed by dermatologists) provided data which are more useful for skin health study (e.g. Dobrev 2002). Some were developed to promote a novel method which however found not relevant (e.g. Retel et al 2001). Nevertheless, some experiments have provided experimental data which could be used further to determine the mechanical properties of skin (e.g. Wan Abas and Barbenel 1982). They developed an experimental procedure and measured skin strain *in vivo* but they did not determine the corresponding mechanical properties. Observing the strain contour they presented, it could be suggested that inverse FEA was still not a popular approach for that era. This also justified that experimental technique by itself could not lead to determining material parameters of skin (or any material). It needs to be combined with the numerical method (e.g. inverse FEA). Therefore, the following sections look into the past studies that employed the numerical methods in characterising skin behaviour.

1.3.5 Analytical approach

Although the experimental approach to studying the properties of skin has been widely used, there have also been attempts to model the skin mathematically and analytically. Studies were carried out to produce the constitutive equations for skin. As early as in 1973, Danielson attempted to derive the equations governing the deformation of human skin. He considered skin as an elastic membrane, however, the model was found not realistic enough to duplicate skin behaviour. In 1987, Oomens et al attempted to generate a general theory to describe the behaviour of skin. They started the work by considering the skin as a mixture of a solid and a fluid. They presented a general theory for the description of the behaviour of mixtures applied to a mixture of a solid and a fluid. A numerical procedure is presented to solve the non-linear field equations describing such a mixture. The abilities of the procedure are demonstrated by means of a confined compression test. It is agreed that the proposed

procedure is flexible in terms of incorporating all kind of constitutive laws for the solid, the fluid and the interaction terms. However, the mathematics is complicated and the success to apply for other mode of deformation (i.e. other than compression) is questionable. It is expected that if the compressive force is applied to the dermis, buckling or wrinkling will occur and thus the concept could not be applied.

Attempts to model the mechanical behaviour of skin have focused on specific behavioural aspects of the tissue such as viscoelasticity or nonlinear elasticity (Bischoff 2000). Bischoff et al (2002) proposed a constitutive model based on entropy change upon stretching of long-chain molecules to represent the collagen network in skin. The proposed strain energy density is given in the following section.

To date, no constitutive equations specifically developed for human skin have been reported. The mechanical properties of skin were determined by adapting the constitutive model for other materials (e.g. rubber, theory of elasticity).

1.3.6 Constitutive equations for hyperelastic materials

Attempts have also been made to develop the numerical model for skin. Besides multilayered, anisotropic and viscoelastic; it is also known that skin is an inhomogeneous material whose mechanical behaviour is nonlinear load-deformation relationship and pre-stressed (Tran et al 2007). It is ideal to incorporate all these properties into the model. However, to analyse them simultaneously would be extremely difficult. Although there were attempts to model skin viscoelasticity (Shoemaker et al 1986), the more common approach is to assume skin to be hyperelastic; notably proposed by Danielson (1973), Tong and Fung (1976) and Lanir (1983). The linear elastic models do not accurately describe skin model. Therefore, the idealisation of hyperelasticity provides a means of modelling the stress-strain

behaviour of materials, whose stress-strain relationship can be defined as non-linearly elastic, isotropic, incompressible and generally independent of strain rate; though according to Ogden (1984) a hyperelastic material refers to an elastic material for which a strain-energy function exists. Hyperelastic materials are characterised by the strain energy function, W and the deformation gradient F. The First Piola-Kirchoff (nominal), P, stress-deformation relation is simply

$$P = \frac{\partial W}{\partial F}$$
(1.1)

In terms of Lagrangian Green Strain, E,

$$P = F.\frac{\partial W}{\partial E}$$
(1.2)

And in terms of right Cauchy-Green deformation tensor, C,

$$P = 2F.\frac{\partial W}{\partial C}$$
(1.3)

The fundamental relation between the first Piola-Kirchoff stress tensor, P and the symmetric second Piola-Kirchoff stress tensor (Holzapfel 2000):

$$P = FS$$
(1.4)

Therefore, the relation of the second Piola-Kirchoff, S and strain energy function, W, in terms of Lagrangian Green Strain, E,

$$S = \frac{\partial W}{\partial E}$$
(1.5)

And in terms of right Cauchy-Green deformation tensor, C,

$$S = 2\frac{\partial W}{\partial C} \qquad (1.6)$$

Similarly, the Cauchy stress is given by;

$$\sigma = \frac{1}{J}\frac{\partial W}{\partial F}\cdot F^T \qquad (1.7)$$

where $J = \det F$.

In terms of the Lagrangian Green strain

$$\sigma = \frac{1}{J}F\frac{\partial W}{\partial F}\cdot F^T \qquad (1.8)$$

In terms of the right Cauchy-Green deformation tensor

$$\sigma = \frac{2}{J}F\frac{\partial W}{\partial C}\cdot F^T \qquad (1.9)$$

The aim of this section is to specify some forms of strain energy functions which are well tried within the constitutive theory of finite elasticity and frequently employed in the literature. For the purpose of computational analyses, hyperelastic material (e.g. rubber) is often regarded as incompressible with the constraint condition $J = \lambda_1\lambda_2\lambda_3 = 1$ (Holzapfel 2000).

1.3.6.1 The Mooney-Rivlin model

Using the assumptions of isotropy and incompressibility, the Mooney-Rivlin model approximates the strain energy function W:

$$W = C_{10}(I_1 - 3) + C_{01}(I_2 - 3) \qquad (1.10)$$

where C_{10} and C_{01} are material constants.

1.3.6.2 The Neo-Hookean model

Using only the first principal variant, the Neo-Hookean model approximate the strain

energy function, W (isotropy and incompressible):

$$W = C_{10}(I_1 - 3) \tag{1.11}$$

This strain energy function involves a single parameter only; where C_{10} is a material

constant.

1.3.6.3 The Ogden model

Ogden (1972) proposed the strain energy function, W (isotropy and incompressible):

$$W = \sum_{i=1}^{N} \frac{\mu_i}{\alpha_i} \left(\lambda_1^{\alpha_i} + \lambda_2^{\alpha_i} + \lambda_3^{\alpha_i} - 3 \right) \tag{1.12}$$

λ_i are the principal stretches;

μ_i and α_i are the material parameters with the function's order of N.

1.3.6.4 The Yeoh model

This is a phenomenological material model which Yeoh (1990) used to simulate the

mechanical behaviour of carbon-black filled rubber vulcanizates with the typical

stiffening effect in the large strain dominant. The strain energy function, W (isotropy

and incompressible):

$$W = \sum_{i=1}^{N} Ci(I_1 - 3)^i \tag{1.14}$$

When a three-term strain energy function is proposed where the second invariant does not appear ($\partial W / \partial I_2 = 0$), it has a specific form

$$W = C_1(I_1 - 3) + C_2(I_1 - 3)^2 + C_3(I_1 - 3)^3 \qquad (1.15)$$

where C_1, C_2 and C_3 are material constants.

1.3.6.5 The Arruda-Boyce model

Another material model for the response of rubber which has a similar structure to Yeoh model. It is however, a statistical model where the parameters are physically linked to the chain orientations involved in the deformation of the 3D network structure of the rubber. The strain energy function, W, is derived from the inverse Langevin function by means of Taylor function. The first three term for the strain energy, W (Arruda and Boyce 1993, Holzapfel 2000):

$$W = \mu\left[\frac{1}{2}(I_1 - 3) + \frac{1}{20n}(I_1^2 - 9) + \frac{11}{1050n}(I_1^3 - 27)\right] \qquad (1.16)$$

where μ denotes the shear modulus and n is the number of segments (each of the same length) in a chain, freely jointed together at chemical cross-links.

Successful modelling and characterisation of hyperelastic materials depend on the selection of an appropriate strain energy function, and the accurate determination of coefficients in the functions (Ruiz and Gonzales 2006). Occasionally, the equations are expanded or modified for adaptation purpose. Among them, the most commonly used are the Mooney-Rivlin, Neo-Hookean and Ogden models.

The Neo-Hookean model is linearly elastic (one term) but takes into account the large deformation. Therefore it is simple but not accurate enough for very nonlinear materials like skin. It relies on phenomenological considerations and includes typical effects known from nonlinear elasticity within the small strain domain.

Compared to the Neo-Hookean model, the Mooney-Rivlin and Arruda Boyce models contain an extra parameter and can include some nonlinearity, but they are still quite restrictive. Therefore, Hendriks et al (2003) used an extended Mooney material behaviour to account for the nonlinear stress-strain relationship of the skin; which the strain energy function, W, was expanded into Equation 1.17.

$$W = C_{10}(I_1 - 3) + C_{11}(I_1 - 3)(I_2 - 3) \qquad (1.17)$$

The Arruda-Boyce is based on an idea of molecules that are stretched and straightened out; some people (e.g. Bischoff 2000) have argued that this is similar to collagen fibres in skin. The function for the force that is required to stretch the molecule is based on entropy calculation and would not apply to a fibre. The Yeoh model has not been used for skin study.

The Ogden model can have any number of terms and any shape of stress-strain curve, and it fits many materials well with only single term. The disadvantage is that it is computationally expensive because of the need to find the principal stretches, but in a 2D model that is not a problem. Note that of all constitutive approaches given, the Ogden model with $N=3$ excellently replicates the finite strain behaviour of rubber-like materials (Holzapfel 2000).

In studying skin wrinkling, Evans (2009) includes the prestretch, λ_p, term to investigate its effect to skin behaviour. The strain energy function, W used was:

$$W = \sum_{i=1}^{N} \frac{\mu_i}{\alpha_i}\left(\left(\lambda_1 + \lambda_p\right)^{\alpha_i} + \left(\lambda_2 + \lambda_p\right)^{\alpha_i} + \left(\lambda_3 + \lambda_p\right)^{\alpha_i} - 3\right) - p(J - 1)$$

(1.18)

Brown et al (2009) assessed all the five constitutions for describing normal and osteoarthritic articular cartilage. For describing normal and degraded articular cartilage, they found out that the Mooney-Rivlin model provided the best compromise between accuracy and required computational power.

Ruiz and Gonzales (2006) compared hyperelastic models in the analysis of fabric but did not make any suggestion.

1.3.7 Computational approach

Through the advances of the computer technology, the computational approach has become more popular for its capability to perform simulation without having to conduct experiments. It enables researchers to avoid complex mathematical formulations that need to be solved using high analytical skills. Moreover, recent software development has produced such a user friendly interface, that most of the time the users do not need to really understand either the computation algorithm, or the solving process.

Molinary et al (2005) confirmed that the use of mathematical models can be adapted extensively in many research areas, particularly medical and surgical fields. They developed a software application that is able to support plastic surgeons interested in applying simulations and soft tissue modelling during presurgical planning activities. To test the results, a FE software, FEAP, was used to determine the mechanical properties of human scalp. The application was found to be simple to use (for

surgeons), however, the computational procedure need to be improved due to large associated error. It also needs further development because other than scalp, the application has not been developed for other parts of the body.

In 1997, Tsap et al used finite element software ANSYS to study and simulate the problem of burn scar assessment. Subsequently, they improved the models (Tsap et al 2000) and claimed that it was capable of detecting the differences in elasticity between normal and abnormal tissue, as well as measuring burn scar elasticity, however, the general inverse problem was not solved and skin properties were not reported.

Hendriks et al (2004) developed FE models to simulate skin deformation during suction test. To gain better insight into the mechanical behaviour of different skin layers, the mechanical response was studied with experiments of various length scales. They reported a range of material constants, C_{10} = 10 to 30 kPa and C_{11} = 9 to 500 kPa for different skin layers. This work followed their earlier research in 2003 (Hendriks et al 2003), where they developed a numerical-experimental method to characterise the non-linear mechanical behaviour of human dermis. The experiment was simulated by a FE model exhibiting extended Mooney (refer Equation 1.17). The work was carried out further to investigate the contributions of different skin layers to the mechanical behaviour of human skin *in vivo* using suction experiments (Hendriks et al 2006). The material parameters for different layers of skin were determined but the results need further investigation. Possibly more aperture sizes could be used and investigated.

Tham et al (2006) acknowledged the work of Hendriks et al (2004) and used their results (C_{10} = 29.6 kPa, C_{11} = 493 kPa) to simulate skin deformation during cupping using Abaqus and Mooney-Rivlin strain energy potential. They also used the properties of rats' skeletal muscle reported by Bosboom et al (2001) to model cupping using Ogden's strain energy potential. They investigated several parameters that have effect on the cupping process (e.g. loading rate, cup size and cup shape). However, their results could be argued because the properties rats' skeletal muscle determined from compression tests could not accurately represent the cupping process on human skin.

Tran et al (2007) used inverse FE to determine the mechanical properties of skin from the data they generated using indentation tests. The MRI technique was used to capture the image of skin during indentation and the deformation was obtained. They model skin using Neo-Hookean slightly compressible material model, where the strain energy function, W:

$$W = C_{10}(I_1 - 3) + 0.5\,K\,(J - 1)^2 \qquad (1.19)$$

This provides the relation between the Young's Modulus, E, with Neo-Hookean parameters, C_{10}, K: E=6 C_{10}. J is volumetric ratio and K is bulk modulus. The assumption of slightly compressible requires that the ratio (K/ C_{10}) $\geq$ 9. The skin was modelled into three distinct layers. However, the study ignored the prestretch effect.

Delalleau et al (2008) used an inverse FE method that they claimed can be adapted to any kind of mechanical tests and behaviour laws. They determined the nonlinear elastic properties for one subject based on the suction tests. The material parameters of skin were determined using Hooke's Law and Neo-Hookean; and compared. They

proved that the nonlinearity was contributed by their proposed inverse FEA method. However, they modelled skin as a single layer and the algorithm has not been tried with the Ogden model. Therefore, their study could not be used to investigate prestretch.

1.3.8 Digital Image Correlation Technique

DIC is an optical method, which uses tracking and image registration to measure high resolution 3D deformation (Moerman et al 2009), and the methodology of this technique is described in Chapter 5. Not much work has been reported of using this technique in skin study.

According to Guan *et al* (2004) DIC (or digital image speckle correlation, DISC) has been used in experimental studies of stress analysis of materials such as metals, concrete and rubbers and fracture dynamics. Utilizing digital image processing techniques, DIC analyzes two images taken before and after the specimen is deformed and yields a displacement field of the specimen surface. They hypothesised that by combining with simple tensile tests, DIC can precisely determine skin properties including Young's modulus, breaking strength and ultimate strain. Therefore, they utilised the technique to study the mechanical properties of skin *in vitro* using rat skin. Using tensile tests, they reported the Young's moduli of rat skin to be 1.6, 1.4 and 0.7 MPa for three different sample conditions.

A similar technique was demonstrated to monitor the effect of aging, formation of wrinkles and the efficacy of topical applications of skin creams on healthy female volunteers *in vivo* (Staloff 2008). They described the experimental technique clearly but skin material parameters were not determined.

Moerman et al (2009) reported their work to assess the use of DIC in combination with FE modelling to determine the bulk material properties of human soft tissue. In a set up of an indentation experiment, tests were performed on a silicone gel soft tissue simulating muscle. Based on a Neo-Hookean FE model, the iterative FE analysis determined material parameters to be C_{10} = 1.80 kPa (material stiffness) and K = 2999 kPa (Bulk Modulus).

On the other hand, Evans (2009) reported his work in investigating wrinkling of skin and developing FE models based on the experimental data he obtained employing DIC technique. The FE model included the prestretch term (Equation 1.18). In a subsequent study, Evans and Holt (2009) used the same technique combined with FE modelling to measure the mechanical properties of human skin *in vivo*. Based on the Ogden's model, they found and reported the skin material parameters of μ = 10Pa (coefficient) and α = 26 (exponent) and an initial strain of 0.2. The advantage of the *in vivo* test they developed was that the boundary conditions could be clearly defined. However, the disadvantages of the DIC technique were that it generated abundant experimental data (50000 data points for each image) and some data was lost at the surrounding area of the loading tab.

1.3.9 Motion Analysis Technique

Optical motion analysis techniques have been widely used in analysing human motion, gait and joints (Cappozzo et al 1995, Andriacchi et al 2000, Jones and Holt 2008, Whatling et al 2008, Kedgley et al 2009). In 2007, Liu et al successfully adapted the optical MA system to be used for measuring small scale deformations to study the periodontal ligament and tooth movement. However, the scope of work still focused to analysing the kinematics of motion and the material parameters of the periodontal

ligament were not determined. Mahmud et al (2008) identified the potential of employing this technique to measure small scale skin deformation. The current study stemmed from this hypothesis and the methodology is described in detail in Chapter 2.

1.3.10 Discussion

Past research has shown that there are a variety of experimental methods that have been developed in attempt to study skin properties (Section 1.3.4). Fundamental testing methods such as tensile and suction tests have been the most commonly used, possibly due to a relatively straight forward method and straight forward corresponding material parameters to be identified.

This review has also revealed that combining the experimental techniques with inverse FEA could provide a tool to determine the mechanical properties of skin (Sections 1.37 to 1.38). Experimental technique by itself has not generated the mechanical properties of skin. Several models have been developed based on linear elastic, viscoelastic or hyperelastic model to determine the corresponding material parameters; such as Young's modulus, E, Poisson's ratio, K, Neo-Hookean's material stiffness, C_{10}, Mooney's extended material constants, C_{10} and C_{11}, and Ogden's coefficients and exponents, μ and α. The mathematical reasoning has been described in Sections 1.35 to 1.37.

Possibly due to the eagerness in developing a very own novel technique, most of the research approach differ from each other and thus provide a variety of results. It lacks of standardisation, qualitatively and quantitatively, makes comparison of results

difficult; and it is also clear that none of the approaches has been accepted as a sole solution.

In measuring skin deformation *in vivo* and non contact, the DIC technique has been demonstrated to be capable of providing full field deformation data as demonstrated by Evans and Holt (2009). In contrast, the MA technique has never been adapted as such a full field deformation measurement tool. The closest, was to measure small scale tooth movements (kinematics). Therefore, the success of adapting the MA technique to measure skin deformation is a great contribution to the success of the current study. It is indisputably very novel; as traditionally, motion analysis techniques have been used to study the kinematics of a moving body/system. Up to the best knowledge, no one has reported using MA in a similar approach (Mahmud et al 2009a). Consequently, the combination of MA-FE modelling is presented as an innovative approach in determining skin properties. Furthermore, the integration of MA-Abaqus-FE-DIC has never been done or reported in literature.

1.4 Thesis summary

This thesis describes the work conducted as an attempt to achieve the aim and objectives of the current study. Each chapter highlights its contributions towards achieving the study objectives and represents significant contributions to the learning and knowledge of human skin behaviour.

Chapter 2 describes the work in developing a novel technique to measure skin deformation *in vivo* employing the MA technique. It starts with a brief review justifying the significance of carrying out the work. The materials and methods are described; and the results are presented and discussed. The skin characteristics for five subjects are presented to exhibit initial findings on the variations of skin behaviour with age and gender.

Chapter 3 presents a novel study to develop FE models and simulate skin deformation using Abaqus. It includes the work on validating FE models. Nine case studies are described; and the results for different models are presented and compared to investigate the effect of several parameters.

Chapter 4 presents the study to determine skin properties using inverse FEA and optimisation procedure based on the data generated in Chapter 2. It includes describing the FE model and how the data was analysed. It also features a parametric study investigate the effect of skin material parameters. The numerical method is explained; and the results are presented extensively. Skin properties for five subjects are presented and compared with results available in literature.

Chapter 5 presents the alternative approach to determine human skin properties using inverse FEA and DIC techniques. It starts by depicting the experimental procedure used to measure human skin *in vivo* using the DIC technique. Then, it explains the method to determine human skin using inverse FEA and optimisation procedure. The results were compared with the previous results (Chapter 4).

Chapter 6 discusses the output from the two experimental and two computational works. The methods are compared to exhibit the advantages and limitations of each technique. It also highlights the overall work that has been performed in the current study.

Chapter 7 provides sets of conclusions drawn from the work undertaken in the current study and leads directions for future studies.

CHAPTER 2

A NOVEL METHOD TO MEASURE SKIN DEFORMATION *IN VIVO* EMPLOYING MOTION ANALYSIS TECHNIQUES

2.1 Introduction

To determine the mechanical properties of human skin accurately, it is essential to possess reliable data of skin deformation measured accurately *in vivo*. Unlike *in vitro* techniques, *in vivo* techniques measure real skin deformation on a living human being. Nevertheless, conducting an *in vivo* measurement has always been more challenging. Therefore, a system that combines a practical experimental protocol and a precision experimental tool is necessary to output reliable data for small scale skin deformation. In this study, by employing the motion analysis technique, an experimental procedure which is repeatable and non invasive has been developed successfully for measuring *in vivo* human skin deformation.

This chapter presents and discusses the following;

- The motivation for employing the motion analysis technique
- Equipment and system set up.
- The preparation prior to *in vivo* measurement on subjects.
- The experimental procedure.
- Control measures in the experimental procedure
- Data analysis

Towards the end, the results of the experiments are presented and critically discussed Finally, a conclusion ends the chapter.

2.2 Motivation

Optical motion analysis techniques have been widely used in analysing human motion, gait and joints (Cappozzo et al 1995, Andriacchi et al 2000, Jones and Holt 2008, Whatling et al 2008, Kedgley et al 2009). For skin study, Tsap et al (1997) have utilised the motion analysis technique to investigate the motion of human hand, which they tried to relate to the biomechanical properties of the skin and soft tissue. It led to a further study, in which Tsap et al (2000) performed nonrigid motion analysis based on dynamic refinement of finite element models. However, the measurement scale that they used, did not really measure the behaviour of the skin.

Despite its potential, the motion analysis technique had not been explored for use in small scale measurements until Liu et al (2006) proved that the system could be used to measure small deformations of biological tissue. They developed a motion capture system using two cameras (Qualisys Proflex-MCU120) with 50mm focal length lenses (higher than normally used for gait analysis applications), to measure and calculate tooth movements for studying the properties of periodontal ligament. The accuracy and repeatability of the system was evaluated and reported (resolution accuracy of 2 μm with 10 μm noise). The success of that motivated the current research, where similar equipment was further explored to measure skin deformation which ultimately aimed to determine skin mechanical properties.

2.3 Developing an accurate motion capture system for small scale deformation

The main challenge in this study was to develop, from scratch, an accurate and reliable small scale measurement system employing the motion analysis technique for a relatively larger measurement volume and a larger number of closely located

markers (an array of 42 markers), compared to a smaller volume using marker clusters (with 6 markers only), as previously developed by Liu et al (2007).

A thorough study using Liu's (2006) system confirmed that it would not be possible to simply apply the technique into measuring skin deformation. So, a new measurement set-up was developed. Moreover, the *in vivo* experimental protocol itself was novel, as no other authors have reported developing a method for measuring skin deformation using this approach, which could potentially be applied in a clinical setting and could be proposed as a standard application (Mahmud et al 2009d).

2.3.1 Equipment and set up

2.3.1.1 Camera system

Initially, the two-camera system (Qualisys Proflex-MCU120) was explored to produce accurate measurements of the displacement of skin markers. However, due to the slightly larger field of view of motion, and a larger number of markers, the system was unable to provide a satisfactory capture of images in the prescribed field of view. The main problem was to position the two cameras that could view the trajectories of all the markers simultaneously. As a consequence, the trajectories of the markers at the corners could not be recorded effectively (data lost). In most cases during motion, these markers were not visible to the cameras due to the circumferential shape of subjects' arm. Consequently, a three-camera system (Qualisys Proflex-MCU1000) with an optimum frequency of 30 Hz was explored. It captured the required images of skin movement with a good resolution and improved the field of view.

2.3.1.2 System calibration

Calibration was crucial in developing this measurement system as the calibration results determine the system accuracy. The factors found to contribute to the calibration results were

- the precision of the calibration frame
- cameras position and angle
- system parameters

Therefore, the following sections address the following:

- How were the calibration frames constructed?
- What was the optimum cameras position so that the markers movement could be viewed clearly?
- What were the significant parameters contributing to system accuracy?
- How accurate was the optical motion capture system?

2.3.1.2.1 Calibration frame

The camera system manufacturer (Qualisys AB, Sweden) refers the calibration frame as a rigid structure with at least five markers attached to it, where the exact location of the markers must be known (QTM User Manual, v1.10.281). It is used to determine the origin and the orientation of the coordinate system of the motion capture field of view. An initial calibration frame (size 20 x 35 x 5 mm) was constructed as shown in Figure 2.1. Diamond markers were attached on it as recommended by Liu et al (2007). The coordinates of the markers were measured using a travelling microscope. Although the calibration results were found to be satisfactory, using a more accurate and sophisticated measuring machine to measure the coordinates of the markers

would improve the result. Moreover, the body of the calibration frame produced some glare that could affect the optical system accuracy.

Therefore, new frames with diamond and circle shape markers were constructed to reduce the glare of the surfaces by using non-glossy paint (matt black). To produce a consistent marker shape, a paper punch was used. Figure 2.2 displays the materials used to construct the frames.
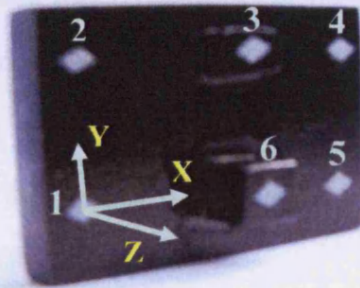
Figure 2.1: Calibration Frame: Diamond Marker (Initial Model)
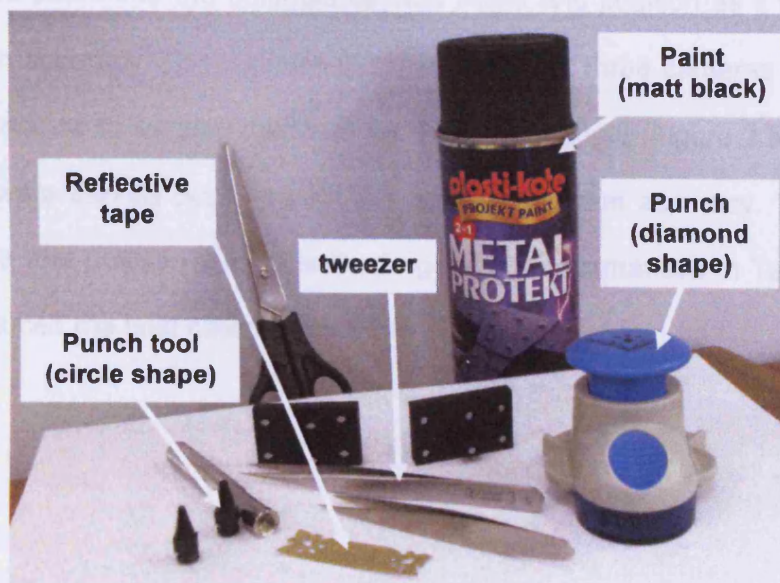
Figure 2.2: The materials used in constructing the calibration frames

More importantly, their relative 3D marker positions were measured accurately using a Visual Measuring Machine (Mitutoyo Quick Vision Accel Pro Machine). The 3D coordinates were then input to the system software as the calibration reference points. Both frames were tested and the results showed that the new frame with diamond shape markers produced better system accuracy (improved by 30%) than the circle shape markers. Compared to the initial frame, the improved frames were of better accuracy and reducing the frame glare increased the markers visibility. Apart from accuracy, the appearance was improved as shown Figure 2.3 and Figure 2.4. Each camera sees the markers in 2D. Based on known markers' position (calibration frame), the system software processes the 2D data to calculate each marker's 3D position. This process is called *tracking*. When tracked, the motion capture system defined its coordinate system. For this study, the system referred the *x*- and *y*-axes to the calibration frame's horizontal and vertical directions respectively.

2.3.1.2.2 Camera position and angle

Camera position and angle were found to affect the calibration results. Therefore, it was crucial to determine the optimum camera angle and position as it would offer a better system accuracy. To maximise the resolution, the three cameras were located in several positions by varying their relative height and angle (Figure 2.5). A series of calibrations were carried out to obtain the optimum system accuracy. The optimum camera angle and position related to the target (X) is summarised in Table 2.3. This position produced the best calibration results.
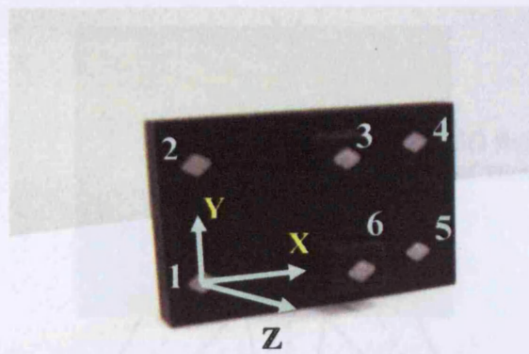
Figure 2.3: Calibration Frame: Diamond Marker (Improved Model)

Table 2.1: Coordinate of Diamond Markers measured using the Visual
Measuring Machine (Refer figure above)

Marker	Coordinate (mm)		
No.	X	Y	Z
1	0.0000	0.0000	0.0000
2	0.4094	14.3000	0.0013
3	18.2280	13.5109	3.1616
4	29.6521	14.3000	-0.0156
5	29.3378	-0.2748	0.0069
6	17.9223	0.1000	6.1137
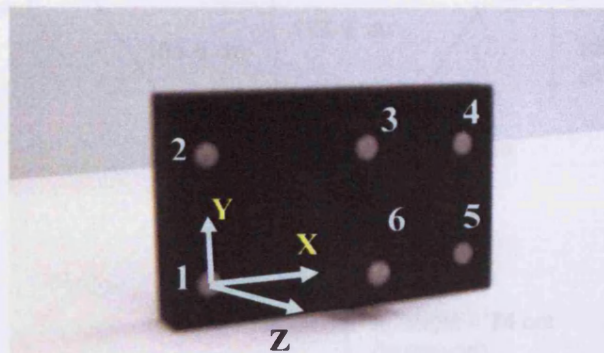
Figure 2.4: Calibration Frame: Circle Marker (Improved Model)

Table 2.2: Coordinate of Circle Markers measured using the Visual
Measuring Machine (Refer figure above)

Marker	Coordinate (mm)		
No.	X	Y	Z
1	0.0000	0.0000	0.0000
2	-0.1357	13.7601	-0.0020
3	16.8853	14.1788	3.1891
4	31.2995	13.7601	-0.0302
5	31.6734	0.4807	0.0000
6	16.9872	0.8924	6.1110
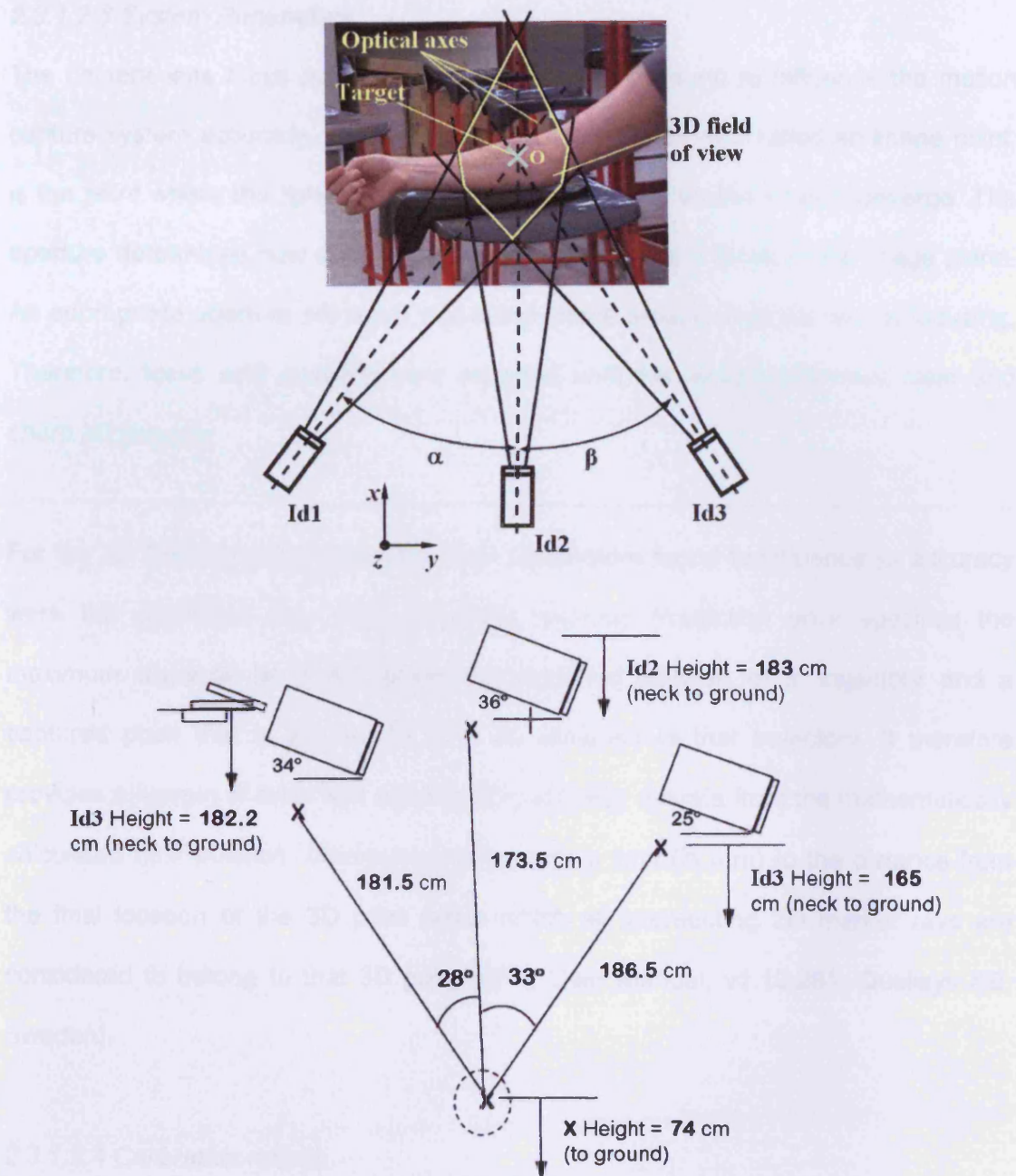
Figure 2.5: Camera angles and positions for measurement of skin deformation at subject's forearm.

Table 2.3: Summary of cameras position and angle

Cameras	Height to ground (z-axis)	Horizontal distance to target (xy-plane)	Vertical angle	Horizontal angle
Id1	165 cm	187 cm	25°	α = 33°
Id2	184 cm	174 cm	36°	β = 28°
Id3	183 cm	182 cm	34°	
Target	74 cm	-		

2.3.1.2.3 System Parameters

The camera lens *focus* point and *aperture* were also found to influence the motion capture system accuracy. In geometrical optics, a focus, also called an image point, is the point where the light rays originating from a point on the object converge. The aperture determines how collimated the rays admitted to a focus in the image plane. An appropriate aperture will result in a sharp image around what the lens is focusing. Therefore, focus and aperture were adjusted until the system produced clear and sharp 2D images.

For the 3D tracking system, the two main parameters found to influence its accuracy were the *prediction error* and *maximum residual*. *Prediction error* specifies the maximum distance (in mm) between a predicted position of a trajectory and a captured point that is allowed for it to be assigned to that trajectory. It therefore provides a margin of error with which a 3D point may deviate from the mathematically calculated next position. *Maximum residual* sets a limit (in mm) to the distance from the final location of the 3D point within which all intersecting 2D marker rays are considered to belong to that 3D point (QTM User Manual, v1.10.281, Qualisys AB, Sweden).

2.3.1.2.4 Calibration results

Calibration results show that the calibration using diamond shape markers (3 x 2 mm) produced very good system accuracy, maintaining an average residual of 50 μm. A sample calibration result shows that the average residual for Camera Id1, Id2 and Id3 are 34, 41 and 53 μm respectively. The detail results in presented in Appendix B.

2.4 Developing a new experimental protocol to measure skin deformation *in vivo*

As discussed in the previous section, great effort was made to ensure the camera system's accuracy. Nevertheless, the success of measuring skin deformation also relied on the experimental procedure. Prior to conducting *in vivo* tests on subjects, several essential tasks were accomplished to successfully develop a reliable, precise, consistent and efficient experimental protocol. This was achieved by responding to concerns that arose at the beginning of this study, such as;

- How to stick the 63 markers precisely and consistently onto the skin at the subjects' forearm?

- How to reduce the time consumed in the process of sticking the markers on the subjects?

- What was the optimum distance of markers that can be measured?

- How to define the principal axes and loading directions?

- What was a suitable tape used to stick the wire to the load point?

- How to apply a pulling load that would induce skin deformation?

Other criteria related to the experimental protocol are addressed as the following, where the experiments should be

- Practical - the protocol should be *in vivo* and not complicated to perform;

- repeatability and reliability - the protocol could be repeated and produce consistent results;

- non-invasive - the protocol would not hurt or induce pain to the subjects; and;

- efficient - where the experiment would not be too long.

The main challenge at this stage of the work was to determine the optimum marker configuration, i.e., the consistent attachment to the participants forearm in the same array dimensions for each test.

2.4.1 Marker Configuration

An extensive study of the marker configuration aimed to ascertain the optimum distance between markers and to determine the optimum field of view, where the movement of the whole marker set could be viewed clearly and measured precisely. The Initial study involved constructing a *phantom* and tests were carried out to track its markers movement. The phantom was made of rubber and markers were fixed on it as shown in Figure 2.6. As this system dealt with small scale measurements in a small field of view, if the markers are placed too far apart, information between them is lost but if the markers are placed too close together, overlapping or merging will occur. Tests were conducted using marker configurations where markers were placed 7, 8, 9 and 10 mm apart respectively and a separation of 8mm was found to be optimum in terms of system accuracy and 3D tracking. The final marker configuration can be viewed in Figure 2.7 indicating the locations of the marker set, load point and the loading directions. Measuring tape was used to locate the centre of the forearm, the load point, forearm crease and wrist crease.

2.4.2 Axes Establishment and Notation

Load was applied along the crease-to-crease (defined as $X=0°$) which parallel to the Langer lines (Section 1.3.3 Chapter 1, Langer 1978) and its transverse directions (defined as $X=90°$) as shown in Figure 2.7b. When load was applied in the $X=0°$ direction, two types of displacements were measured. They are axial (active) displacement, u_0, and lateral (passive) displacement, v_0. u and v refers to the axial

and lateral displacements respectively. The subscript 0 refers to the direction where load was applied.
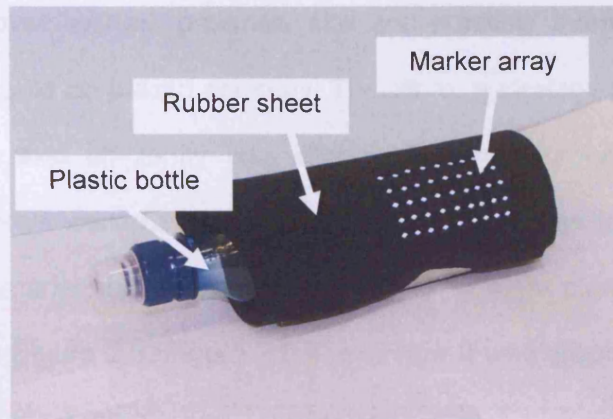
Figure 2.6: The *phantom* used for initial tests. Markers were attached on a rubber sheet and wrapped over a bottle to imitate human ventral forearm.
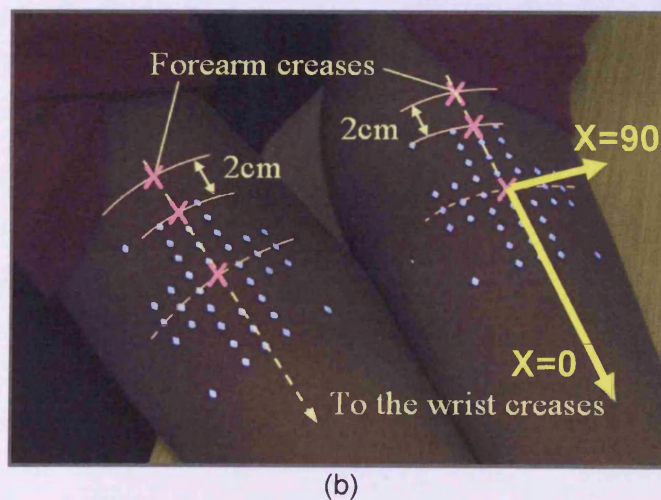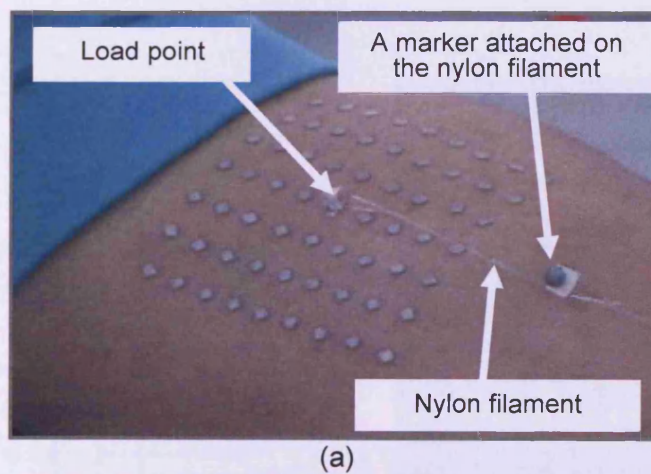
Figure 2.7: Marker configuration on the forearm of two volunteers.
(a) initial full marker configuration and the nylon filament.
(b) optimised marker configuration and the loading directions (X=0° and X=90°).

2.4.3 Designing a template for the marker configuration

Attaching 42 to 65 small diamond shape markers to the skin was tedious and time consuming. Moreover, without patience, skill and practice, there was no guarantee that the markers could be placed correctly. Therefore, a strategy to attach the marker array consistently and efficiently was crucial. For this purpose, a template was designed. The marker configuration was drawn as a template to produce a precise configuration and markers were overlaid on a sheet of clear plastic film, producing a patch as shown in Figure 2.8. Figure 2.9 shows how it was prepared and used to aid the process of attaching the markers onto subjects' skin.

(a)   (b)
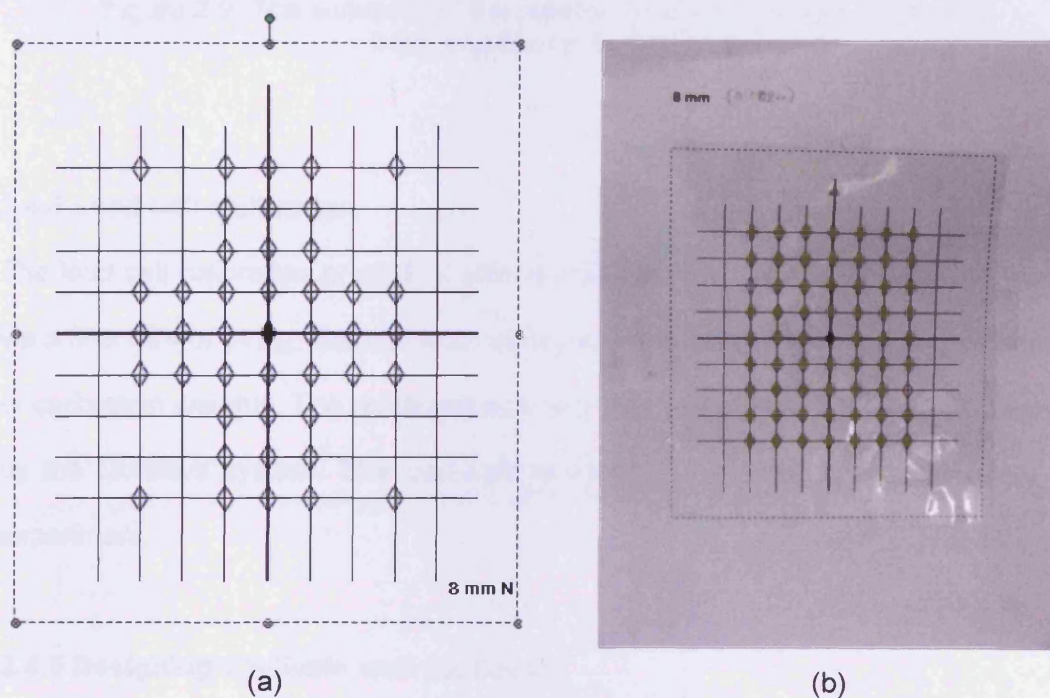
Figure 2.8: (a) Paper pattern of the marker configuration (b) Retro-reflective stickers stuck on the plastic film.

Template:
markers configuration

Final outcome

Loosening the
stickers

Puncher and other tools

Retro-reflective stickers
stuck on the plastic film

The patch
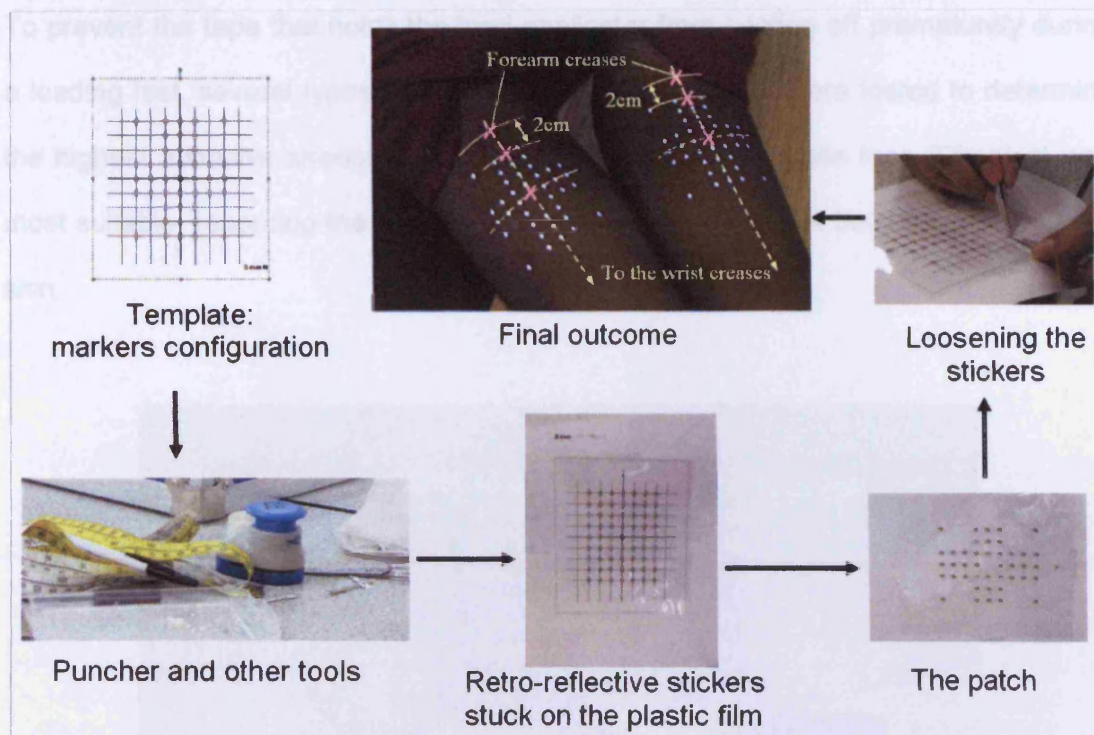
Figure 2.9: The summary of the process to attach markers on the skin:
from template to the forearm.

2.4.4 Load cell calibration

The load cell calibration procedure utilises calibration weights hung onto the load cell via a fine wire or string. Several tests were carried out using a variety of combinations of calibration weights. The resolution was found to be 1.948 mV per Newton recorded by the Qualisys system. The load calibration procedure was carried for every new experiment.

2.4.5 Designing a reliable load applicator

It was very important to attach the wire firmly to the skin during testing. Furthermore, the wire itself should be stiff enough so that it would not yield during pulling. In addition, precaution was taken into account to ensure that the load was applied precisely at the load point.

To prevent the tape that holds the load applicator from peeling off prematurely during a loading test, several types of adhesive tape (Figure 2.10) were tested to determine the highest adhesive strength. The results show that VIP toupee tape (Dimples) was most suitable, recording the highest pulling force of almost 3 N before peeling off the skin.

Figure 2.10: Adhesive tapes that were tested

To induce the pulling force, a fishing line (nylon filament) was used due to its high strength and small diameter (Figure 2.11). To seat it precisely on the desired load point, the tape was cut into an optimum shape and dimension as shown in Figure 2.12. Consistency was important as the input of an exact load condition would be significant in developing an FE modelling and simulation. Figure 2.13 exhibits the action during pulling.

Figure 2.11: A fishing line was used as the load filament.
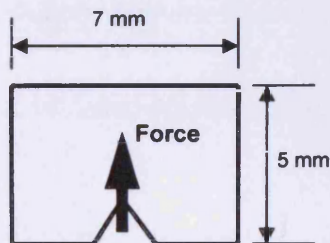
Fig. 2.12: The optimum shape.

Fig. 2.13: Pulling in action.

2.4.6 Determining the effect of misalignment during loading

As the experiment was conducted *in vivo*, it was impossible to apply load manually exactly aligned in the desired direction (even though (i) there was marking as a guide and (ii) the load direction could be traced by tracking the markers attached on the nylon filament). For that reason, the loading procedure was investigated to confirm whether the method of applying load was reliable or not. The load direction was varied ±20° and the effect was observed. The result clearly shows that a variation of ±10° gave an error of 2% error of displacements, while ±20° variation in load direction produced a maximum error of 7% (at 1.5N). Figure 2.14 shows the displacements of marker L5 when load direction varied up to ±20°. Thus, the loading method was reliable.
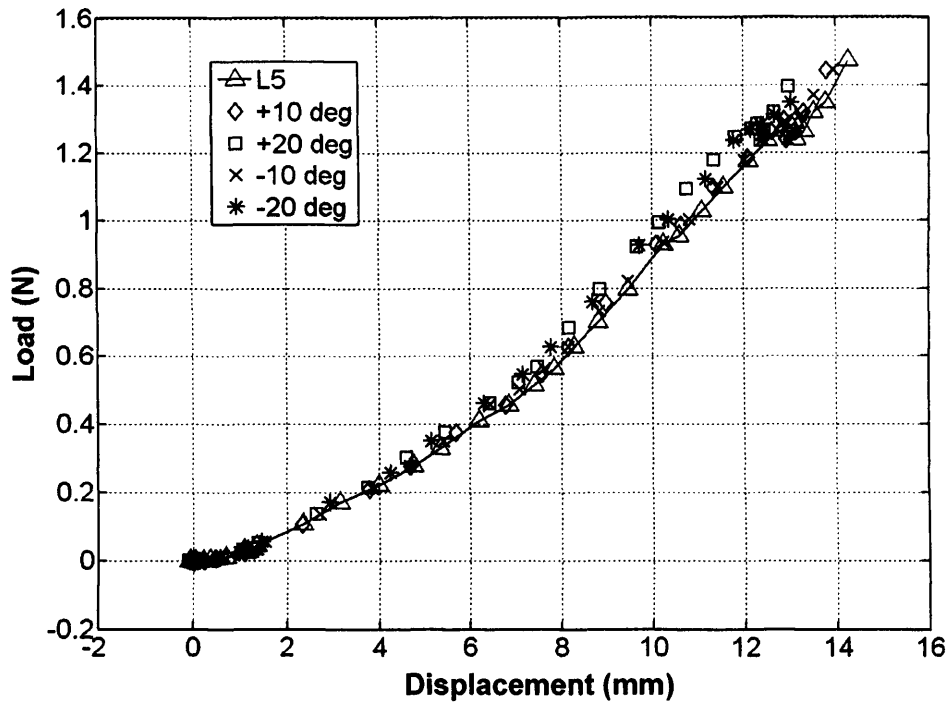
Figure 2.14: Load-displacement graph (L5) when load direction varied up to ±20°.

2.4.7 Repeatability test

The repeatability of the experimental protocol was tested by analysing the variations of results for a repeated test. For this purpose, the test for a subject (Subject 1) was repeated five times in the X=45° load directions. This is because applying the load in the X=45° direction would be the most difficult to control and controversial due to the nature of work during testing. Therefore, the results for this test are presented here and shown in Figure 2.15. To magnify the effect and determine the source of error, the axial displacements, u_{45} was decomposed into its x- and y component. Figures 2.15a and 2.15b show the displacement in x- and y-direction, named as u_{45x} and u_{45y} respectively. For the five tests, the computed variance of x-component displacements, $\bar{u}_{45x}$, is less than 0.04 (Figure 2.15a). However, for y-component displacements, u_{45y}, (Figure 2.15b), the four tests accumulated a variance of less than 0.05 but one test (Test3) deviated.
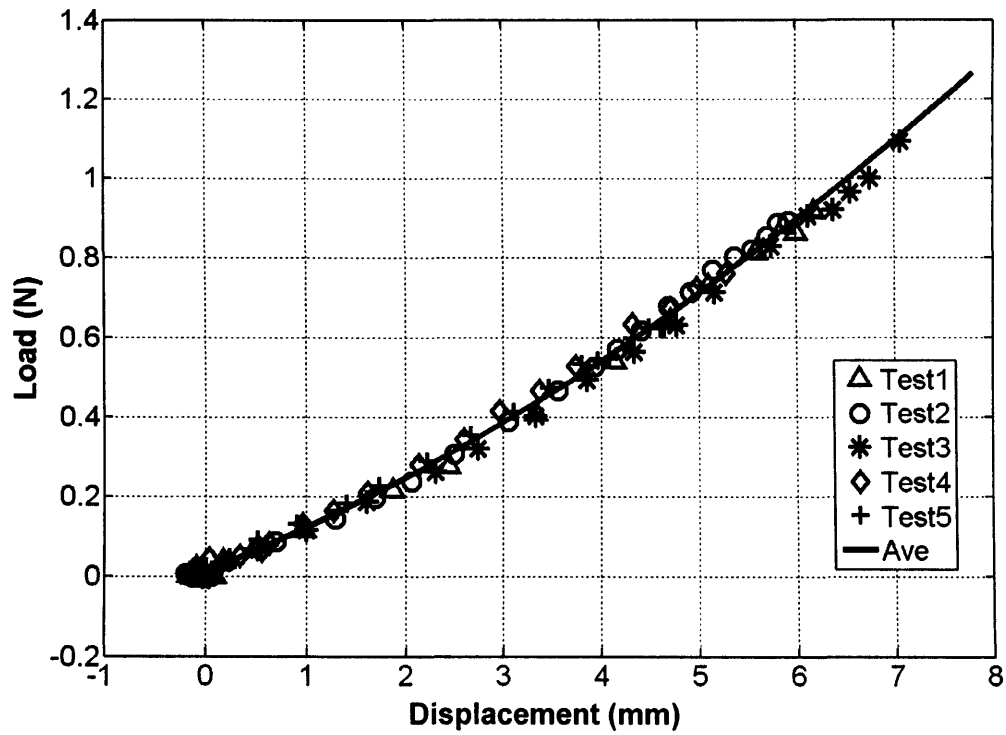
(a)
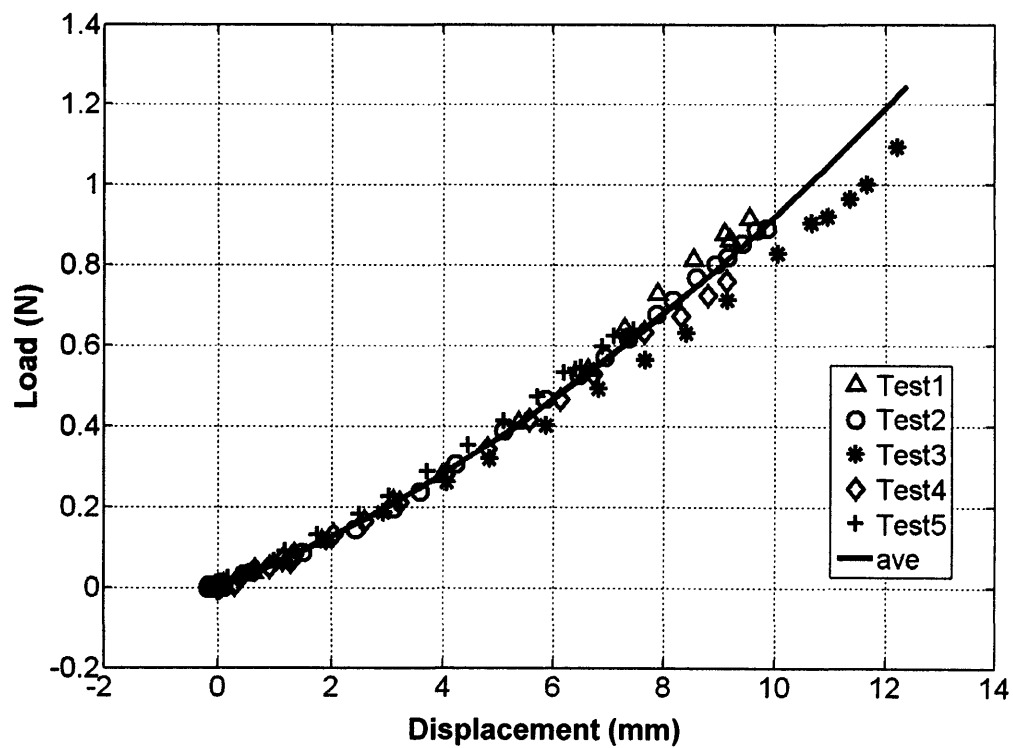
(b)

Figure 2.15: Results of 5 tests (Subject 1, X=45°) for (a) u_{45x} and (b) u_{45y} including the average lines (solid thick lines).

2.5 Experimental protocol

The subjects chosen for the test were normal and healthy volunteers (Table 2.4) with no signs of skin disease, injury, burn mark, surgery mark or skin modification and abnormality at the area of testing. Informed consent was obtained from all the volunteers with ethical approval from the Cardiff School of Engineering Research Ethics Committee. The subjects' height and weight were measured and their particulars (e.g. gender, date of birth, dominant arm) were documented. The forearm length and size were measured and several important markings defined to establish field of view, markers positions, load direction and area of skin to be tested. An array of diamond shape retro-reflective markers was attached firmly and precisely.

Table 2.4: Subjects information

	S1	S2	S3	S4	S5	S6	S7	S8
Gender	F	M	F	M	M	M	M	F
Age	25	26	42	23	26	39	31	23
Height (cm)	168	160	173	165	172	161	164	165
Weight (kg)	85	58	67	64	72	68	67	73
Dominant arm	R	L	R	R	R	L	R	R

A load was applied to the centre of the marker (load point) by pulling an instrumented nylon filament in X=0° and X=90° directions. Additional tests were conducted at X=45° on three subjects (Subjects 1, 2 and 3). The system provided synchronised output of motion captured and load applied. For each loading direction, tests were carried out three times.

2.6 Tracking markers

The trajectories of the markers were tracked using Qualisys Track Manager (QTM 2008 v2.0, Qualisys AB, Sweden,) software. (Appendix B2 shows and describes the typical windows (file mode) of the QTM user interface). In this study, all 42 markers

tracked in 3D were labelled as L1 to L42 respectively as shown in Figure 2.16. The markers sitting exactly on the crease-to-crease line (X=0°) are labelled as L1 to L9; and throughout this thesis referred as the midline markers. Marker L5 represented the load point. The processed data (3D coordinates of markers trajectories) were then exported as a data file (*.tsv).

Video cameras were used to record the scene throughout conducting the experiments. These video served as a control measure. Together with data obtained from markers tracking and recorded loading, the videos were then analysed to confirm that the experimental protocol has been carried out correctly or to justify any unusual output.

(a)   (b)

Fig. 2.16: Markers (a) positioned on the forearm and (b) tracked and labelled using Qualisys Tracking Manager (QTM 2008, v2.0).

2.7 Quantifying displacement
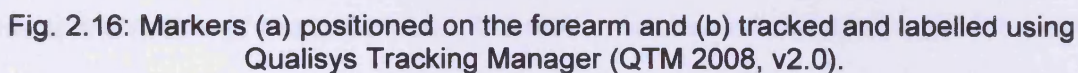
In general, it can be mentioned that in this study, displacements were measured *in vivo* using the marker coordinates (data produced by QTM via the tracking of markers trajectories). Despite the capability of QTM to measure the distance between two markers in a single frame, the marker coordinate data was manipulated using Matlab which was preferred due to its flexibility in terms of visualisation and computation. The

flow of the work carried out from reading the load and marker coordinate data until quantifying skin deformation is illustrated in Figure 2.17.

A programme was written using Matlab to read the raw 3D data from QTM and subsequently produce graphical outputs and animations. The raw marker coordinate data (QTM) was input to simulate the movement of markers both in 2D and 3D for visualisation and checking purposes. An example of a 3D plot/animation is shown in Figure 2.18 where x, y and z refers to the coordinate axes. By analysing the animation, unwanted and unreliable data was discarded.

Initially, the 3D data for all timeline frames was re-arranged as 2D data. However, the corresponding load data remained. Since the current study was focussed on the in-plane displacements, a systematic and consistent coordinate system was established throughout the analysis as described in Section 2.4.2 earlier. The original position (Load = 0N) of marker L1 was set as the origin (0,0). Figure 2.19 shows the transformation process in aligning the raw data according to the established coordinate system.

Due to the nature of the experiment, the motion capture rate was set to 30 Hz. Using higher frequencies produced abundant data and lower frequencies produced insufficient data. Consequently, 10 seconds of motion capture produced 300 frames of image. The mean of 10 initial frames was set as the reference, i.e., at this instance, no load was applied (load = 0N) and constituted skin in its undeformed state. The displacements of the markers were computed by measuring the relative distance of marker coordinates to the reference. This so called length between deformed and undeformed was calculated for all frames (throughout the experiment).

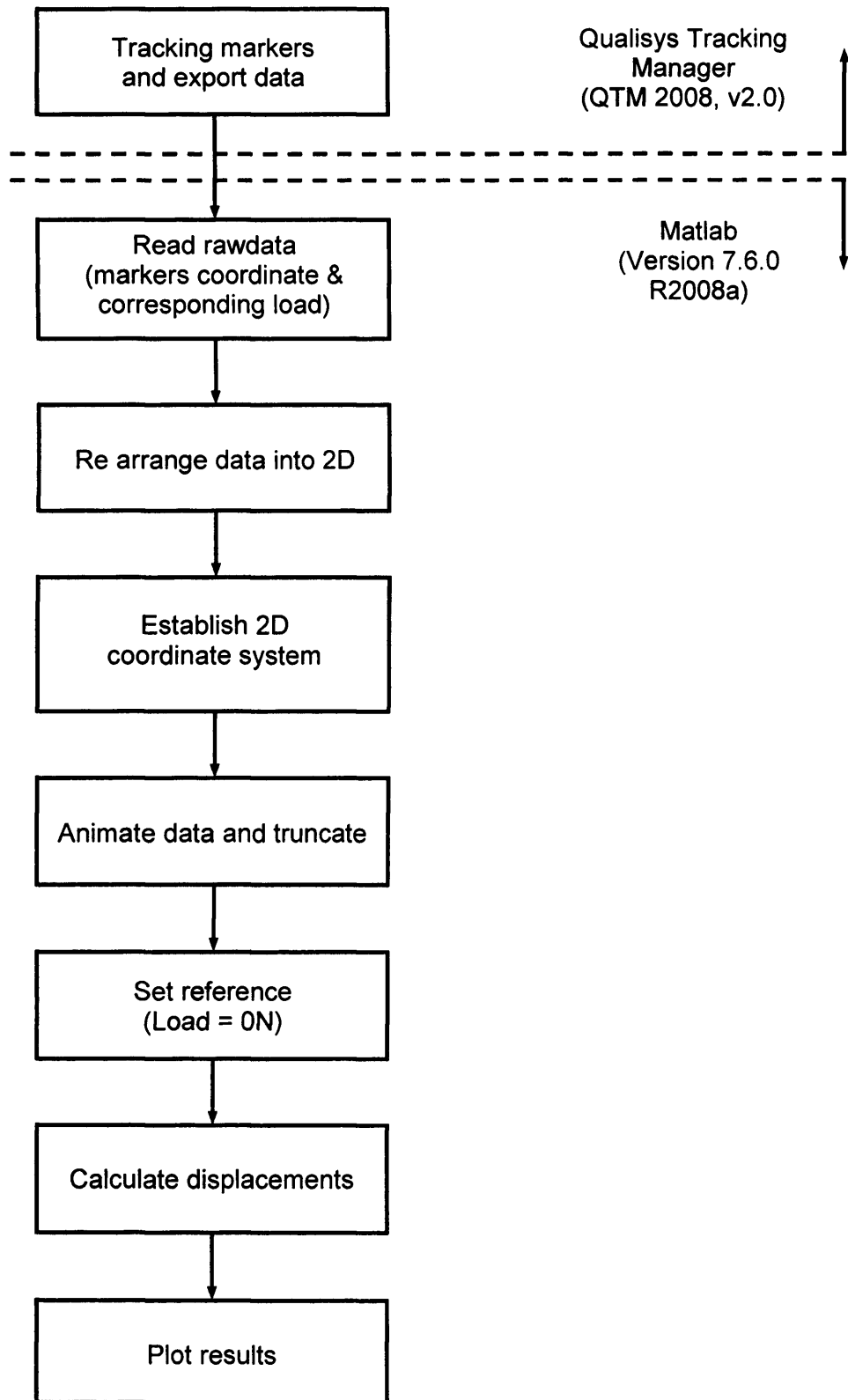Figure 2.17: Flowchart illustrating work flow in processing and analysing the motion capture data.
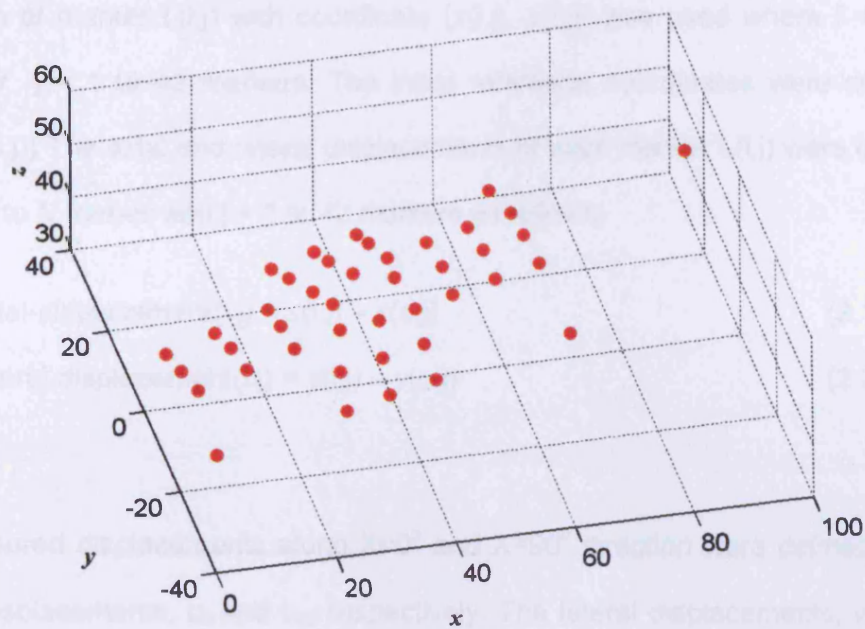
Figure 2.18: Animating raw 3D data using a Matlab programme.
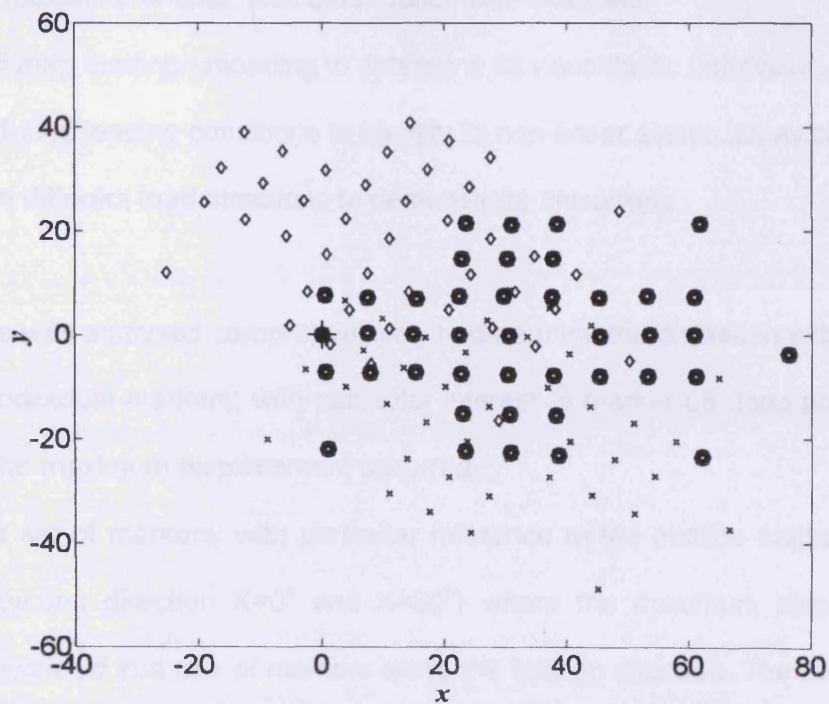
Figure 2.19: The coordinates of the raw data were transformed to establish a consistent 2D coordinate system. Initial markers were first translated to set L1 as origin; then rotated to align the midline marker parallel to *x*-axis.
(diamonds → crosses → bold circles).

A notation of marker L(i,j) with coordinate (x(i,j), y(i,j)) was used where i = 11 to N frames for j = 1 to 42 markers. The initial reference coordinates were defined as (x(o,j), y(o,j)) The axial and lateral displacements of each marker L(i,j) were computed for i = 11 to N frames and j = 1 to 42 markers as follows;

$$\text{axial-displacement}(i,j) = x(i,j) - x(o,j) \tag{2.1}$$

$$\text{lateral-displacement}(i,j) = y(i,j) - y(o,j) \tag{2.2}$$

The measured displacements along X=0° and X=90° direction were defined as axial (active) displacements, u_0 and u_{90} respectively. The lateral displacements, v_0 and v_{90}, were the passive displacements along X=0° and X=90° direction respectively.

From the displacements data, skin deformation was analysed:

(i)   during loading-unloading to determine its viscoelastic behaviour;

(ii)   during loading conditions to identify its non-linear elastic behaviour and;

(iii)   in different load directions to demonstrate anisotropy.

And the data was analysed comprehensively to determine the displacements of

(i)   individual markers; with particular interest to marker L5 (load point) where the maximum displacement occurred.

(ii)   a set of markers; with particular reference to the midline markers, (along loading direction X=0° and X=90°) where the maximum displacements occurred in a row of markers along the loading direction. The ratio of axial displacement (u_{90}/u_0) was also computed.

(iii)   the whole marker set in the xy-plane, where the analysis provided information on the distribution of the displacement for the whole area of testing.

The results from these analyses were used to describe the deformation of human skin accurately. Where appropriate, the mean, standard deviation (SD) and variance were determined (i) to examine the accuracy of the measurement system; and (ii) to study the variation of skin deformation.

The ultimate aim of this research was to determine the mechanical properties of human skin, thus, this displacement data generated by the experiments was later used for the computation. The details of this process are discussed in Chapter 4.

2.7.1 Results

All the scheduled experiments were carried out efficiently and data was successfully obtained for all subjects. The experimental protocol was non-invasive as neither pain was reported nor damage to the skin was observed; and the repeatability test results (Figure 2.15) confirmed its repeatability. The loading procedure was found reliable based on the $X=0° \pm 20°$ test. Calibration results confirmed system accuracy. More importantly, the movement of the markers successfully tracked using QTM and the data served as input to the programme written to compute markers displacements.

2.7.1.1 Viscoelastic behaviour

Skin deformation for Subject 1 was considered. The force applied in $X=0°$ direction is shown in Figure 2.20 to indicate the loading and unloading curve. It could be observed that the loading curve is almost linear and consistent. This indicates that the method of applying load in the experiments was reliable. The load had induced skin deformation and the displacements were measured. Figure 2.21 shows the axial displacement, u_0, of selected markers in the midline (L1, L3, L5, L7 and L9). The graphs clearly demonstrate hysteresis and this indicates the viscoelastic behaviour of human skin (Taylor, 1990). This effect was observed for all 5 subjects and proves

that the experiments are capable of generating compelling data on the viscoelastic nature of human skin which can be used for further investigation. For the same test, the measured lateral displacement, v_0, for the midline markers (L1 to L9) is shown in Figure 2.22. It is observed that the displacements are minimal producing an average discrepancy of 0.25 mm. Again, this proves that the loading method was reliable.
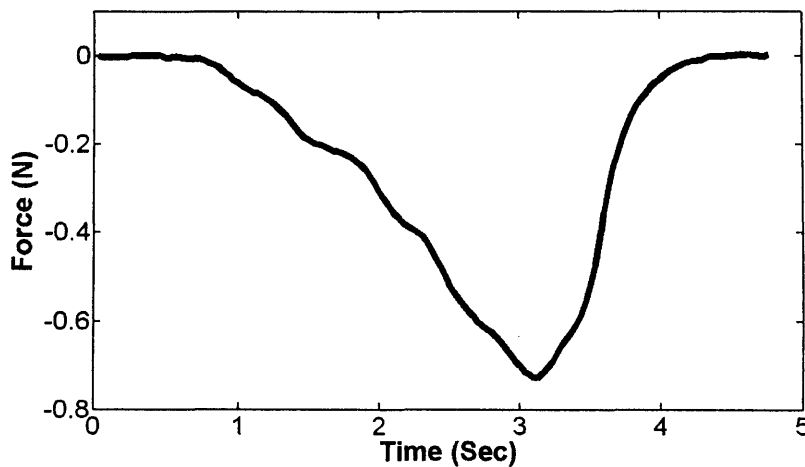
Figure 2.20: The force applied in the X=0° direction: loading and unloading curve.
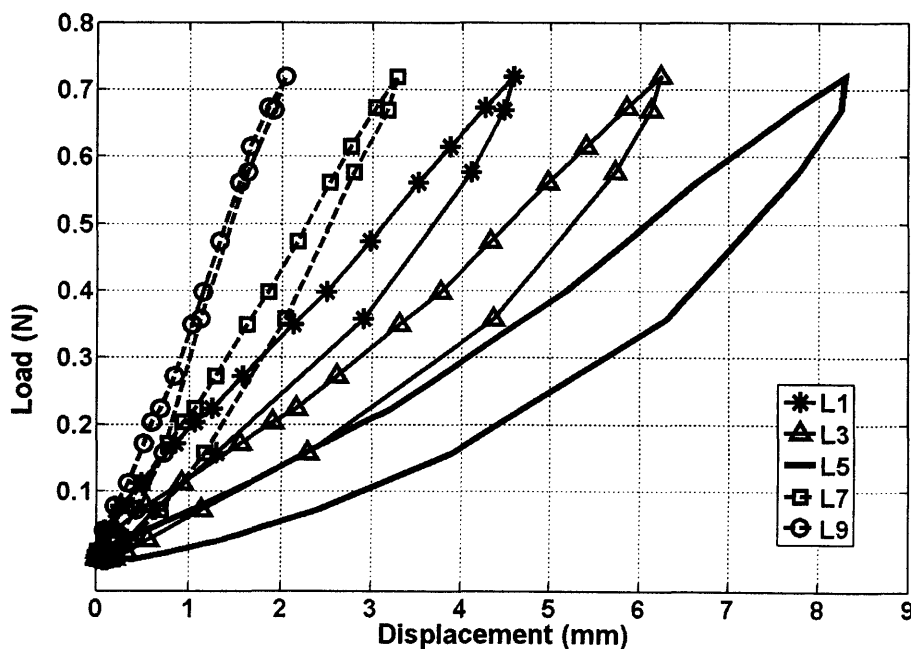
Figure 2.21: The load-displacement graph for 5 markers along the X=0° loading direction (L5 was the load point).
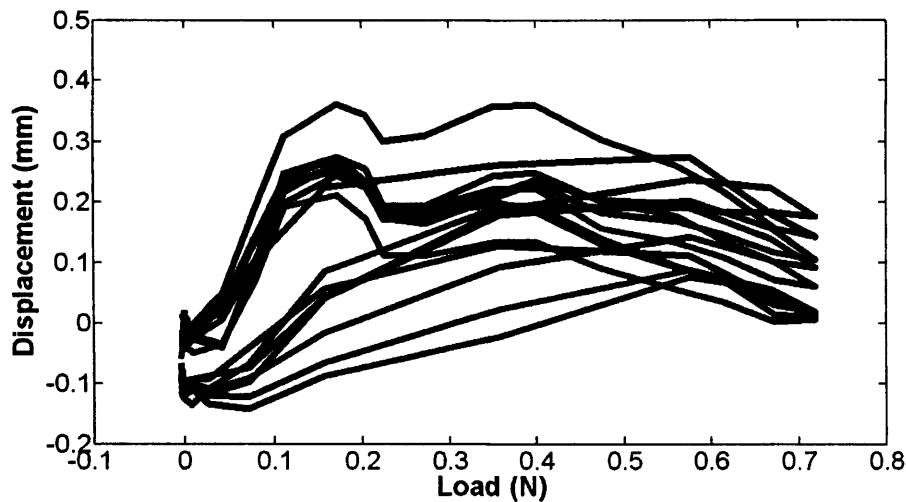
Figure 2.22: Lateral displacement for the midline markers (L1 to L9) along load direction (X=0°).

2.7.1.2 Nonlinear behaviour

Initial analysis focused on the displacement of individual markers on individual subject. As an example, the results for Subject 1 is presented for the case of load applied up to 1.45 N in the X=0° direction (Figure 2.23) to analyse the trend of gradual displacements of individual markers.
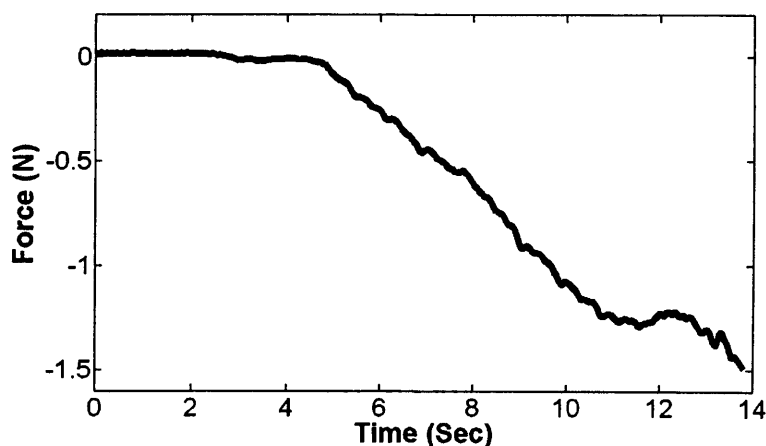
Figure 2.23: The recorded load (X=0°, Subject 1). Observe that the load has been applied at a reasonably consistent rate with low noise at below 1N.

The graph in Figure 2.24a shows the load-displacement curves for individual markers (L1 to L9) along the load direction (X=0°, Subject 1). Figure 2.24b shows a similar graph but for the midline markers transverse to the loading direction. Both graphs portray skin nonlinear elasticity.
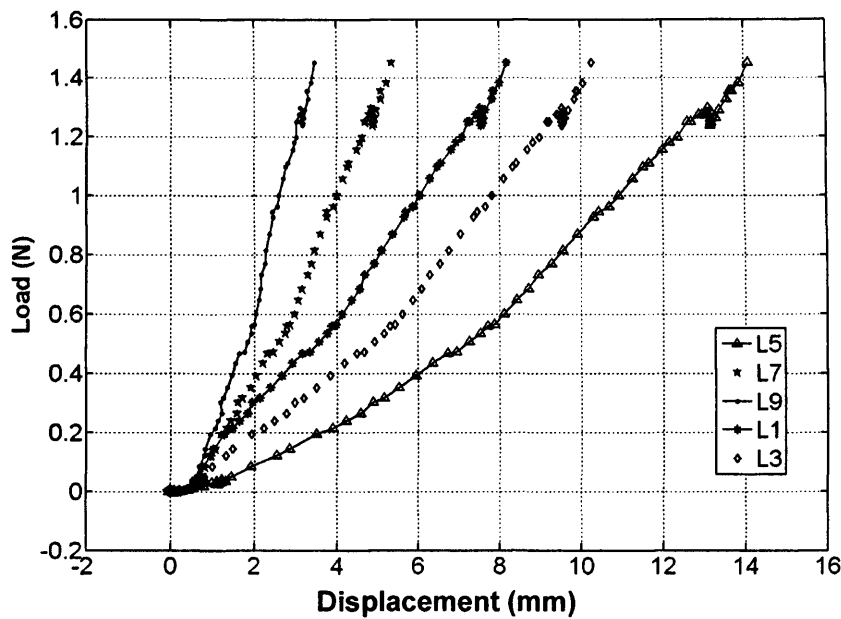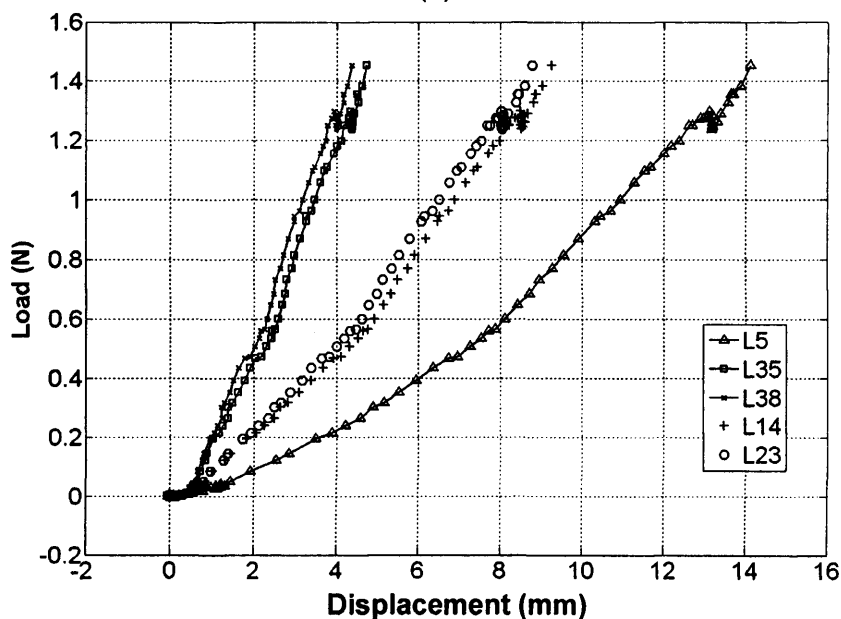
Figure 2.24: The load-displacements graphs at the midline (a) along; and
(b) transverse to loading direction (X=0°, Subject 1)

For the same test and set of markers, a displacement-markers graph is shown in Figure 2.25 to observe skin deformation along the loading direction (x=0°). Note that load was applied at marker L5 (load point) towards L9; and marker L1 and L9 were initially 32 mm away from L5. It could be observed that the graphs produced an approximate *bow wave* shape.
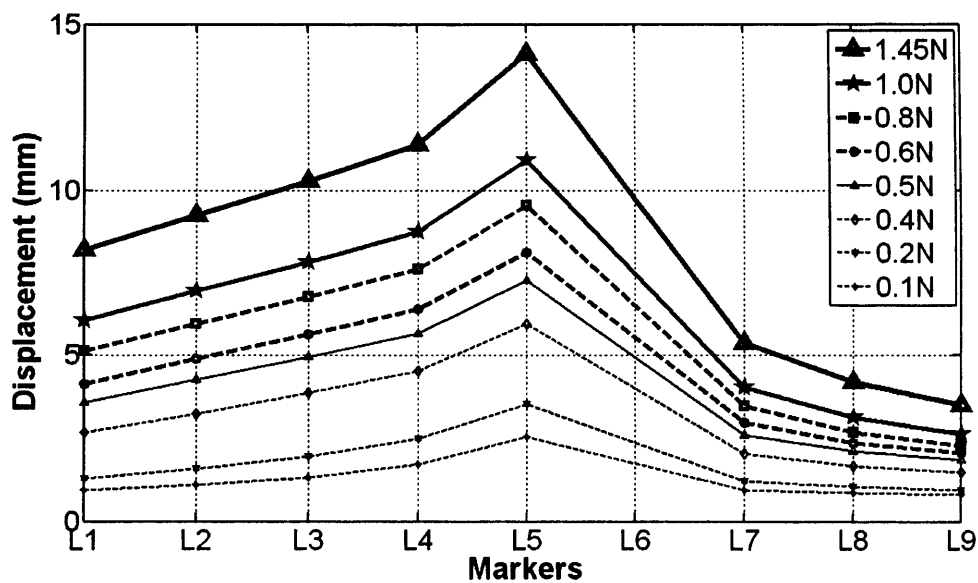
Figure 2.25: The axial displacements for midline markers along load direction
(X=0°, Subject 1).

Next, the results for skin deformation for 5 subjects (left arm) based on the load applied in X=0° and X=90° directions are presented. Figure 2.26 shows the load-displacement graphs for axial displacements, u_0 and u_{90}, illustrating the gradual displacement of marker L5 (load point). Figure 2.27 shows the axial displacements, u_0 and u_{90}, for the midline markers along the X=0° and X=90° respectively. Figure 2.27a shows the displacements of the midline markers (L1 to L9) parallel to the loading direction (X=0°) at 1N for 4 of the 5 subjects. For Subject 4, three markers merged when the loading approached 1N (at 0.8N), thus this data is omitted from the figure.

(a)

(b)
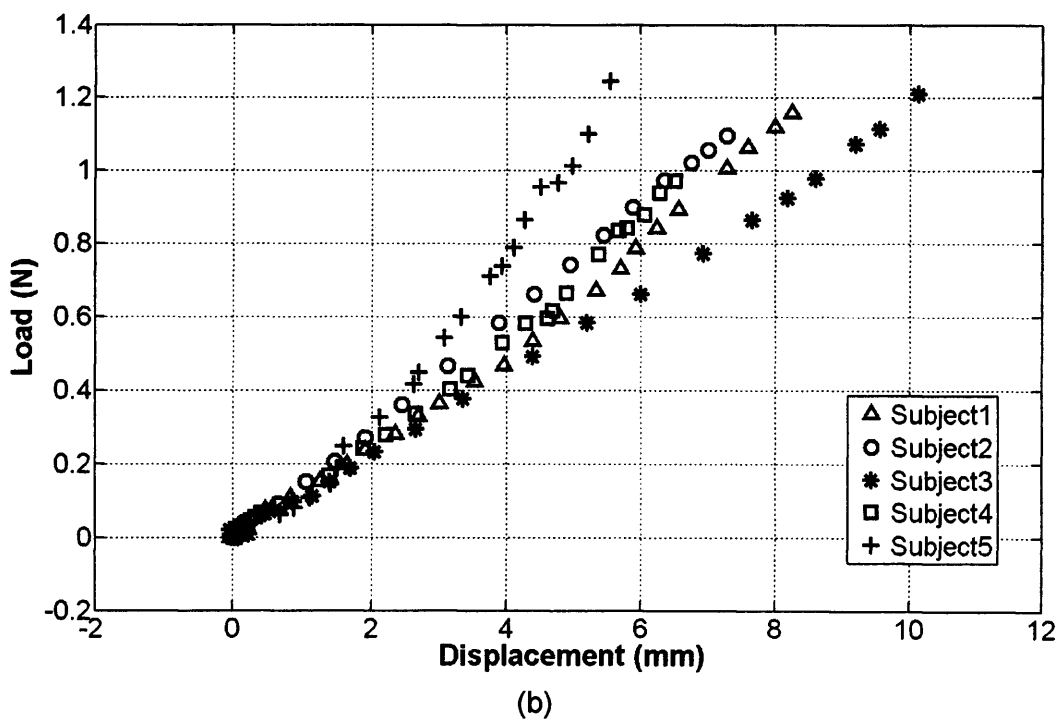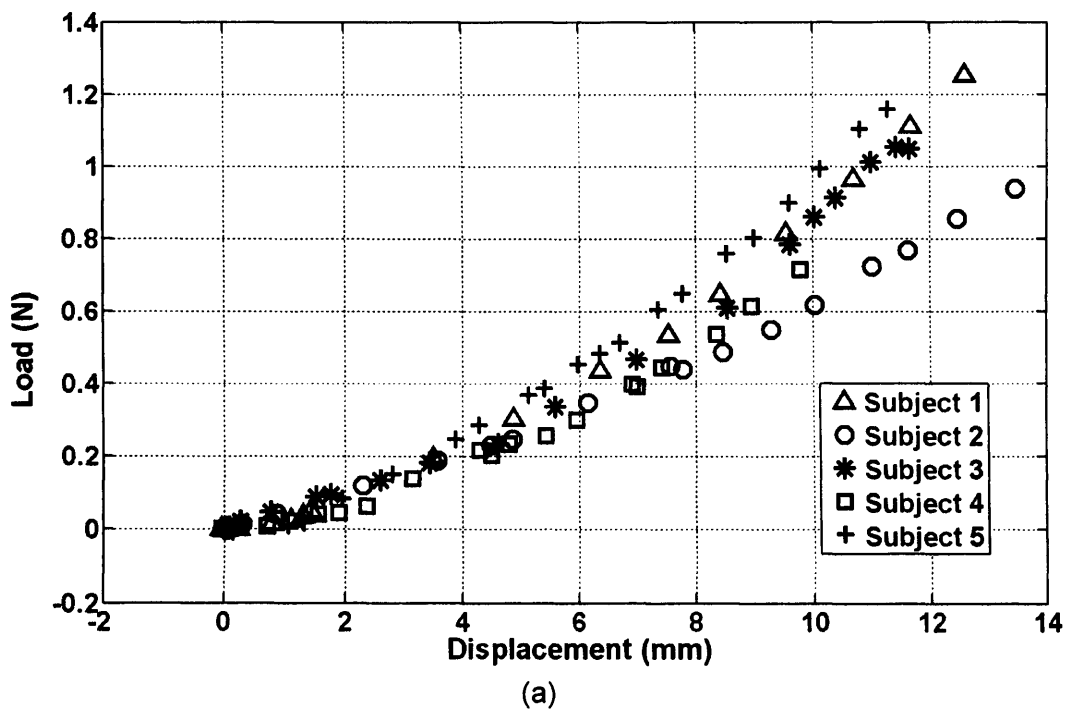
Figure 2.26: The load-displacements graphs at load point (L5) in (a) X=0° and (b) X=90° directions for 5 subjects' left arms.
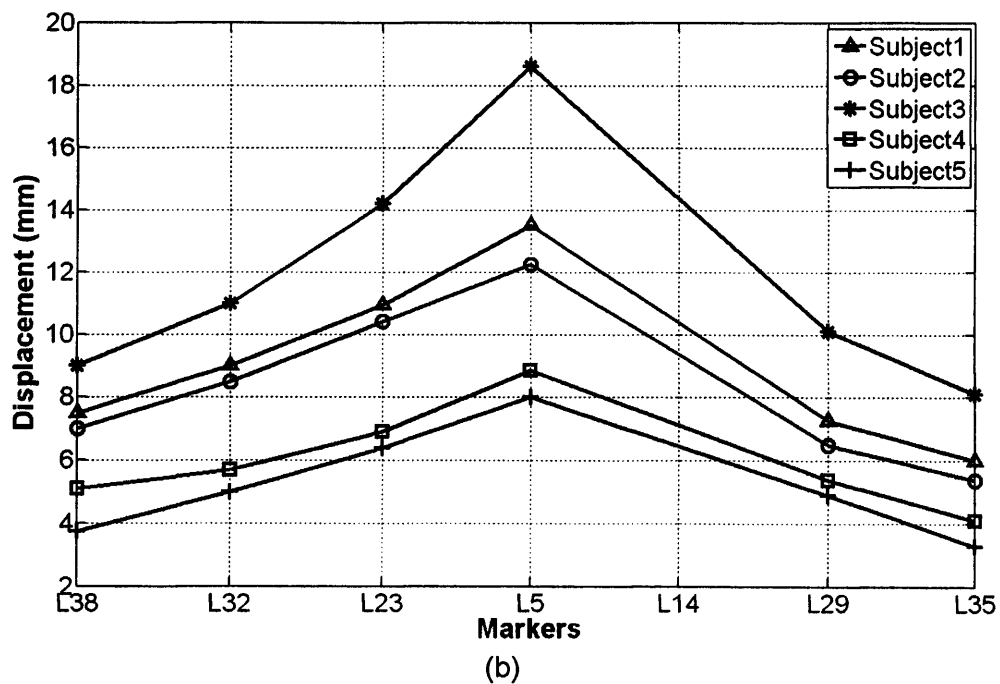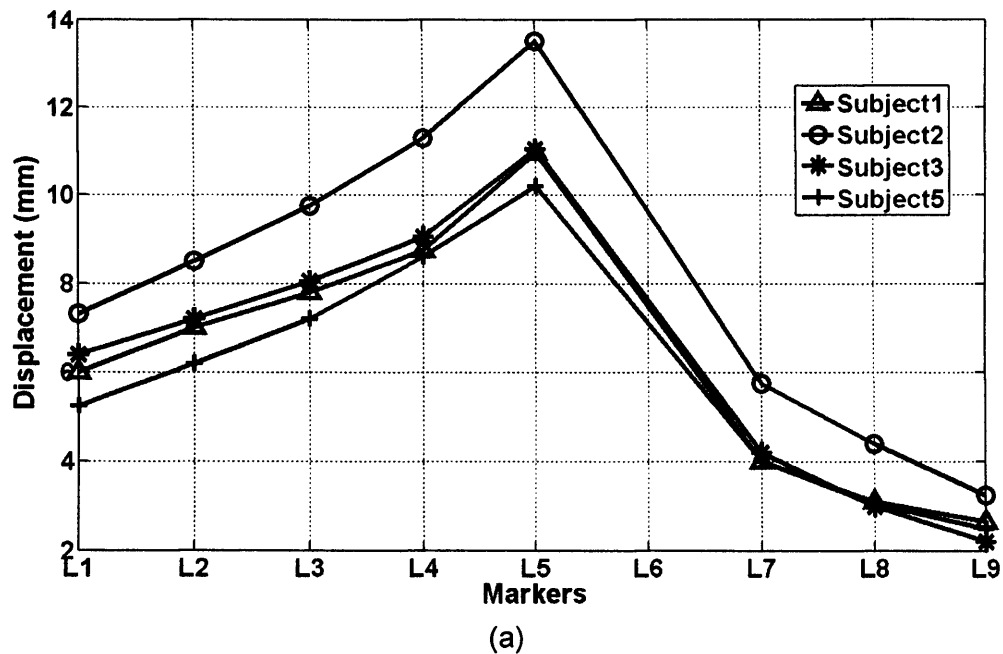
Figure 2.27: The displacement-markers graphs for the midline markers (L1 to L9) showing the axial displacements (a) u_0 in X=0° and (b) u_{90} in X=90° directions (1N, 5 subjects' left arms). Note that Subject 4 in (a) was omitted due to merged-markers when load reaching 0.8N.

2.7.1.3 Anisotropy

Skin deformation in different directions was observed to demonstrate the anisotropic behaviour of human skin. The results are presented in Figures 2.28 to 2.29 and Table 2.5. Figure 2.28 shows the maximum axial displacements for three subjects' left and right arm (at L5) in three different directions (X=0°, 45° and 90°). In all cases, the same amount of load (1N) was applied. However, it is observed for each subject that the amount of displacements was not the same for in every direction. This indicates the anisotropic behaviour of skin. Out of the three, Subject 3 showed the largest variation of the measured displacement for both arms (left and right) which shows that her skin was the most anisotropic. The graphs for the right arm (dotted line) show a more consistent trend that the left arm (continuous line).
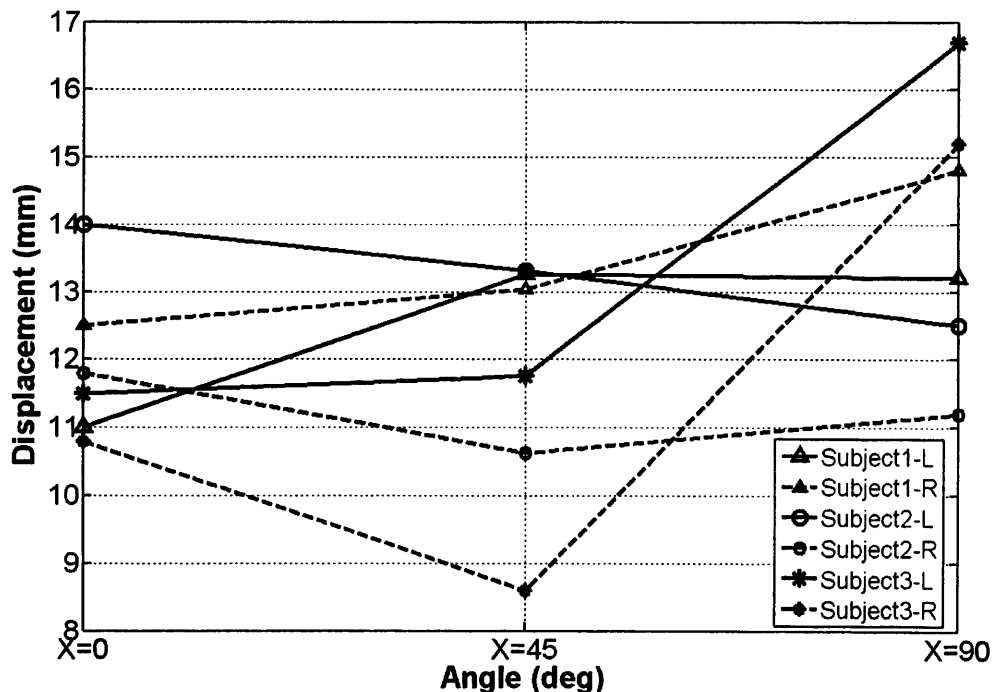
Figure 2.28: The axial displacements, u, for three subjects' left arm (continuous line) and right arm (dotted line) in three directions (X=0°, 45° and 90°).

As an alternative representation, the axial displacement was split into its x- and y-components. Considering X=0° as x-axis and X=90° as y-axis, the displacements (namely x-displacement and y-displacement) were observed and the results are shown in Figure 2.29. By doing this, the trend of the anisotropy could be visualised more clearly.
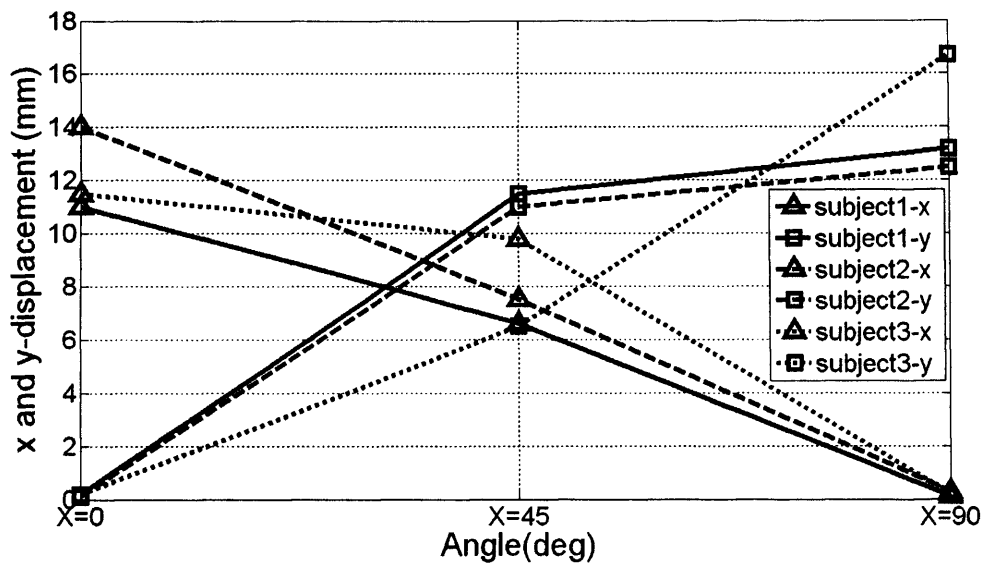
(a)
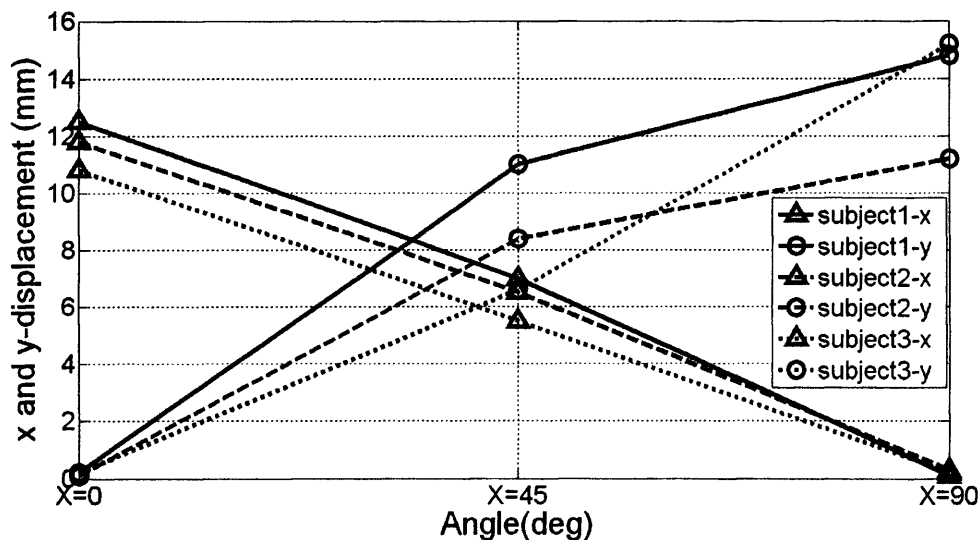
(b)

Figure 2.29: The displacements in three load orientation for three subjects at 1N load: (a) Left arm and (b) Right arm

The Table 2.5 shows, for all 5 subjects, the ratio of axial displacements (u_{90}/u_0) for loading directions $X=90°$ (for u_{90}) and $X=0°$ (for u_0) at 1N load, which again exhibiting the anisotropic behaviour of human skin. It could be observed for all subjects that the ratio is consistent between the left and right arms. If the ratio ≈ 1, it shows that the anisotropy is not significant. Therefore, the results in Table 2.5 show that the skin of Subject 3 and Subject 4 behaved the most anisotropically. However, the skin stiffness was dominant in the opposite directions.

Table 2.5: Ratio of axial displacement ratio (u_{90}/u_0) for 5 subjects at 1N load.

	Subject 1		Subject 2		Subject 3		Subject 4		Subject 5	
Age	25		26		42		23		26	
Gender	F		M		F		M		M	
Arm	L	R	L	R	L	R	L	R	L	R
U_{90}/u_0	1.2	1.18	0.89	0.95	1.45	1.41	0.63	0.66	0.74	0.71

2.7.1.4 Discrete deformation distribution

As the ultimate aim of this study was to determine the mechanical properties of human skin, the final challenge in conducting the experiments was to generate data that could be readily input to an inverse FEA. For that reason, skin planar deformation in the xy-plane was computed for the whole marker set (whole area of testing). At the initial stage, the movement of markers in xy-plane was observed. As an example, Figure 2.30 shows the trail of the markers movement for Subject 1 when load (0 to 0.7N) applied in the $X=0°$ direction. From that data, a representation similar to an FEA output was generated (Figure 2.31). It shows the undeformed (reference) and deformed skin ($X=0°$, 0.7N, Subject 1).
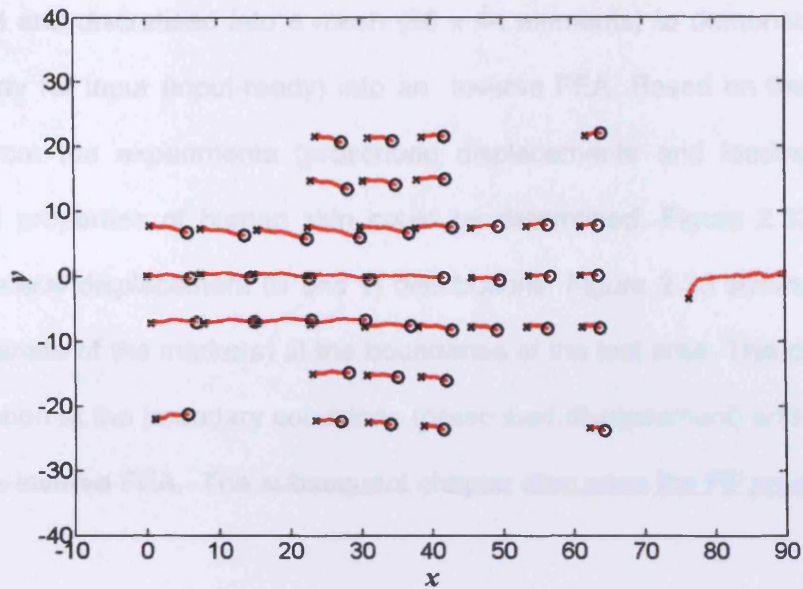
Figure 2.30: The trail of the markers movement (*xy*-plane). The crosses are the original position of the markers.The cross to the far right represents the marker attached to the nylon filament. Initially, it rested on the arm. The circles are the position of markers at 0.7N load. The red lines show the trails of the markers movement.
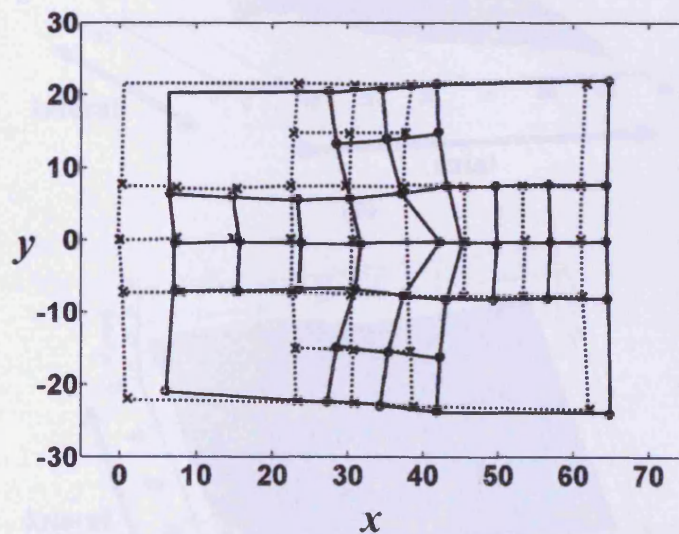
Figure 2.31: Using the experimental data, this illustration was produced to replicate the FEA output. This undeformed-deformed visualisation is a common feature to FEA. The dotted lines show the original (undeformed) position and the continuous lines show the deformed skin area (membrane) at 1N load.

For the same data (X=0°, 0.7 N, Subject 1), the displacement distribution was interpolated and discretised into a mesh (56 x 44 elements) to demonstrate that the data is ready for input (input-ready) into an inverse FEA. Based on the information obtained from the experiments (prescribed displacements and loading data), the mechanical properties of human skin could be determined. Figure 2.32 shows the axial and lateral displacement (u and v) distributions. Figure 2.33 shows the original data (coordinate of the markers) at the boundaries of the test area. This data provided the information at the boundary conditions (prescribed displacement) and was used to develop the inverse FEA. The subsequent chapter discusses the FE procedure.

(a)

(b)
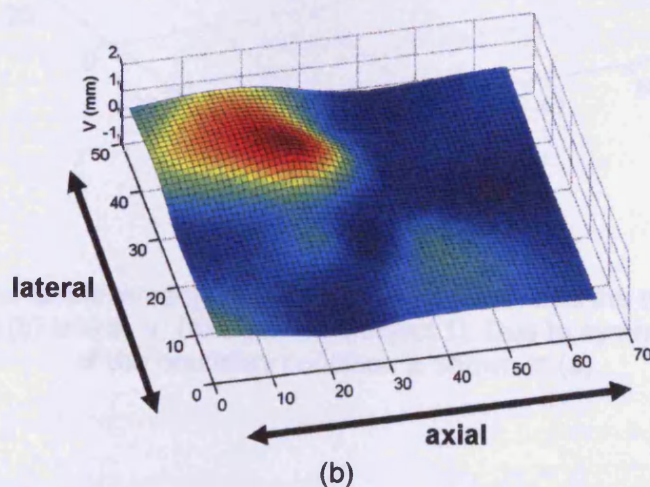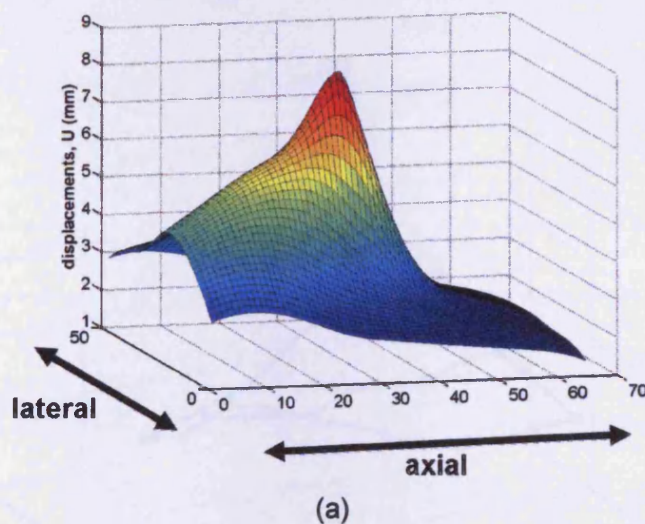
Figure 2.32: The distribution of the: (a) axial displacement and (b) lateral displacement (X=0°, 0.7N, Subject 1).
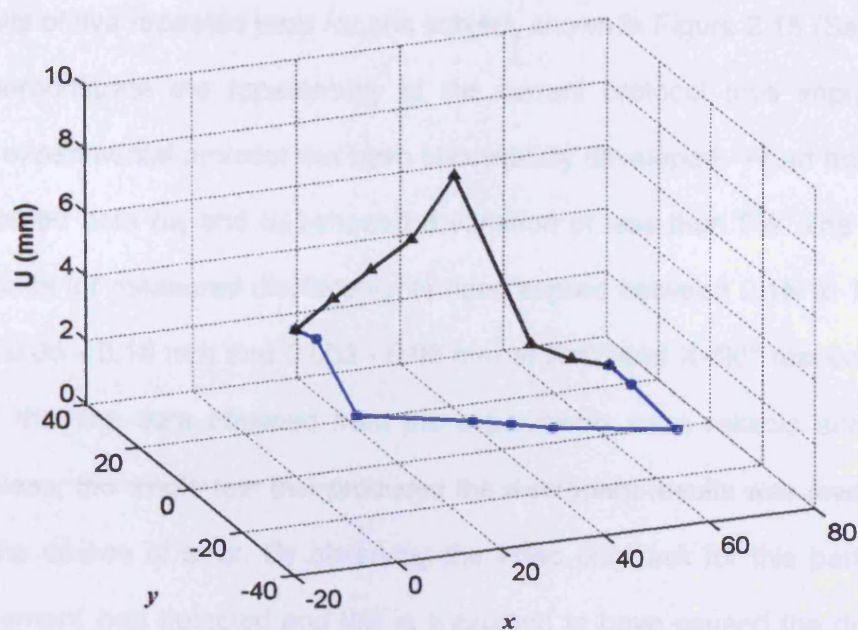
(a)
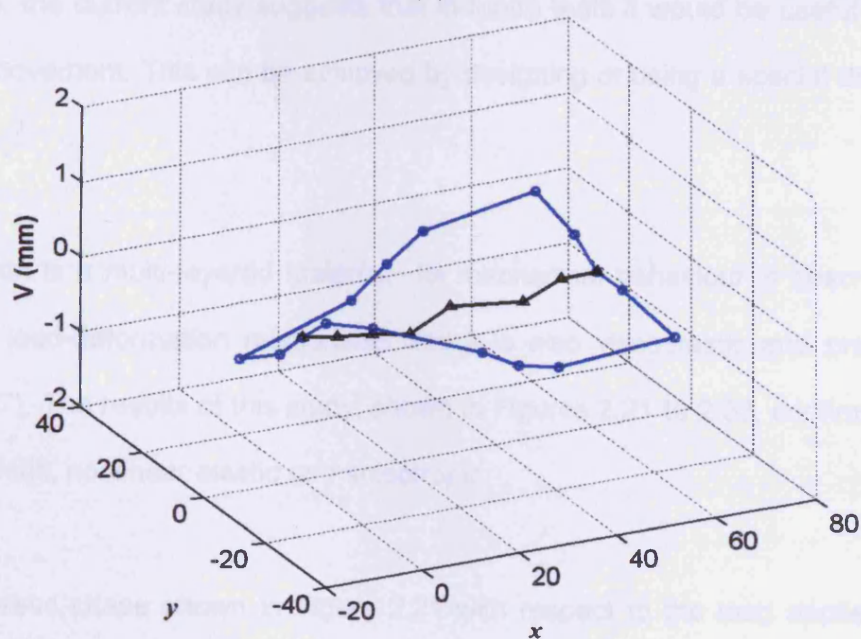
(b)

Figure 2.33: The displacements at the boundaries (blue) and the midline (black) for (a) axial, u; and (b) lateral, v, (X=0°, 0.7N, Subject 1). Due to symmetry, only the half of the boundary condition is shown in (a).

2.7.2 Discussion

The results of five repeated tests for one subject, shown in Figure 2.15 (Section 2.4.7), clearly demonstrate the repeatability of the current protocol thus implying that a practical experimental protocol has been successfully developed. Apart from one test, the measured data (u_0 and u_{90}) showed a variation of less than 5%. The overall SD and variance for measured displacements (load applied between 0.1N to 1N), ranges between 0.05 - 0.18 mm and 0.003 - 0.05 mm at $X=0°$ and $X=90°$ respectively. This indicates that the data obtained from the experiments were reliable and accurate. Nevertheless, the single test that produced the discrepant results was investigated to identify the source of error. By observing the video playback for this particular test, arm movement was detected and this is presumed to have caused the discrepancy. Therefore, the current study suggests that in future tests it would be useful to restrict the arm movement. This can be achieved by designing or using a special device (e.g. a fixture).

Human skin is a multi-layered material. Its mechanical behaviour is described by a nonlinear load-deformation relationship and it is also viscoelastic and pre-stressed (Tran 2007). The results of this study, shown in Figures 2.21 to 2.33, confirm that skin is viscoelastic, nonlinear elastic and anisotropic.

The hysteretic shape shown in Figure 2.21 with respect to the load applied (Figure 2.20), clearly confirms viscoelastic behaviour. Five markers (L1, L3, L5, L7 and L9) were observed. When a 0.72 N load was applied along $X=0°$, the maximum displacement was 8.3 mm at the point of applied load (L5) and the minimum displacement was only 2 mm at L9. Figure 2.22 shows the lateral displacement for the midline markers during for the same test loading condition. The results show that the lateral displacements are less than 0.4 mm with an average of 0.25 mm confirming

that the control measures imposed during the experiments were successful and the results were reliable.

Investigating individual subjects (taking Subject 1 as the example), Figures 2.23 to 2.25 confirms that the experimental and loading protocol produced significant results to demonstrate skin nonlinear deformation. Skin deformation at the midline parallel to the load direction for various load steps was also observed. One interesting point to observe is the approximate *bow wave* shape of the graphs (Figure 2.25), where the markers to the left of the load point (L1 to L4) displaced more than the markers to the right (L7 to L9). This is similar to the experimental results obtained by Evans et al (2007) using the DIC technique. A wrinkle could be observed at the region (between L5 and L7) where the displacement drastically dropped. This effect (skin tension-compression) is further investigated in the subsequent section (Section 2.8) by measuring the strains. The result for all five subjects is shown in Figures 2.26 and 2.27, where similar effect was observed. This confirms that the experiments are capable of generating compelling data on the nonlinearly elastic nature of human skin which can be used for further analysis.

Based on the results for five subjects skin deformation (Figures 2.26 to 2.29 and Table 2.5), several initial findings were observed and are worth discussed here.

i. The load-displacements curves (Figure 2.26) are different for each subject, thus implying that the degree of skin nonlinear elasticity for all subjects varies. Based on the five subjects, the overall mean ± SD for the axial displacement, u_0, was found to be 11.7 ±1.6 mm for a 1N load applied at X=0°, while the axial displacement, u_{90}, was 12.3 ± 3.3 mm for a 1N load applied at X=90°. For the

same tests, the displacement-marker graphs are shown in Figure 2.27 to exhibit the variation of the approximate *bow wave* shape for all subjects.

ii. It has been described in Section 1.3.3 (Chapter 1) that the biomechanical properties of skin differ according to age and gender. The current study analysed the skin deformation for five subjects (different age and gender, Figures 2.26 to 2.29 and Table 2.5) and initial observations confirm to this. For example, Subject 3 (F, age 42) skin deformed the most compared to the others (M & F, mean age 25). Subject 3 was intentionally recruited to compare older skin to younger skin; and as expected younger skin is stiffer. Subject 5 (M, 26) skin was the stiffest of all and in both directions (X=0° and X=90°). The skin of two female subjects (age 42 and 25) deformed more in the X=90° compared to X=0° (displacement ratio >1). An interesting potential study could be carried out to further investigate whether all female skins behave similarly.

iii. Experiments were also performed to analyse the deformation behaviour of skin when it was stretched in various directions. The results of applying load in the X=0°, 90 and 45 direction (Figure 2.28 and 2.29) show that between subjects, the trend of skin deformation varied significantly. However, for each subject, skin was found to deform in a similar manner for the left and right arm. This merits a further investigation.

iv. For all five subjects, the ratio of axial displacements, (u_{90}/u_0), was determined to compare skin deformation at 1N load in X=0° and X=90° direction. The results (Table 2.5) shows that the ratio ranges from 0.63 to 1.45 with a mean ± SD of 0.982 ±0.34 and 0.982 ±0.32 for left and right arms respectively. They explicitly show the anisotropy of skin. Table 2.5 also shows that the (u_{90}/u_0) ratio for

loading of 1N to the left and right arm for each subject was similar. This data can be used to investigate the anisotropic behaviour of human skin. However, more samples (subjects and loading directions) must be tested.

Figures 2.30 to 2.32 demonstrate that the data generated by the experimental protocol are useful and it could produce output that is similar and comparable (having common features) to FEA outputs. Figure 2.32 shows the deformation distributions in 2D which are discretised into elements. The results are in very good agreement with the results computed for the midline markers earlier (*bow wave* shape, Figure 2.25) and similar to DIC (Evans, 2009). Figure 2.33 shows that the data for the boundaries at the area of testing could easily be extracted for further use. These data was used as prescribe displacements and input into the FE programme with an optimisation procedure to determine the mechanical properties of human skin. The details are presented in Chapter 4.

Despite generating reliable and accurate data, this experiment could not be used to investigate skin wrinkling. It was visible that wrinkling occurred between L5 and L7; however, based on the current optimum marker configuration, it could not be seen by the cameras. More data points (higher resolution) could be created by placing more markers but would be compromised by markers merging and overlapping. A possible solution would be to use smaller markers, which certainly requires a further and thorough investigation to assure its success. As an alternative, the experimental procedure was conducted using the DIC system but a similar problem was encountered: data loss at the area of wrinkle. The details are presented in Chapter 5.

2.8 Quantifying strain

In addition to displacement, strain is an important parameter to determine when studying skin biomechanics. It describes the deformation of a solid in relation to applied stress, moreover, for the biomechanics of skin, the stretch ratio, λ, is an important property (Fung 1993) which is determined using strain data. In terms of strain analysis on human skin, a comprehensive study to analyse strain distribution has been reported utilising uniaxial tension test (Wan Abas and Barbenel 1982) and biaxial tension test (Wan Abas 1994). The actual surface distribution produced during the uniaxial tension test was measured at the test zone.

In this study, strain was measured to demonstrate the significance of the data generated from the developed motion capture system as described in the previous section. Screen and Evans (2009) reported measured strain distributions in the tendon using confocal microscopy and FEA. However, no similar study, combining motion analysis methods with FEA, has been reported. Therefore, the current study aimed to develop such a technique.

Raw QTM marker coordinates were input and, as in the displacement computation, the same coordinate system was established; where the crease-to-crease midline was defined as the $X=0°$ loading axis. 2D analyses were carried out to investigate the in-plane strains. Two frames, reference, undeformed and deformed were considered. Upon applying a load, the markers moved from the reference frame through sequential deformed frames. Based on the reference frame, the coordinate of markers $(x(i,o), y(i,o))$ were set as nodes and elements were constructed by adjoining the nodes using a Delaunay mesh (Delaunay function, Matlab, The Mathworks, Inc.). The importance of the Delaunay mesh has been recognised (Dyer 2007) and it is often

used because it guarantees optimal angles and for its fast triangulation algorithms. Strains were deduced from the strain-displacement matrix, commonly known as the B-matrix, $[B]$ in finite element theory. For the triangular elements the B-matrix was calculated as follows:

$$[B] = \left(\frac{1}{\Delta}\right)\begin{Bmatrix} y_2 - y_3 & y_3 - y_1 & y_1 - y_2 \\ x_3 - x_2 & x_1 - x_3 & x_2 - x_1 \end{Bmatrix}$$

$$\Delta = x_1(y_2 - y_3) + x_2(y_3 - y_1) + x_1(y_1 - y_2) \tag{2.3}$$

Where $(x_1, y_1), (x_2, y_2)$ and (x_3, y_3) are the coordinates of the corners of the triangle.

As described by Screen and Evans (2009), the strain was then determined in a 2x2 tensor form by premultiplying a matrix containing the displacements u, v of the three corners of the triangle by the B-matrix

$$\begin{Bmatrix} \varepsilon_{11} & \varepsilon_{12} \\ \varepsilon_{21} & \varepsilon_{22} \end{Bmatrix} = [B]\begin{Bmatrix} u_1 & v_1 \\ u_2 & v_2 \\ u_3 & v_3 \end{Bmatrix} \tag{2.4}$$

In the 2x2 strain tensor, the shear strain was split into two off-diagonal components, which were added together to give the more conventional Voight notation.

$$\begin{Bmatrix} \varepsilon_x \\ \varepsilon_y \\ \varepsilon_{xy} \end{Bmatrix} = \begin{Bmatrix} \varepsilon_{11} \\ \varepsilon_{22} \\ \varepsilon_{12} + \varepsilon_{21} \end{Bmatrix} \tag{2.5}$$

For each subject, strains were measured for load applied in different directions. The results were presented as contour colour plots using Matlab to visualise the measured axial, lateral and shear strain distributions.

2.8.1 Results

In general, the results of strain analysis are presented to;

(i)   demonstrate the usefulness of the developed experimental method as described earlier and;

(ii)   exhibit strain distribution at the testing area (human skin, forearm).

A complete set of results for Subject 1 is presented to reflect the essential work carried out in quantifying the strains for all subjects. Figures 2.34 to 2.45 show the displacement and corresponding contour plots of the measured strain for load applied in $X=0°$, 45 and 90 directions (0.7N). For each direction, the result consists of figures displaying the measured displacements, averaged strains at nodes and elemental strains. Histograms depicting the strain distribution across the elements are presented for Subject 1, Subject 2 and Subject 3 for comparison.

Strain results for Subject 1: X=0° direction
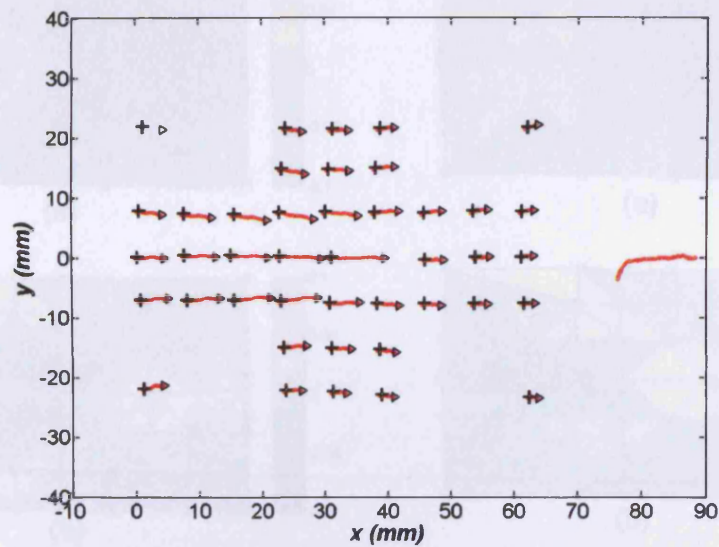
Figure 2.34: The movement of the markers during testing (X=0°):
from initial position (crosses) to load at 0.7N (triangles).

(a)

(b)
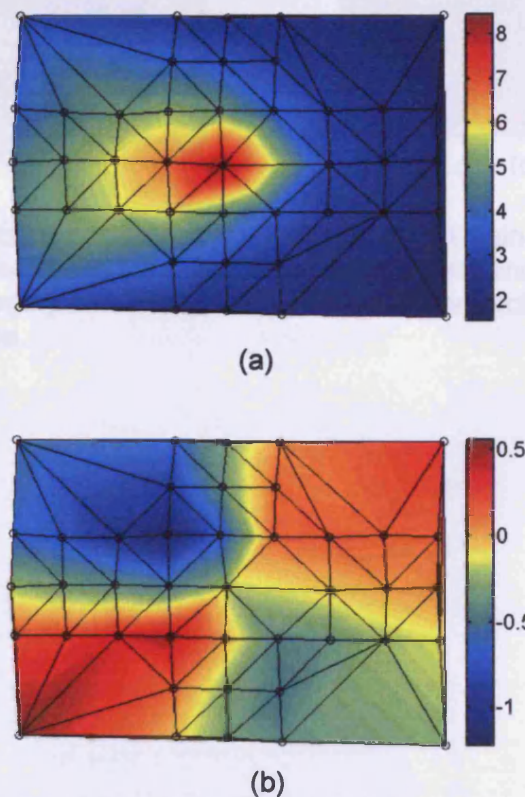
Figure 2.35: The displacement distribution: (a) axial, u_0; and (b) lateral, v_0 (in mm, X=0°). The triangular elements were constructed using Delaunay mesh by joining the nodes (markers).

(a)

(b)

(c)
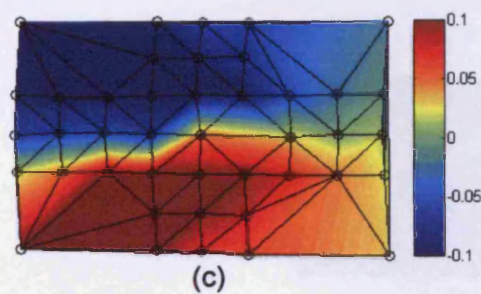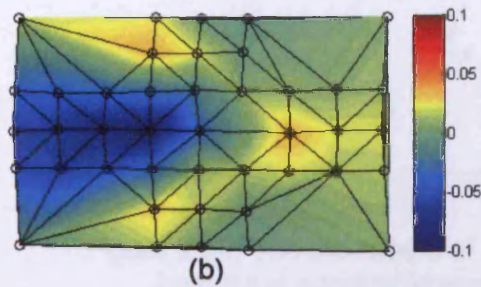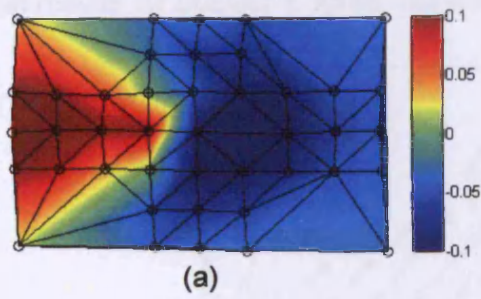
Figure 2.36: The strain distribution (X=0°): (a) axial (b) lateral and (c) shear; computed by averaging it values at nodes.

(a)

(b)

(c)
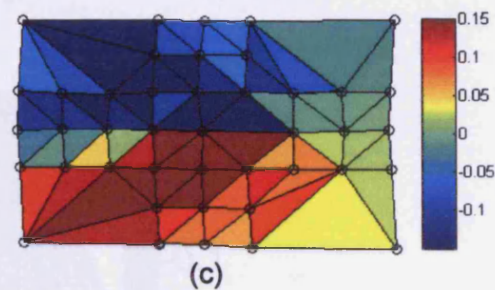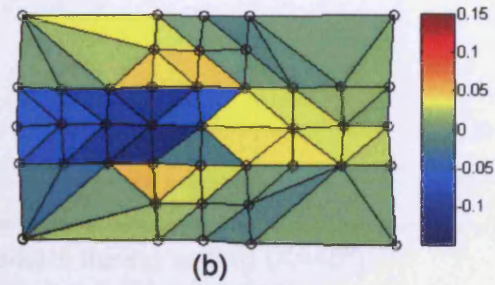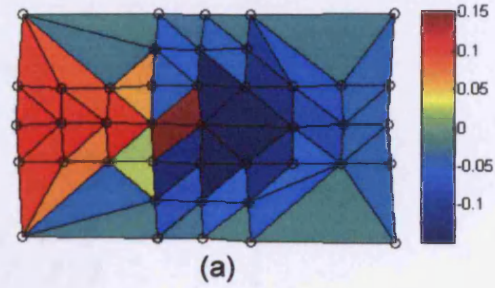
Figure 2.37: Strain distribution (X=0°): (a) axial (b) lateral and (c) shear; computed for each elements.

Strain results for Subject 1: X=45° *direction*
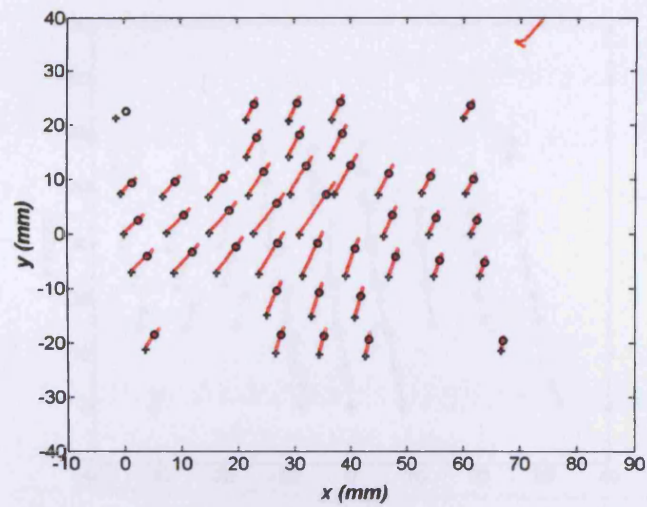
Figure 2.38: The movement of the markers during testing (X=45°): from initial position (crosses) to load at 0.7N (triangles).
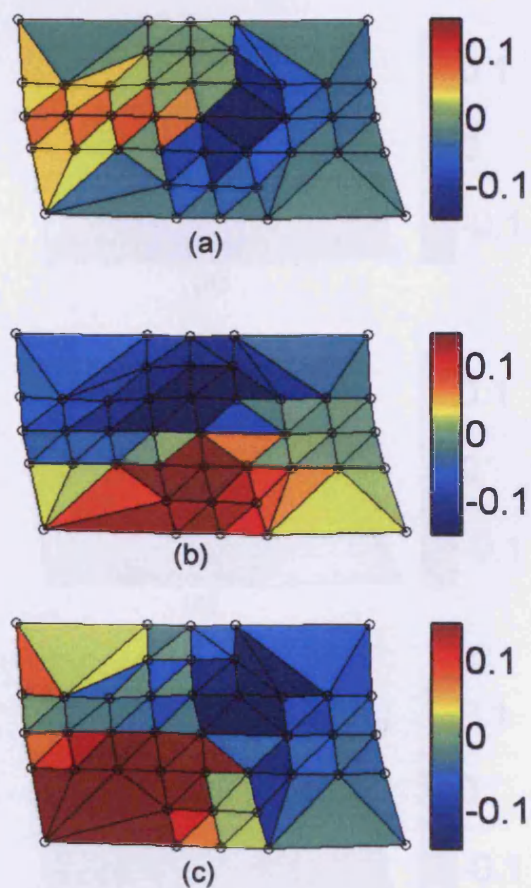
Figure 2.39: Strain distribution (X=45°): (a) *x*; (b) *y* and (c) *xy*; computed for each elements.

Strain results for Subject 1: X=90° direction
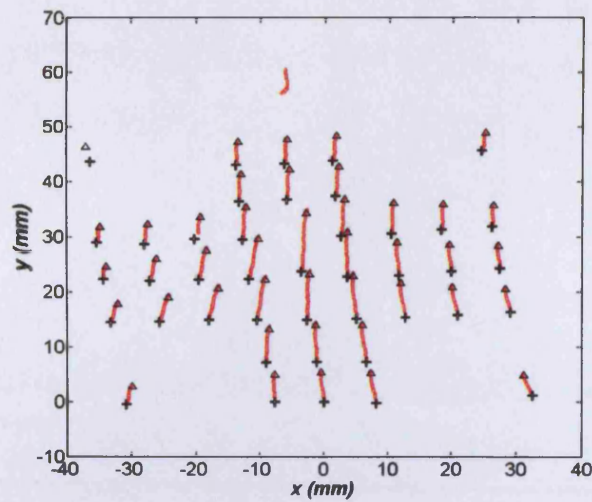
Figure 2.40: The movement of the markers during testing (X=90°):
from initial position (crosses) to load at 0.7N (triangles).
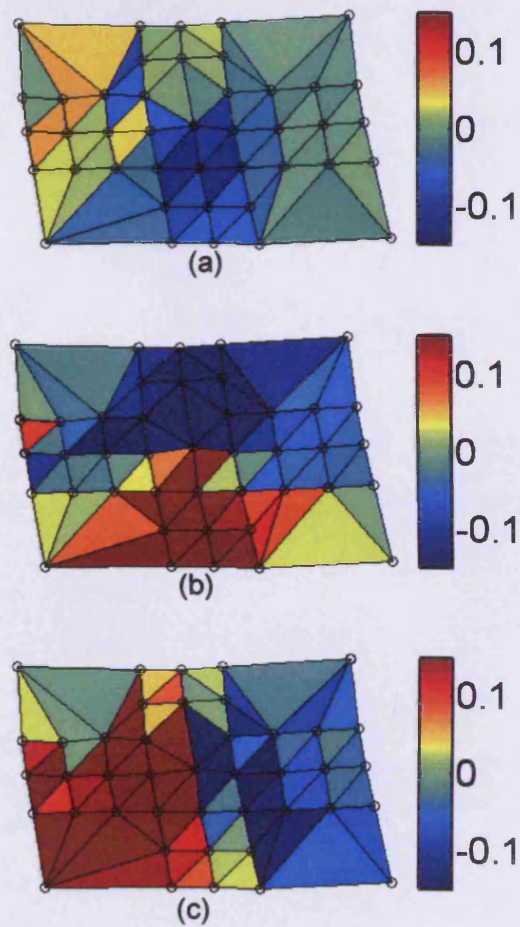
Figure 2.41: Strain distribution (X=90°):
(a) axial (b) lateral and (c) shear; computed for each elements

Subject 1   **Subject 2**   **Subject 3**
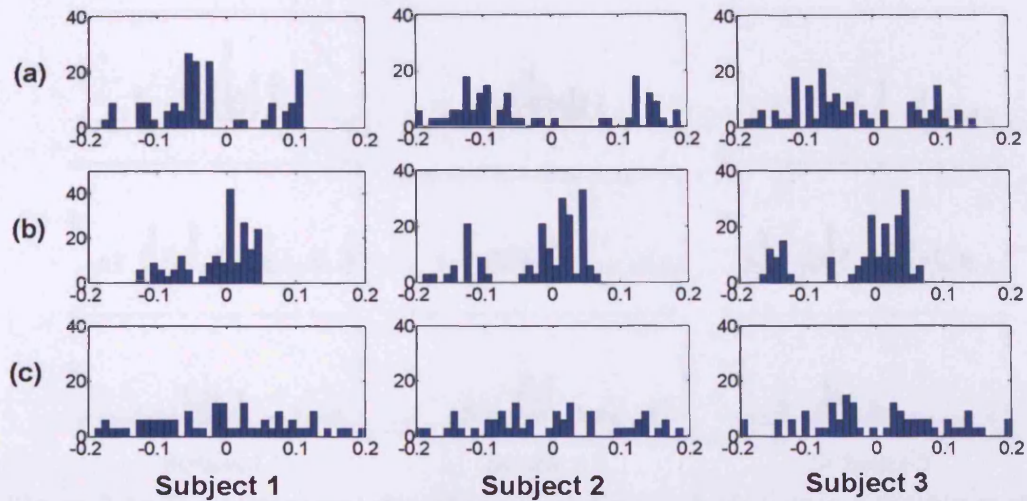
Figure 2.42 The histograms depicting the strain distribution across the elements
(a) axial strain, (b) lateral strain and (c) shear strain for subject 1,2,3 (0.7N, X=0°).
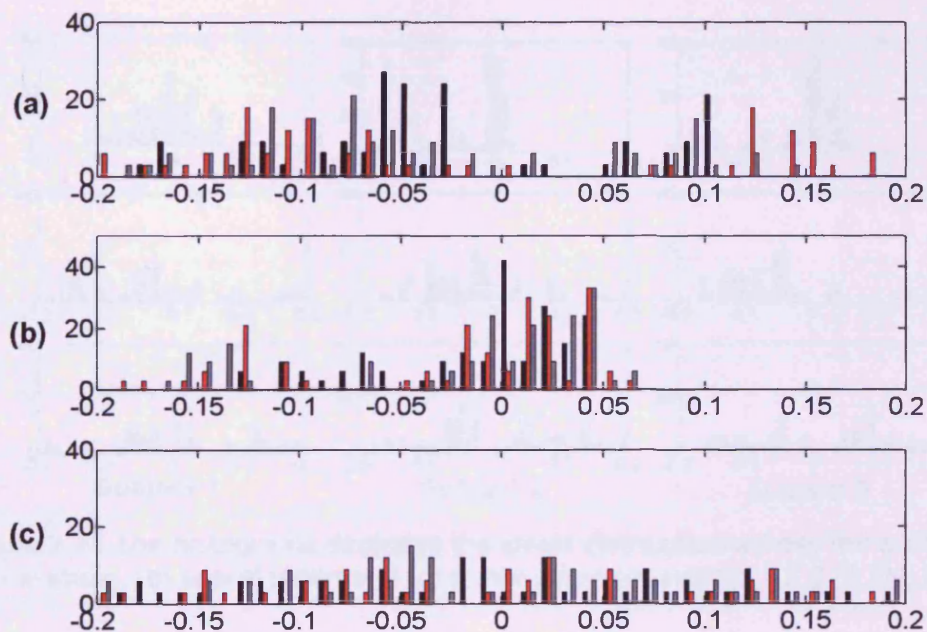
Figure 2.43 The histograms depicting the strain distribution across the elements
(a) axial strain, (b) lateral strain and (c) shear strain
combined for subject 1,2,3 (0.7N, X=0°).
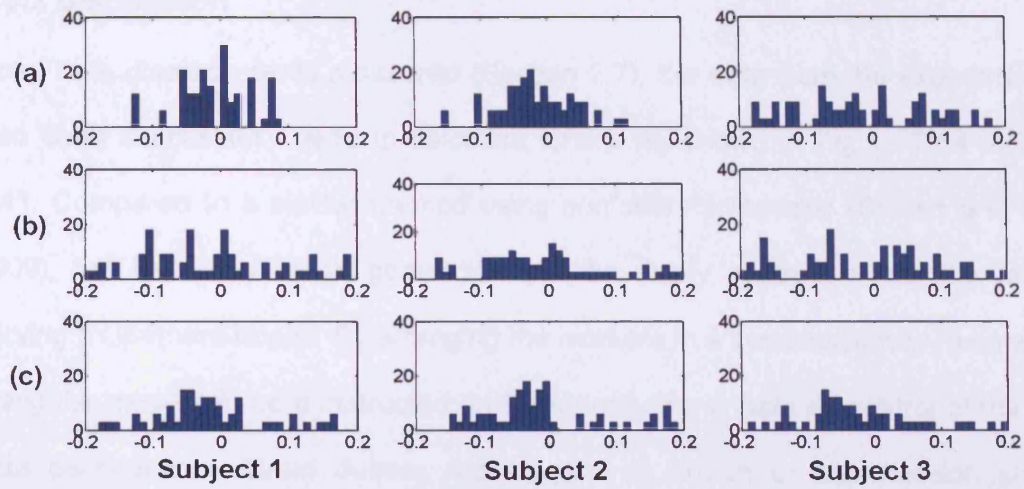
Figure 2.44 The histograms depicting the strain distribution across the elements (a) x-strain, (b) y-strain and (c) xy- strain for subject 1,2,3, (0.7N, X=45°).
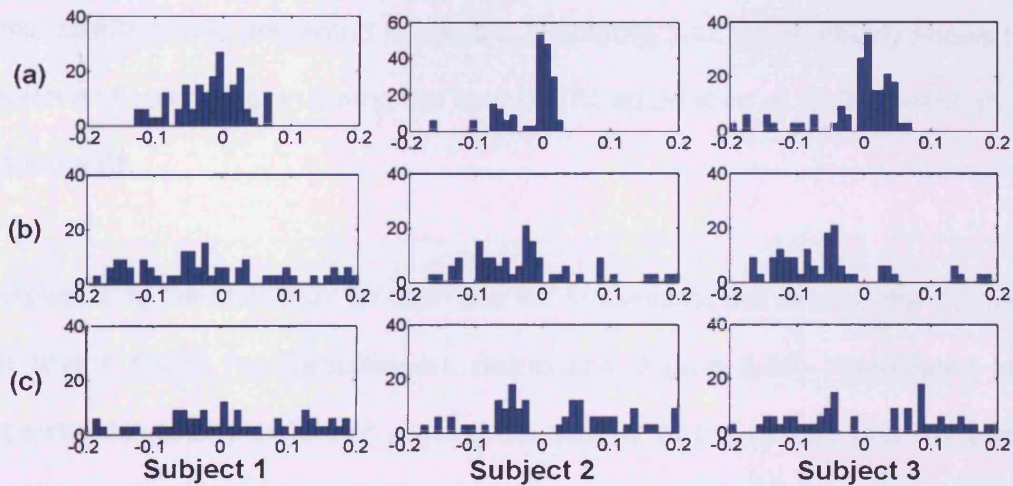
Figure 2.45 The histograms depicting the strain distribution across the elements (a) axial strain, (b) lateral strain and (c) shear strain for subject 1,2,3 (0.7N, X=90°).

2.8.2 Discussion

Apart from displacements measured (Section 2.7), the data from the experiment has also been successfully used to calculate strains as shown in Figure 2.34 to Figure 2.41. Compared to a similar method using confocal microscopy (Screen and Evans 2009), the Delaunay mesh generation can be easily controlled with the markers serving as element nodes. By arranging the markers in a systematic way, a consistent triangular mesh can be constructed and this produces enhanced control of the strain data distribution. Strain defines the amount of stretch or compression along a materials line of elements or fibres, i.e., *normal strain*, and the amount of distortion associated with the sliding of plane layers over each other, i.e., *shear strain*, within a deforming body (Rees 2006). Thus, by taking results for Subject 1 as an example, the strain distribution is presented in figure 3.1 to figure 3.12 which clearly shows the skin stretch and compression during the load (0.7N) application at $X=0°$, $X=45°$ and $X=90°$ respectively.

Despite using the Delaunay function and FE to calculate the strains, the distribution of the strains match the displacement distribution (Figure 2.35) interpolated from the experimental data that further proving the validity of the results and the successful development and implementation of the new experimental protocol. The strain distribution (e.g. Figures 2.42 to 2.43 for $X=0°$) clearly show that skin deforms in a complex manner, whereby when skin is stretched in one direction, the region beyond the load point experiences relatively high compressive strain thus causing wrinkling. In general, axial and lateral strains are distributed across the test area in a similar manner where the maximum magnitude occurred at region of loading point.

Histograms (Figures 2.42 to 2.45) showing the strain distribution (axial, lateral and shear) for each element for loading in the $X=0°$, 90 and 45 directions are useful in

defining the significant regions of compression and/or tension. Moreover, the results for Subject 1, 2 and 3 confirms the trend of the distribution. For X=0°, the histograms (Figure 2.42) show the axial strain significantly distributed in compression and tension (Figure 2.42a and Figure 2.43a), the axial strain concentrated around zero (Figure 2.42b and Figure 2.43b) and the shear strain distributed over a wide range (Figure 2.42 and Figure 2.43c). For X=45°, the histograms (Figure 2.44) show a more normal distribution of x-strain in tension and compression (Figure 2.44a), a wide ranging distribution of y-strain (Figure 2.44b) and the distribution of shear strain is significantly in compression (Figure 2.44c). For X=90°, the histograms (Figure 2.45) show a concentration of lateral strain around zero (Figure 2.45a), a significant distribution of axial strain in compression (Figure 2.45b) and equal distribution of compressive and tensile shear strain (Figure 2.45c). These results agree to Wan Abas and Barbenel (1982) where the strain field across the test area was grossly non uniform.

2.9 Conclusion

This chapter has comprehensively described the work done in developing a new and useful experimental procedure to measure small scale deformation of human skin *in vivo* using the motion capture system. The optimum experimental set up was confirmed and calibration results proved that the measurement system was accurate. The results of several tests proved that the *in vivo* experimental protocol was practical, reliable, repeatable and non-invasive. A great effort was made to achieve this as discussed earlier in Section 2.3 and 2.4.

The outputs from the experiments were found to be useful and input-ready for an inverse FEA to determine the mechanical properties of human skin. In addition, the

experiments demonstrated skin viscoelasticity, nonlinear and anisotropy and produced significant data which could be used to further investigate these characteristics. In addition the data generated from this system has been successfully used to measure strain, where the strain results match the experimentally measured deformation of skin.

This emphasises that the work accomplished has successfully adapted the motion analysis technique to be used as an equivalently full-field small scale deformation measurement tool and it would be a major contribution of this study. It is indisputably very novel; as traditionally, motion analysis techniques have been used to study the kinematics of a moving body/system and no previous studies have reported using the system in a similar manner (Mahmud et al 2009a).

The success of this work shows that this system which utilises motion analysis techniques has a great potential and can be developed further for other applications, especially in analysing small scale motion and full-field deformation of biological systems.

The experiment outputs described in this chapter are further analysed to determine the mechanical properties of human skin using an inverse FE analysis based on the Ogden model. These are comprehensively discussed in the following chapter.

3-1

CHAPTER 3

THE DEVELOPMENT OF FINITE ELEMENT MODELS TO SIMULATE SKIN DEFORMATION

3.1 Introduction

The previous chapter highlights the success of a new experimental method that has been used to measure the deformation of human skin *in vivo*. The experimental results were found to be reliable and useful, demonstrating that the employed motion analysis technique has a great potential for other similar applications. The experimental data has been analysed extensively to explore the viscoelastic, nonlinear and anisotropic behaviour of skin deformation. However, it has not fulfilled the ultimate objective of the current study to determine the mechanical properties of human skin. One of the approaches that could lead to the establishment of skin properties is by simulating skin deformation as a reproduction of the experimental procedure developed earlier (Chapter 2). One of the most popular methods used in performing simulation is the finite element method (FEM).

Therefore, this study attempted to develop a simple but robust computational model employing the FEM that could simulate skin deformation with reasonable accuracy. For this reason, a parametric study was designed by varying the material properties, elements types and sizes. The output was compared to the experimental output to evaluate the reliability and significance of the FE models.

This chapter describes the work performed in modelling and simulating skin behaviour based on the experiments developed in the previous chapter. The study started by re-developing previous case studies that solved engineering problems using FEM producing validated results; and finally led to the development and evaluation of several new FE models. For clarity, this chapter presents and discusses the followings;

- Previous approaches in modelling skin that motivated this study
- Scope of work
- Reconstructing validated problem
- The development of current FE models
- Comparison of models

The results are presented and critically discussed. Finally, a conclusive remark ends the chapter.

3.2 Motivation

The practice of numerical simulation in structural analysis has now matured into an established and efficient method for modelling engineering materials. Numerical models are increasingly reliable in simulating the deformation and stress distribution through a material or structure. Such models assist in designing the structure or the materials itself; such as composite materials. Moreover, it is also needed for inverse calculation to find the material properties from the experimental data. Therefore, the need for numerical modelling of skin deformation is unquestionable. At present there is no generally accepted model that has been reported that could be used directly for this study. Therefore, it is crucial for the current to attempt to model and simulate skin deformation as it could contribute to understanding better the skin behaviour.

The literature review on the analytical and computational approaches has been discussed in Sections 1.2.5 to 1.2.7 (Chapter 1). However, it is important to highlight again here that the attempts to develop a computational model of skin started as early as in early 70s where skin was modelled as an elastic membrane (Danielson 1973) and a hyperelastic material (Tong and Fung 1976). Due to a lack of computer software and modelling tools, mathematical equations were the main approach to describing the deformation of human skin. With the advances in computer technology, engineering software has been vigorously developed and commercially available. Using FE software, attempts to simulate and animate skin behaviour has become possible. A few examples include the work of Tsap et al (1997) using ANSYS to analyse human tissue motion analysis, Hendriks et al (2003) using MSC.MARC to simulate suction tests, Tham et al (2006) using Abaqus to simulate the cupping process, Retel et al (2001) using SYSTUS to simulate wound closure, Molinari et al (2005) using FEAP to simulate of the biomechanical behaviour of the skin from a virtual surgery.

These studies motivated the current study to adapt FEM in simulating skin deformation based on the experimental procedure developed in Chapter 2. Moreover, it could be seen that the FE software has not been aggressively explored compared to using experimental techniques in characterising skin properties. This might be due to the unavailability of sufficient information from the published experimental work that can help in developing an accurate skin model. Therefore it is necessary to develop both the experiments (*in vivo*) and the FE model together for quantifying the material properties of skin.

Due to the lack of work on simulating skin behaviour using FE software, the current study aims to develop such as a study.

3.3 Scope of work

The ultimate aim of the current study is to determine the mechanical properties of human skin and therefore, the work described in this chapter provides the tools to achieve that aim. A parametric study was designed to investigate the effect of varying the material parameters, elements types and sizes and the results were compared with the experimental data generated in the previous chapter. The FE models developed and the modelling procedures were evaluated. The material parameters that produce the closest results to the experiments yield an estimate of the mechanical properties of skin. Even so, a comprehensive parametric study itself has provided a general explanation on skin deformation behaviour.

3.4 FE modelling and validation

The results of FE simulation could be very misleading if no attempts were made to compare and validate the FE model. This is certainly crucial especially when exploring new problems. Initial attempts in this study involved reconstructing a validated FE model that was available in the literature. This is a common practice in FE modelling, where the success in modelling a problem model provides confidence and better understanding to solve further related problems; and it has been an acceptable method to at least prove that the modelling procedures undertaken and the solving technique have been correct and trustworthy. For this purpose, two case studies were conducted.

3.4.1 The deformation of a composite plate under a transverse load

The first case was modelling a composite plate with variations in lamination. Although it was not much related to the current work, it provided a basic knowledge to FE modelling using Abaqus (Abaqus v6.6-1, Dassault Systemes Simulia Corp,

Providence, RI, USA) and possibly useful in future to consider modelling skin as a

multilayer and transversely isotropy. The results are presented in Table 3.1. Further

details are presented in Appendix C.

Table 3.1: Comparison of the exact and the FE solution, (z-displacement) for a
laminated   composite plate with various lamination schemes.

Lamination scheme	Type of Laminate	UDL (p.s.i)	Maximum displacement (z-direction in inches)	
			*Exact solution	FE solution using Abaqus/CAE v6.6-1
[0 / 90]$_T$	cross-ply	0.1	1.884	**1.884**
[0/ 90/ 0/ 90]$_T$		0.1	0.134	**0.1349**
[0/ 90/ 90/ 0]$_T$		0.1	0.229	**0.2299**
[45/-45/45/-45]$_T$	anti-symmetric angle ply	0.1	0.1086	**0.1087**
[15/-15/15/-15]$_T$		0.1	0.2515	**0.2515**
[45 / -45]$_T$		0.1	1.6006	**1.601**
[15 / -15]$_T$		0.1	2.6039	**2.604**

Note*: Source of exact solution: *Reddy and Pandey (1987).
       UDL refers to uniformly distributed load.

3.4.2 Stretching of a square sheet with a circular hole

This example is considered primarily due to the nature of the problem that related to

the current study. It was published by Basar and Itskov (1998) to validate their model

by comparing to others (Gruttman and Taylor 1992, Basar and Ding 1997). The in-

plane displacements of a stretched hyperelastic sheet were determined based on the

material parameters, mesh, loading and boundary conditions as shown in Figure 3.1.

undeformed geometry (f = 0.0)   deformed geometry (f = 1.0)
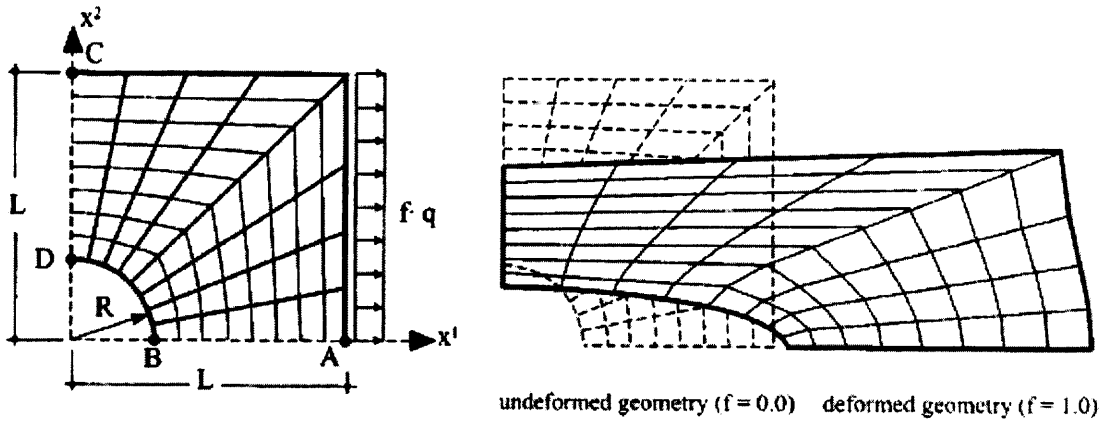
Geometry:
L = 10, R = 3, thickness h = 1

OGDEN material:
$\mu_1 = 50, \alpha_1 = 2$
$\mu_2 = -14, \alpha_2 = -2$

MOONEY-RIVLIN material:
$c_1 = 25, c_2 = 7$,
Basar and Ding, 1997

Load: q = 90.0

Figure 3.1: The details of the FE model (Basar and Itskov 1998, page 1293)

The similarity to the current problem is that it used 2D elements, Ogden materials (hyperelastic) and considered a plane stress condition. The main challenge in solving a hyperelasticity problem was to obtain a converged solution. A sample output is shown in Figure 3.2. U1 is the axial displacement (X^1-direction). Table 3.2 involves some characteristic numerical results, which have been found to be in full agreement with those obtained by earlier FE models (Basar and Itskov 1998). ΔX^1_A and ΔX^1_B refers to the axial displacements at point A and B respectively, while ΔX^2_C refers to the lateral displacements at point C (Figure 3.1). Figure 3.3 shows the load-displacements diagram which reveals that the results are very close.
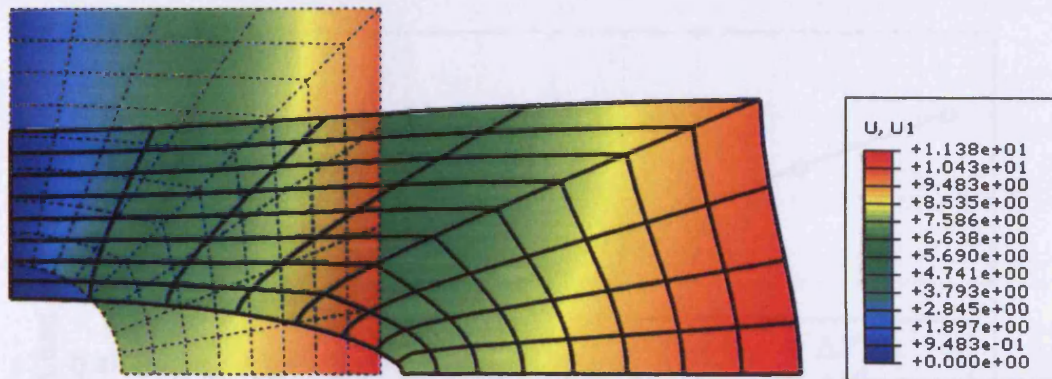
Figure 3.2: A sample output portraying the original (dotted line) and deformed plate (continuous line). (Abaqus v6.8-1, Dassault Systemes Simulia Corp, USA).

Table 3.2: Comparison of FE solutions: Current and Basar and Itskov (1998)

Load factor, f	ΔX^1_A		ΔX^1_B		ΔX^2_C	
	Current	*B&I	Current	*B&I	Current	*B&I
0.125	0.9451	0.9319	0.6925	0.6699	-0.4947	-0.4837
0.250	1.9636	1.9434	1.4156	1.3765	-0.9563	-0.9389
0.375	3.1062	3.0807	2.2080	2.1543	-1.4019	-1.3801
0.500	4.4073	4.3764	3.0931	3.0256	-1.8354	-1.8101
0.625	5.8870	5.8501	4.0819	4.0009	-2.2535	-2.2256
0.750	7.5502	7.5064	5.1731	5.0789	-2.6501	-2.6201
0.875	9.3876	9.3362	6.3551	6.2485	-3.0196	-2.9876
1.000	11.3796	11.3205	7.6111	7.4930	-3.3585	-3.3245

Note*: B&I refers to Basar and Itkov (1998).
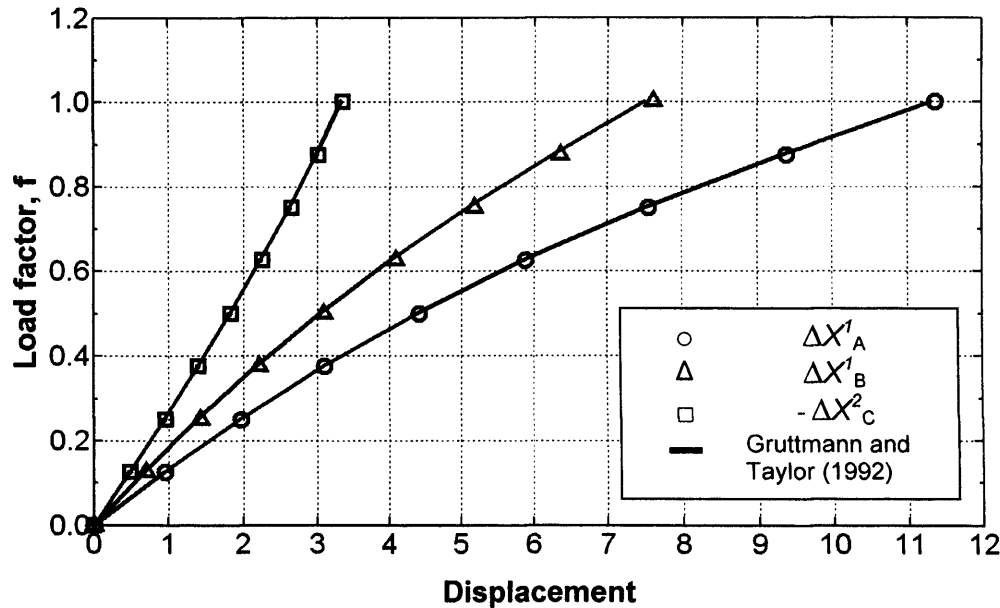
Figure 3.3: The load-displacement diagram to compare current results to Gruttmann and Taylor (1992).

3.5 The Development of a Skin Model

The success in modelling a rubber sheet provides a guideline in developing a FE skin model. Other than the model was accurately developed in Abaqus, it also shows that the solver used to solve the analysis was accurate. The understanding of basic FE modelling in Abaqus was crucial and it was extended to develop the skin model based on the experiments conducted employing the motion analysis technique as described in Chapter 2. For this study, 2D and 3D models of skin for Subject 1 (0.7 N) were developed and the results are compared with the experimental results. By comparing the FE solutions to the experimental results (curve fitting), the material parameters for human skin could be identified.

Although it is best to develop a model with high accuracy, it demands a realistic and complicated model, which will increase modelling complexity as well as computation

time. Therefore, this study attempted to develop a simple but robust FE model that can simulate skin behaviour with reasonable accuracy. There were two main challenges to accomplish this;

i. to simulate skin deformation according to the experimental procedure

ii. to produce with results of good accuracy.

For this purpose, a parametric study was designed, in which the following were varied:

i. material parameters;

- Ogden's material coefficient, μ;

- Ogden's material exponent, α, and;

- strain energy potential order, N.

ii. element size; and;

iii. element type;

- linear (with and without hourglass control), and;

- quadratic;

iv. load application;

- concentrated, and;

- distributed;

to observe comprehensively their effects to the FE solutions.

3.5.1 2D Skin Model

3.5.1.1 Geometrical description of the model

The skin was modelled as a rectangular 2D planar deformable membrane with its initial size was constructed according to the test area on the forearm (64 x 48 mm). Prestrain was considered by an initial prescribed displacement via enlarging the plate by 25 percent (80 x 60 mm). Its section was assumed homogeneous solid with a

plane stress thickness of 1.5 mm. By considering markers as nodes, quad elements (plane stress) were constructed.

3.5.1.2 Mesh and elements

Mesh sizes of 8 x 6 (Figure 3.4) and 32 x 24 (Figure 3.5) were considered.
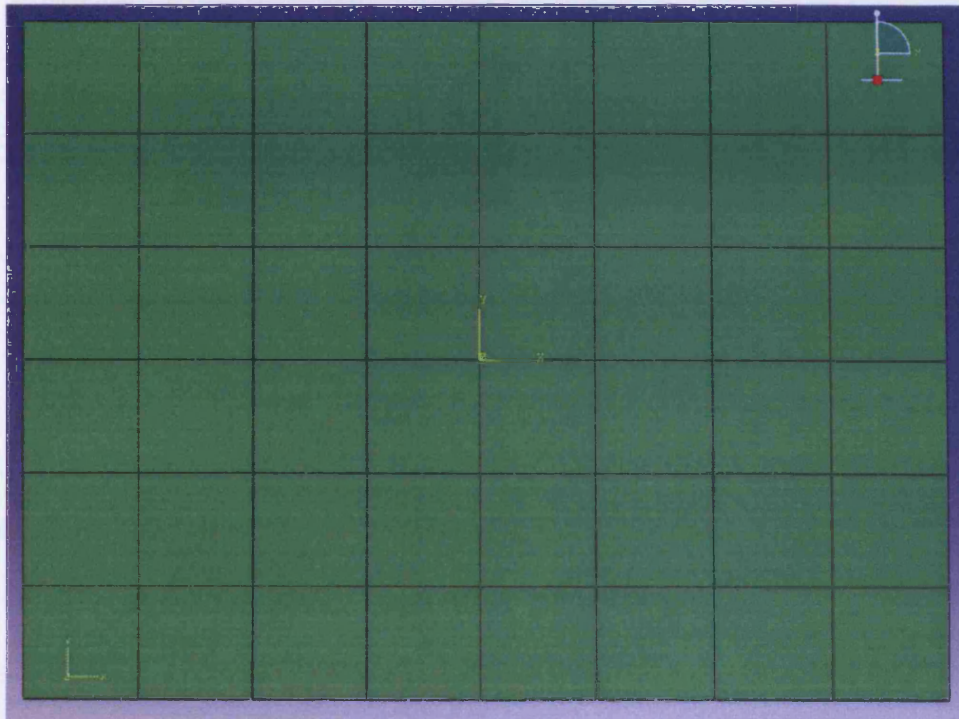
Figure 3.4: 80 x 60 mm membrane meshed into 48 (8 x 6) elements.
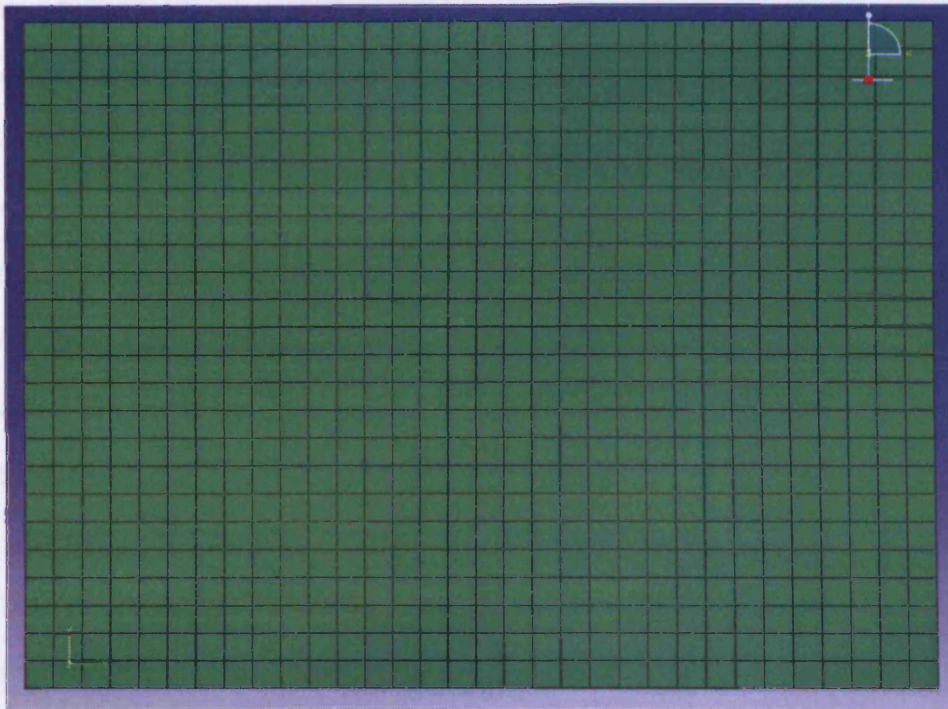
Figure 3.5: 80 x 60 mm membrane meshed into 768 (32 x 24) elements.

The elements used were:

- CPS4 – A 4-node bilinear plane stress quadrilateral.

- CPS4R – A 4-node bilinear plane stress quadrilateral, reduced-integration, hourglass control.

- CPS8 – An 8-node biquadratic plane stress quadrilateral.

- CPS8R – An 8-node biquadratic plane stress quadrilateral, reduced-integration.

In FE computation, the element matrices determine the element behaviour; and calculating element matrices are a very important phase of a FE solution (Bathe 1996). The formulation refers to the mathematical theory used to define the elements matrices (or behaviour). All of the stress/displacement elements in Abaqus are based on the Lagrangian or material description of behaviour (Hibbit, Karlson & Sorenson, Inc. 2000). Numerical techniques are used to integrate various quantities over the

volume of each element. Using Gaussian quadrature, the material response is evaluated at each integration point in each element. There are two types of integration which are the full integration and reduced-integration, which can have significant effects on the FE solution. The expression "full integration" refers to the number of Gauss points required to integrate the polynomial terms in an elements stiffness matrix exactly when the element has a regular shape. The expression "reduced-integration" elements use one fewer integration point in each direction than the fully integrated elements. The reduced-integration bilinear elements (CPS4R) have just a single integration point located at the elements' centre. Because of this, the elements could deform and distort excessively. The hourglass control formulation is an option to limit the distortion of the element. The reduced-integration biquadratic elements (CPS8R) have four integration points, which make their deformation are more restricted and do not require the hourglass control.

3.5.1.3 Load and boundary conditions

Load was applied at the centre of the membrane (at load point, L5 (Figure 2.19), as described in Section 2.6.2, Chapter 2). The boundary conditions were extracted directly from the displacements measured at the boundaries of the test area. For this case, a 0.7N load was considered and the corresponding displacements at the boundaries are shown in Figure 3.6.
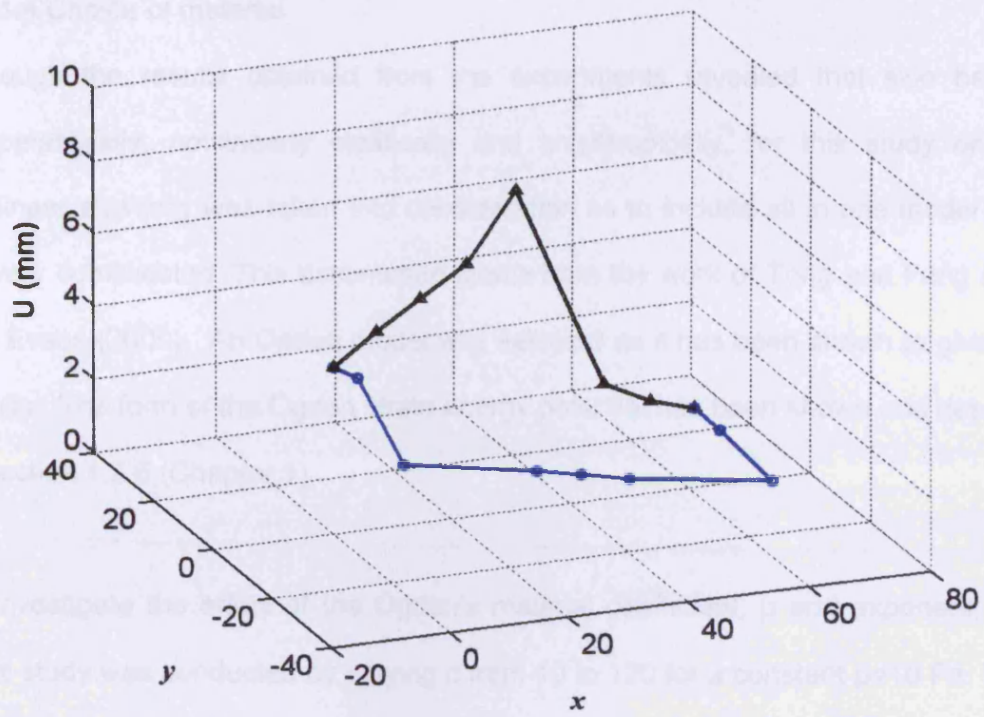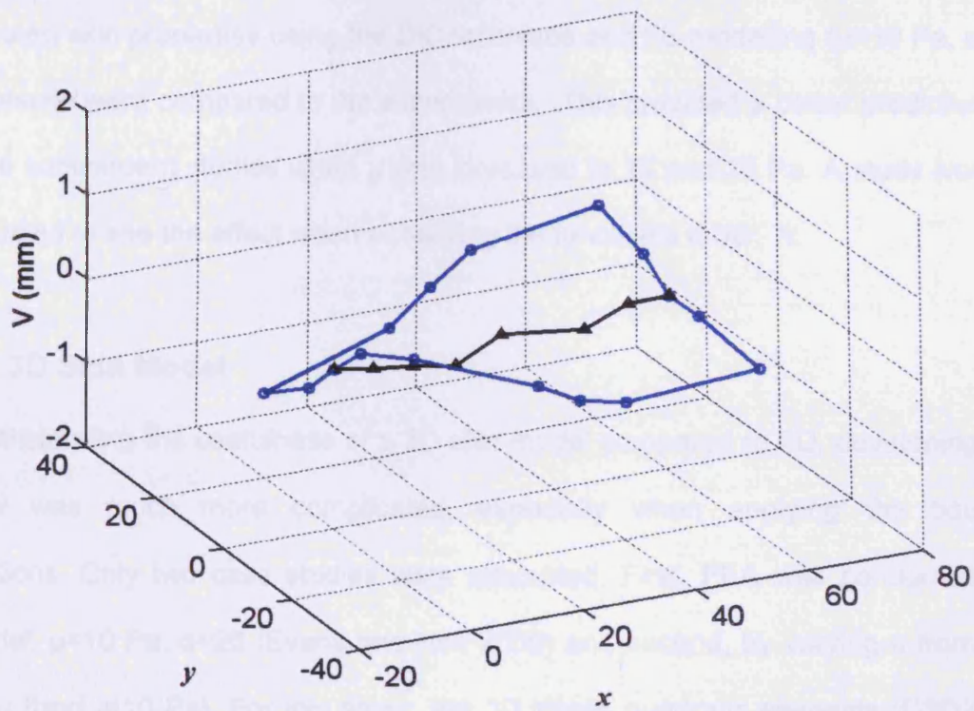
Figure 3.6: The displacements at the boundaries (a) axial, u; and (b) lateral, v (X=0°, 0.7N, Subject 1).

3.5.1.4 Choice of material

Although the results obtained from the experiments revealed that skin behaved viscoelastically, nonlinearly elastically and anisotropically, for this study only the nonlinear elasticity was taken into consideration as to include all in one model would be very complicated. This assumption stems from the work of Tong and Fung (1976) and Evans (2009). An Ogden model was selected as it has been shown to give good results. The form of the Ogden strain energy potential has been shown and described in Section 1.2.6 (Chapter 1).

To investigate the effect of the Ogden's material coefficient, μ and exponent, α, an initial study was conducted by varying α from 10 to 120 for a constant $\mu=10$ Pa. These values were selected based on the findings of Evans and Holt (2009) when they measured skin properties using the DIC technique and FE modelling ($\mu=10$ Pa, $\alpha=26$). The results were compared to the experiments. This provided a better prediction of α for the subsequent studies when μ was increased to 15 and 20 Pa. A study was also conducted to see the effect when increasing the function's order, N.

3.5.2 3D Skin Model

Notwithstanding the usefulness of a 3D skin model compared to 2D, developing a 3D model was much more complicated, especially when applying the boundary conditions. Only two case studies were attempted. First, FEA was conducted for a material, $\mu=10$ Pa, $\alpha=26$ (Evans and Holt 2009) and second, by varying α from 70 to 110 (μ fixed at10 Pa). For this study, the 3D stress quadratic elements (C3D20H, A 20-node quadratic brick, hybrid, linear pressure) were assigned (Figure 3.7). The load and boundary conditions were applied as shown in Figure 3.7, 0.7N distributed load was applied.
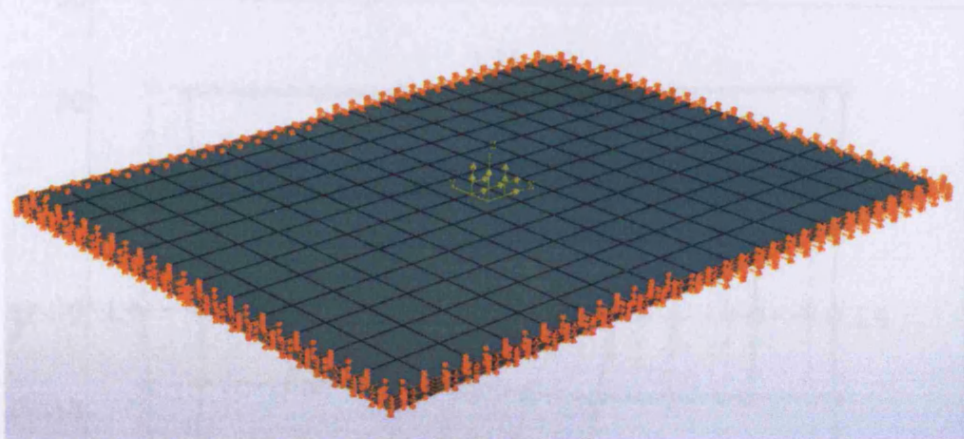
Figure 3.7: The 80 x 60 mm plate, meshed into 384 (16 x 12 x 2) brick quadratic elements. The yellow arrows indicate the distributed load applied. The orange arrows indicate the boundary conditions which could be observed abundant along the edges.

3.6 Results

The general outputs from a FEA are displacement and stress information for a deformed body. The experiments described in Chapter 2 provided the displacement information for the deformed skin. Therefore, a direct approach to relate both experiments and simulations is by comparing the displacements. The results of the experiments were used to plot such an undeformed-deformed diagram for the skin. As an example, the original and displaced markers (0.7N, X=0°, Subject 1) are presented in Figure 3.8. This serves as the reference data and all the case studies stemmed from it. It required tremendous effort to compare the displacements for the whole marker set, hence, in this study, the midline markers parallel to the load direction (L1 to L9) and transverse to it (row of L35-L38, refer Chapter 2) were observed.
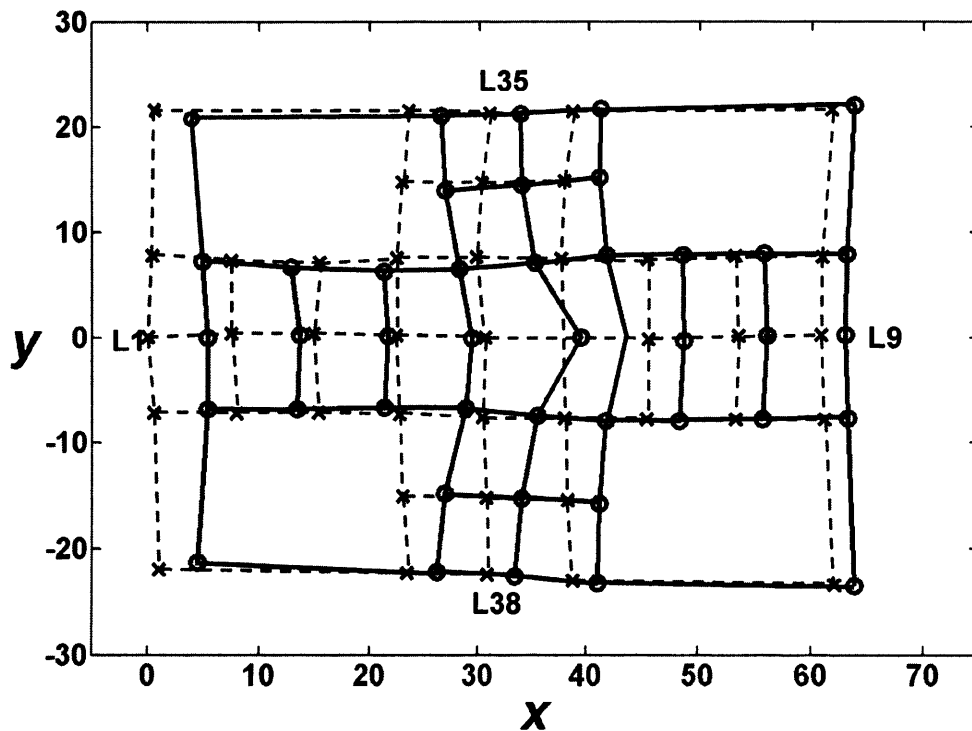
Figure 3.8: A sample experiment output (undeformed-deformed diagram) of skin deformation presented in 2D. (0.7N, X=0°, Subject 1). The dotted line represents the initial position and the continuous line shows its new position.

3.6.1 *Case study 1*: μ=10, α=26.

This was the initial study where the material parameters (μ=10 Pa α=26) were used as proposed by Evans and Holt (2009). The membrane was meshed into 8x6 elements and the boundary conditions were assigned according to experiments result (Figure 3.8). A concentrated load (0.7N) was applied at the load point. Nodes (model) were intended to represent markers (experiment), therefore, two types of 4-node elements were used, CPS4R and CPS4 (4-noded bilinear plane stress quadrilateral, with and without hourglass control respectively). An initial study was conducted using CPS4 elements (the effect of hourglass control was omitted). Figure 3.9 shows the shape of the deformed plate which can be visually compared to Figure 3.8. Figure 3.10 shows the distribution (contour) of the axial displacements with and without showing the contour edge. The figure showing the contour edge (Figure 3.10b) was a

good explanation to the earlier observation where the contour (Figure 3.10a) was not

symmetric.
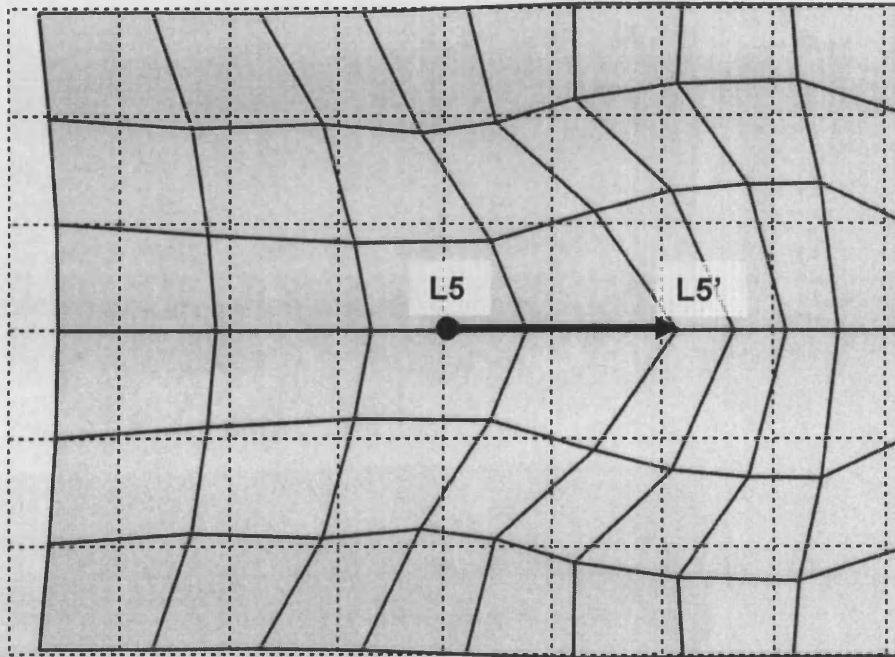
Figure 3.9: The shape of initial (dotted line) and deformed plate (continuous line) when subjected to 0.7 N load in x-direction using CPS4 elements. The arrow indicates the displacement of marker L5 (load point).
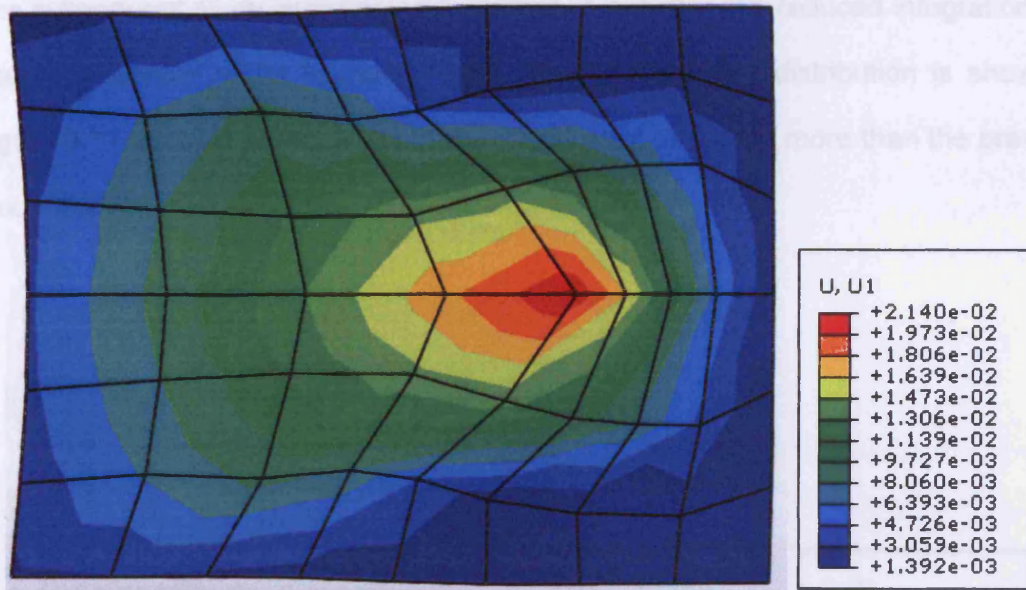
(a)
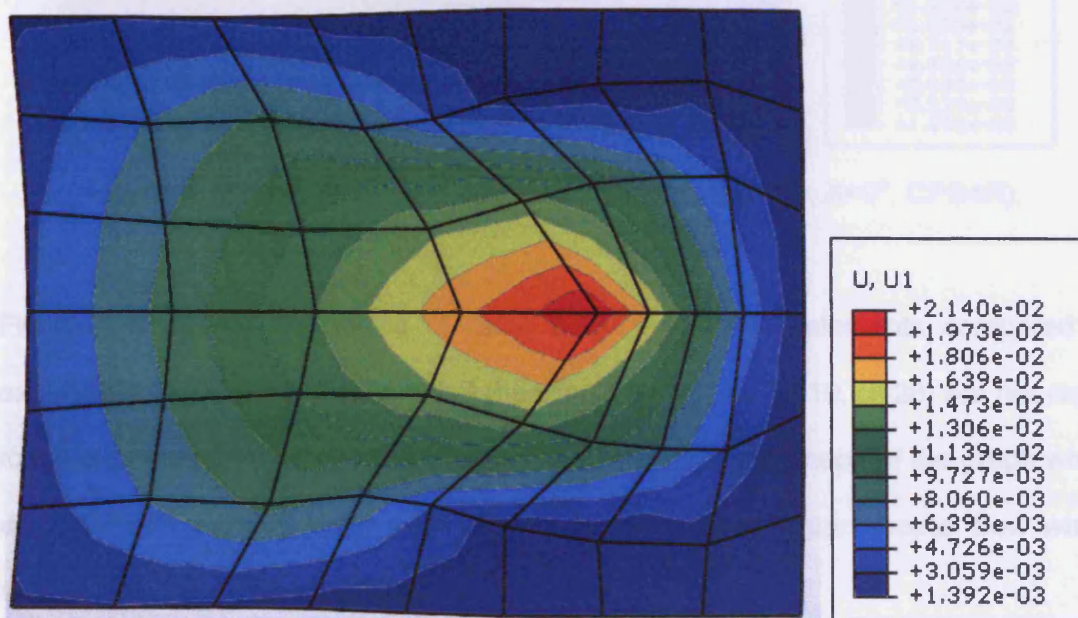
(b)

Figure 3.10: The distribution of axial displacement (0.7N, X=0°) using CPS4 element; (a) without contour edges and (b) showing contour edges. It could be observed that without showing the contour edges (a), the contour is not symmetric.

The subsequent study investigated the effect of including the reduced integration and hourglass control effect (using CPS4R). The displacement distribution is shown in Figure 3.11. It could be observed that the load point displaced more than the previous model (CPS4).

U, U1
+2.337e-02
+2.154e-02
+1.971e-02
+1.787e-02
+1.604e-02
+1.421e-02
+1.238e-02
+1.055e-02
+8.717e-03
+6.886e-03
+5.055e-03
+3.223e-03
+1.392e-03
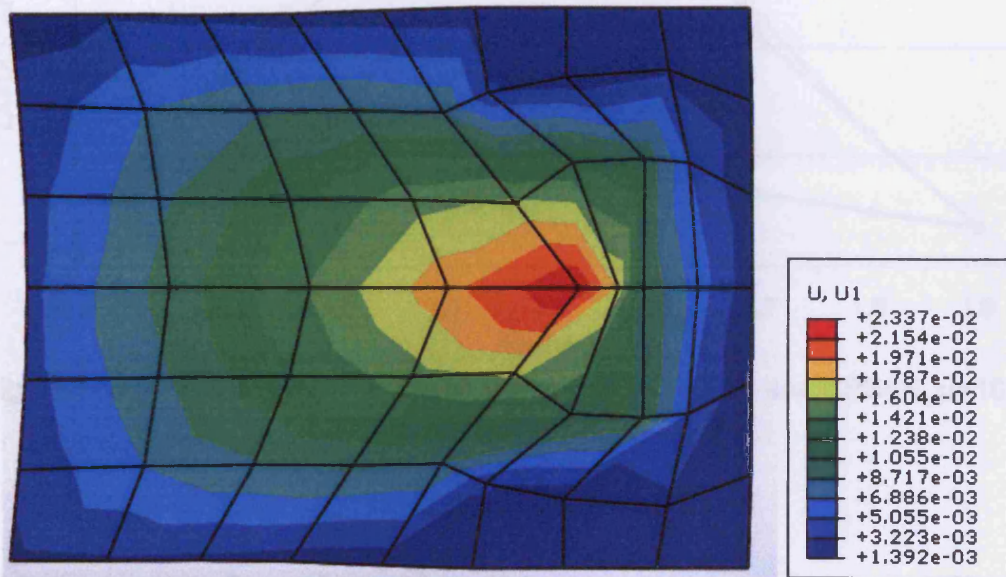
Figure 3.11: The distribution of axial displacement (0.7N, X=0°, CPS4R).

Figure 3.12 shows the results of using CPS4 and CPSR elements compared to experiment. It could be observed that the simulated results (μ=10, α=26) are not close to the experiment. Another interesting observation is that the shape of the graph when using CPS4R element looks more alike to the experiment (approximate 'bow wave' shape) than the graph for CPS4.
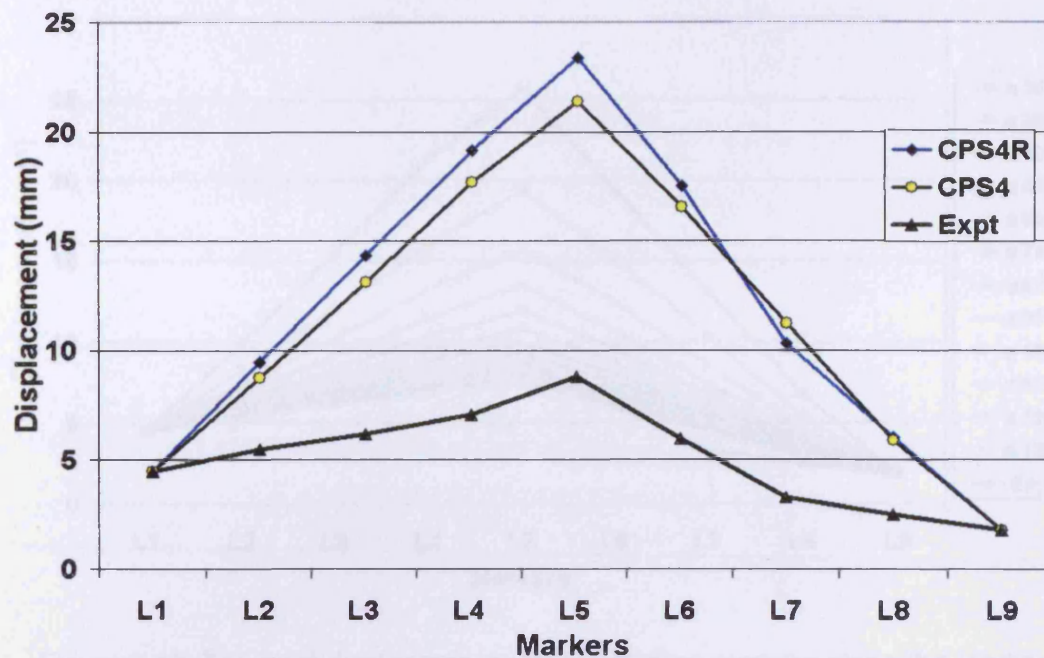
Figure 3.12: The comparison of the simulated results (CPS4 and CPS4R, μ=10 Pa, α= 26) to experiment.

3.6.2 *Case study 2*: μ=10, α= 20 to 130.

The result for case study 1 was not very close to the experiment, therefore, a further study was attempted to determine the value of α that could produce better results closer to the experiment. This subsequent study was conducted to see the effects of varying α, ranged from 20 to 130. The membrane was meshed into 8 x 6 linear elements using CPS4, the most basic elements for 2D analysis. For α=10, several elements were excessively distorted, therefore, the solution failed to converge. For other α, the results are presented in Figures 3.13 to 3.16. Figure 3.13 shows the axial displacements for the midline markers (L1 to L9) along the loading (X=0°) direction. Figure 3.14 shows the axial displacements for the transverse midline markers.
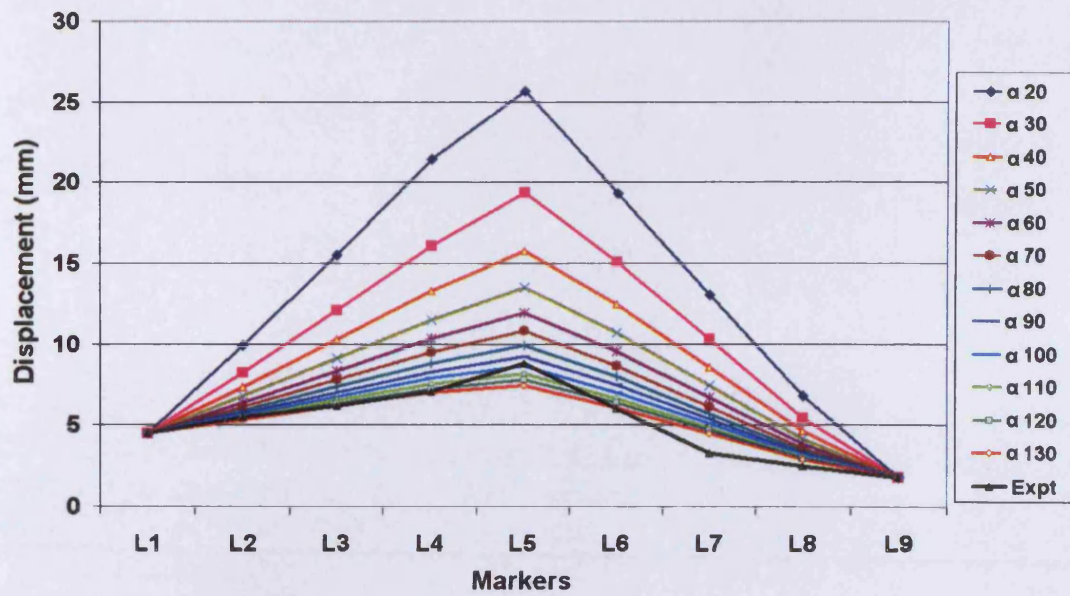
Figure 3.13: The axial displacements for the midline markers along the loading direction. The graphs (for several α) are compared with the experiment.
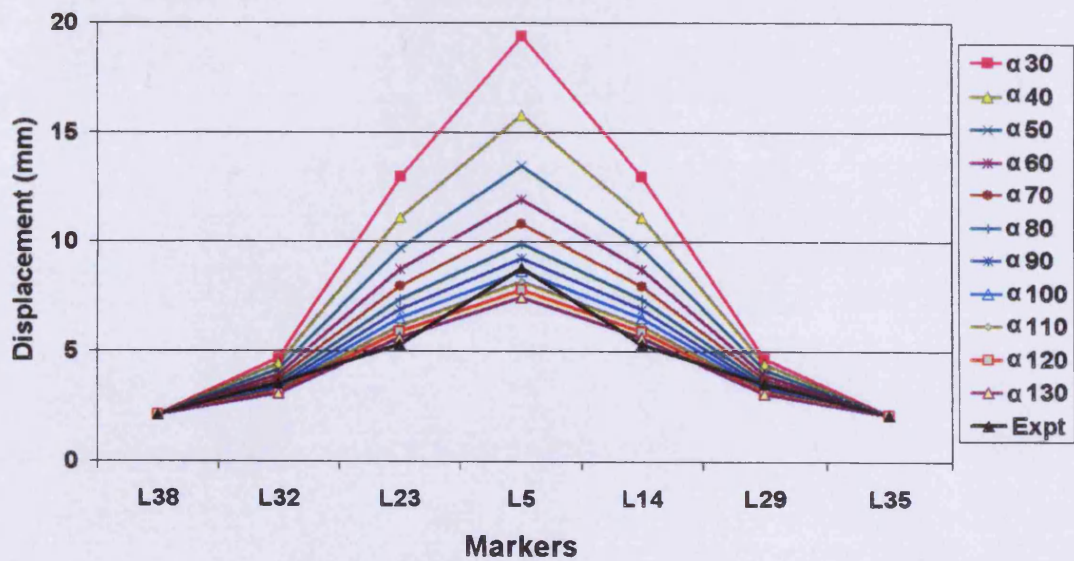
Figure 3.14: The axial displacements for the transverse midline markers. The graphs (for several α) are compared with the experiment.

Both figures served for initial observation, which show that most of the graphs are not very close to the experiment and consequently, it was difficult to compare the results. Therefore, the graphs for a selection of α were shown in Figures 3.15 and 3.16 to exhibit a better comparison between experiments and current results.
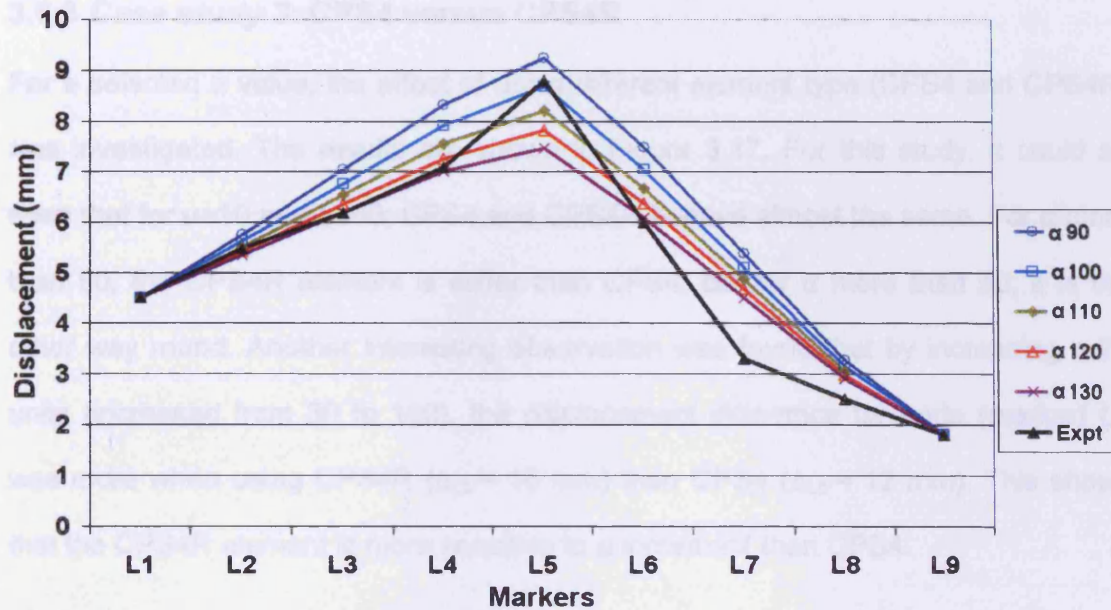
Figure 3.15: The axial displacements for the midline markers along the loading direction, a simulation-experiment comparison.
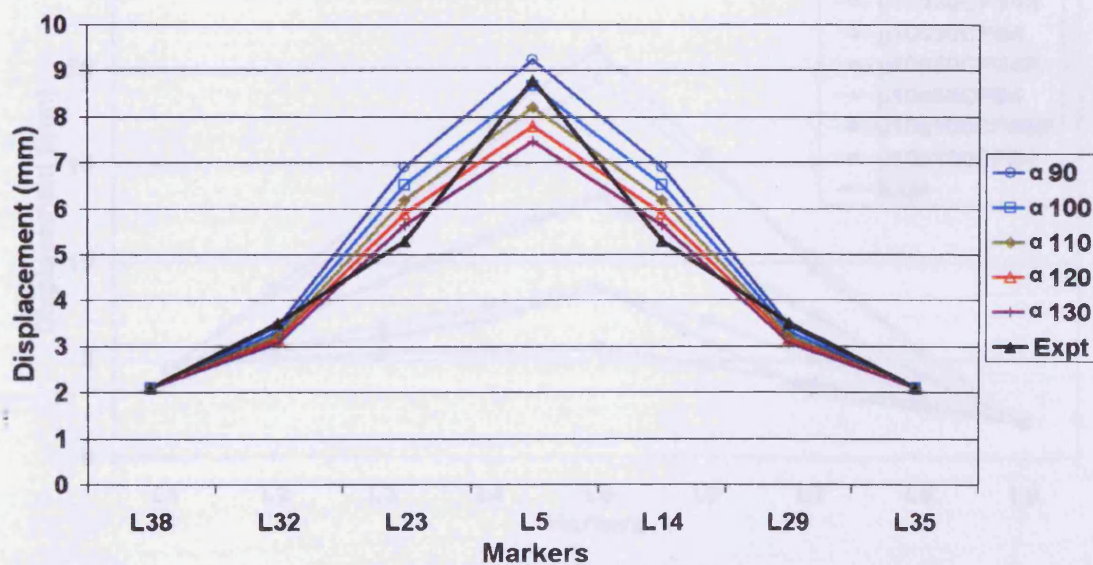
Figure 3.16: The axial displacements for the transverse midline markers, a simulation-experiment comparison.

It could be observed in Figure 3.16 that for $\mu=10$, the experimental results fit the range of α between 100 and 130. However, Figure 3.15 shows that the fitting is not as good as in Figure 3.16. The outcome of this study shows that larger value makes the material stiffer (active displacement reduced).

3.6.3 *Case study 3*: CPS4 versus CPS4R

For a selected α value, the effect of using different element type (CPS4 and CPS4R) was investigated. The results are shown in Figure 3.17. For this study, it could be seen that for $\mu=10$ and $\alpha=50$; CPS4 and CPS4R behave almost the same. For α more than 50, the CPS4R element is stiffer than CPS4; but for α more than 50, it is the other way round. Another interesting observation was found that by increasing α 70 units (increased from 30 to 100), the displacement difference for node (marker) L5 was more when using CPS4R ($\Delta_{L5} \approx 16$ mm) than CPS4 ($\Delta_{L5} \approx 12$ mm). This shows that the CPS4R element is more sensitive to α increment than CPS4.
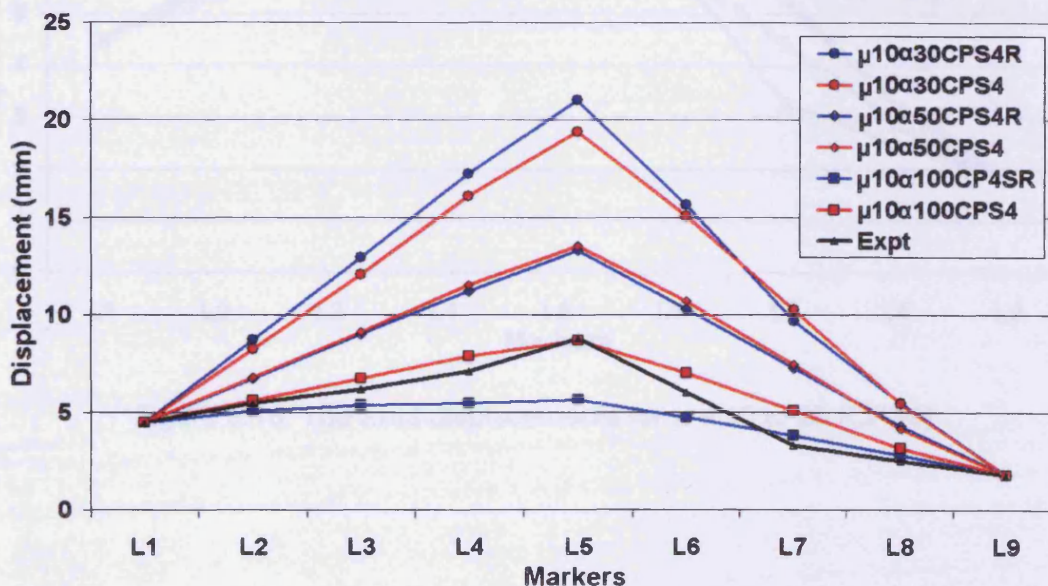
Figure 3.17: Comparison of using CPS4 and CPS4R for a selected α value.

3.6.4 *Case study 4*: μ=10 to 20.

The study was continued to observe the effect of varying μ (μ=10, 15 and 20). The relevant values for α were selected from the previous case study. Both CPS4 and CPS4R elements were used and the results are shown in Figure 3.18 and Figure 3.19. It could be observed that when μ was increased, the material became stiffer. When comparing the elements, the effect of increasing μ by 5 Pa was shown to be more significant for CPS4R. Looking at marker L5, increasing μ from 10 to 20 induced about 0.2 mm displacement for CPS4 and 0.8 mm for CPS4R. This shows that the CPS4R element is more sensitive to μ increment than CPS4 (as to α).
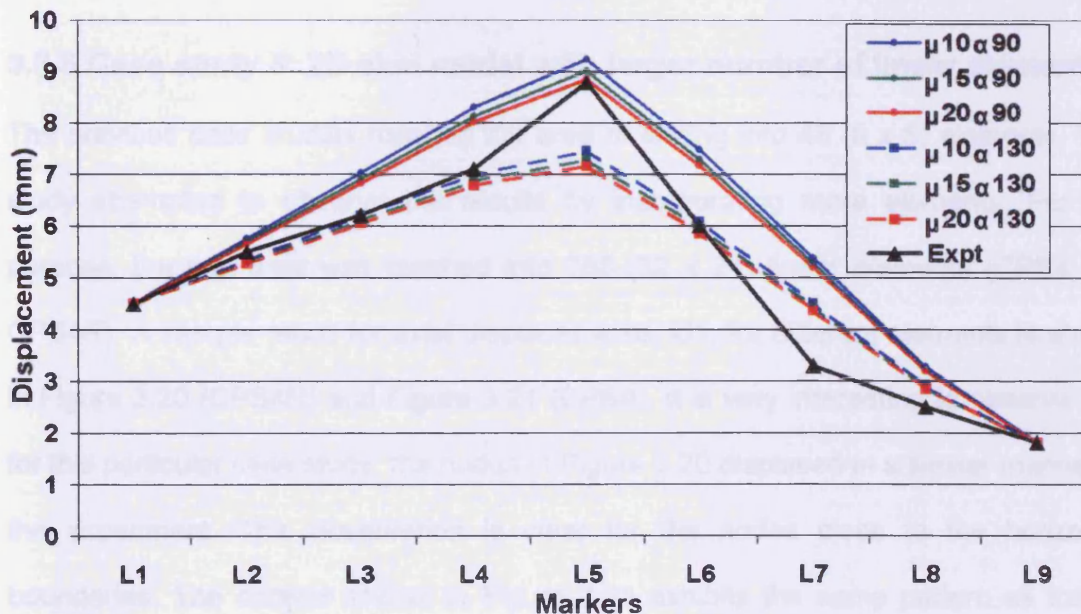
Figure 3.18: The axial displacements for μ = 10 to 20 (CPS4).
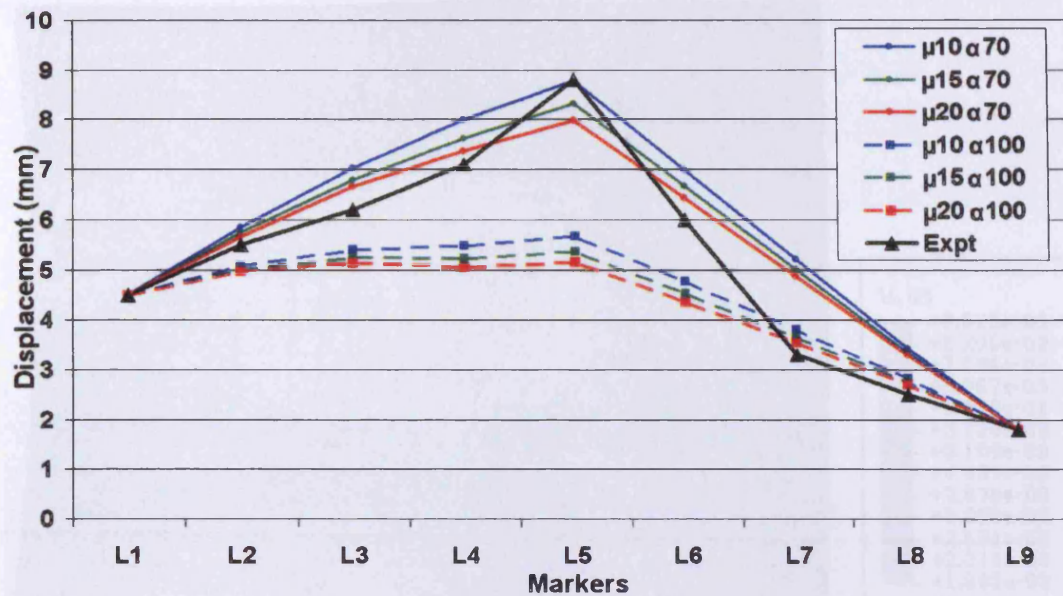
Figure 3.19: The axial displacements for µ = 10 to 20 (CPS4R).

3.6.5 *Case study 5*: 2D skin model with larger number of linear elements.

The previous case studies meshed the area of testing into 48 (8 x 6) elements. This study attempted to observe the results by incorporating more elements. For this purpose, the test area was meshed into 768 (32 x 24) linear elements (CPS4 and CPS4R). A sample result for axial displacements, U1, for different elements is shown in Figure 3.20 (CPS4R) and Figure 3.21 (CPS4). It is very interesting to observe that for this particular case study, the nodes in Figure 3.20 displaced in a similar manner to the experiment. This observation is clear for the nodes close to the horizontal boundaries. The contour shown in Figure 3.21 exhibits the same pattern as former models (Section 3.6.1: *Case study 1*).
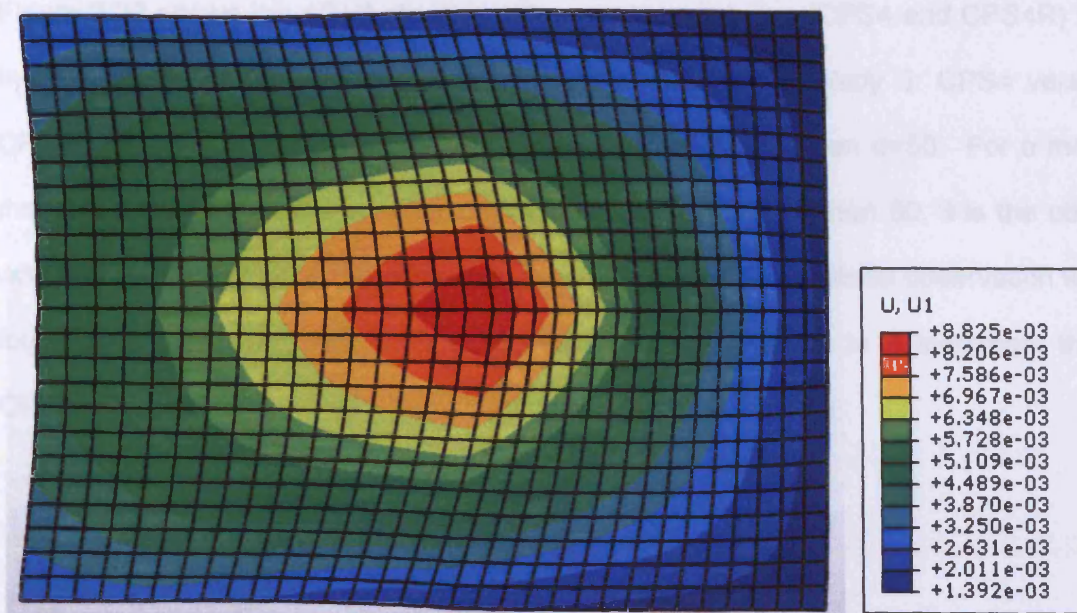
Figure 3.20: A contour showing the distribution of axial displacement
(μ=10, α=90, CPS4R).
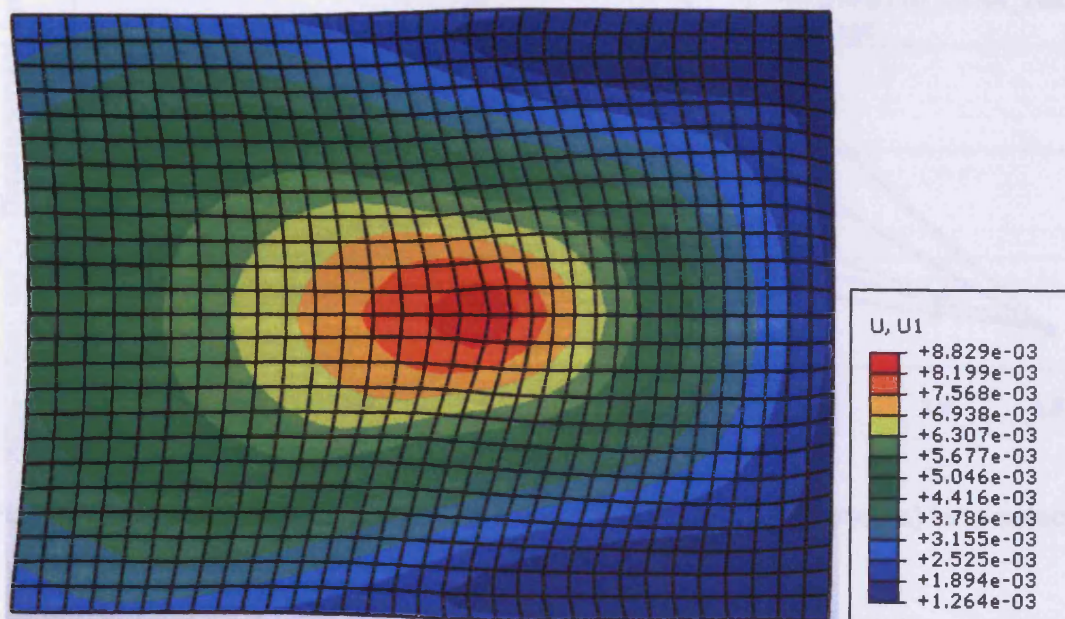
Figure 3.21: A contour showing the distribution of axial displacement
(μ=10, α=110, CPS4).

Figure 3.22 shows the effect of using different element types (CPS4 and CPS4R) for the model. Similar to a previous case (Section 3.6.3 *Case study 3*: CPS4 versus CPS4R, 8 x 6 elements), the displacement graph coincides when α=50. For α more than 50, CPS4R element is stiffer than CPS4; but for α more than 50, it is the other way round. Considering the difference in displacements, Δ, a similar observation was found thus confirming that CPS4R element is more sensitive to α increment than CPS4.
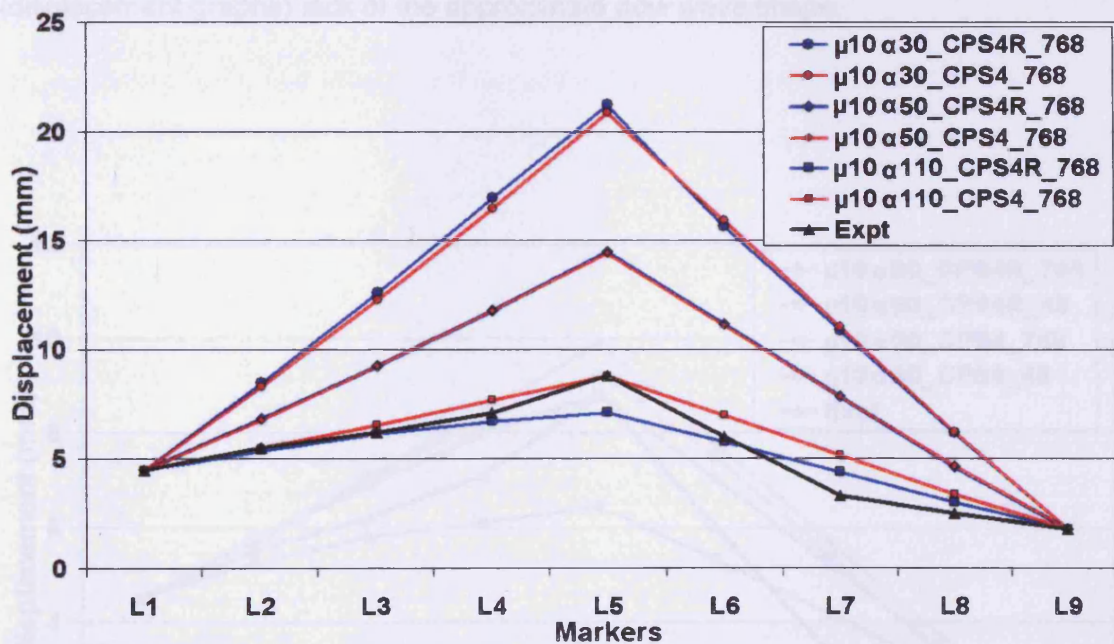
Figure 3.22: Comparison of using CPS4 and CPS4R (32 x 24 elements) for a selected α value (30, 50 and 100).

For a selected material parameter (μ=10 Pa, α=90), the linear element types (CPS4 and CPS4R) were compared for different mesh sizes (8 x 6 and 32 x 24 elements) and the result is shown in Figure 3.23. It was observed that the model using CPS4 (irrespective of its mesh size) displaced more than CPS4R. However, when using the same element type, the model with a few mesh (768 elements) displaced more.

The result for a set of material parameter for each element type is shown in Figure 3.24 to highlight the linearity of CPS4 graph compared to CPS4R for current model (768 elements). The results seem close to the experiment but both curves (displacement graphs) lack of the approximate *bow wave* shape.
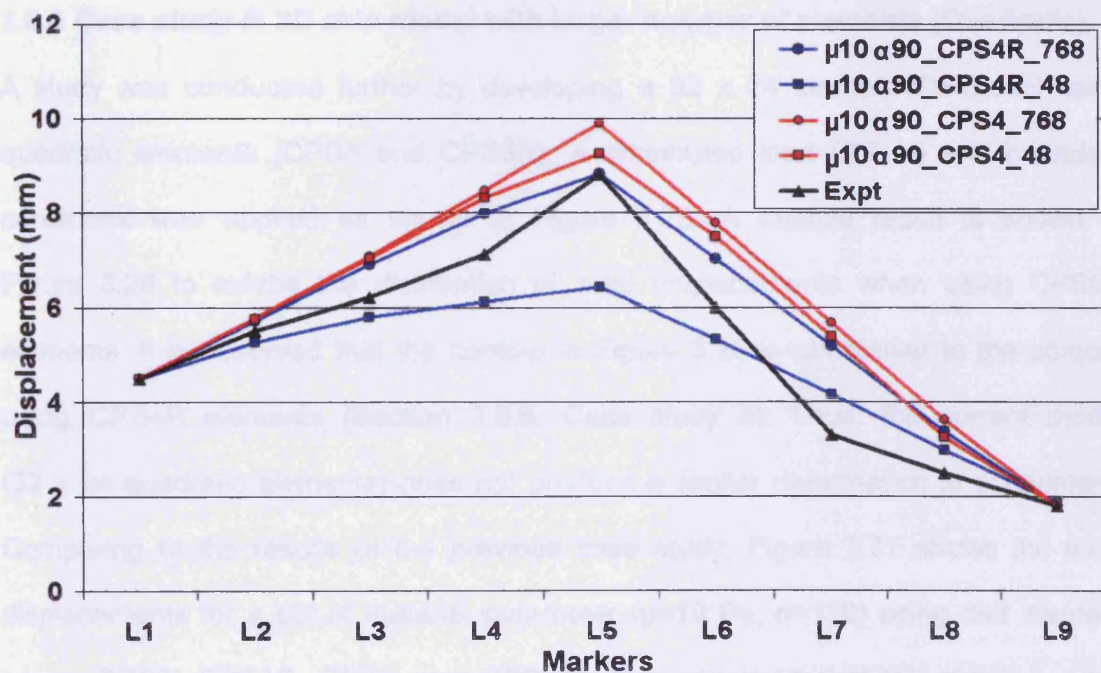
Figure 3.23: The effect of using different element types and mesh sizes.
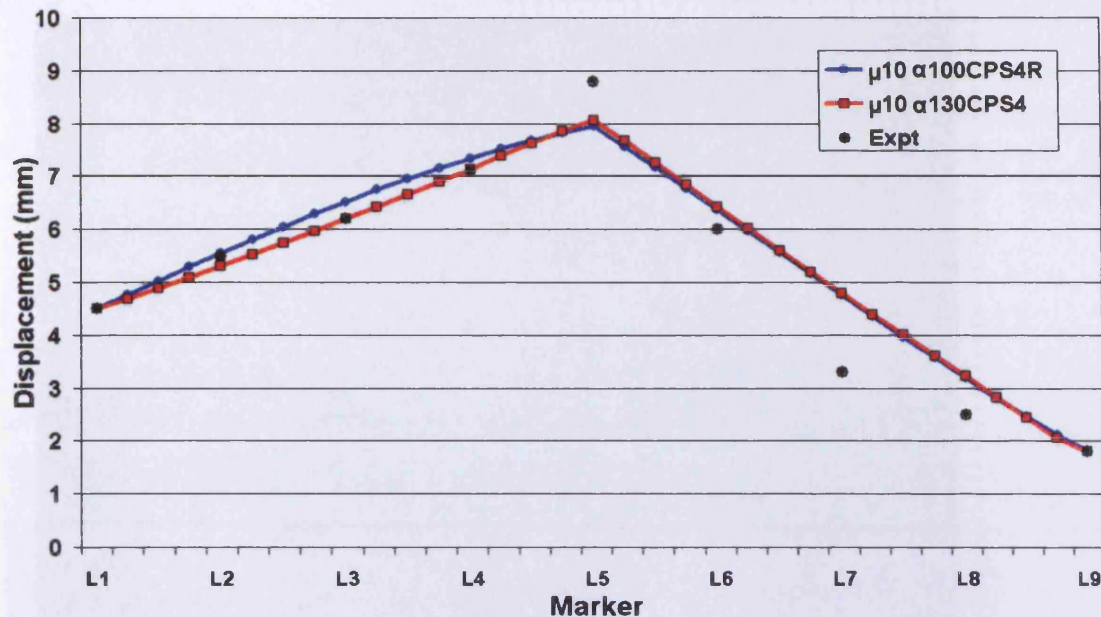
Figure 3.24: The effect of using different element types and mesh sizes.

3.6.6 *Case study* 6: 2D skin model with larger number of elements (Quadratic).

A study was conducted further by developing a 32 x 24 element FE model using quadratic elements (CPS8 and CPS8R). A distributed load (0.7 N) and boundary conditions was applied as shown in Figure 3.25. A sample result is shown in Figure 3.26 to exhibit the distribution of axial displacements when using CPS8R elements. It is observed that the contour in Figure 3.26 is not similar to the contour using CPS4R elements (Section 3.6.5, *Case study* 5). Thus, the current model (32 x 24 quadratic elements) does not produce a similar deformation to experiment. Comparing to the results of the previous case study, Figure 3.27 shows the axial displacements for a set of material parameter (μ=10 Pa, α=110) using four element types (CPS4, CPS4R, CPS8 and CPS8R). It is observed that the solution using quadratic elements (CPS8 and CPS8R) converged to a same curve. The same result is observed for CPS4R element. However, the displacement curve for CPS4 is not close to the rest but its shape is quite similar to the experiment.
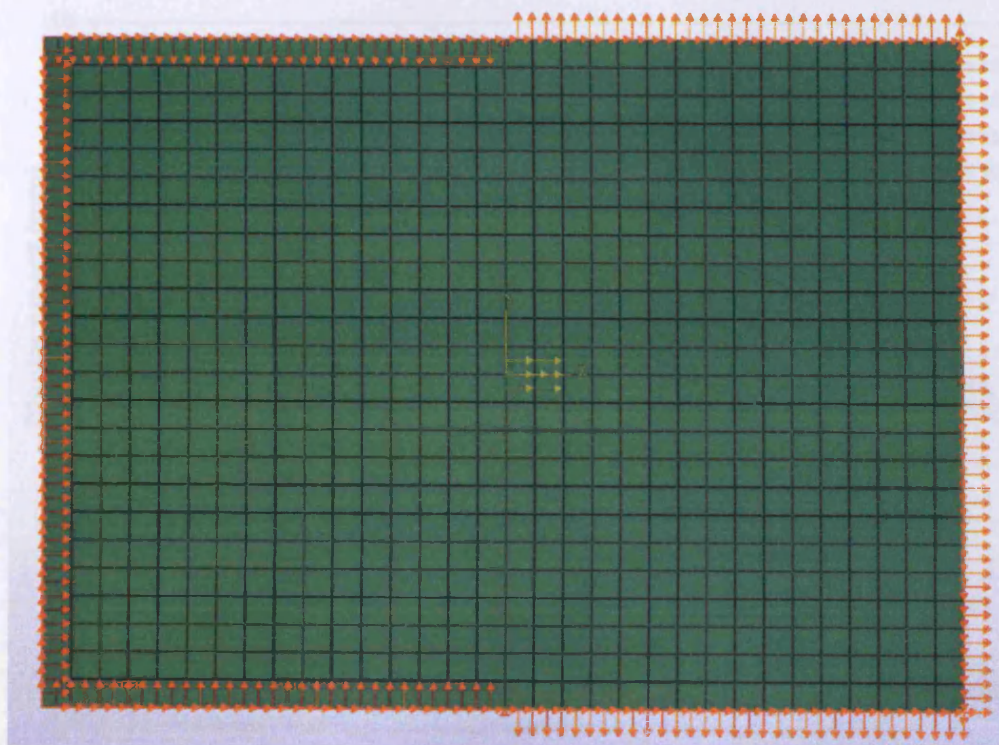
Figure 3.25: The load and boundary conditions for the model
(32 x 24 quadratic elements).

U, U1
+8.903e-03
+8.255e-03
+7.607e-03
+6.959e-03
+6.310e-03
+5.662e-03
+5.014e-03
+4.366e-03
+3.718e-03
+3.070e-03
+2.422e-03
+1.774e-03
+1.126e-03
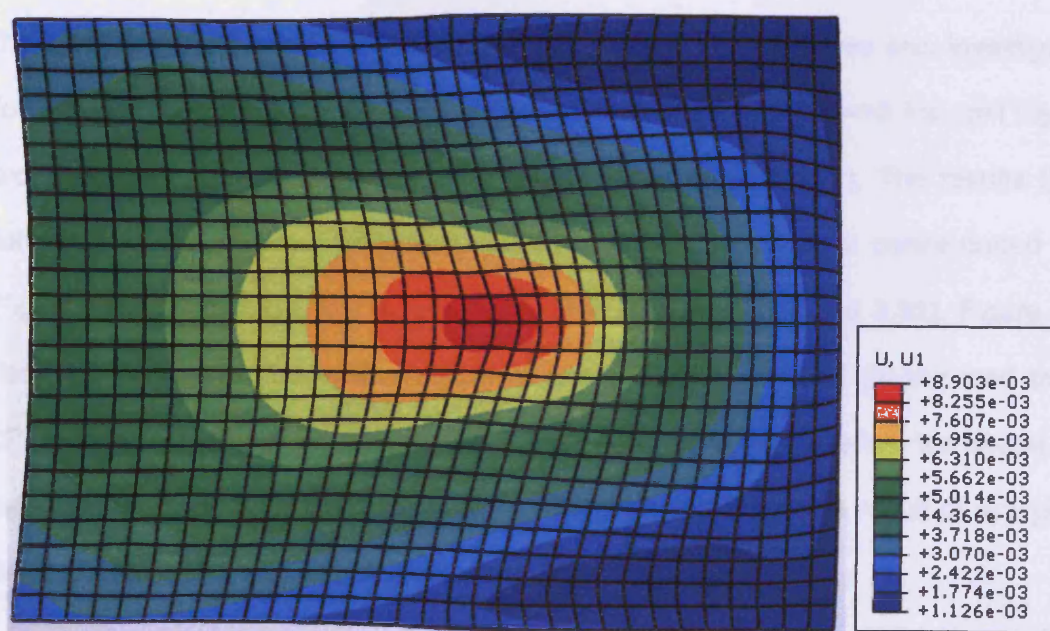
Figure 3.26: A contour showing the distribution of axial displacement
(μ=10, α=110, CPS8R).
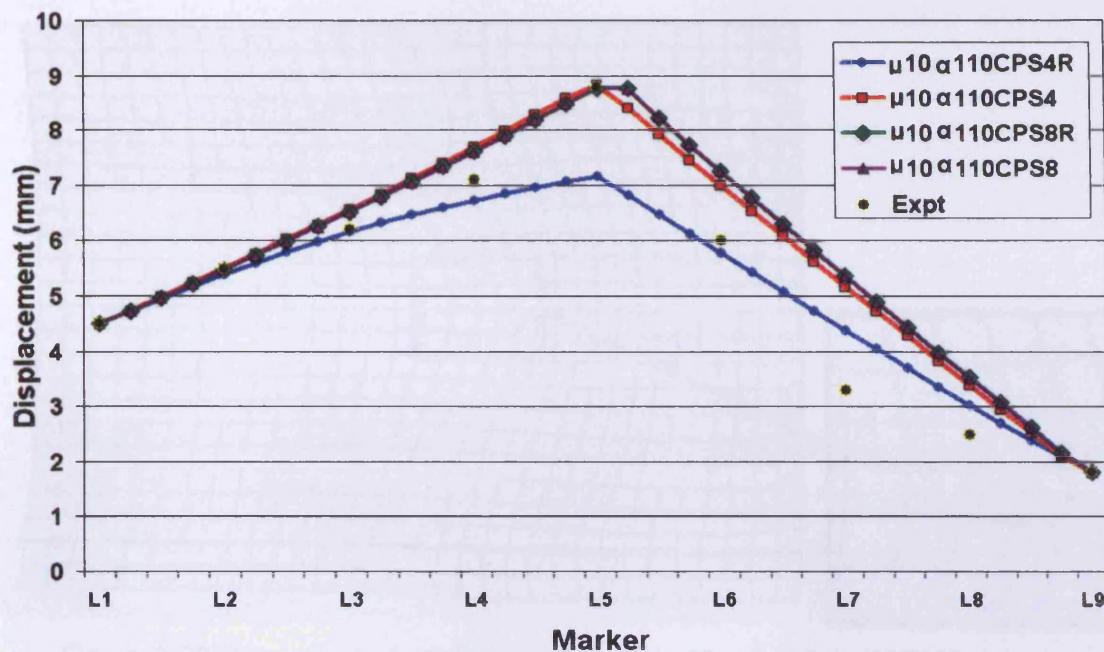
Figure 3.27: The results of using four element types (32 x 24 elements).

3.6.7 *Case study 7*: **Type of loading effect**.

The type of loading (concentrated and distributed, 0.7 N) effect was also investigated. For this study, a set of material parameters were considered (μ=10 Pa, α=110) and two types of quadratic elements were used (CPS8 and CPS8R). The results (plate deformation) are shown to demonstrate the effect of applying a concentrated load (Figures 3.28 and 3.29) and a distributed load (Figures 3.30 and 3.31). Figure 3.28 clearly highlights the hourglass shape of using CPS8R element (at the load point). CPS8 elements do not include the hourglass control effect, therefore the shape of a deformed element at the load point (Figure 3.29) is similar to the result of applying a distributed load (Figure 3.30 and Figure 3.31)
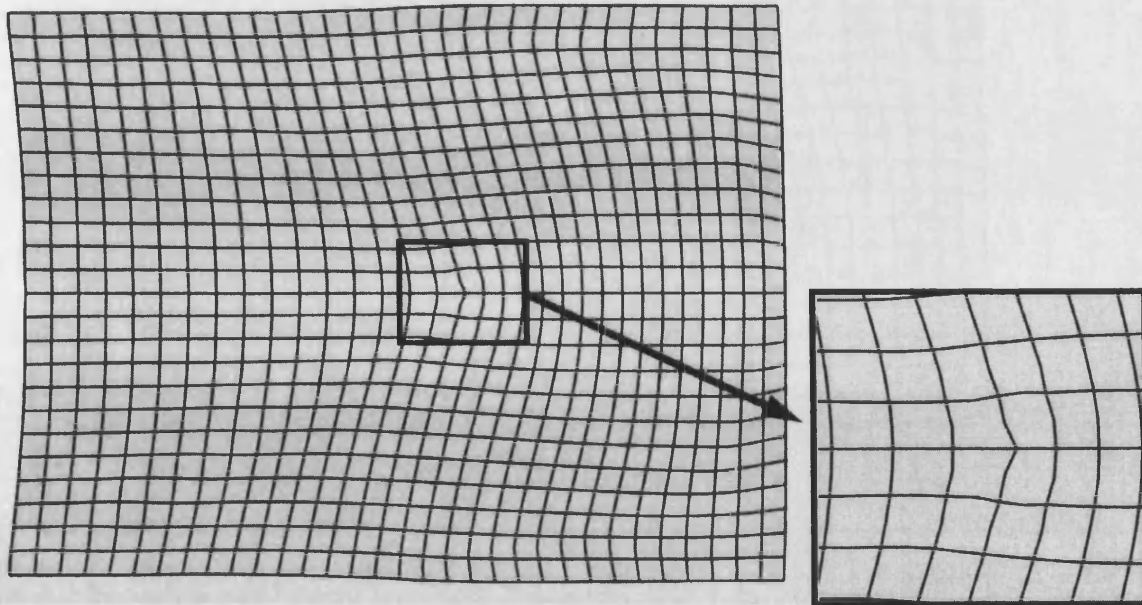
Figure 3.28: The effect of applying concentrated load (0.7N, CPS8R) to plate deformation. The area surrounding the load point is magnified to highlight the hourglass shape (maximum axial displacement: 9.03 mm).
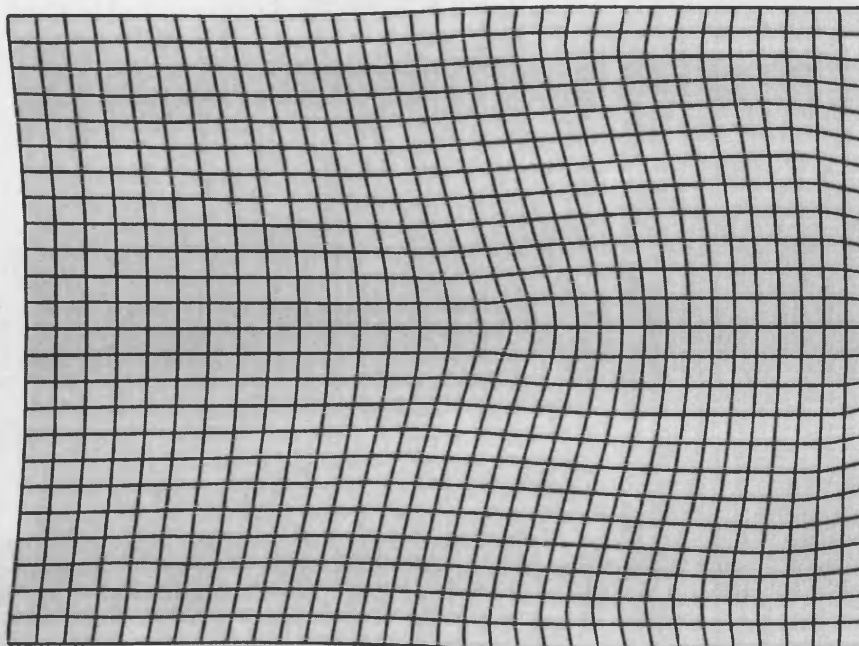
Figure 3.29: The plate deformation due to applying concentrated load (CPS8, 0.7N, μ=10 Pa, α=110, maximum axial displacement: 8.96 mm).
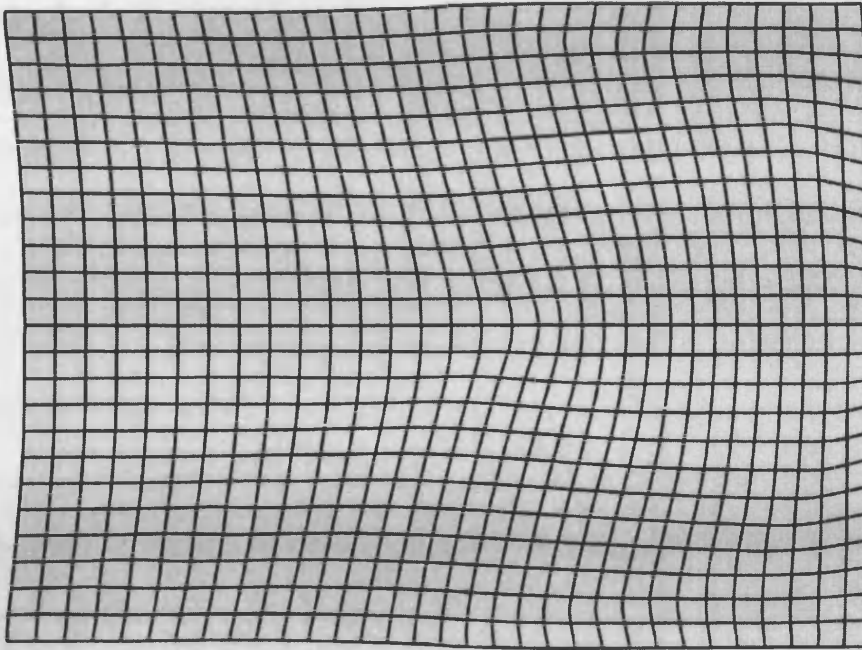
Figure 3.30: The plate deformation due to applying distributed load
(CPS8R, 0.7N, μ=10 Pa, α=110, maximum axial displacement: 8.90 mm).
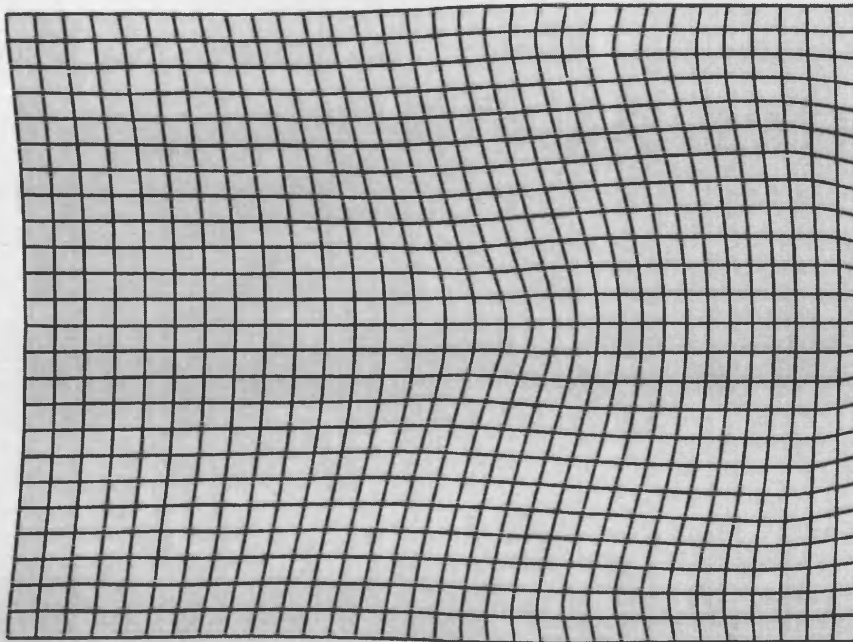
Figure 3.31: The plate deformation due to applying distributed load
(CPS8, 0.7N, μ=10 Pa, α=110, maximum axial displacement: 8.88 mm).

3.6.8 *Case study 8*: Increasing *N*.

As described in Section 2.4.1.2, the general strain energy density function for Ogden's model (equation 3.1) consists of N pairs of material parameter sets. However, the previous case studies (Section 3.6.1 to 3.6.7) only considered for the case when $N=1$. This study attempted to investigate the effect of increasing the pair of material parameter sets, N. The results (plate deformation) for a selection of material parameters are shown in Figures 3.32 to 3.36. This work stemmed from the first case study (Section 3.6.1 *Case study 1*) using a single pair of parameter ($N = 1$, $\mu_1=10$ Pa, $\alpha_1=26$) and then adding more pairs ($N = 2$ and 3) with an objective to maintain the results close to experiment. For simplicity, the model with the mesh size of 8 x 6 linear elements (CPS4R) was considered. 0.7 N concentrated load was applied at L5. Figure 3.32 shows the trend of deformation for a parameter set with $N=1$ ($\mu_1=10$ Pa, $\alpha_1=110$). The maximum axial displacement was found to be 23.37 mm (Figure 3.11, Section 3.6.1) and the shape of deformation does not match to experiment (Figure 3.8, section 3.6). By adding a second pair of parameter sets ($\mu_2=10$ Pa, $\alpha_2=70$), the maximum axial displacement reduced to about 8.8 mm. More interestingly, the shape of deformation matches to experiment.
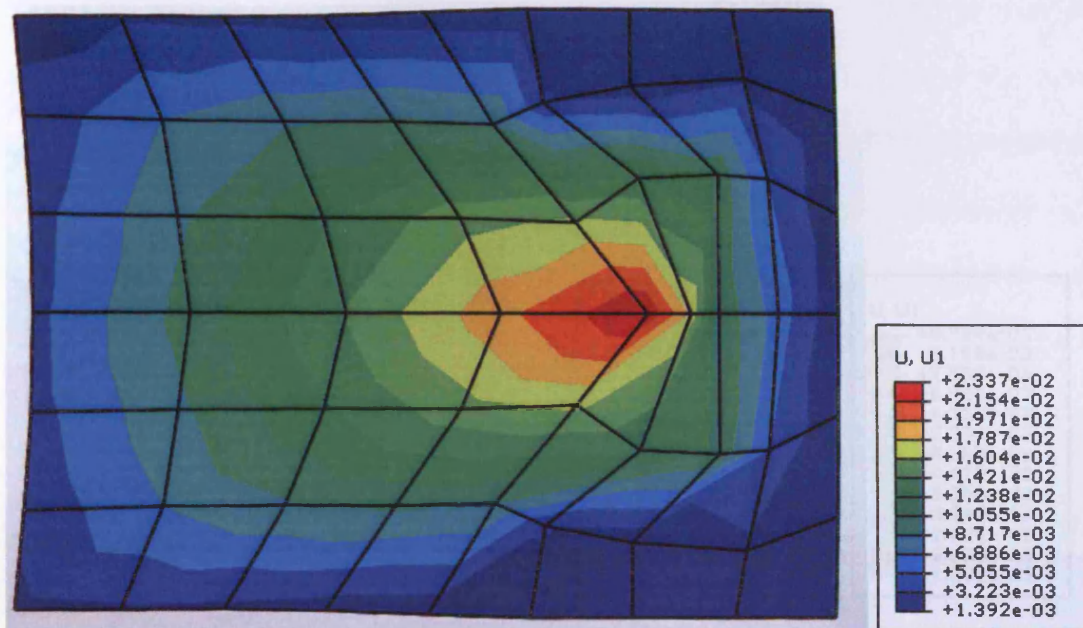
Figure 3.32: The plate deformation for $N=1$ ($\mu_1=10$ Pa, $\alpha_1=26$, CPS4R, 0.7N).
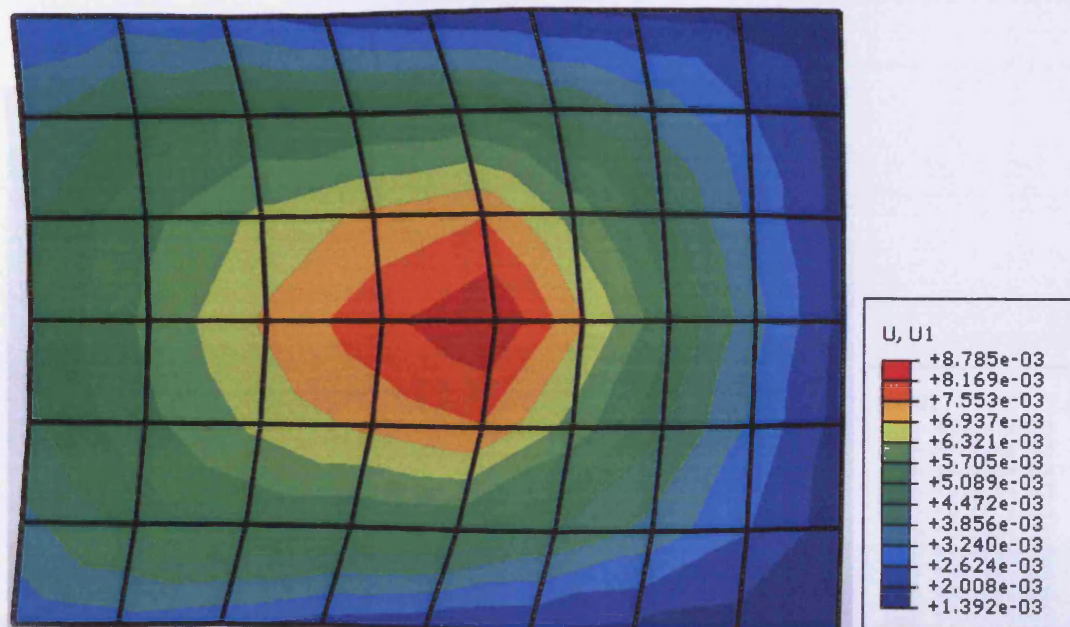
Figure 3.33: The plate deformation for $N=1$ ($\mu_1=10$ Pa, $\alpha_1=70$, CPS4R, 0.7N).
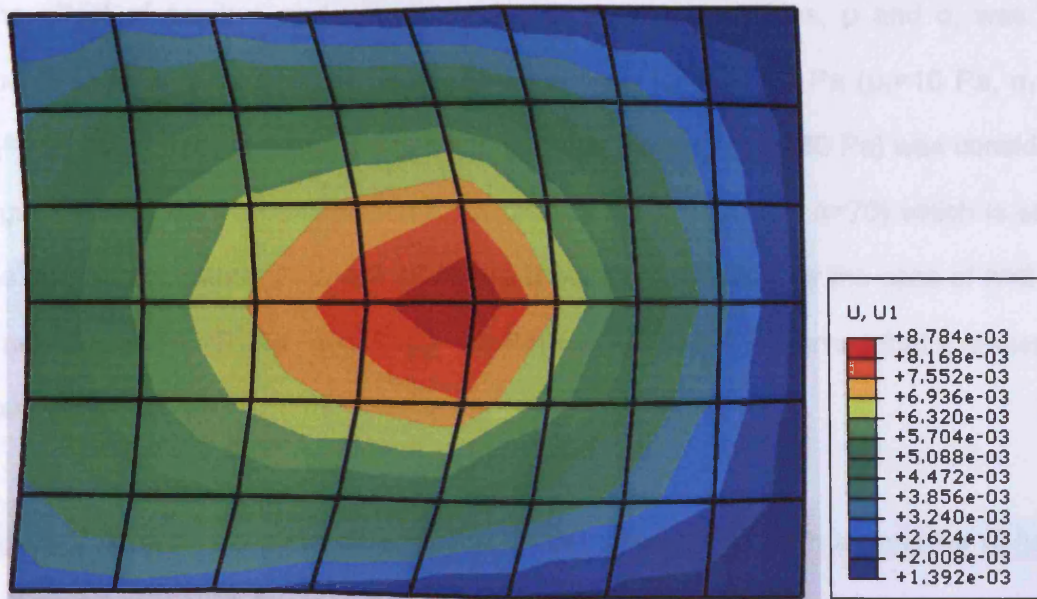
Figure 3.34: The plate deformation for N=2 (μ_1=10 Pa, α_1=26, μ_2=10 Pa, α_2=70).

By adding a third parameter set (μ_3=10 Pa, α_3=70), the maximum axial displacement

reduced to 8 mm (Figure 3.35). The correct shape of deformation is still observed.
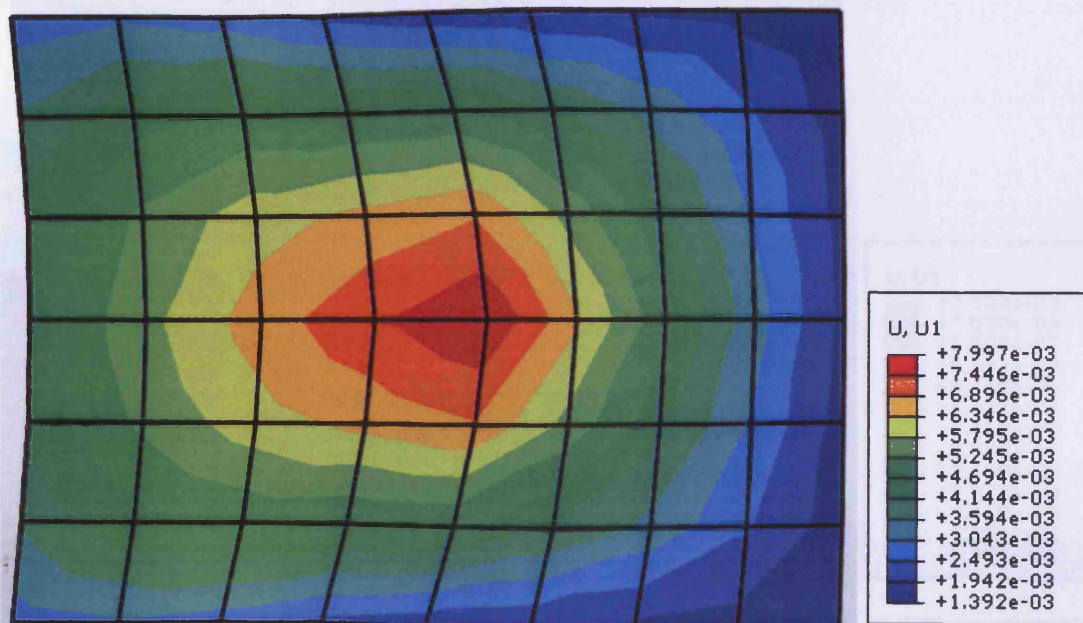
Figure 3.35: The plate deformation for N=3
(μ_1=10 Pa, α_1=26, μ_2=10 Pa, α_2=70, μ_3=10 Pa, α_3=70).

The effect of positive and negative material parameter values, μ and α, was also observed for the case where $N > 1$. Since solving for $\mu_2 = -10$ Pa ($\mu_1 = 10$ Pa, $\alpha_1 = 26$, $\mu_2 = -10$ Pa, $\alpha_2 = 70$) crashed the system, a higher value of μ ($\mu = 30$ Pa) was considered. Figure 3.36 shows a deformation for a case of $N=1$ ($\mu = 30$ Pa, $\alpha = 70$) which is set as the reference contour. Figure 3.37 shows a plate deformation for the case of $N=2$ with a negative α_2 ($\mu_1 = 10$ Pa, $\alpha_1 = 26$, $\mu_2 = 30$ Pa, $\alpha_2 = -70$). It is observed that it makes the plate stiffer.

Figure 3.38 shows a plate deformation for the case of $N=2$ with a negative μ_2 ($\mu_1 = 10$ Pa, $\alpha_1 = 26$, $\mu_2 = -30$ Pa, $\alpha_2 = 70$). It is interesting to observe that the plate deformed towards the opposite of the load direction. When a third parameter set was added with another negative μ ($\mu_3 = -30$, $\alpha_3 = 70$, $N=3$), the plate became stiffer as shown in Figure 3.39.

U, U1
+7.532e-03
+7.020e-03
+6.509e-03
+5.997e-03
+5.485e-03
+4.974e-03
+4.462e-03
+3.950e-03
+3.439e-03
+2.927e-03
+2.415e-03
+1.904e-03
+1.392e-03
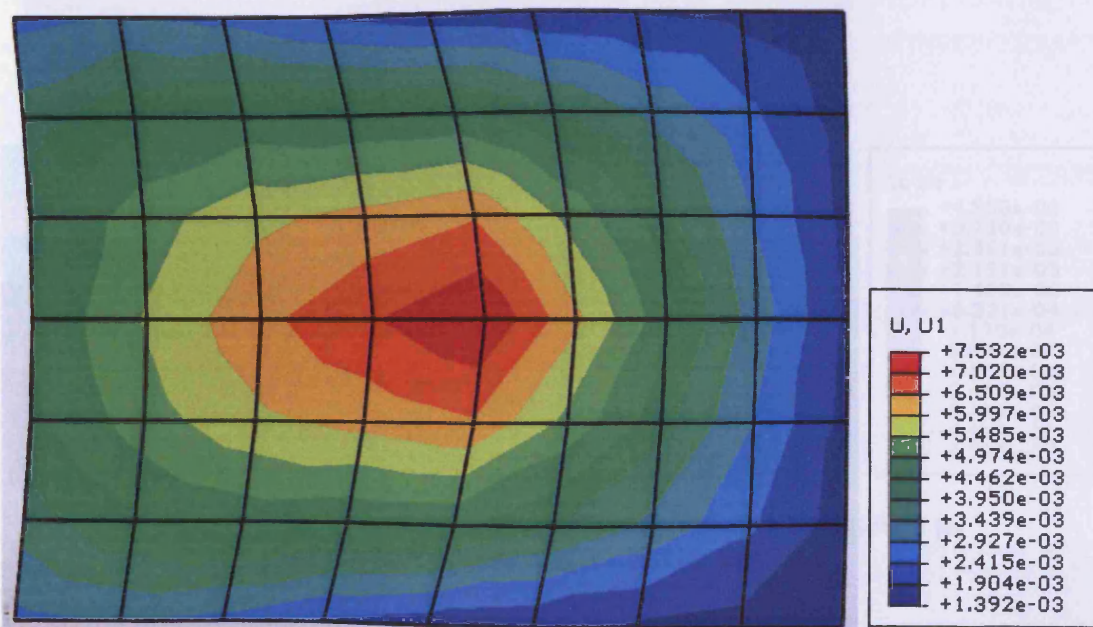
Figure 3.36: The plate deformation for $N=1$ ($\mu = 30$ Pa, $\alpha = 70$).
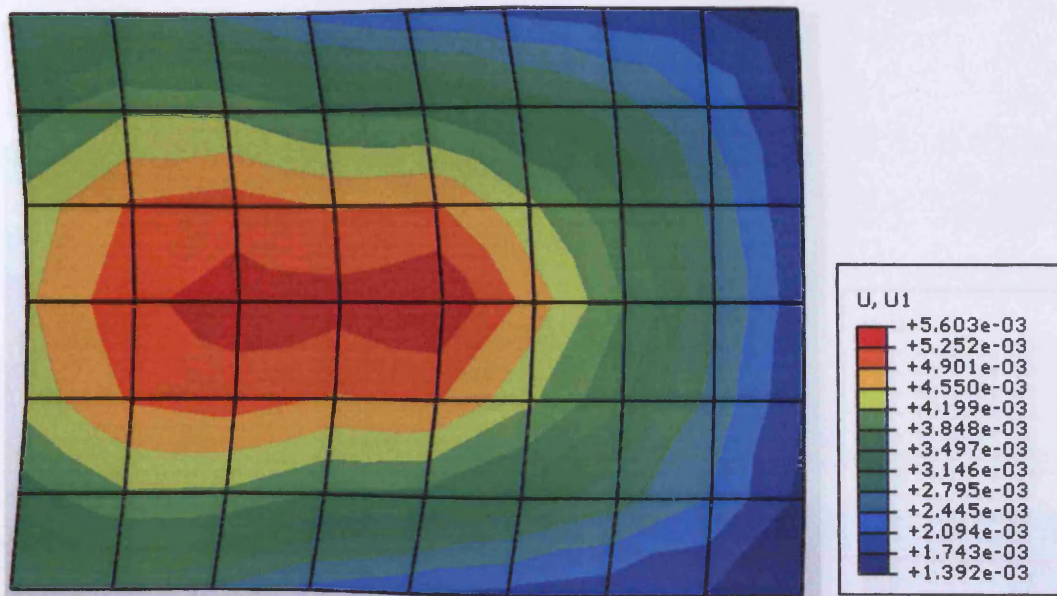
Figure 3.37: The plate deformation for N=2 with a negative α₂
(μ₁=10 Pa, α₁=26, μ₂= 30 Pa, α₂= -70).
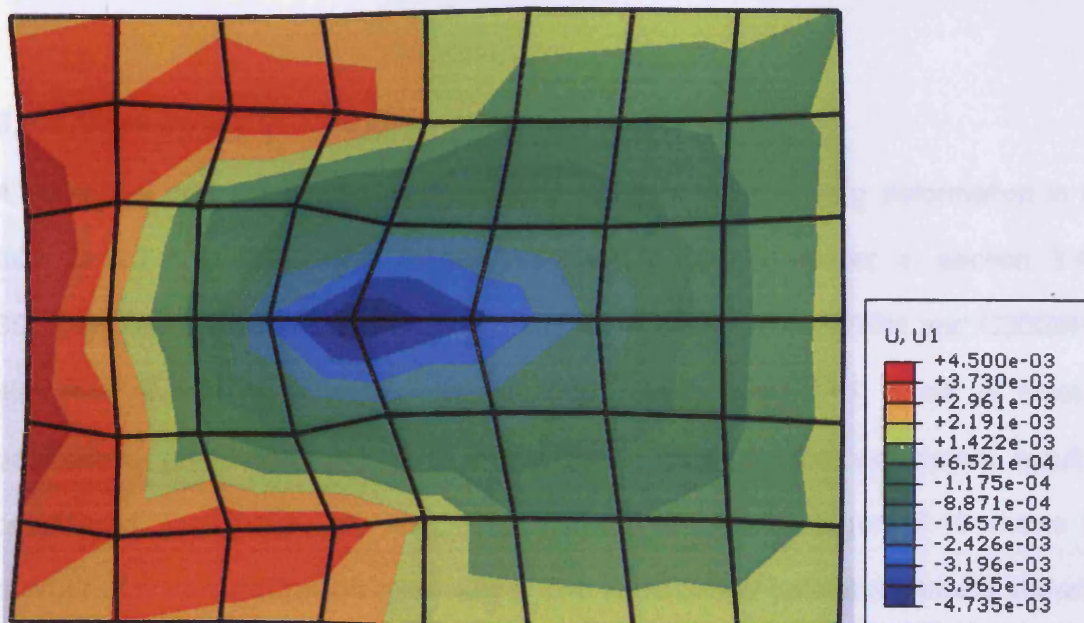
Figure 3.38: The plate deformation for N=2 with a negative μ₂
(μ₁=10 Pa, α₁=26, μ₂= -30 Pa, α₂=70).
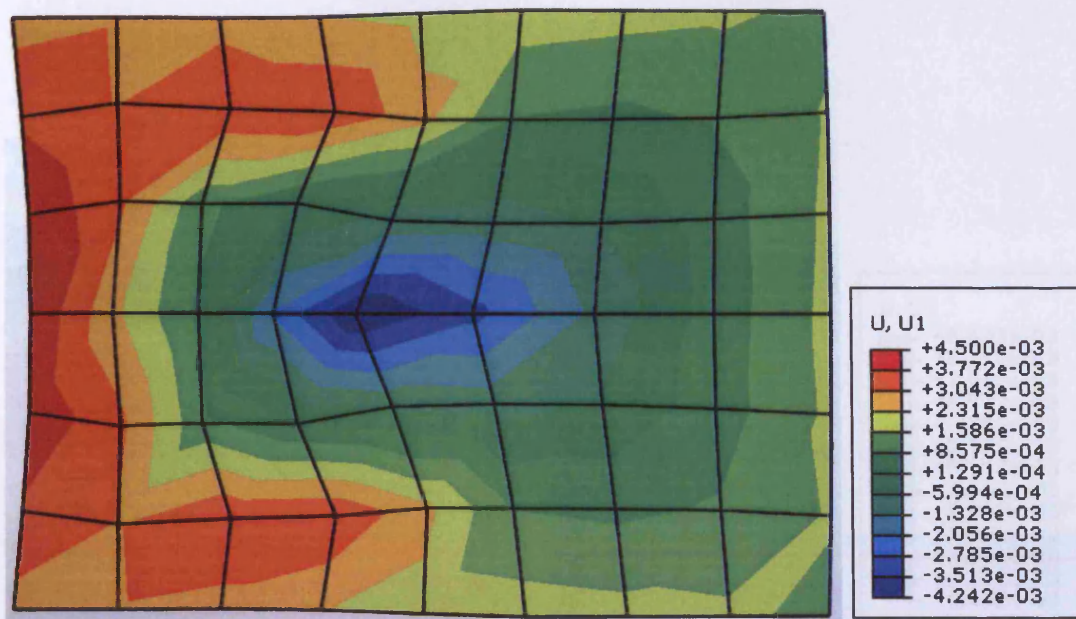
Figure 3.39: The plate deformation for $N=3$ with negative μ_2 and μ_3
($\mu_1=10$ Pa, $\alpha_1=26$, $\mu_2=-30$ Pa, $\alpha_2=70$, $\mu_3=-30$ Pa, $\alpha_3=70$).

3.6.9 *Case study 9*: 3D skin model.

A 3D model was developed to investigate effect of incorporating deformation in the third direction (z-axis). The model has been described earlier in section 3.4.2. 3D plane stress hybrid quadratic elements were assigned (C3D20H and C3D20HR) elements. Based on previous case studies' result, using $N=1$, a set of material parameters ($\mu=10$ Pa, $\alpha=110$) that was found close to the experiment result is considered. The results are shown in Figure 3.40 to 3.44. Figure 3.40 shows the contour of plate deformation (plan view). The undeformed-deformed plate is shown in Figure 3.41. The shape is in good agreement with the experiment (Figure 3.8, section 3.6).
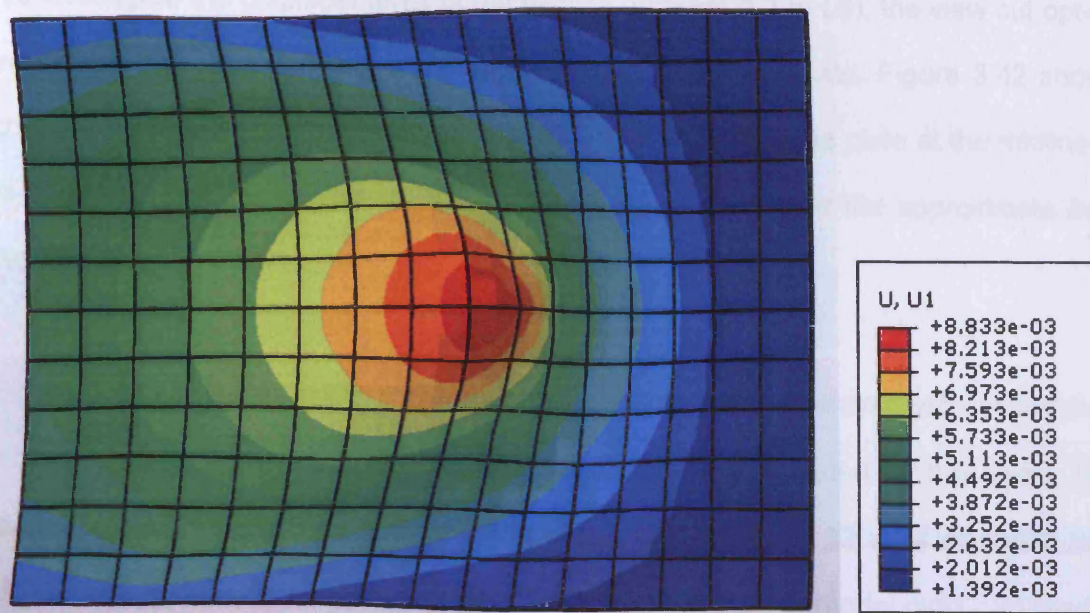
Figure 3.40: The plate deformation using 3D model (μ=10 Pa, α=110, C3D20H, 0.7N, plan view).
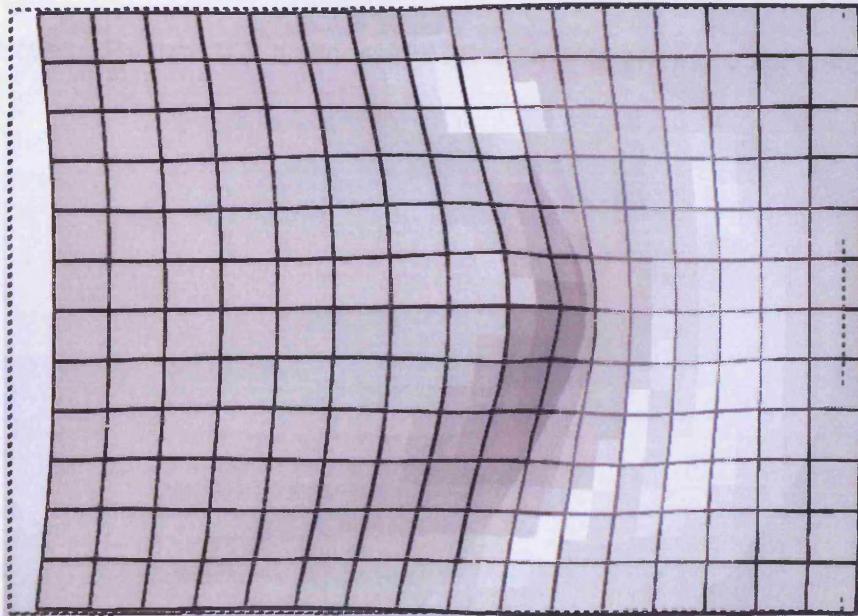
Figure 3.41: The undeformed-deformed plate for the 3D model (μ=10 Pa, α=110, C3D20H, 0.7N, plan view)

To investigate the displacements of the midline markers (L1 to L9), the view cut option was utilised to visualise the cross section of the deformed plate. Figure 3.42 shows the isometric view, cross section and the shape of the deformed plate at the midline. It is observed that the midline markers (L1 to L9) deformed into the approximate *bow wave* shape.

Figure 3.43 compares the displacement graphs for all the elements without reduced integration (CPS4, CPS8 and C3D20H) and mesh sizes assigned for this study. The legend showing '48' refers to 8 x 6 elements, '768' refers to 32 x 24 elements and '384' refers to 16 x 12 x 2 elements. It is found that the current model produced results which were very close to the experiment.

Figure 3.44 compares the axial displacements at midline nodes between 2D (CPS4 and CPS8) and 3D elements (C3D20H and C3D20HR) for the same material parameter (μ=10 Pa, α=110). It shows that 3D elements are more accurate.

(a)

(b)

(c)

U, U1
+8.833e-03
+8.213e-03
+7.593e-03
+6.973e-03
+6.353e-03
+5.733e-03
+5.113e-03
+4.492e-03
+3.872e-03
+3.252e-03
+2.632e-03
+2.012e-03
+1.392e-03

(d)
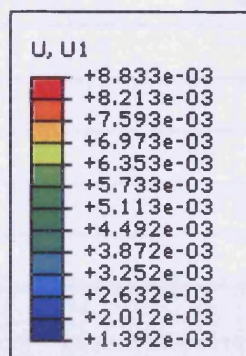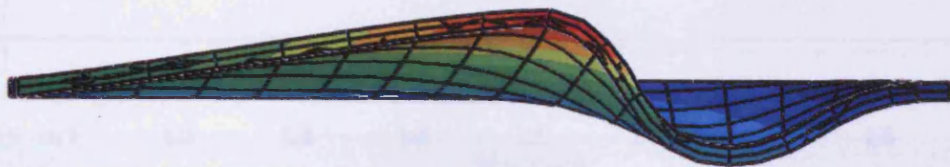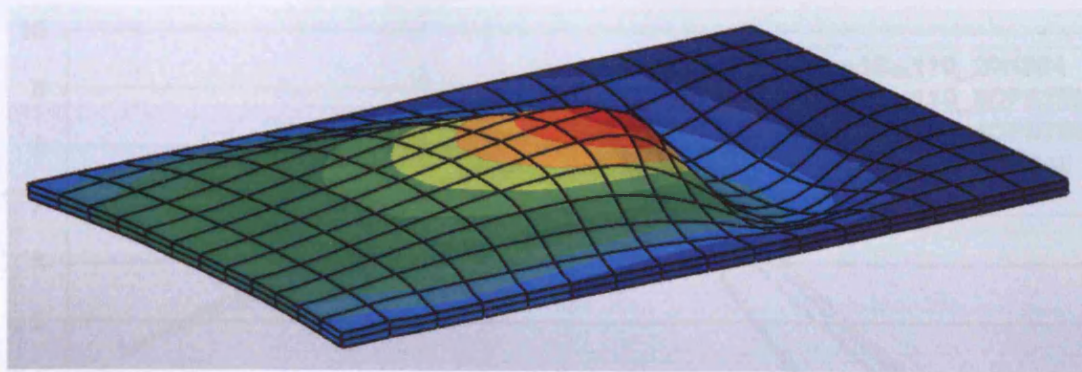
Figure 3.42: The shape and contour for the deformed plate; (a) isometric view;
(b) cross sectional view; (c) midline markers and (d) its contour legend.
(μ=10 Pa, α=110, C3D20H, 0.7N).
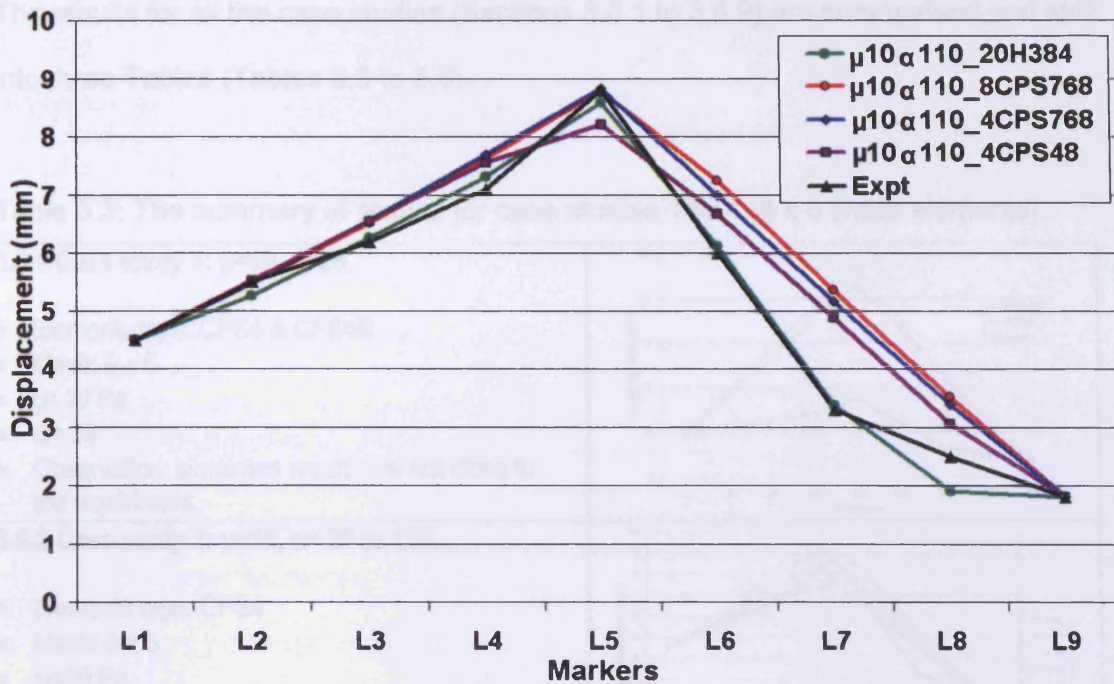
Figure 3.43: The axial displacement of midline markers for several elements and mesh sizes. It is obvious that the graph for current model (C3D20H, 16 x 12 x 2, green line) is very close to the experiment (black line).
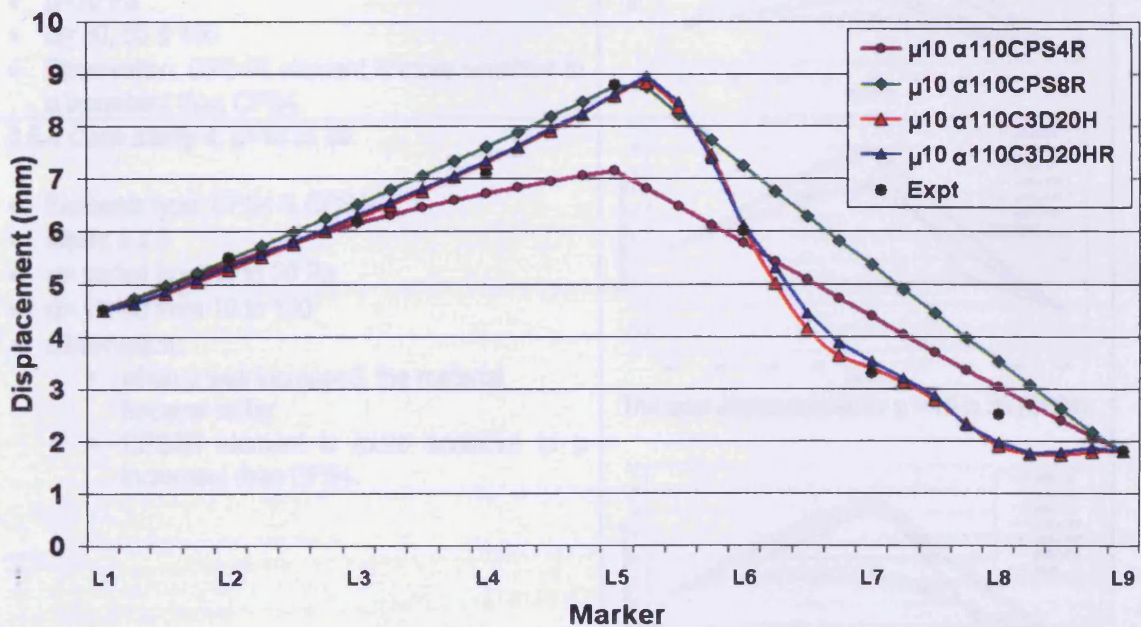
Figure 3.44: The axial displacement of midline markers for several elements and mesh sizes. It is obvious that the graph for current model (C3D20H, 16 x 12 x 2, green line) is very close to the experiment (black line).

The results for all the case studies (Sections 3.6.1 to 3.6.9) are summarised and split

into three Tables (Tables 3.3 to 3.5).

Table 3.3: The summary of results for case studies 1 to 4 (8 x 6 linear elements).
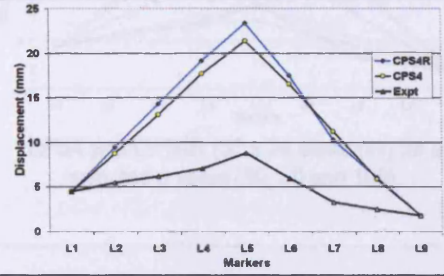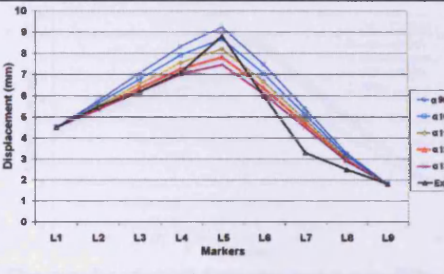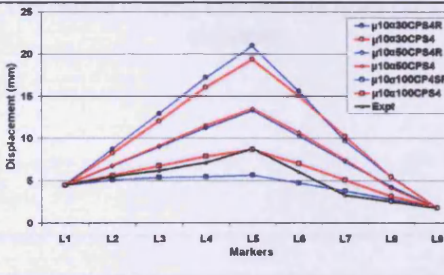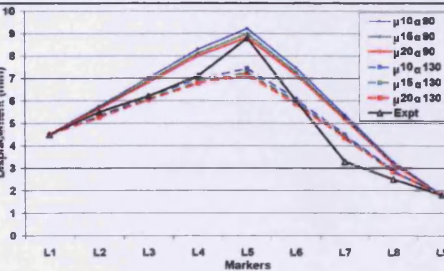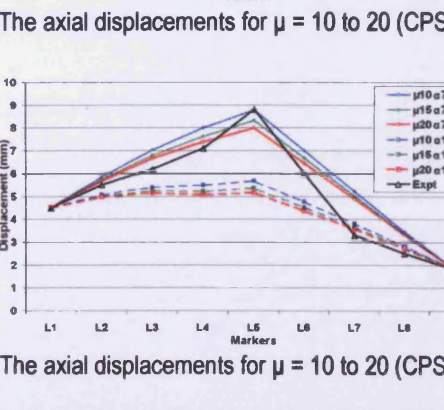
3.6.1 *Case study 1*: µ=10, α=26. • Elements type: CPS4 & CPS4R • Mesh: 8 x 6 • µ=10 Pa • α= 26 • Observation: simulated results are not close to the experiment.	
3.6.2 *Case study 2*: µ=10, α= 20 to 130. • Elements type: CPS4 • Mesh: 8 x 6 • µ=10 Pa • α= varied from 10 to 130 • Observation: for µ=10, the experimental results fit the range of α between 100 and 130	
3.6.3 *Case study 3*: CPS4 versus CPS4R • Elements type: CPS4 & CPS4R • Mesh: 8 x 6 • µ=10 Pa • α= 30, 50 & 100 • Observation: CPS4R element is more sensitive to α increment than CPS4.	

3.6.4 *Case study 4*: µ=10 to 20.
 	
• Elements type: CPS4 & CPS4R
• Mesh: 8 x 6
• µ= varied from 10 to 20 Pa
• α= varied from 10 to 130
• Observation:
  ■ when µ was increased, the material became stiffer.
  ■ CPS4R element is more sensitive to µ increment than CPS4.
	
	The axial displacements for µ = 10 to 20 (CPS4).
	
	The axial displacements for µ = 10 to 20 (CPS4).

Table 3.4: The summary of results for case studies 5 and 6 (32 x 24 elements).

3.6.5 *Case study 5*: 2D skin model with larger number of linear elements.

- Elements type: CPS4 & CPS4R
- Mesh: 32 x 24
- µ= 10 Pa
- α= varied from 10 to 130
- Observation: CPS4 (irrespective of its mesh size) displaced more than CPS4R. However, when using the same element type, the model with a few mesh (768 elements) displaced more.
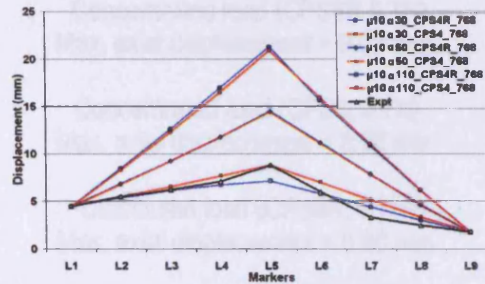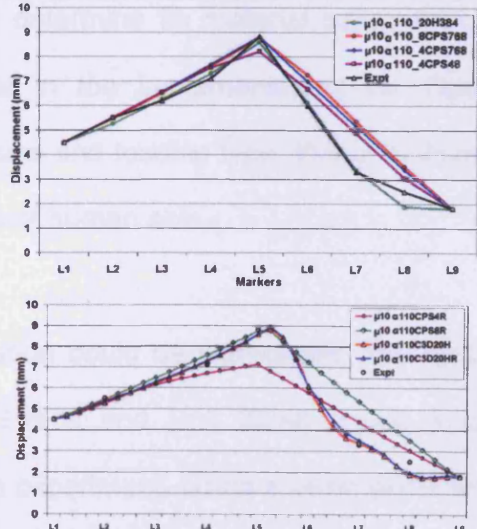
CPS4 and CPS4R (32 x 24 elements) for a selected α value (30, 50 and 100).

3.6.6 *Case study 6*: 2D skin model with larger number of elements (Quadratic).

- Elements type: CPS8 and CPS8R
- Mesh: 32 x 24
- µ= 10 Pa
- α= 110
- Observation:
  - the solution using quadratic elements (CPS8 and CPS8R) converged to a same curve.
  - CPS4R element behaves the same.
  - CPS4 result is not close to the rest but its shape is quite similar to the experiment.
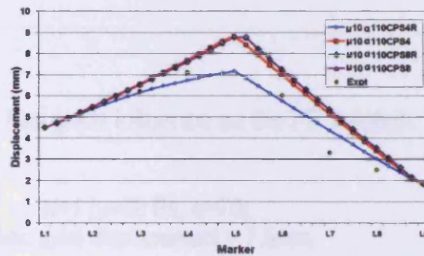
The results of using four element types (32 x 24 elements).

Table 3.5: The summary of results for case studies 7 to 9.

3.6.7 *Case study* 7: Type of loading effect.
 	
• Elements type: CPS8 and CPS8R
• Mesh: 32 x 24
• μ= 10 Pa
• α= 110
• Loading type: concentrated and distributed load.
• Observation:
   ▪ the type of loading has a significant influence to the FE solution
   ▪ CPS8R element highlights the hourglass shape
	Results:
	Concentrated load (CPS8R 0.7N)
	Max. axial displacement = 9.03 mm.
	
	Concentrated load (CPS8, 0.7N)
	Max. axial displacement = 8.96 mm.
	
	Distributed load (CPS8R, 0.7N)
	Max. axial displacement = 8.90 mm.
	
	Distributed load (CPS8, 0.7N)
	Max. axial displacement = 8.88 mm).

3.6.8 *Case study* 8: Increasing *N*.

• Elements type: CPS4R
• Mesh: 32 x 24
• *N*: varied
• Observation: number of pairs of Ogden parameters, *N*, has great influence on the FE solution.

Results:

$N=1$ (μ_1=10 Pa, α_1=26, CPS4R, 0.7N) Max. axial displacement = 23mm	$N=1$ (μ=30 Pa, α=70). Max. axial displacement = 7.5mm
$N=1$ (μ_1=10 Pa, α_1=70, CPS4R, 0.7N) Max. axial displacement = 8.8mm	$N=2$ with a negative α_2 (μ_1=10 Pa, α_1=26, μ_2= 30 Pa, α_2= -70) Max. axial displacement = 5.6mm
$N=2$ (μ_1=10 Pa, α_1=26, μ_2=10 Pa, α_2=70). Max. axial displacement = 8.8mm	$N=3$ (μ_1=10 Pa, α_1=26, μ_2=10 Pa, α_2=70, μ_3=10 Pa, α_3=70) Max. axial displacement = 8.0mm
$N=2$ with a negative μ_2 (μ_1=10 Pa, α_1=26, μ_2= -30 Pa, α_2=70). Max. axial displacement = 4.5mm	$N=3$ with negative μ_2 and μ_3 (μ_1=10 Pa, α_1=26, μ_2= -30 Pa, α_2=70, μ_3= -30 Pa, α_3=70). Max. axial displacement = 4.5mm

3.6.9 *Case study* 9: 3D skin model.

Elements type: C3D20H and C3D20HR
• Mesh: 16 x 12 x 2
• *N*=1, μ=10 Pa, α=110
• Observation: 3D model gave better results (closer to experiment)

3.7 Discussion

In general, the results produced from the case studies conducted (Section 3.6.1 to 3.6.9) have drawn several issues to be discussed. Despite that, producing a converged solution for each analysis was already considered as an achievement as for analysing a hyperelastic material, the main challenge was to obtain a converged solution. Several reasons were found to contribute to the failure (system abortion or warning) in such an analysis. They were excessive distortion of elements, too much step increment required, the system matrix contained several negative eigenvalues, zero pivot was encountered and/or the strains were so large that the programme ignored the hyperelasticiy calculation at several points. This is the possible reason why the model did not behave as nonlinear as it should be.

Prior to the case studies, the FE implementation used successfully for conducting the FE validation tasks was further developed to model and simulate skin deformation (Subject 1, X=0°, 0.7N). The case studies were developed systematically initially using material parameters found by other researchers (Section 3.6.1 *Case study 1*) and progressed up to developing a 3D skin model (Section 3.6.9 *Case study 9*). The objectives were not only to model skin and determine its material parameters, but more importantly, to investigate the effects in the implementation; i.e. Ogden's material parameters, element type, element size and loading type; that contributed to the knowledge in FE modelling and simulation of human skin.

From the results, several interesting observation could be highlighted. The result of the first case study (μ= 10 Pa, α = 26, Evans and Holt 2009) shows a large discrepancy of the current result compared to experiment. Using a basic plane stress linear quadrilateral element, CPS4, the maximum axial displacement recorded a

difference of 12 mm (133 percent), while using a similar element but with reduced integration (CPS4R), a 14 mm (155 percent) difference was calculated. Despite the difference, it provided a rough value for further analysis where by maintaining μ= 10 Pa, α was varied and it was observed that higher α increased the membrane stiffness. The results also show that α between 100 and 130 (μ=10 Pa, CPS4) were close to experiment. Therefore, this proves that the material parameters, μ and α, have a significant influence on the deformation of the membrane.

In this study, it was also observed that higher μ increased the membrane stiffness and its rate depends on using the element type as a element with hourglass control (CPS4R) was more sensitive to the change of μ and α. Considering the density of the mesh (8 x 6 or 32 x 24) and types of element (CPS4, CPS4R, CPS8 and CPS8R), it was found that the membrane meshed into a large number of quadratic element (32 x 24) produced a similar result (converged to a value) despite the types of its elements (CPS8 or CPS8R) for the same material parameters (μ = 10 Pa, α = 110). This shows that the quadratic elements have no significant effect in this particular case study (32 x 24 elements). Moreover, the graphs were found to be a much more in linearly manner and not exhibiting the approximate *bow wave* shape. Therefore it was found that it was more beneficial to use elements (CPS4, CPS4R) as they have less number of nodes and thus makes the task to assigning the boundary conditions easier.

The type of loading was known to have a significant influence to a large element when it underwent large deformation. However, for the case when applying a concentrated load on plate with a large number of quadratic elements with the hourglass control effect (32 x 24, CPS8R), the relevant element deformed into an hourglass shape (Figure 3.28 Section 3.6.7) how much it displaced was not significant to distributed

load. Despite its shape, it displaced 9.027 and 8.903 mm for concentrated and distributed load respectively (1.3 percent in difference). To create an accurate skin model, the load (0.7 N) should be distributed across the area of the load tab (Figure 2.14, Section 2.4.7). However, this could not be possible for a model with less number of nodes (8 x 6 elements).

Based on the results (Section 3.6.8), it is found that the number of pairs of Ogden parameters, N, has the greatest influence on the deformation of the skin model. Adding a second pair of material parameter, (μ_2= 10 Pa, α_2= 70) to an initial μ_1= 10 Pa, α_1= 26 reduced the maximum axial displacement significantly (from 23.4 mm to 8.8 mm, 62 percent reduction, Figures 3.32 to 3.34). The sequence of the parameters (which one μ_1, α_1 or μ_2 α_2) had no effect in the FE computation. And additional pair (μ_3= 10 Pa, α_3= 70) would further stiffen the membrane. It is also observed that if α is negative in one of the pairs, then the membrane will be stiffer. It is more interesting to observe that if μ is negative, the elements will deform in the opposite to the load direction. For a combination of μ_1 = 10 and μ_2= -10 or vice versa, the system will crash.

In this study, it was found that the most accurate model was using 3D elements (Figure 3.43 and 3.44, Section 3.6.9). Using the material properties of μ= 10 Pa, α= 110 (N=1), both elements (C3D20H and C3D20HR) produced an approximate *bow wave* shape and the results were very close to the experiments. Moreover, it shows wrinkling at the test area. Notwithstanding that the 3D model was the most realistic and has produced the accurate and reliable results, the procedure in developing it was found to be more tedious compared to the 2D models. The simplest 2D model that produced a result with acceptable accuracy was using 8 x 6 CPS4 elements,

where the error for maximum axial displacements was found to be 7 % compared to experiment.

From all the results from the case studies, the hyperelastic material parameters of skin for Subject 1, based on the Ogden model with N=1, was estimated to be close to μ = 10 Pa, α = 110 (N=1, Ogden model, Figures 3.43 and 3.44, Section 3.6.9). The lowest α that can match the maximum axial displacement was α = 110 using CPS4R, 8 x 6 elements (Figure 3.23, Section 3.6.5). These are not close to values of μ = 10 Pa, α = 26 determined by Evans and Holt (2009).

The warnings of excessive element distortion and some cases where the programme ignored the hyperelasticity calculation at several points were assumed to cause this discrepancy. This has restricted the model from behaving nonlinearly and thus large deformation did not occur. Moreover, the simulation-experiment data for comparison was focused on the axial displacements of the midline markers (L1 to L9) and not for the whole membrane. To compare axial and lateral displacements data obtained from simulation to experiment at every node was desired (to determine distribution of error) but in FE modelling using Abaqus, this would be very difficult and time consuming as it has to be done manually. Furthermore, even if a programme is written to read the data from the simulation, it would be tedious to determine the same location of nodes (on skin model, Abaqus) and data points (on skin test area) for accurate comparison of data.

Apart from that, although the current study is aiming to determine skin properties, the main limitation lies in the tediousness in developing an accurate and reliable skin model. All the described case studies were conducted based on the data referred to Subject 1 at 0.7N load at X=0° direction. At different loading conditions or for different

subject, the corresponding data would be applied. Applying the boundary conditions was found to be the most tedious task and it was extremely difficult when applying to a 3D model.

Since the approach was found not appropriate, the FE modelling and simulation was not carried out further for other subjects. Therefore, a FE program which is able to simulate and at the same time optimise the parameters is desired to determine the mechanical properties of human skin. One possible solution was to adapt an FE programme which had been developed earlier by Evans for measuring skin properties using the DIC technique (Evans 2009).

3.8 Conclusion

The objective to determine the mechanical properties of human skin using FE modelling and simulation has been achieved successfully and based on the results, the hyperelastic properties for Subject 1 was estimated to be μ = 10 Pa, α = 110. Although it was not close to the result obtained by other researchers and the FE implementation was found to be tedious, the thorough study conducted in this chapter has produced several useful findings that contribute to the knowledge of modelling skin using FEA and Abaqus.

The outcome of this study suggests further exploration of an optimisation procedure to determine the optimum Ogden's material parameters by minimising the deformation error for every possible point on the membrane compared to the measured skin deformation using MA technique as described in Chapter 2.

The subsequent Chapter describes the work carried out using a combination of FEA and optimisation procedures as a tool to determine the mechanical properties of skin based on the experiment described in Chapter 2.

CHAPTER 4

MEASURING THE MECHANICAL PROPERTIES OF HUMAN SKIN

4.1 Introduction

Chapter 2 highlights the success of a new experimental method that has been used to measure full-field deformation of human skin *in vivo* employing small scale motion analysis (MA) techniques. The results of the experiments were found reliable and useful, demonstrating that the system has a great potential for other applications. The experimental data has been analysed extensively to portray the nonlinear viscoelastic, and anisotropic behaviour of skin. Moreover, the data has been formed into FEA input, ready for computing skin properties.

The previous chapter (Chapter 3) describes the work carried out in modelling skin deformation using a commercially available FEM software, Abaqus v6.8-1. The FE models developed was found to be useful and capable of estimating the hyperelastic material parameters of skin. However, the job was tedious and time consuming as only one set of material parameters, μ and α, can be input and analysed for each simulation. The parameters were manually and frequently changed to obtain an optimum result for a match to experimental data. Therefore, an optimisation procedure that could automatically optimise μ and α values by reducing the error between simulated and experiment result was desired. For this purpose, a FE programme with an optimisation procedure was employed in this study.

This Chapter describes a continuation from the work carried out in Chapter 2 and Chapter 3, which aims to further analyse the experimental output and skin properties. It starts by justifying the need for the current approach and ends up by analysing the hyperelastic properties of skin. In compliment to this, the followings are discussed;

- The motivations to employ the current approach

- Scope of the work

- Inverse FEA using Matlab

- Optimisation procedure

- Quantifying the mechanical properties of skin

The results are presented and critically discussed. Finally, a conclusive remark ends the chapter.

4.2 Motivations to employ current approach

At the beginning of this thesis, it is already justified how important it is to understanding the mechanical properties of skin for clinical and engineering applications (Section 1.1, Chapter 1). However, determining the mechanical properties of skin has always been a great challenge. Chapter 2 (Section 2.2) describes several previous studies that has motivated the current study to develop novel *in vivo* experiments employing the MA techniques. Chapter 3 (Section 3.2) emphasises the need to develop simple but reasonably accurate FE models that could simulate skin deformation accurately. By using Abaqus, it has led to the determination of the hyperelastic material parameters for Subject 1 (X=0°) but the job was tedious and time consuming. It was assumed not practical if to be used for five subjects with three different load orientations (X=0°, 45° and 90°) each. A method which could solve this matter is thus inevitable. One possible solution is to utilise an optimisation procedure.

Evans (2009) developed an inverse FE programme to determine the mechanical properties of skin, modelled as an Ogden hyperelastic membrane, with a tension field wrinkling model and initial stretch identified as an additional parameter. The success in applying the programme to the experimental data obtained from *in vivo* testing employing a DIC technique, has inspired this study to adapt this procedure. It justifies the significance of the current study aimed to adapt a FE programme with an optimisation procedure to determine the hyperelastic material parameters of human skin. No one has reported using this or similar procedures previously in relation to the current experimental work employing MA techniques, thus confirming the novelty of the current approach.

4.3 Scope of work

The ultimate aim of the current study is to determine the mechanical properties of human skin and therefore, the work conducted and described in this study and chapter provides the tools to achieve this. An attempt was made to determine the hyperelastic material parameters for five subjects using a combination of experiments employing MA techniques and FE programming with an optimisation procedure using Matlab (Matlab v7.7 R2008b, The MathWorks, Inc.). The work stemmed from the success of generating data from a novel technique described in Chapter 2 and the need for a programme that could optimise skin material parameters from those data. The work can be summarised into a flowchart diagram (Figure 4.1).

The key to the success of this study was to adapt a FE programme with an optimisation procedure to determine the hyperelastic materials for five subjects and different load directions. This was achieved and the skin properties for the five subjects are presented and compared.

Finite Element Analysis
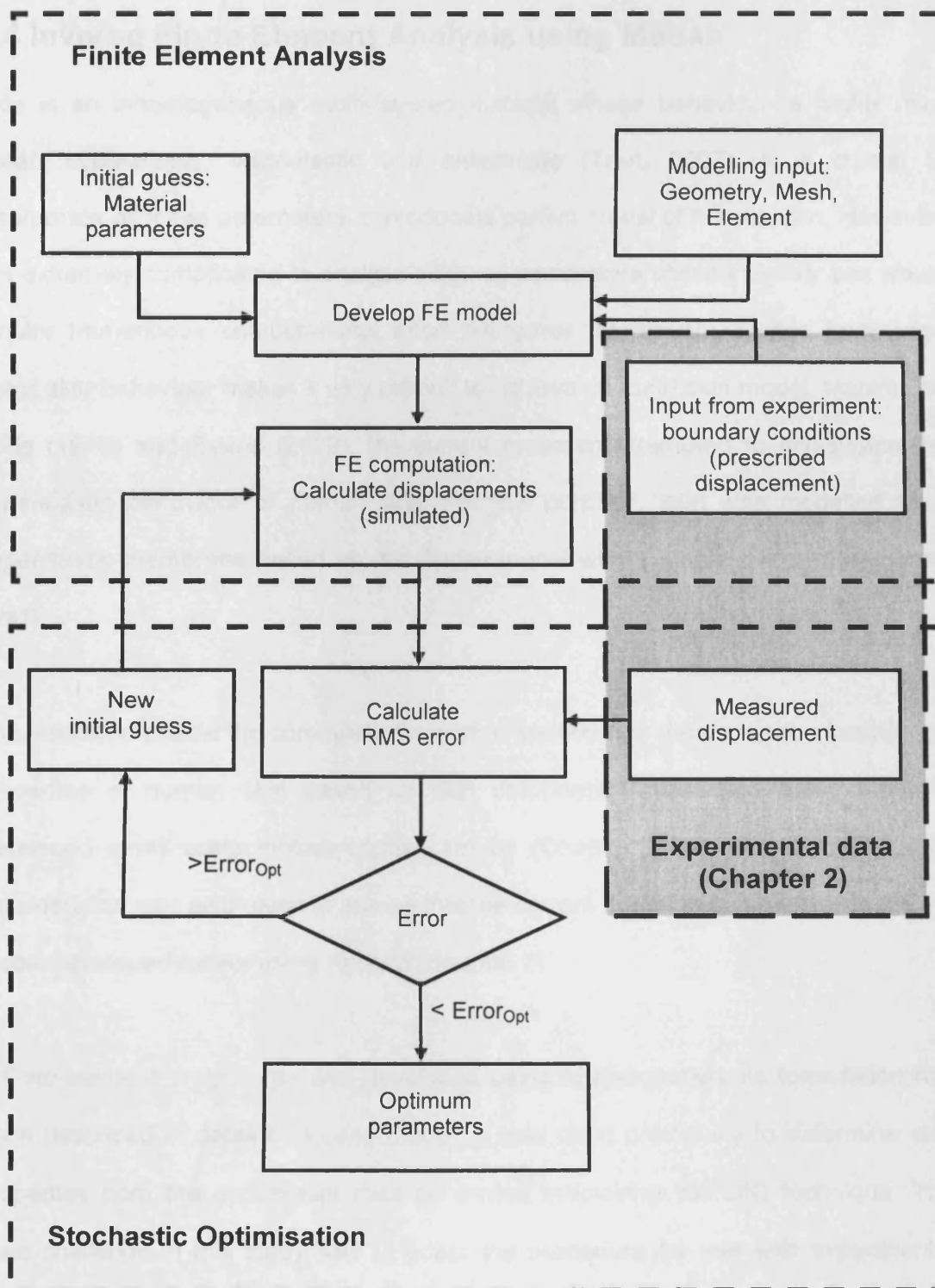
Figure 4.1: A diagram describing the flow of the current work.

4.4 Inverse Finite Element Analysis using Matlab

Skin is an inhomogeneous multi-layered material whose behaviour is highly non-linear, hyperelastic, viscoelastic and anisotropic (Tran, 2007). It is crucial to incorporate all these parameters to produce a perfect model of human skin. However, it is extremely complicated to analyse all these parameters simultaneously and would require tremendous computational effort. Moreover, at present, limited knowledge about skin behaviour makes it very difficult to achieve an ideal skin model. Inspired by Fung (1976) and Evans (2009), the current research attempted to investigate the hyperelastic behaviour of human skin. For this purpose, skin was modelled as a hyperelastic membrane based on the Ogden model with a single pair of parameters (N=1).

This section presents the computational work undertaken to determine the mechanical properties of human skin based on skin deformation measured using a newly developed small scale motion capture set up (Chapter 2). In the attempt, ample consideration was also given to ensure that the current model is comparable to the FE model developed earlier using Abaqus (Chapter 3).

A finite element programme was developed using Matlab, where its formulation has been described in detail by Evans (2009). It was used previously to determine skin properties from the experiment data generated employing the DIC technique. The main challenge in this study was to adapt the procedure for use with experimental data developed earlier employing the MA techniques. The raw output from QTM was not in the same format as the output from DIC. Therefore, an additional programme was written to specifically read the experimental data (MA) and prepared it as input for the main FE programme. This has been discussed and demonstrated in Section

2.7.1.4 (Chapter 2) where the data (i.e. the displacement distribution, Figure 4.2) generated from the experiment has been converted to become input-ready for this FE programme.
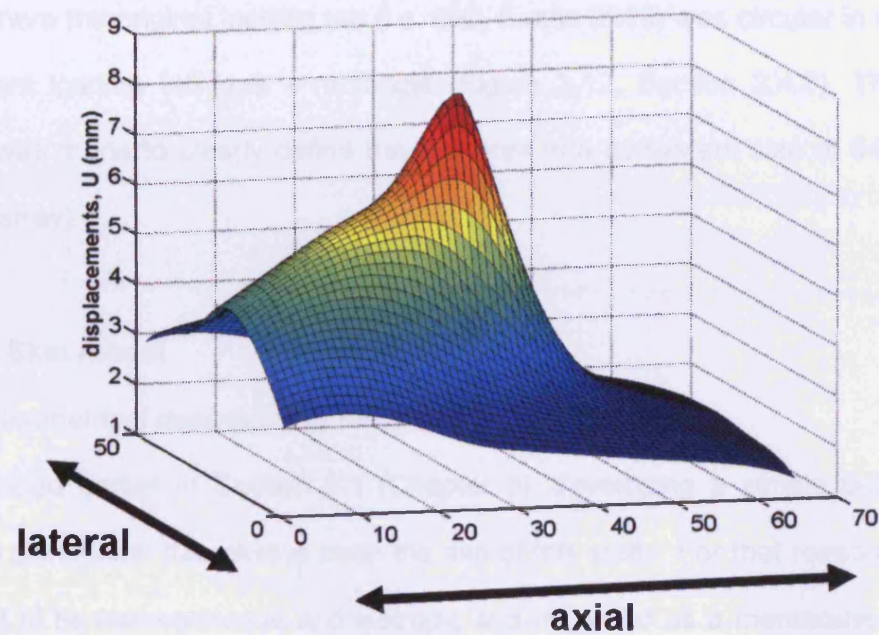
(a)
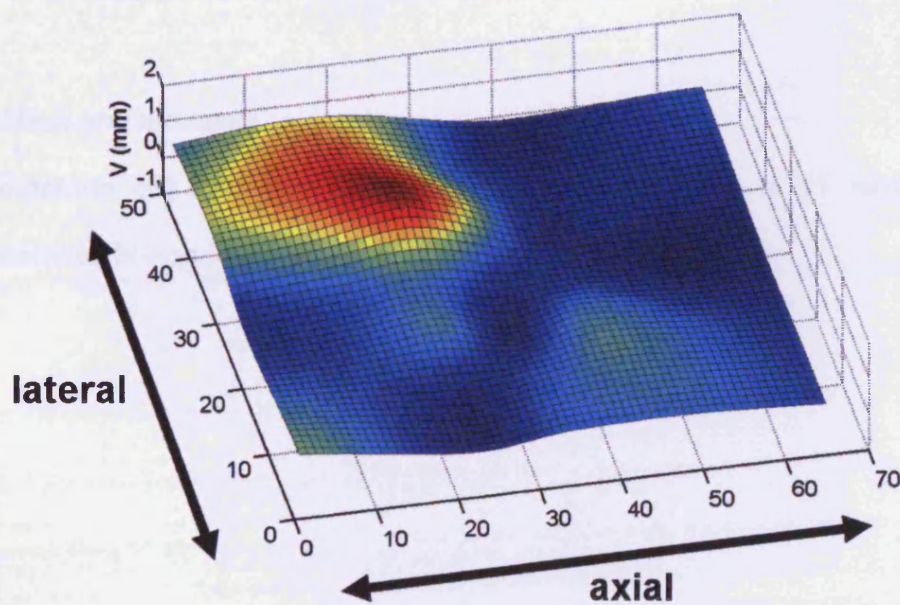
(b)

Figure 4.2: A sample experiment output; i.e. (a) axial displacement distribution and (b) lateral displacement distribution (Subject 1, X=0°, 0.7N); which served as input for the current FE programme.

Apart from that, some modifications in the main programme itself had to be made. This was because the programme was originally based on the DIC experimental set-up (Evans 2009). Therefore, some changes were made to tailor the FE model according to the MA experimental set-up. The first main difference was the loading region where the original loading tab (i.e. DIC, Evans 2009) was circular in shape and the current loading tab was a rectangle (Figure 2.12, Section 2.4.5). The second change was made to clearly define the test area in a consistent size of 64 x 48 mm (marker array).

4.4.1 2D Skin model

4.4.1.1 Geometrical description of the model

As described earlier in Section 3.1 (Chapter 3), developing a simple but relatively accurate skin model has always been the aim of this study. For that reason, skin was assumed to be homogeneous and isotropic and modelled as a membrane (64 mm x 48 mm, single layer) with a plane stress thickness of 1.5 mm.

4.4.1.2 Mesh and elements

The membrane (64 mm x 48 mm) was meshed into 15 x 11 isoparametric quadrilateral eight-noded elements as shown in Figure 4.3.
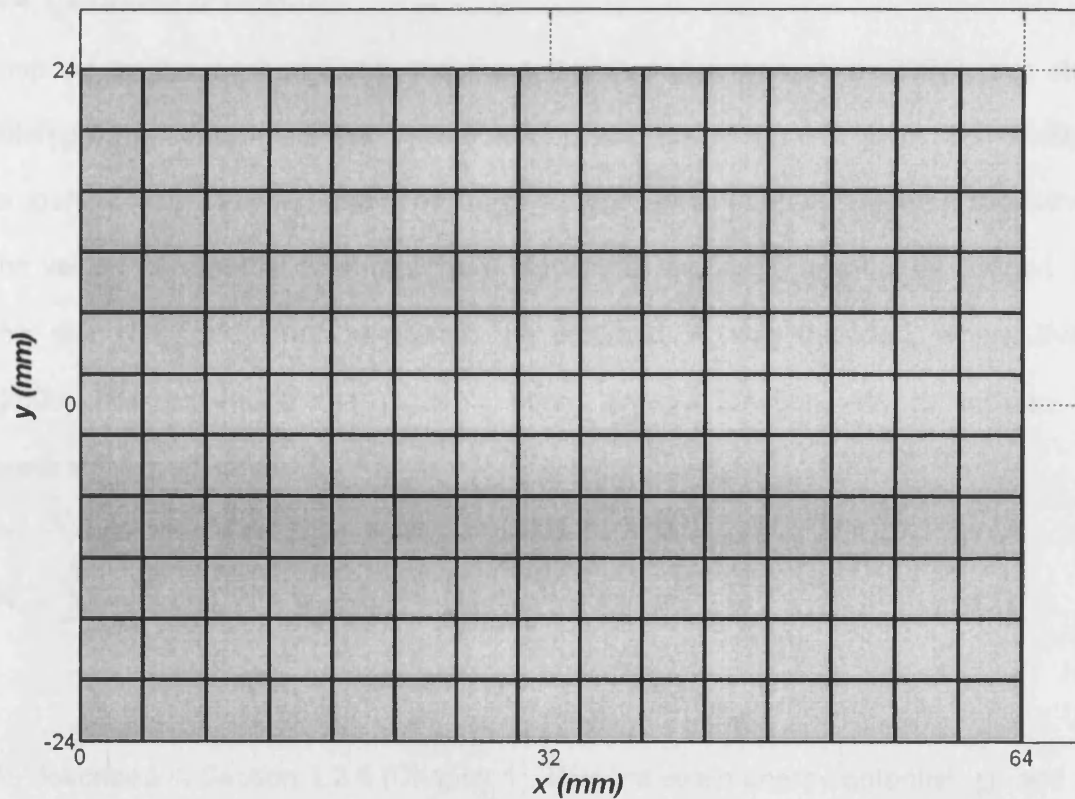
Figure 4.3: 64 x 48 mm membrane meshed into 165 (15 x 11) 8-noded elements.

4.4.1.3 *Load and boundary conditions*

Load was applied at the centre of the membrane according to experimental procedures. The critical part was to apply a distributed load (0.7 N) that matched the shape and size of the loading tab accurately (Figure 2.12, Section 2.4.5, Chapter 2).

Similar to the FE model developed in Chapter 3, the boundary conditions were extracted directly from the displacements measured at the boundaries of the test area (Section 2.7.1.4, Chapter 2) and applied as prescribed displacements. These data were interpolated to suit the number of nodes at the boundary.

4.4.1.4 *Choice of material*

Inspired by the work of Tong and Fung (1976) and Evans et al (2007), this study attempted to determine the hyperelastic properties of human skin. The material properties were based on the constitutive equation developed by Ogden (1972) where the values for material coefficient, μ, and material exponent, α, must be defined. For this study, an additional parameter, the prestrain, λ_p was included, where Evans (2009) has expanded the Ogden's strain energy function, W, to include the prestretching effect as

$$W = \sum_{i=1}^{N} \frac{\mu_i}{\alpha_i} \left(\left(\lambda_1 + \lambda_p\right)^{\alpha_i} + \left(\lambda_2 + \lambda_p\right)^{\alpha_i} + \left(\lambda_3 + \lambda_p\right)^{\alpha_i} - 3 \right) - p(J - 1) \qquad (4.1)$$

As described in Section 1.2.6 (Chapter 1), W is the strain energy potential. μ_i and α_i are the material parameters with the function's order of N. The term $p(J-1)$ represents the incompressibility constraint, where p is the hydrostatic pressure and J is the volume ratio $\lambda_1\lambda_2\lambda_3$. λ_i are the principal stretches and λ_p is the prestrain.

4.4.2 The optimisation procedure

Stochastic optimization (SO) methods are optimization algorithms which incorporate probabilistic (random) elements, either in the problem data (the objective function, the constraints, etc.), or in the algorithm itself (through random parameter values, random choices, etc.), or in both (Spall 2003). For this study, the stochastic optimisation programme starts with an initial set of values X0 (initial guess of μ, α and λ_p) and sets bounds which are initially 30 % higher and lower than X0. Then it generates random values within these bounds and tries them. It stores 20 sets of parameters as initial reference and positions them in an ascending manner (a hierarchical ladder where the set with the least error sits at the top and the most error at the bottom). By trying a

new set of values (Xi), the corresponding rms error is calculated. If the error for Xi is found lower than any of the 20 sets (X0) in the ladder, the new set will climb up to its position and thus removing the one at the bottom. This moves the bounds in iteratively to contain the best 20 results.

In this study, the measured displacements (for example Figure 4.2, Subject 1, X=0°, 0.7 N) were set as the reference data. Using the FE procedure, the distribution (axial and lateral displacements) was extrapolated into nodal displacement of the membrane (15 x 11 8-noded elements) as shown in Figure 4.3.

By guessing an initial value of μ, α and λ_p, the finite element programme calculated the axial and lateral displacements (simulated displacements) for the membrane. For each node, the root mean square (rms) error was calculated by comparing these with the measured displacements (from experiment). Based on the sum of the error, the programme optimised μ, α and λ_p values until the rms error reduced to its minimum (generally less than 0.2 mm). In general, for every experiment, the initial optimisation was run for > 24 hours with the number of iterations limited to 7000. When necessary, the optimisation was carried out further using the new initial guesses based on the previous results until a satisfactory result was achieved. The result is presented in Section 4.5.

4.4.3 Data Analysis

The ultimate aim of this study is to determine the mechanical properties of human skin. However, the results (skin properties) deduced from this study must be evaluated before any conclusions can be drawn. Therefore, the analysis is split into three stages:

- *Stage 1*: determining the material parameters for all subjects.

- *Stage 2*: evaluating the parameters.

- *Stage 3*: comparing skin properties among subjects.

4.4.3.1 *Stage 1*: determining the material parameters for all subjects.

This was the main work of this study, where the skin hyperelastic material parameters were determined for an individual subject. For each subject and load direction, the optimisation procedure was used to generate the best 20 sets of parameters (i.e. those that recorded the least rms error). Due to a large amount of data generated, a set of results is presented in detail for Subject 1 ($X=0°$, 0.7 N) as a sample output. For Subject 1, $\mu=10$, $\alpha=110$ and $\lambda_p=0.25$ were used as the first initial guess. It was based on the parameters determined using Abaqus (Section 3.6, Chapter 3). However, the solution failed to converge and gave a large rms error (1.6 E11). The initial guess values were changed to $\mu=10$, $\alpha=80$ and $\lambda_p=0.26$ and then based on its output, a third optimisation process was implemented using $\mu=11$, $\alpha=25$ and $\lambda_p=0.24$ as the initial guess values. The results are presented in the following section.

For other subjects, the results are summarised in tables to show the upper and lower values of the optimum parameters. For each subject, a single material parameter set (μ, α and λ_p) was proposed by averaging the first 10 out of 20 sets of optimum parameters. By achieving this, the aim of this study to determine the skin properties for all subjects is fulfilled.

4.4.3.2 *Stage 2*: evaluating the parameters.

Although skin properties have been determined, the main concern was how to represent and interpret the results in an appropriate way so that it can be compared among subjects. This was mainly because each parameter consists of 3 variables (μ, α and λ_p) to compare and the main option was to use a 3D graph. However, in a 3D graph, the variation in parameters is difficult to visualise (as demonstrated in the following section). One possible option is to plot the results in 2D utilising a stress-strain diagram based on μ and α (Evans and Holt 2009, Shergold and Fleck 2005). Despite ignoring prestrain, λ_p, this approach could be used to compare current results with literature (Evans and Holt 2009, Shergold and Fleck 2005) and thus at this stage, it is adapted for this study.

Considering the Ogden model, where the material is assumed to be isotropic, hyperelastic and incompressible (Section 3.4.1.4, Chapter 3), the relation of engineering stress, σ_E and principal stretches, λ, is described by

$$\sigma_E = \frac{\mu}{\lambda}\left(\lambda^\alpha - \lambda^{-\alpha/2}\right) \tag{4.2}$$

This equation has been used by Evans and Holt (2009) to compare their results with others. A brief derivation of it is represented in Appendix D. Before applying this approach to the current results, a parametric study designed to investigate the sensitivity of Equation 4.2 to the variation in μ and α is investigated.

4.4.3.3 *Stage 3*: comparing skin properties among subjects.

Using Equation 4.2, stress-stretch diagrams were constructed for all subjects and the skin properties are compared.

4.5 Results

In general, the current study generated two types of output. First, the FEA generated displacements data for the deformed membrane. Second, the stochastic optimisation procedure produced 20 sets of optimum (i.e. those that recorded the least rms error) material parameters for every single experiment (subjects and load directions).

4.5.1 *Stage 1*: The optimised material parameters

A set of results is presented in detail for Subject 1 (X=0°, 0.7 N) as a sample output (Sections 4.5.1.1 to 4.5.1.3). For all subjects, the results are presented in Sections 4.5.1.4 and 4.5.1.5.

4.5.1.1 The optimisation output: 20 sets of material parameters

The ultimate aim of this study is to determine the hyperelastic material s for each subject. The result (optimum 20 sets of material parameters) for Subject 1 is presented as an example (Table 4.1). The similar results for all subjects are attached in Appendix E. The data presented in Table 4.1 the table is the actual extraction from the optimisation output. Out of the 20 sets of data, the programme highlights the best set of parameter that produced the least rms error. The programme also recorded the duration of optimisation process and showed it as the elapsed time. For this specific sample, the optimisation process converged after 35648 seconds ($\approx$10 hours).

4.5.1.2 The material parameters in different directions

For simplicity, the 20 sets of data could also be represented based on its upper and lower bounds. The result for Subject 1 in three directions (X=0°, 45° and 90°) is presented in Table 4.2. Despite using the least computation time, it is found that the data for X=0° was the most converged (rms error = 0.16 mm) compared to other

directions (X=45° and 90°). The large rms error found for X=90° could possibly

contribute to the large gap, Δ, between lower and upper bounds for its α ($\Delta\alpha$ = 10) and

λ_p ($\Delta\lambda_p$ = 0.17); compared to other directions (X=0° and 45°).

Table 4.1: The best 20 sets of material parameters
(Subject 1, X=0°, 0.7N, initial guess values: μ=11, α=25 and λ_p=0.24)

μ (Pa)	α	λ_p	rms error
11.1881	24.1344	0.2834	0.1578
12.5497	21.8875	0.3272	0.1647
9.5866	28.7934	0.2124	0.1653
10.7613	24.9642	0.2665	0.1657
10.9056	25.1671	0.2660	0.1657
10.2341	24.0189	0.2885	0.1662
11.0177	24.1048	0.2818	0.1693
11.7263	22.2255	0.3235	0.1694
9.4121	27.8135	0.2241	0.1696
10.2413	24.1855	0.2888	0.1699
9.5848	24.0210	0.2926	0.1700
10.5816	25.2334	0.2706	0.1705
12.2535	23.9371	0.2697	0.1713
9.4933	27.7201	0.2290	0.1713
10.7455	28.4961	0.2095	0.1716
10.4870	26.2363	0.2454	0.1717
9.4946	27.0425	0.2371	0.1719
12.4148	28.2321	0.2068	0.1721
11.7692	23.4086	0.3041	0.1721
11.6577	26.3559	0.2396	0.1723

Best results:
11.1881   24.1344   0.283436

Minimum rms error (m): 0.00015775

Bounds:9.41207   21.8875   0.2068
Bounds:12.5497   28.7934   0.327244

Elapsed time is 35648.874873 seconds.

Table 4.2: The optimum material parameters in three different directions
(Subject 1, 0.7 N).

Load direction		X=0°	X=45°	X=90°
Minimum rms error (mm)		0.16	0.31	0.35
μ (Pa)	Lower	8.11	9.23	9.10
	Upper	9.76	13.79	10.62
α	Lower	24.15	25.01	22.47
	Upper	25.99	29.27	32.64
λ_p	Lower	0.26	0.20	0.16
	Upper	0.29	0.26	0.33
Elapsed time (hours)		10	23	24

For the set same of data, a 3D graph showing the distribution of material parameters is presented in Figure 4.4. It could be observed that the optimised data for X=45° did not converge very well compared to other directions (X=0° and 90°). A few data for X=90° are found to be isolated which contribute to its large rms error.
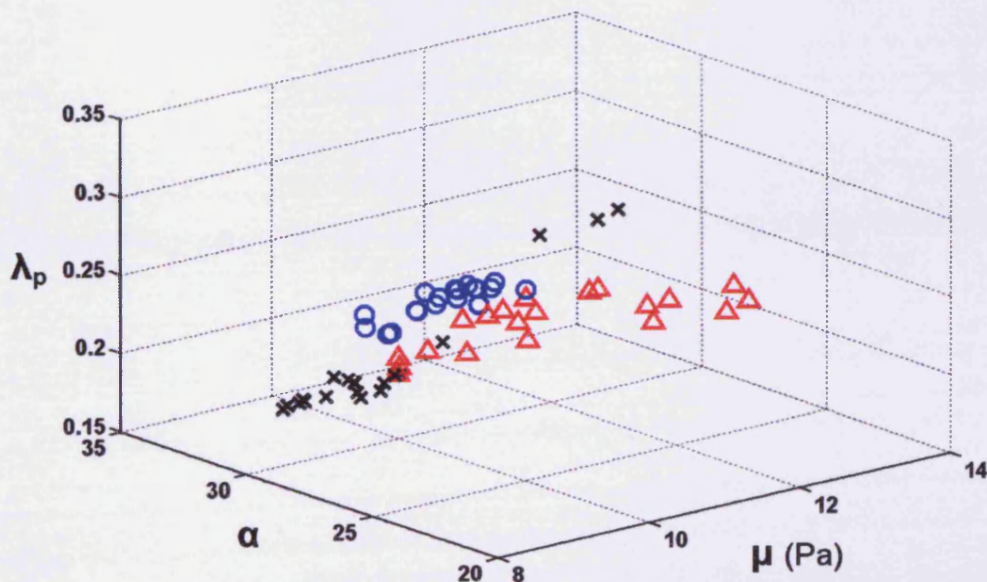
Figure 4.4: Optimum parameter sets for Subject 1 when 0.7N load applied at X=0° (circles), X=45° (triangles) and X=90° (crosses). The best 20 parameter sets for each are shown, as found after evaluating several thousand parameter sets in the stochastic optimisation procedure.

4.5.1.3 Simulated versus measured displacements

The determined skin property is used to simulate skin deformation. A sample result (Subject 1, X=0°, 0.7 N) for the measured and simulated axial displacements is shown in Figure 4.5. The corresponding error (rms) is shown in Figure 4.6.

Although in general, the simulated deformation is found to be similar in shape to the measured deformation, two main differences could be observed; (i), the simulated displacement at the load point was less than the measured data; (ii), the slope of the deformed shape at the midline markers is more of a concave shape rather than a convex (measured data). These two phenomenon might occur due to the use of a 1st order Ogden model (N = 1) and the restriction of the elements used that could not undergo a larger distortion. Despite this, the average computed rms error is still in an acceptable range (less than 0.2 mm). The largest error was found at the surrounding area of the loading tab. This was due to the difficulty in modelling the exact shape, size and location of the loading tab.
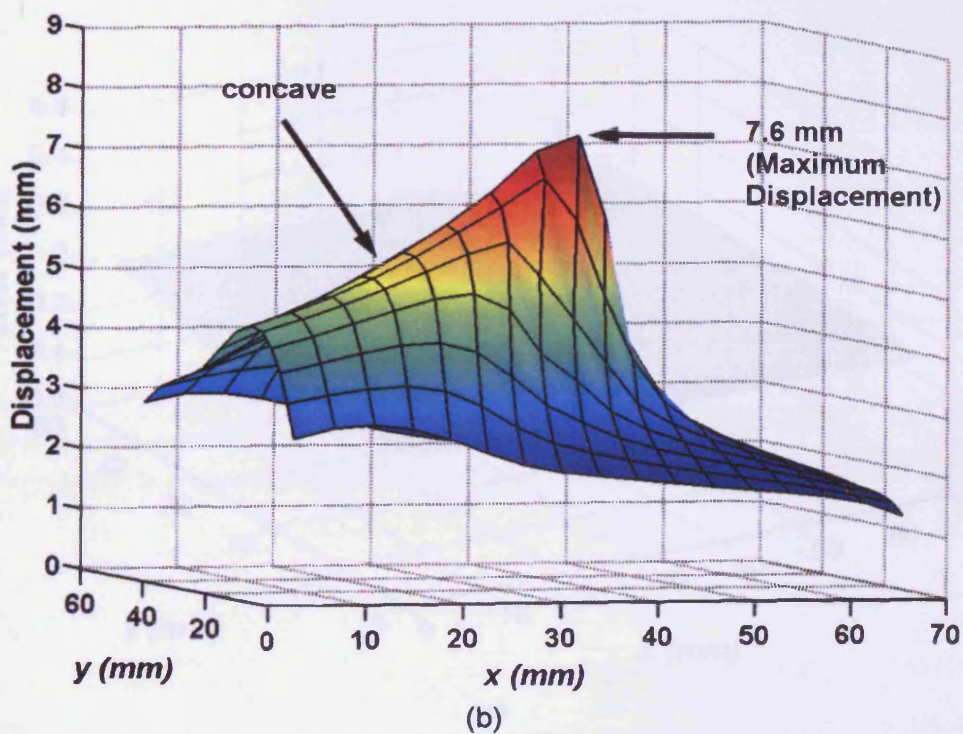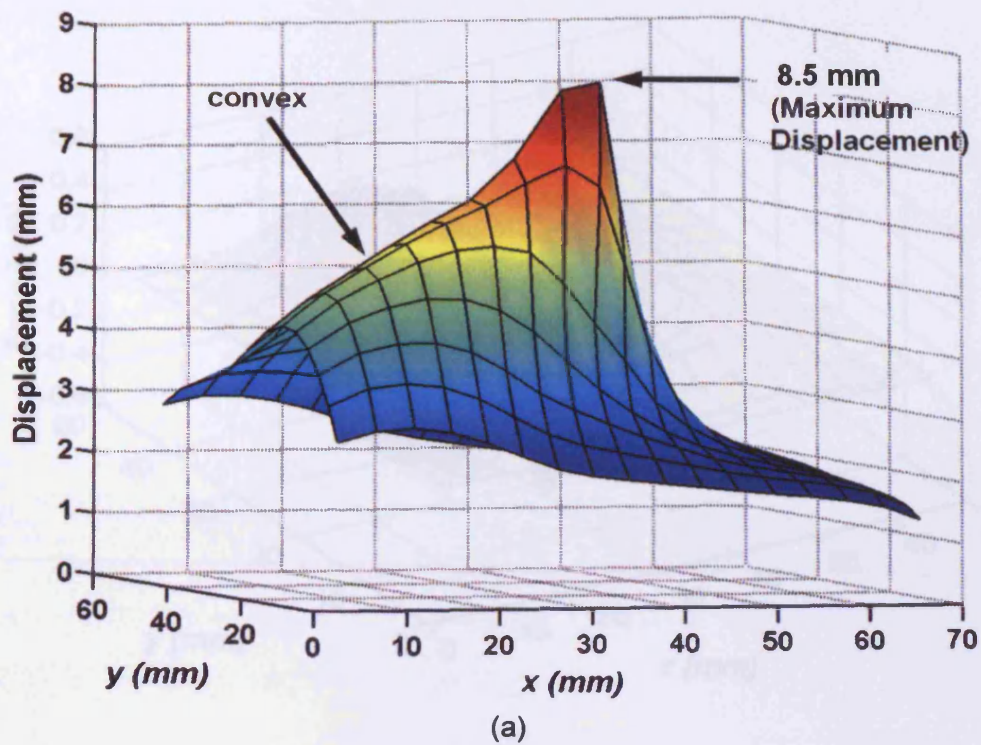
Figure 4.5: A sample result to compare measured and simulated displacement (Subject 1, X=0°, 0.7N). Three dimensional graphs, where the vertical axis and the colour contours show the axial displacements for (a) measured (b) simulated using the optimised parameters (μ=8.95 Pa, α=24.92, λ_p=0.28).
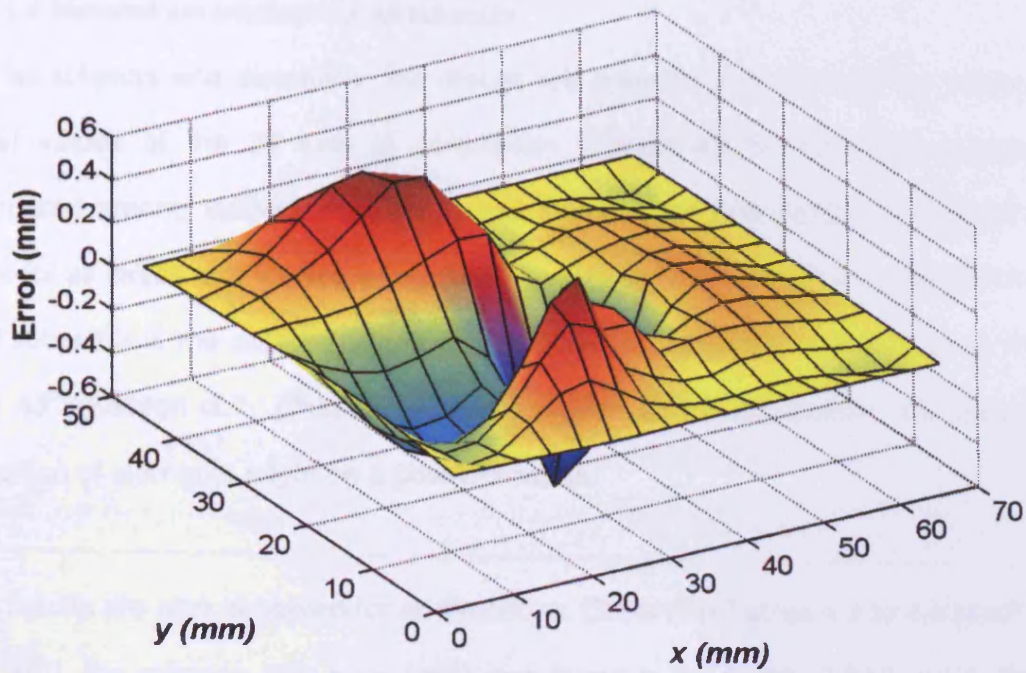
(a)
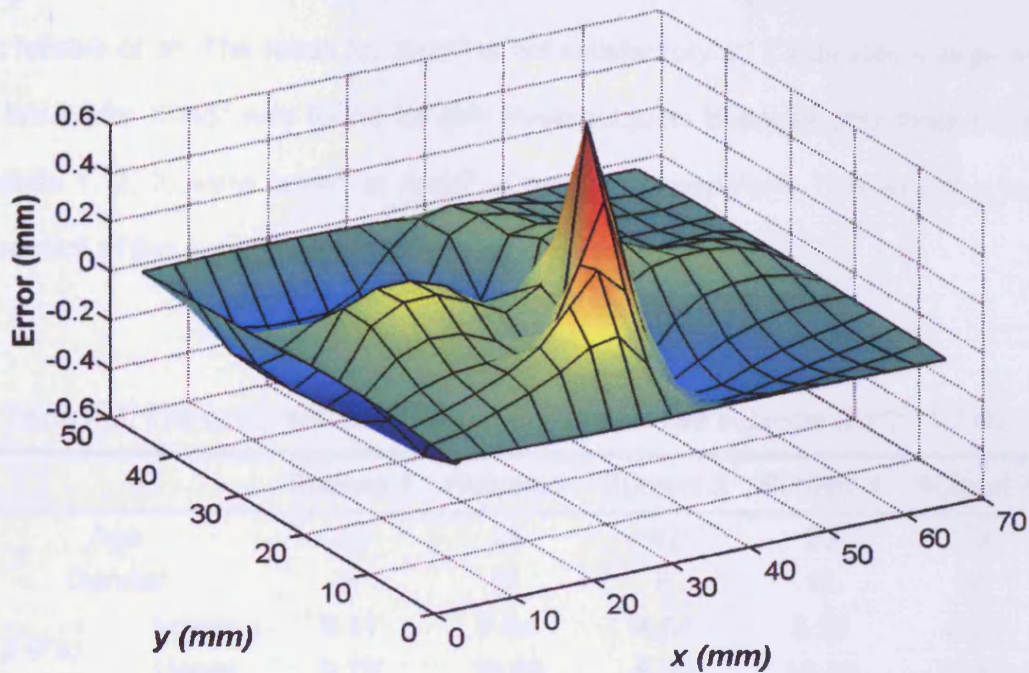
(b)

Figure 4.6: The difference (error) distribution between the FE simulation and the experimental measurement, for the (a) axial displacement and (b) lateral displacement (Subject 1, X=0°, 0.7 N, μ=8.95 Pa, α=24.92, λ_p=0.28). The average rms error was found to be less than 0.2 mm. It could be observed that the largest error occur at the surrounding area of the loading point.

4.5.1.4 Material parameters for all subjects

For all subjects and directions, the results are presented in terms of the upper and lower values of the 20 sets of parameters (Tables 4.3 to 4.5). The results are compared among subjects. It is observed that Subject 3 produced the largest rms error for all cases and therefore this result is not satisfactory. This was due to the fact that subject 3 is the oldest and her skin underwent the largest deformation at $X=90^\circ$ and 45° (Section 2.7, Chapter 2) and as been described earlier, the excessive distortion of elements might be a possible cause.

The results are also observed for all directions. Observing Tables 4.3 to 4.5 ($X=0^\circ$, 90° and 45°), the average rms error (mm) was found to be 0.196, 0.343 and 0.286 for $X=0^\circ$, $X=45^\circ$ and $X=90^\circ$ respectively. This indicates that the results for $X=0^\circ$ are the most reliable of all. The result for $X=45^\circ$ is not satisfactory as it indicates a large error. The results for $X=45^\circ$ was found for only three subjects because only three subjects (Subjects 1, 2, 3) were tested at $X=45^\circ$ during the experiment. This was due to the evolvement of the experimental procedure.

Table 4.3: The optimised material parameters for five subjects ($X=0^\circ$, 0.7 N).

		Subject 1	Subject 2	Subject 3	Subject 4	Subject 5
Age		25	26	42	23	26
Gender		F	M	F	M	M
μ (Pa)	Lower	8.11	7.84	4.94	8.26	8.63
	Upper	9.78	10.88	6.80	13.88	13.64
α	Lower	24.15	24.25	19.84	21.98	23.88
	Upper	25.99	33.74	23.01	31.27	32.02
λ_p	Lower	0.26	0.13	0.35	0.16	0.16
	Upper	0.29	0.28	0.47	0.32	0.29
Min. rms error		0.16	0.19	0.33	0.18	0.12

Table 4.4: The optimised material parameters for five subjects (X=90°, 0.7 N).

		Subject 1	Subject 2	Subject 3	Subject 4	Subject 5
Age		25	26	42	23	26
Gender		F	M	F	M	M
μ (Pa)	Lower	9.10	4.15	8.41	9.98	9.08
	Upper	10.62	6.32	10.71	12.53	13.24
α	Lower	22.47	22.97	14.16	11.61	24.68
	Upper	32.64	27.47	15.93	13.11	31.96
λ_p	Lower	0.16	0.19	0.48	0.80	0.13
	Upper	0.33	0.31	0.61	1.02	0.23
Min. rms error		0.35	0.17	0.49	0.32	0.10

Table 4.5: The optimised material parameters for three subjects (X=45°, 0.7 N).

		Subject 1	Subject 2	Subject 3
Age		25	26	42
Gender		F	M	F
μ (Pa)	Lower	9.23	11.12	17.88
	Upper	13.79	14.56	23.16
α	Lower	25.01	23.06	20.79
	Upper	29.27	26.47	32.88
λ_p	Lower	0.20	0.21	0.17
	Upper	0.26	0.28	0.39
Min. rms error		0.31	0.33	0.39

4.5.1.5 A single parameter to represent skin properties for each case

By observing the bounds (lower and upper) of the material properties (Tables 4.3 to 4.5), the estimated μ, α and λ_p values for each subject could be determined. However, it is quite difficult to compare skin properties among subjects based on this information.

Therefore, a single parameter representing each case (subject and load direction) is determined by averaging the best 10 sets of optimum parameters (Ave). The results are presented in Tables 4.6 to 4.10. The abbreviation 'B' and 'Ave' represents the best and averaged set of material parameters respectively. For comparison among subjects, the results are plotted in 3D graphs (Figures 4.7 to 4.9).

Table 4.6: Skin properties for Subject 1 measured *in vivo* in three directions (0.7 N).

Load direction	μ (Pa)	α	λ_p	rms error
X=0° (B)	8.11	25.57	0.27	0.16
X=0° (Ave)	8.95	24.92	0.28	0.17
X=45° (B)	10.93	25.20	0.26	0.31
X=45° (Ave)	10.69	26.70	0.24	0.34
X=90° (B)	10.61	31.68	0.18	0.35
X=90° (Ave)	9.96	28.98	0.22	0.37

Table 4.7: Skin properties for Subject 2 measured *in vivo* in three directions (0.7 N).

Load direction	μ (Pa)	α	λ_p	rms error
X=0° (B)	10.84	24.25	0.26	0.19
X=0° (Ave)	9.68	29.65	0.19	0.20
X=45° (B)	13.46	25.77	0.21	0.33
X=45° (Ave)	13.36	25.40	0.23	0.35
X=90° (B)	4.57	26.91	0.21	0.17
X=90° (Ave)	5.41	26.16	0.22	0.18

Table 4.8: Skin properties for Subject 3 measured *in vivo* in three directions (0.7 N).

Load direction	μ (Pa)	α	λ$_p$	rms error
X=0° (B)	6.80	20.92	0.40	0.33
X=0° (Ave)	5.67	21.07	0.42	0.33
X=45° (B)	22.36	32.53	0.17	0.78
X=45° (Ave)	20.63	27.02	0.23	0.82
X=90° (B)	9.85	14.34	0.58	0.49
X=90° (Ave)	9.57	14.94	0.54	0.50

Table 4.9: Skin properties for Subject 4 measured *in vivo* in two directions (0.7 N).

Load direction	μ (Pa)	α	λ$_p$	rms error
X=0° (B)	13.81	29.54	0.16	0.18
X=0° (Ave)	11.13	29.41	0.19	0.20
X=90° (B)	10.81	12.44	0.88	0.32
X=90° (Ave)	11.22	12.18	0.92	0.33

Table 4.10: Skin properties for Subject 5 measured *in vivo* in two directions (0.7 N).

Load direction	μ (Pa)	α	λ$_p$	rms error
X=0° (B)	12.39	25.13	0.27	0.12
X=0° (Ave)	11.93	27.39	0.23	0.13
X=90° (B)	11.89	28.60	0.17	0.10
X=90° (Ave)	11.66	29.22	0.17	0.11
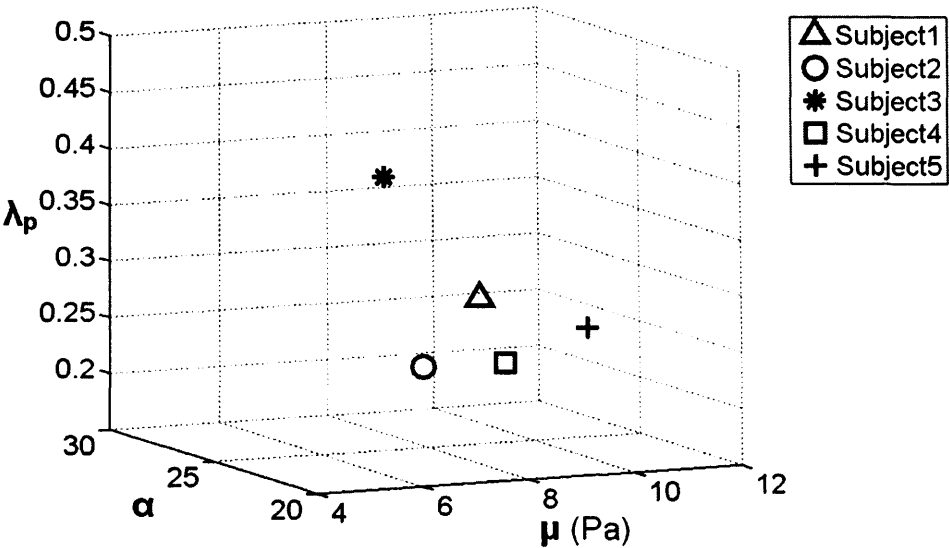
Figure 4.7: A graph comparing skin properties for five subjects (X=0°, 0.7 N) using individual set of material parameter.
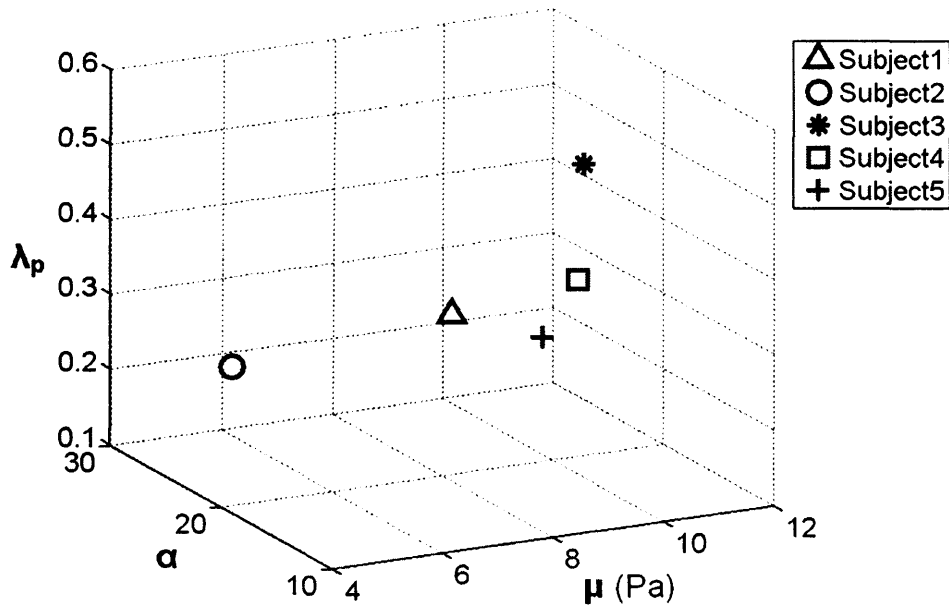
Figure 4.8: A graph comparing skin properties for five subjects (X=90°, 0.7 N) using individual set of material parameter.
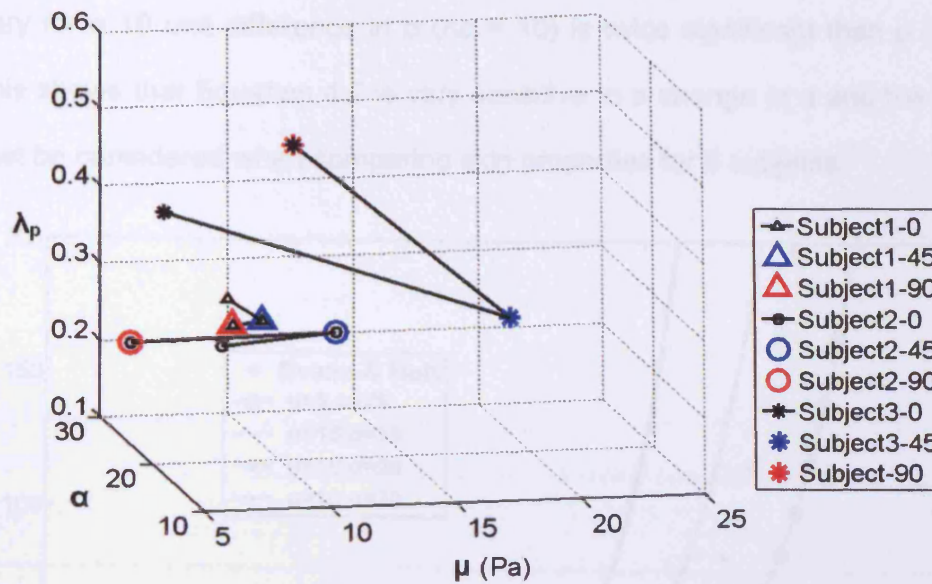
Figure 4.9: A graph comparing skin properties for three subjects in three directions (X=0°, 45° and 90°, 0.7 N) using individual set of material parameters.

Figures 4.7 to 4.9 confirm that by using a 3D graph, the variations in the material parameters could not be traced with certainty. Skin properties for different subjects and different load directions could not be easily compared. This justifies the need to use a stress-strain diagram because it could show a combination effect of the material properties in 2D.

4.5.2 *Stage 2*: The parametric study

The result showing the sensitivity of Equation 4.2 to the variations in μ and α is presented in Figure 4.10. For this purpose, two sets of curves are plotted to observe the boundaries. The first set aimed to observe the effect of variations in μ. Therefore, while keeping α constant (α = 26; as proposed by Evans and Holt, 2009), μ was varied from 5 to 15 Pa (Δμ = 10 Pa). The second set aimed to observe the effect of variations in α. Therefore, while keeping μ constant (μ = 10 Pa; as proposed by Evans and Holt, 2009), α was varied from 20 to 30 (Δα = 10). Evans and Holt (2009) parameter (μ = 10 Pa, α = 26) is included as a reference. It is observed that the

boundary for a 10 unit difference in α ($\Delta\alpha$ = 10) is twice significant than μ ($\Delta\mu$ = 10 Pa). This shows that Equation 4.2 is very sensitive to a change in α and the effect of this must be considered when comparing skin properties for 5 subjects.
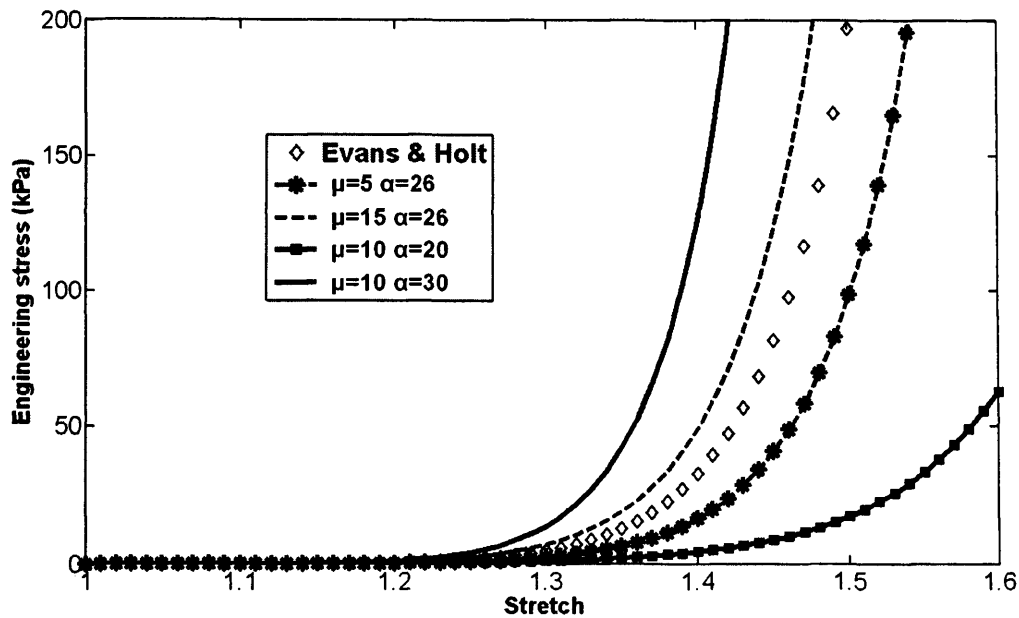
Figure 4.10: The bounds for variations in μ ($\Delta\mu$ = 10 Pa, dotted lines) and α ($\Delta\alpha$ = 10, continuous lines).

When applying the curve fitting technique, it is known that several equations could fit into a curve. A similar effect could be seen when performing the current optimisation procedure. The possible solution (optimised material parameters) is not unique. During conducting a FEA, a set of material parameters will produce one set of skin deformation. In contrary, several sets of material parameters could produce a similar skin deformation. To demonstrate this, several material parameters were investigated and the result is shown in Figure 4.11. It is observed that the curves for several material parameters could match one another. It indicates that the solution is not unique. Ignoring prestretch, λ_p, five sets of material parameters that could produce a similar stress-strain curve are shown in Table 4.11.

The findings deduced from the current parametric study provided a better understanding in interpreting the results from the stress-stretch diagrams. The knowledge was then used in comparing skin properties among subjects and discussing the results.

Table 4.11: An example of five sets of material parameters producing a similar graph

Set	Material parameters
Set 1	$\mu = 5$ Pa, $\alpha = 28$
Set 2	$\mu = 7$ Pa, $\alpha = 27$
Set 3	$\mu = 10$ Pa, $\alpha = 26$
Set 4	$\mu = 15$ Pa, $\alpha = 25$
Set 5	$\mu = 20$ Pa, $\alpha = 24$
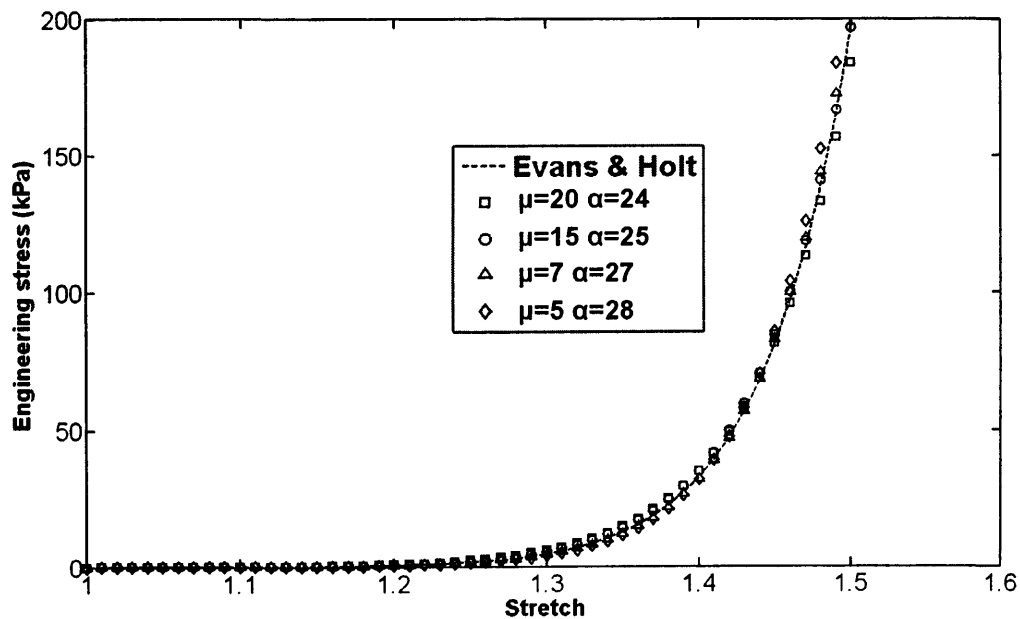
Figure 4.11: The curves for a few sets of material parameters which fit into one another. Evans and Holt (2009) data ($\mu = 10$ Pa, $\alpha = 26$, dotted line) is used as a reference.

4.5.3 *Stage 3*: Comparing skin properties among subjects

4.5.3.1 Stress-stretch diagram for Subject 1

As described in the previous section (Section 4.5.2), one possible method to analyse skin properties is by observing its stress-stretch diagram. Based on Equation 4.2 (Section 4.4.3), the stress-stretch curves are plotted for the optimum skin properties (single set of parameter) determined in this study (Tables 4.6 to 4.10).

For the first case, a stress-stretch diagram (Figure 4.12) is presented to compare the current result (Subject 1, X=0°, 0.7 N) with several known Ogden's material parameters for skin. The known material parameters are shown in Table 4.12. It is observed that the current curve is quite close to the skin property curve determined by Evans and Holt (2009). However, the material parameters determined from the FEA using Abaqus (μ = 10 Pa, α = 110, Section 3.5.9, Chapter 3) produce a very steep curve which reflects a very high stiffness.
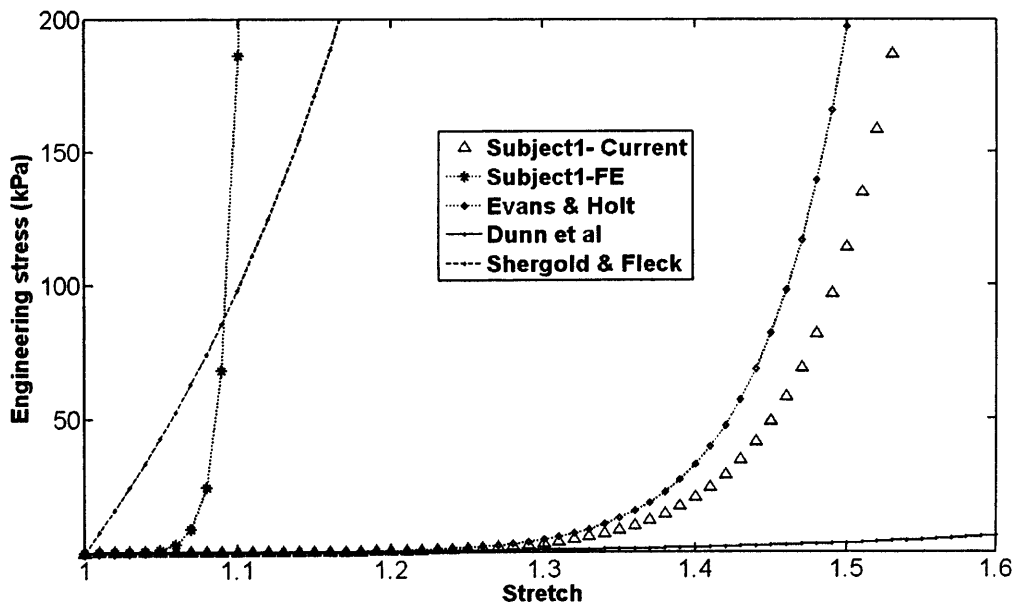
Figure 4.12: Comparing skin properties for Subject 1 (X=0°, 0.7 N) with others. The curve for Subject 1-FE is extracted from the results of analysis using Abaqus.

Table 4.12: The skin property of Subject 1 compared to other researchers.

Load direction	μ (Pa)	α	λ_p
Subject 1, X=0°, FEA + optimisation	8.95	24.92	0.28
Subject 1, X=0°, FE model using Abaqus (Section 3.5.9, Chapter 3)	10	110	0.25
Evans and Holt (2009) DIC experiment and FEA	10	26	0.2
Evans and Holt (2009), who fitted experiment data from Dunn et al (1985)	110	10	-
Shergold and Fleck (2005), who fitted tensile test data from Jansen and Rottier (1958)	1.1×10^4	9	-

4.5.3.2 Stress-stretch diagram with respect to load direction for all subjects

For each subject, a stress-stretch diagram is shown (Figures 4.13 to 4.17) to observe skin properties in different direction. The curve for the material parameter with least rms error is plotted in blue. The curve for the averaged material parameters is plotted in black. For the case of material parameters that produce a large rms error (>0.3 mm), its corresponding symbols are not filled with colour. In the legend, the numbers representing the load direction X=0° (0), X=45° and X=90° and represented by triangles, circles and squares respectively.
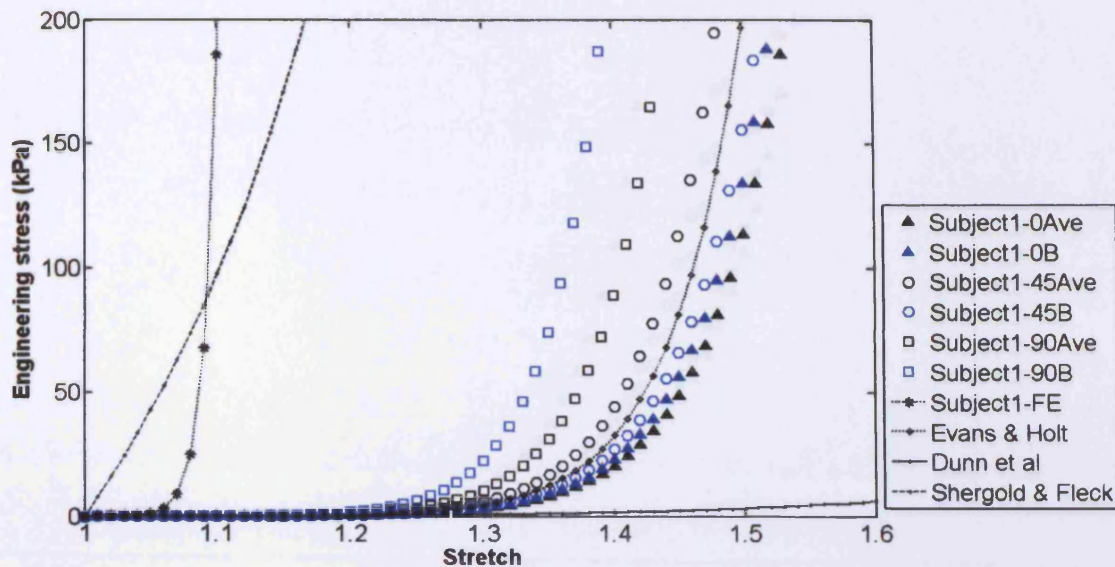
Figure 4.13: Skin properties in different directions (Subject 1, 0.7 N) represented by optimum (blue) and averaged (black) material parameters. Outline symbol indicates a large rms error (>0.3 mm)

It is observed that for Subject 1, the stress-strain curves for all directions ($X=0^\circ$, 45° and 90°) are quite close together considering how sensitive Equation 4.2 to the variations of parameters. However, only the results for $X=0^\circ$ could be accepted with full confidence. The curves for other directions ($X=45^\circ$ and 90°) are plotted without fill-colour due to large error (>0.3mm). The results for averaged and optimum material parameters are close.

The result for Subject 2 is shown in Figure 4.14. It is observed that the averaged and optimum curves for $X=0^\circ$ (triangles) are quite separated compared to $X=45^\circ$ and 90°. It indicates that the optimisation procedure provides a range of solution between the optimised parameters. However, it is still acceptable as Equation 4.2 is sensitive to the change of α (in this case $\alpha_{Ave} = 29.65$ and $\alpha_B = 24.25$).
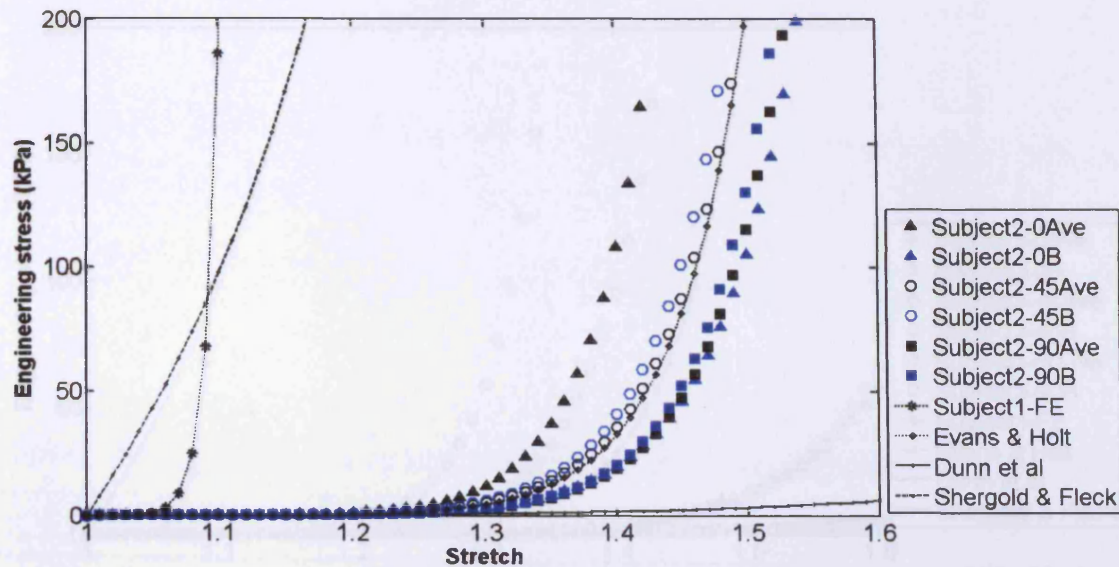
Figure 4.14: Skin properties in different directions (Subject 2, 0.7 N).

The result for subject 3 is presented in Figure 4.15. Among all, subject 3 produced results with the largest averaged rms error of 0.33, 0.50 and 0.82 for X=0°, 45° and 90° respectively and minimum error of 0.33, 0.78 0.49 for 0.82 for X=0°, 45° and 90° respectively. The result for X=90° is found close to Dunn et al (1985). The same observation is found for Subject 4 (Figure 4.16). Subject 5 (Figure 4.17) shows a consistent results where all the curves are close to each other. For all loading directions, the calculated rms error < 0.13.
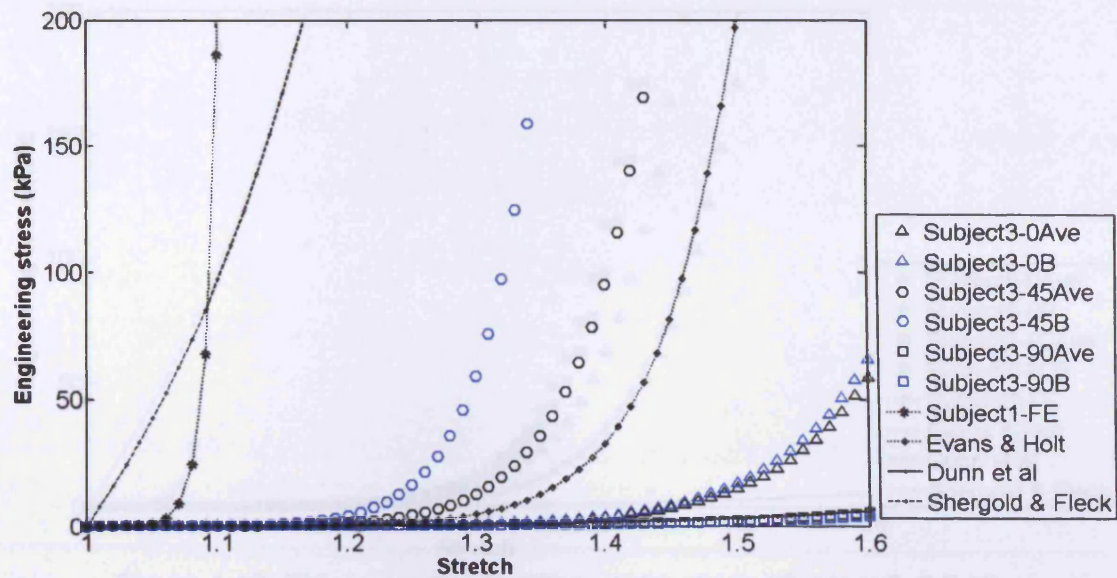
Figure 4.15: Skin properties in different directions (Subject 3, 0.7 N).
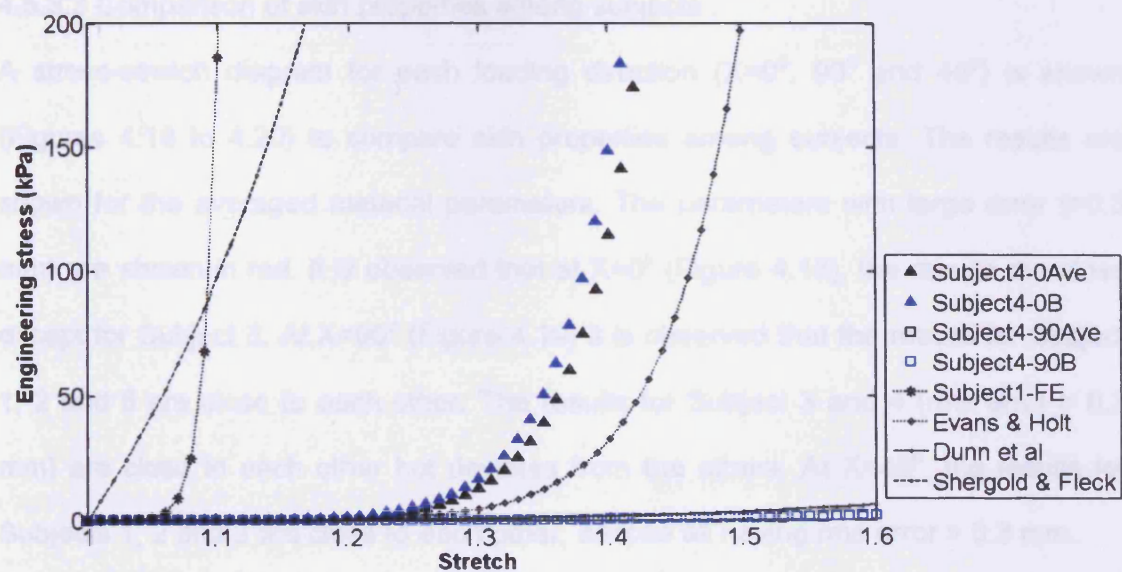
Figure 4.16: Skin properties in different directions (Subject 4, 0.7 N).
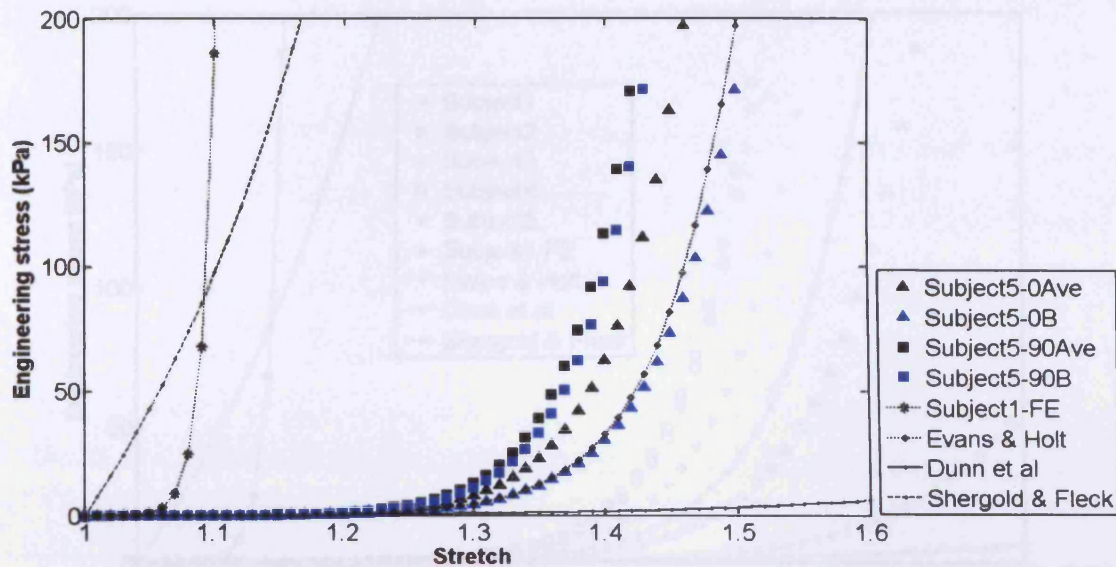
Figure 4.17: Skin properties in different directions (Subject 5, 0.7 N).

4.5.3.3 Comparison of skin properties among subjects

A stress-stretch diagram for each loading direction (X=0°, 90° and 45°) is shown (Figures 4.18 to 4.20) to compare skin properties among subjects. The results are shown for the averaged material parameters. The parameters with large error (>0.3 mm) are shown in red. It is observed that at X=0° (Figure 4.18), the results are close except for Subject 3. At X=90° (Figure 4.19) it is observed that the results for Subject 1, 2 and 5 are close to each other. The results for Subject 3 and 4 (rms error > 0.3 mm) are close to each other but deviates from the others. At X=45°, the results for Subjects 1, 2 and 3 are close to each other, despite all having rms error > 0.3 mm.
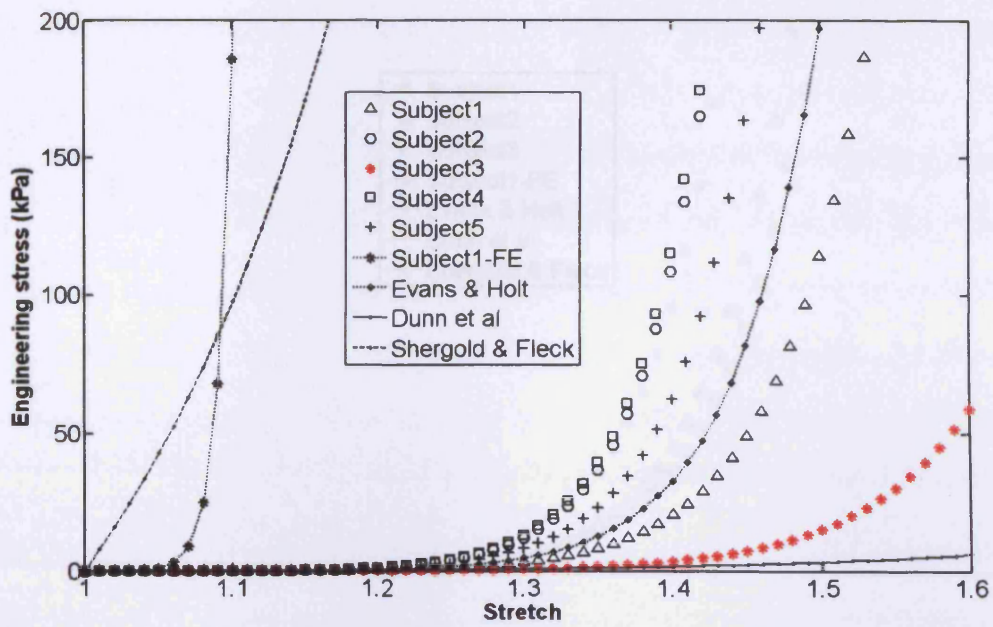
Figure 4.18: Comparison of skin properties among subjects (X=0°, 0.7 N).
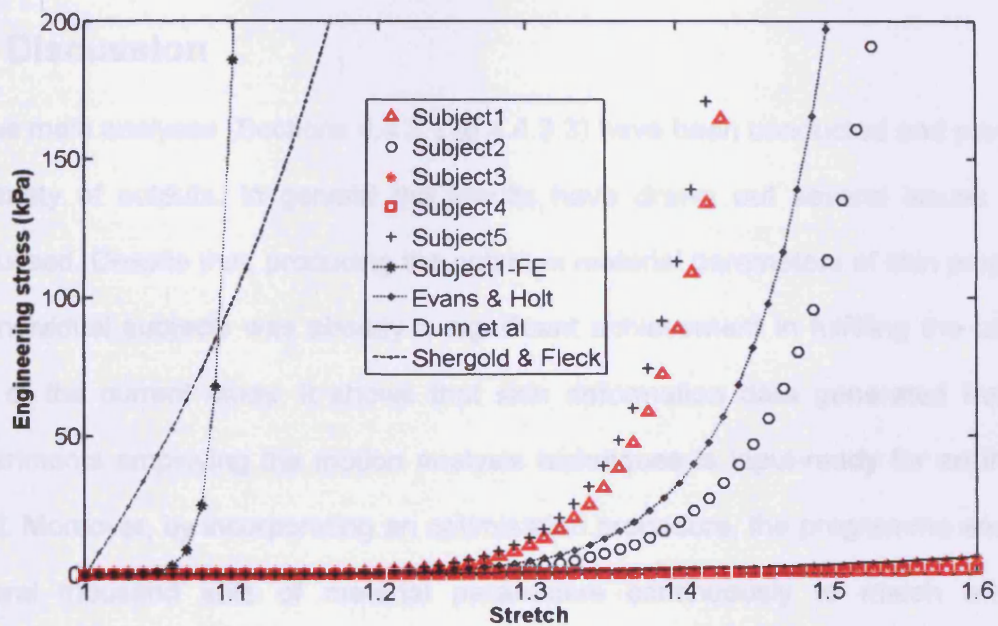
Figure 4.19: Comparison of skin properties among subjects (X=90°, 0.7 N).
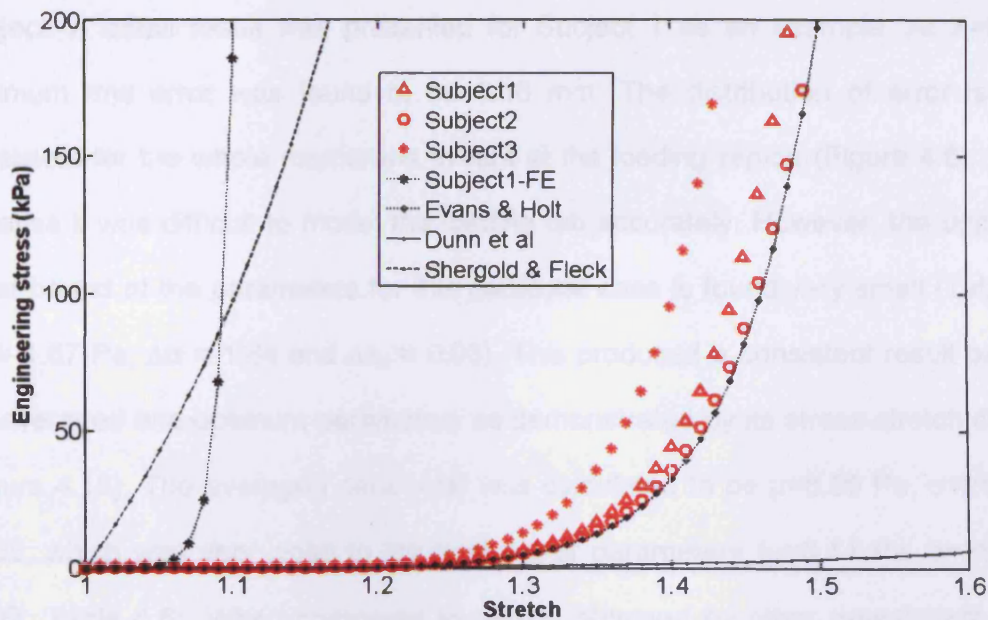
Figure 4.20: Comparison of skin properties among subjects (X=45°, 0.7 N).

4.6 Discussion

Three main analyses (Sections 4.4.3.1 to 4.4.3.3) have been conducted and produced

a variety of outputs. In general the results have drawn out several issues to be

discussed. Despite that, producing the optimum material parameters of skin properties

for individual subjects was already a significant achievement in fulfilling the ultimate

aim of the current study. It shows that skin deformation data generated from the

experiments employing the motion analysis techniques is input-ready for an inverse

FEM. Moreover, by incorporating an optimisation procedure, the programme analysed

several thousand sets of material parameters continuously to match with the

experimental data. This has saved a huge amount of time consumed compared to the

tediousness of using a FE software such as Abaqus as demonstrated in Chapter 3.

The first stage of the current study was to determine skin properties for individual

subjects. The optimisation procedure has produced 20 sets of optimum data for each

Subject. A detail result was presented for Subject 1 as an example. At X=0°, the minimum rms error was found to be 0.16 mm. The distribution of error is found consistent for the whole membrane except at the loading region (Figure 4.6). This is because it was difficult to model the loading tab accurately. However, the upper and lower bound of the parameters for this particular case is found very small (Table 4.2, $\Delta\mu$ = 1.67 Pa, $\Delta\alpha$ = 1.84 and $\Delta\lambda_p$ = 0.03). This produced a consistent result between the averaged and optimum parameters as demonstrated by its stress-stretch diagram (Figure 4.13). The averaged parameter was calculated to be μ=8.95 Pa, α=24.92, λ_p =0.28, which was very close to the best set of parameters (μ=8.11 Pa, α=25.57, λ_p =0.27, Table 4.6). When compared to results obtained by other researchers (Table 4.12), the skin properties for Subject 1 are found close to skin properties (μ=10 Pa, α=26, λ_p =0.2) found by Evans and Holt (2009). From the stress-strain diagram (Figure 4.13), it is observed that these 3 curves (Subject 1's averaged, Subject 1's best parameter and Evans and Holt, 2009) are close to each other. However, the curve for skin parameter determined using Abaqus deviates from them (far left). This has been described in the previous chapter (Section 3.6, Chapter 3), which is possibly due to the stiff FE elements.

The current result for Subject 1 at X=0° is proposed to be good and the procedure was implemented for other directions and then for all subjects. For each case, 20 sets of optimum material parameters are produced. The overall results were found to be good but for some cases, however, the results did not converge very well. There are several possible causes contributing to this occurrence. The main cause was the inability of the current FE model to deform exactly to the measured deformation (Figure 4.5). It is observed that the shape of the steep slope for the current FE model is quite linear compared to the measured data. It is predicted that the current element (8-node isoparametric element) is not hyperelastic enough (as in the case for FEA

using Abaqus, where its system warned of excessive distortion to the element). Therefore, developing a special element that can distort excessively would be useful. The alternative is to create a finer mesh for the model. The current study has attempted to create a finer mesh for the model, however, the analysis failed to converge. Therefore, in future, a study is recommended to resolve this matter. Apart from that, the results could also be improved by increasing the order ($N>1$) of Ogden's parameter as demonstrated in Section 3.5.8 (Chapter 3). However, this increment will increase the complexity in the optimisation procedure as more parameters have to be optimised and therefore it is not practical to apply this.

Having determined the skin properties for individual subjects and different directions, the results are further analysed to (i) investigate the skin behaviour at different direction for individual subject and (ii) compare skin properties among subjects.

Observing the stress-strain diagrams (Figure 4.13 to 4.17), no particular trend could be found to describe specific skin behaviour for loading in different directions. Although it is known that skin is anisotropic, the current graphs failed to reveal any special finding. Skin behaviour for different loading directions ($X=0°$, $45°$ and $90°$) is found close to each other for Subjects 1, 2 and 5 which indicates that there is no significant change of skin properties for the different direction. Moreover, the stress-strain graph was proven sensitive to a parametric variation and therefore, a slight divergence of the curves could not describe a significant variation in skin properties.

Figures 4.18 to 4.20 compare skin properties among subjects. Generally, it is observed that the stress-strain curves for all subjects are close to each other. However, at $X=90°$, the graphs for Subjects 3 and 4 deviate and are closer to Dunn's (Dunn et al 1985). As described in Section 4.5.3.2 the results at $X=90°$ for these

subjects were not very good with rms error of 0.5 and 0.33 respectively. As in the previous case, no particular trend could be found to describe specific skin behaviour among subjects. The curves are comparatively close to each other, while a few deviate (to the far right) due to large rms error. An attempt was made to compare prestretch, λ_p, for all cases (Table 4.6 to 4.10). It is found that although its optimum value lies in the range of 0.17 to 0.92, the good results (rms error < 0.2 mm) reveal a narrower gap between 0.17 and 0.28. Evans and Holt (2009) measured the skin prestretch for their subject to be 0.2. Again, no specific trend is found.

The current study failed to reveal a specific trend for skin behaviour among subjects. There are two main reasons that can explain this. Firstly, the number of subjects is too small. However, it is stated that the current study attempts to adapt an inverse FEA to determine the mechanical properties of human skin. Therefore, this justifies the small number of subjects (five). The work conducted was focused more towards the implementation of the procedure rather than comparing skin properties among subjects. Therefore, it is recommended that the test is carried out for more subjects (large sample) as it would be interesting to observe and compare skin properties for subjects with different age and gender.

Secondly, some of the optimisation processes did not converge very well and its large error contributes uncertainty to the results. The results for skin properties at X=45° produce the largest error. Therefore, it is evident that the current approach could not be used for this purpose. It is found that the current FE model could not simulate skin deformation accurately at this direction (X=45°). Further investigation is recommended to overcome this matter in future.

In numerical method, the accumulation and propagation of error has always been an issue. Figure 4.5 clearly demonstrate the discrepancy of the maximum displacements at the load point. The displacement experimentally measured at the load point (peak) was 8.8 mm (Section 2.7.1.2, Chapter 2). The measured data when interpolated into discretised elements recorded a displacement at the load point to be 8.5 mm. The optimum simulation predicted the load point displacement to be 7.6 mm. This is an example of error propagation that contributes an uncertainty in the results that might affect the final finding of the current study.

4.7 Conclusion

The objective to determine the mechanical properties of human skin by adapting an inverse FEA with an optimisation procedure has been achieved successfully and based on the results, the hyperelastic material parameters for Subject 1 was approximated to be μ = 8.95 Pa, α = 24.92, λ_p = 0.28. For all subjects, the mean $\pm$ SD set of material parameters is μ = 9.5 $\pm$ 2.4 Pa, α = 26.5 $\pm$ 3.6, λ_p = 0.26 $\pm$ 0.1 for X=0° (5 subjects), μ = 9.6 $\pm$ 2.5 Pa, α = 22.3 $\pm$ 8.1, λ_p = 0.4 $\pm$ 0.3 for X = 90° (5 subjects), and μ = 14.9 $\pm$ 5.1 Pa, α = 26.4 $\pm$ 0.9, λ_p = 0.23 $\pm$ 0.006 for X=45° (3 subjects). In general, the results are found close to skin properties proposed by Evans and Holt (2009), despite a few producing significant error and invoke uncertainty. Some recommendations are addressed to remedy this. It is undeniable that the work conducted has produced several useful findings that contribute to the knowledge in inverse FEA and with an optimisation procedure using Matlab.

The outcome of the current study highlights the success of combining a novel experimental and computational approach initially used to measure small scale deformation of human skin *in vivo* to produce a set of reliable and accurate

mechanical properties of skin. This combination produces a powerful tool and has a great potential which can be developed further for other applications, from measuring small scale motion of biological systems to determining the associated mechanical properties.

However, it would be useful to compare the current result with a similar result obtained using an alternative approach. For this purpose, a DIC technique is employed and combined with the current optimisation procedure to measure *in vivo* the mechanical properties of human skin.

The subsequent chapter describes the work of using the DIC technique to replicate the experimental protocol developed earlier (Chapter 2) and accordingly determine skin properties using the current optimisation procedure.

5-1

CHAPTER 5

MEASURING SKIN PROPERTIES USING DIGITAL IMAGE CORRELATION TECHNIQUES

5.1 Introduction

The previous chapter highlights the success of fulfilling the ultimate aim of this study that is to determine the mechanical properties of human skin. Based on the Ogden's model, the skin parameters for five subjects were determined using a combination of inverse FEM and MA techniques. The FE programme with the optimisation procedure adapted for the work was found to be useful. Therefore it is used for the current study and combined with an alternative non-invasive experimental technique, which could measure human skin deformation *in vivo*.

This chapter describes an alternative approach that combines experimental work employing digital image correlation techniques and the inverse FEM to produce outputs (material parameters for skin) that are comparable (having features in common) to the previous work (Chapter 4). As described in Section 1.2 (Chapter 1), the current alternative approach attempts to compliment the work carried out in the previous chapters and support the overall findings of this study.

5.2 Motivations to employ current approach

The DIC technique was first proposed in the 1980s (Guan et al 2003, Stallof et al 2007) and originally used for experimental studies of stress analysis and fracture dynamics of engineering materials, such as metals, concrete and rubber. Its versatility shows tremendous promise for applications involving biological tissues and biomaterials (Zhang and Arola 2004, Moerman et al 2009). It has also been used for skin studies (Guan et al 2003, Stallof et al 2007, Evans 2009, Evans and Holt 2009) as described in Section 1.3.8 (Chapter 1).

The FE simulation and optimisation procedures implemented as described in Chapter 4 successfully determined the skin properties for five subjects. Evans and Holt (2009) have earlier demonstrated a similar success when it was used in combination with DIC techniques. Therefore, the current study adapted their method and the current result is compared to the result obtained from the MA experiments (Section 4.5, Chapter 4).

5.3 Scope of work

The ultimate aim of the current study is to determine the mechanical properties of human skin and therefore, the work conducted in this study and chapter provides the tools to achieve this. An attempt was made to measure skin deformation using the DIC technique and the data generated was used to determine the hyperelastic material parameters using the inverse FE programme with an optimisation procedure described in Section 4.4.2 (Chapter 4).

The challenge of the current study was to use the DIC technique to replicate the experimental protocol described in Section 2.5 (Chapter 2) and produce outputs

comparable to Section 4.5 (Chapter 4). Unlike the previous chapter, this chapter adds skin prestretch, λ_p in calculating the engineering stress to investigate its effect. Based on this, the results for the combination of MA-FEA and DIC-FEA are compared and thus, several findings are deduced.

5.4 Measuring skin deformation using DIC system

5.4.1 Experimental set up

For this purpose, a Correlated Solutions DIC system and equipment were employed (Limess Messtechnik und Software GmbH, Germany). The experimental setup consists of two cameras with 28 mm lenses (Figure 5.1) and a computer loaded with the system software, namely Vic-Snap and Vic3D. Vic-Snap is used during image capturing, while Vic3D processes the images to generate full-field displacements and strains data. The cameras were placed 54 mm apart and 122 mm from the target. The target was placed on a table with a height of 93 mm. Additional lighting (Figure 5.1) was used as the ambient illumination in the laboratory was not sufficient. The system was calibrated using a target of 5mm grid (Figure 5.2). The cameras lenses and apertures were adjusted to obtain sharp images. Thirteen images of the calibration target were captured at different angles and locations within the cameras field of view. The result was good with a standard deviation for residuals of 0.015 mm.
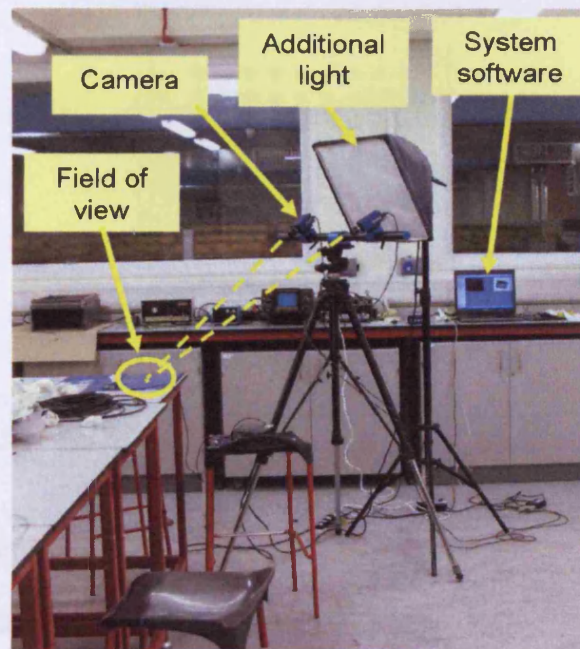
(a)

(b)

Figure 5.1: The system equipment (a) cameras, light and computer and (b) 28 mm lens.
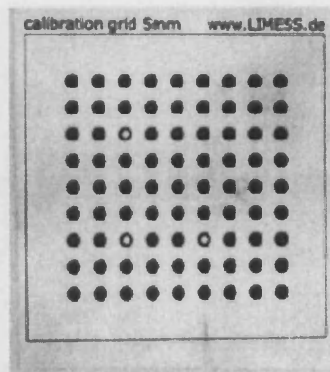
Figure 5.2: Calibration target (5mm grid).

5.4.2 Experimental protocol

Due to time constraint and subject availability, only two of the 5 subjects in the previous study (Subject 2 and Subject 4) were able to return for the tests. They were confirmed healthy with the condition of the skin surface similar since last tested using the MA system. Informed consent was again obtained with ethical approval from the Cardiff School of Engineering Research Ethics committee. The test area at the forearm was marked to indicate load direction, load point and the boundaries (Figure 5.3). To produce a random dot pattern on the skin, black colour theatrical face paint was speckled using a sponge and toothbrush. Skin deformation was induced by pulling a loading tab attached to it; via a nylon filament connected to a load cell (Interface Force Measurements, Crowthorne, UK). On average 30 images were captured for 15 seconds (0.5 seconds per image) where the load was applied up to 1N.
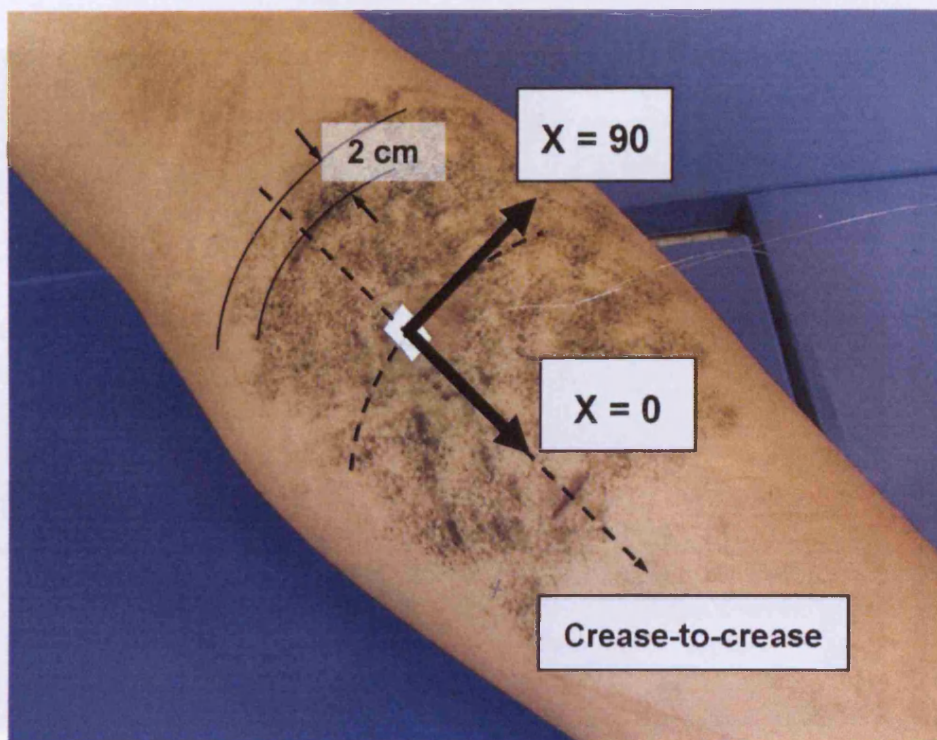
Figure 5.3: Speckles painted on the forearm and the loading directions.

5.4.3 Generating data using Vic3D

Using the DIC system software, Vic3D, the 30 images were analysed. Each camera records the deformation process. The software analysed the images from both cameras using its in-house image correlation algorithm. For every object point (camera pixel) the 3D displacements and strain components are calculated. Sample outputs are shown in Figure 5.4 and 5.5. Figure 5.4 shows the distribution of the axial displacement at the test area for Subject 2 when 0.63 N load was applied in the X=0° direction. It is observed that some information at the surrounding area of the loading tab and beneath the nylon filament is lost. This might be because the system could not detect the speckles (i) on the loading tab (low contrast), (ii) at the wrinkle (speckles jostled) and beneath the nylon filament (hidden speckles).
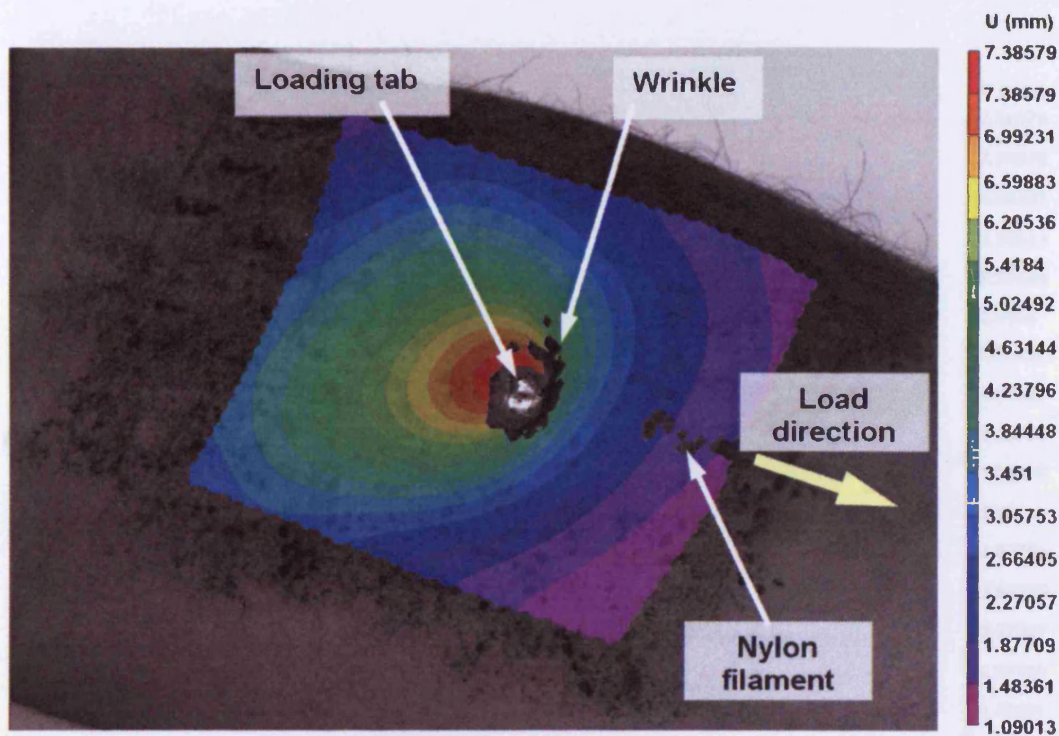
Figure 5.4: The axial displacement distribution (2D contour) as measured by the DIC system. It shows that some information lost.

Figures 5.5a and 5.5b show the 3D contour of the axial and lateral displacement distribution for the same case (Subject 2, X=0°, 0.63 N). The shape of skin deformation at the wrinkle is clearly shown (Figure 5.5a). It is interesting to observe that the current result agrees to the results obtained using FE simulation (Chapter 3). The contour for the lateral displacement distribution (Figure 5.5b) is found to be similar to Figure 3.16. (Section 3.5.1, Chapter 3). Figure 5.6 shows the contour for the axial displacements when load was applied at X=90° for the same subject (Subject 2). The maximum displacement is found lower than at X=0°. It is also observed that the loss of information is higher than at X=0°. However, the area where the loss occurred remains the same (at loading tab and beneath nylon filament). This effect is also observed for Subject 4 (X=90°) which suggests that the larger area of loss might possibly due to the larger gap between skin surface and the nylon filament during pulling.
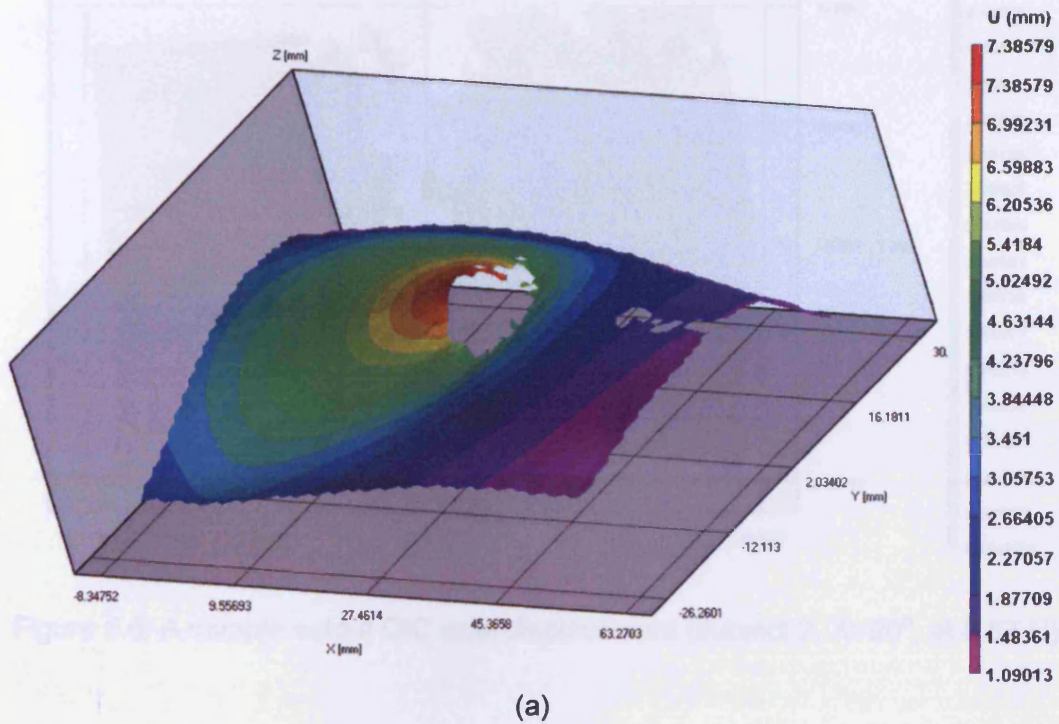
(a)
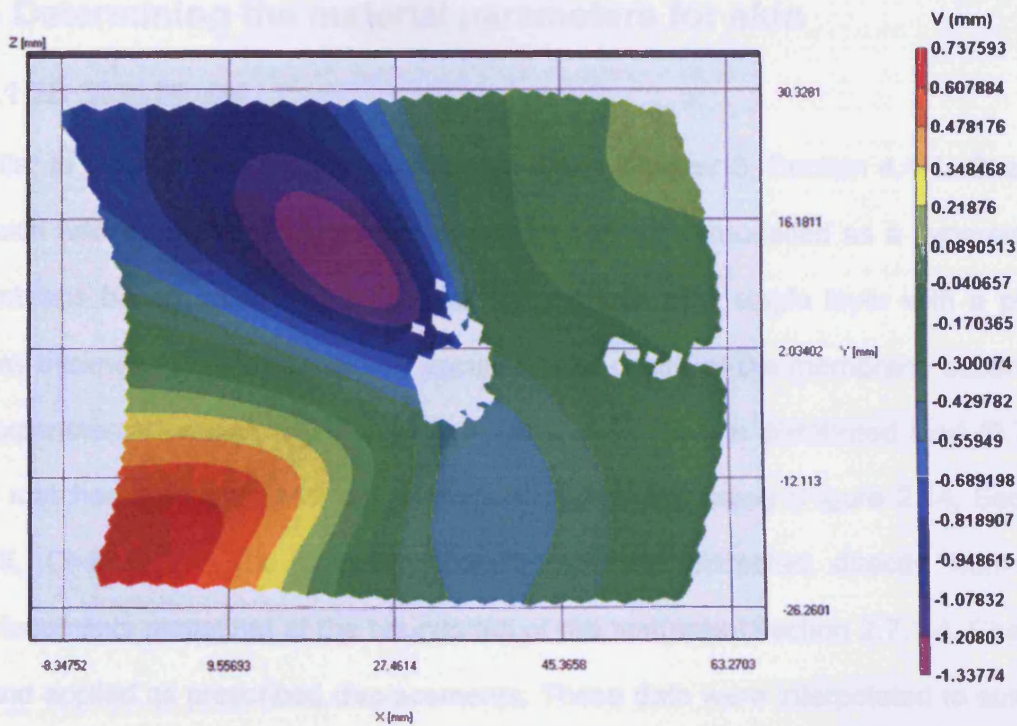
(b)

Figure 5.5: A set of sample output (3D contour) from the DIC experiments
(a) axial displacement and (b) lateral displacement distribution
(b) (Subject 2, X=0°, 0.63 N)
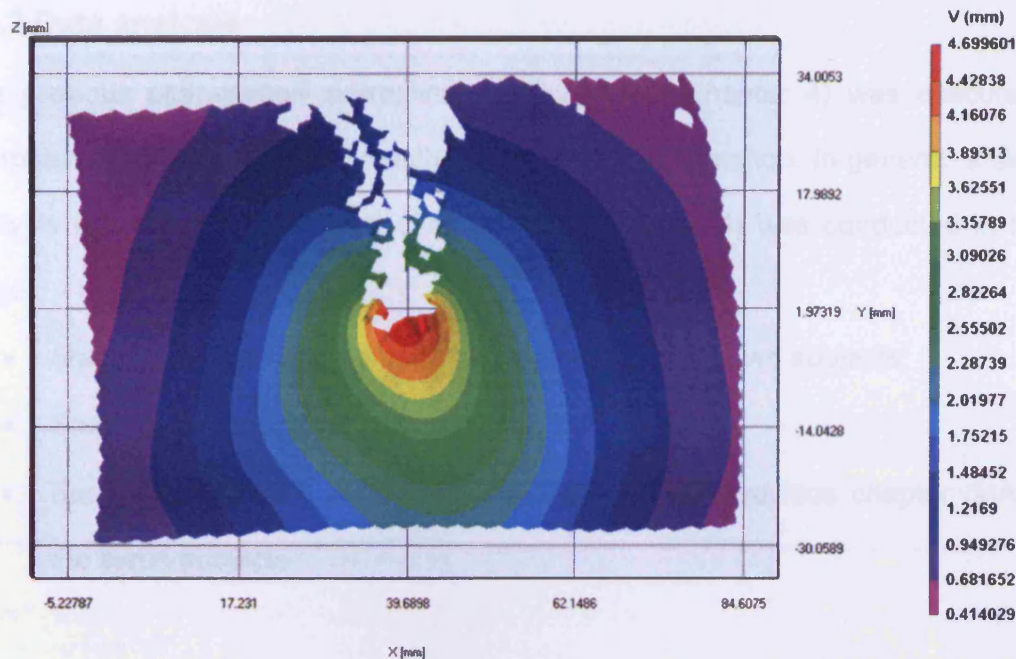
Figure 5.6: A sample output DIC axial displacement (subject 2, X=90°, at 0.87 N)

5.5 Determining the material parameters for skin

5.5.1 2D Skin Model

Similar to the previous FE models (Section 3.4.1, Chapter 3, Section 4.4.1, Chapter 4); skin was assumed to be homogeneous, isotropic and modelled as a hyperelastic membrane based on the Ogden's model. It is made of a single layer with a plane stress thickness 1.5 mm. Load was applied at the centre of the membrane according to experimental procedures. The critical part was to apply a distributed load (0.7 N) that matched the shape and size of the loading tab accurately (Figure 2.14, Section 2.4.5, Chapter 2). The boundary conditions were extracted directly from the displacements measured at the boundaries of the test area (Section 2.7.1.4, Chapter 2) and applied as prescribed displacements. These data were interpolated to suit the number of nodes at the boundary. The membrane (64 mm x 48 mm) was meshed into 14 x 11 isoparametric quadrilateral (eight-noded) elements.

5.5.2 Data analysis

The previous optimisation subroutine (Section 4.4.2, Chapter 4) was executed to compute parameters that best match the measured deformation. In general, a similar analysis to the previous chapter (Section 4.4.3, Chapter 4) was conducted in three stages:

- *Stage 1*: determining the material parameters for the two subjects.

- *Stage 2*: evaluating the parameters (λ_p is included).

- *Stage 3*: comparing current results (DIC) with the previous chapter (MA) for the same subjects.

Unlike the previous chapter, the current chapter enhanced the analysis of skin properties by including prestretch, λ_p in the stress-strain relation. This was conducted to observe the contribution of the prestretch to the determined mechanical properties of human skin. Another interesting point in this chapter is comparing the determined skin properties for the same subjects using two different measurement techniques.

5.5.2.1 *Stage 1*: Determining skin property for individual subjects

The ultimate aim of this study is to determine the mechanical properties of human skin. Therefore, using current technique (DIC and FEM) the skin hyperelastic material parameters were determined for the individual subjects (Subject 2 and 4). Similar to the previous approach, for each subject and load direction, the optimisation procedure was used to generate the best 20 sets of parameters (recorded the least rms error). Due to a large amount of data generated, a set of results is presented in detail for Subject 2 (X=0°, 0.63 N) as a sample output. μ=11, α=25 and λ_p=0.24 were used as the first initial guess. It was based on the same initial parameters used in the previous chapter (Section 4.4.3.1 Chapter 4).

As presented in Section 4.5 (Chapter 4) the results are summarised in tables to show the upper and lower values of the optimum parameters. For each subject, a single material parameter set (μ, α and λ_p) was proposed by averaging the first 10 out of 20 sets of optimum parameters. By achieving this, the aim of this study to determine the skin properties for human skin using DIC techniques is fulfilled.

5.5.2.2 *Stage 2*: Evaluating the prestretch term in the stress-stretch relation

The previous chapter (Section 4.5, Chapter 4) presented it results (skin properties) using the stress-stretch diagrams (2D) based on the value of μ and α. However, the current analysis attempts to add the prestretch, λ_p to investigate its contribution to the stress-stretch relation. For this purpose, based on Equation 4.1 (Section 4.4.1.4, Chapter 4), the relation of engineering stress, σ_E and principal stretch, λ, (Equation 4.2, Section 4.4.3.2, Chapter 4) was re-derived to include the prestretch term:

$$\sigma_E = \frac{\mu}{(\lambda + \lambda_p)}\left(\left(\lambda + \lambda_p\right)^{\alpha} - \left(\lambda + \lambda_p\right)^{-\alpha/2}\right) \tag{5.1}$$

Using Equation 5.1, a parametric study was designed and conducted to:

(i) analyse the sensitivity of the parameters, μ, α and λ_p to the solution.

(ii) prove the non-uniqueness of the current solutions; and determine several sets of parameters that producing similar solution.

5.5.2.3 *Stage 3*: comparing current results (DIC) with the previous chapter (MA)

Using Equation 5.1, stress-stretch diagrams were constructed for the two subjects. Based on this, the results for the combination of MA-FEA and DIC-FEA are compared and thus, several findings are deduced.

5.6 Results

Similar to the previous chapter, the current study generated two types of output. Firstly, the FE analysis produced displacements information for the deformed membrane. Secondly, the stochastic optimisation procedure produced the 20 sets of optimum (least rms error) material parameters for every single experiment (subjects and load directions).

5.6.1 *Stage 1*: the optimised material parameters.

A set of results is presented in detail for Subject 2 ($X=0°$, 0.63 N) as a sample output. The result of the best 20 sets of material parameters for Subject 2 is presented as an example (Table 5.1). Detailed results for the subjects (Subjects 2 and 4) are attached in Appendix G. The data in the table is the actual extraction from the optimisation output. Out of the 20 sets of data, the programme displays the best set of parameters that produced the least rms error. The programme also recorded the duration of optimisation process and shows it as the elapsed time (Table 5.1). For this specific sample, the optimisation process converged after 21745 seconds ($\approx$6 hours).

Table 5.1: The best 20 sets of material parameters
(Subject 2, X=0°, 0.63N, initial guess values: μ=11, α=25 and λ_p=0.24)

μ (Pa)	α	λ_p	rms error
11.6924	28.0643	0.1844	0.0987
10.4159	26.7507	0.2050	0.1009
10.1243	27.2212	0.2018	0.1012
8.8428	27.4872	0.1992	0.1015
9.5809	26.9502	0.2030	0.1018
11.2480	25.5372	0.2187	0.1022
11.5710	26.1061	0.2076	0.1024
11.9566	23.9143	0.2418	0.1025
8.7780	26.9842	0.2141	0.1027
9.7336	27.0351	0.2075	0.1027
12.5761	26.9889	0.1930	0.1033
10.3462	26.4466	0.2010	0.1034
11.8980	27.4024	0.1904	0.1035
11.7360	26.2613	0.2060	0.1035
13.2573	25.4364	0.2082	0.1035
13.4239	26.6259	0.1941	0.1036
9.0412	25.9446	0.2204	0.1039
8.9830	26.5894	0.2131	0.1039
11.8716	24.3730	0.2371	0.1041
9.6833	27.1006	0.2050	0.1044

Best results:
11.6924   28.0643   0.184371

Minimum:9.8722e-005

Bounds:8.77804   23.9143   0.184371
Bounds:13.4239   28.0643   0.241833

Elapsed time is 21745.770539 seconds

5.6.1.1 The material parameters for two subjects in different directions

As described in the previous chapter, for simplicity, the 20 sets of data could also be represented based on its upper and lower bounds. The result for Subject 2 in three directions (X=0°, 45° and 90°) is presented in Table 5.2. Despite using the least computation time, it is found that the data for X=90° converged the best (0.06 mm rms error) compared to other directions (X=0° and 45°). In general, all the results are very good; producing rms error < 0.2 mm.

Table 5.2: The optimum material parameters for Subject 2 (M, 26) in three different directions

Load direction		$X=0°$	$X=45°$	$X=90°$
Load applied		0.63	0.57	0.87
Minimum rms error (mm)		0.10	0.16	0.06
μ (Pa)	Lower	8.78	8.52	9.32
	Upper	13.42	13.23	11.64
α	Lower	23.91	26.42	29.14
	Upper	28.06	33.15	31.87
λ_p	Lower	0.18	0.18	0.20
	Upper	0.24	0.25	0.24
Elapsed time (hours)		6	4	4

For the set same of data, a 3D graph showing the distribution of material parameters is presented in Figure 5.7. It could be observed that the optimised data for $X = 45°$ did not converge very well compared to other directions ($X=0°$ and $90°$). The data is shown more scattered. Even so, the rms error is small (< 0.2 mm) although compared to others, it has the highest.

Table 5.3 shows the result for Subject 4 in two directions ($X=0°$ and $90°$). It is found that the data for $X=90°$ converged faster than $X=0°$ to produce a similar rms error (0.15 mm). Both results are found very good producing rms error < 0.2 mm.
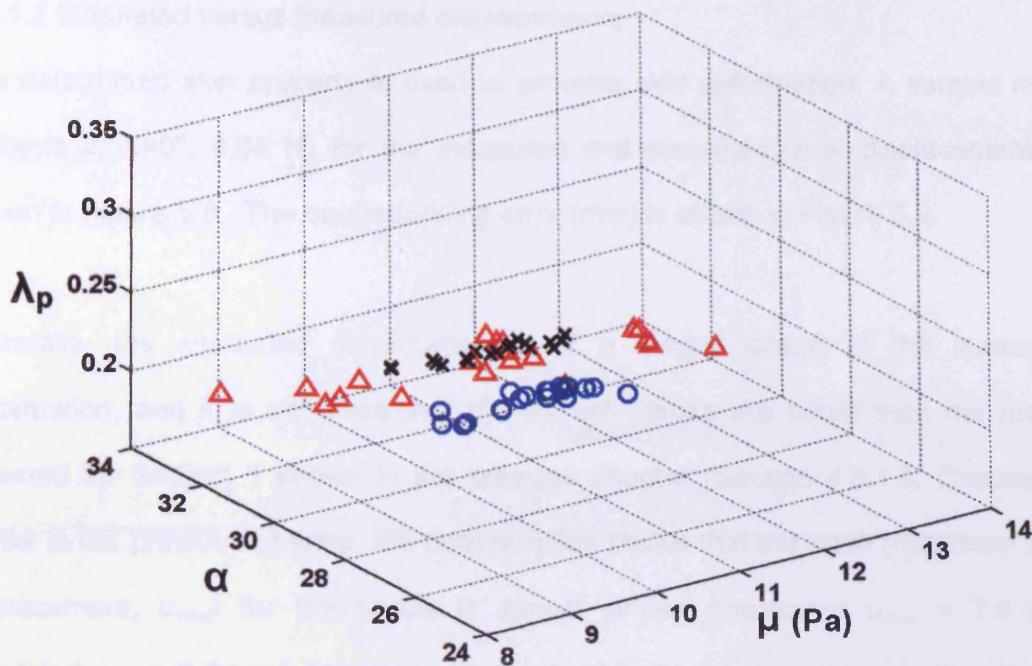
Figure 5.7: Optimum parameter sets for Subject 2 load applied at X=0° (circles), X=45° (triangles) and X=90° (crosses). The best 20 parameter sets for each are shown, as found after evaluating several thousand parameter sets in the stochastic optimisation procedure.

Table 5.3: The optimum material parameter for Subject 4 (M, 23) in two different directions.

Load direction		X=0°	X=90°
Load applied		0.83	0.6
Minimum rms error (mm)		0.15	0.15
μ (Pa)	Lower	8.19	8.60
	Upper	10.66	11.77
α	Lower	25.13	31.14
	Upper	30.17	32.37
λ_p	Lower	0.23	0.14
	Upper	0.33	0.16
Elapsed time (hours)		39	14

5.6.1.2 Simulated versus measured displacements

The determined skin property is used to simulate skin deformation. A sample result (Subject 2, X=0°, 0.63 N) for the measured and simulated axial displacements is shown in Figure 5.8. The corresponding error (rms) is shown in Figure 5.9.

Generally, the simulated deformation is of a similar shape to the measured deformation, and it is observed that the current results are better than the results obtained for Subject 1 shown in the previous chapter (Section 4.5.1.3, Chapter 4). Unlike in the previous chapter, the current result shows that the peak (maximum axial displacement, u_{max}) for the shape is almost similar (measured u_{max} = 7.6 mm, simulated u_{max} = 7.5 mm). However, as observed in the previous chapter, the slope of the deformed shape at the midline markers is more of a linear shape rather than a quadratic shape (measured data). This is further discussed in the following section (Section 5.7 Discussion).

Figure 5.9 shows that the overall rms error is small (<0.1 mm) and this supports the current result. As found in the previous chapter, the largest error was found at the surrounding area of the loading tab. This has been described due to the difficulty in modelling the exact shape, size and location of the loading tab.
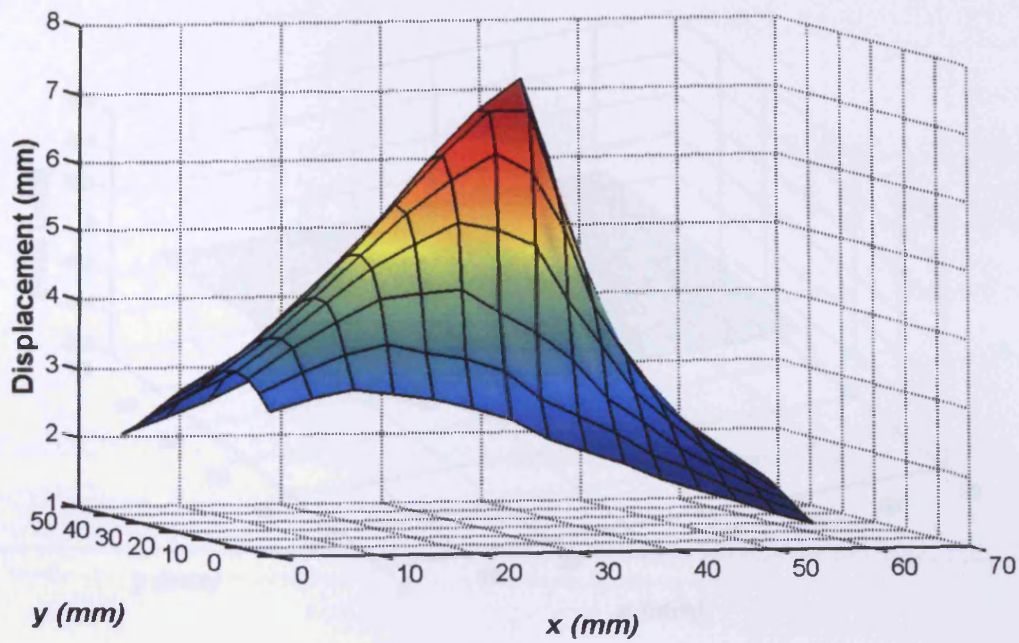
(a)
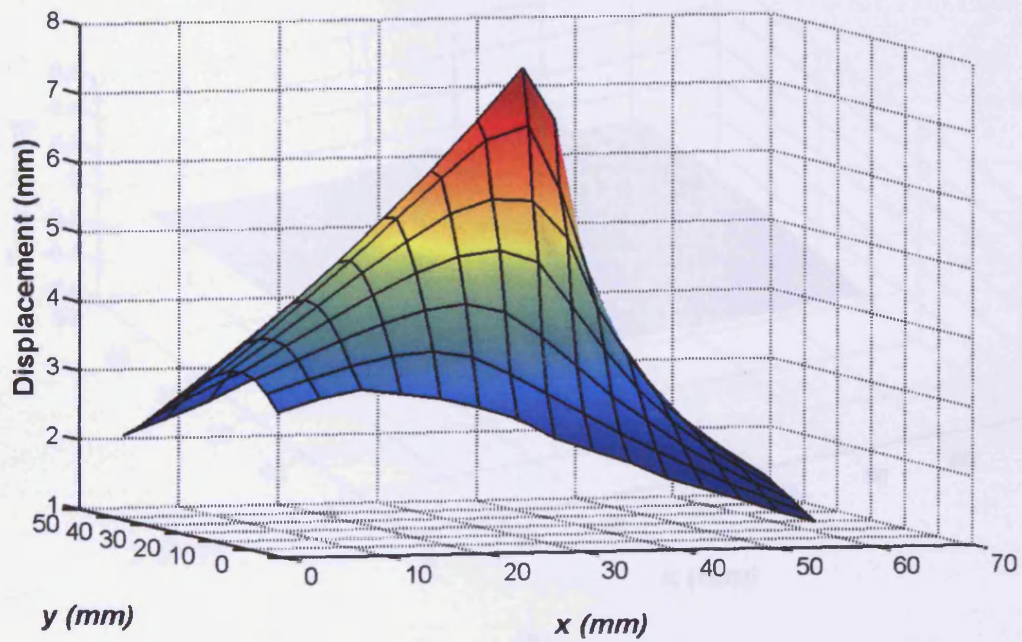
(b)

Figure 5.8: A sample result to compare measured and simulated displacement (Subject 2, X=0°, 0.63N). Three dimensional graphs, where the vertical axis and the colour contours show the axial displacements for (a) measured (b) simulated using the optimised parameters (μ=11.69 Pa, α=28.06, λ_p=0.18).
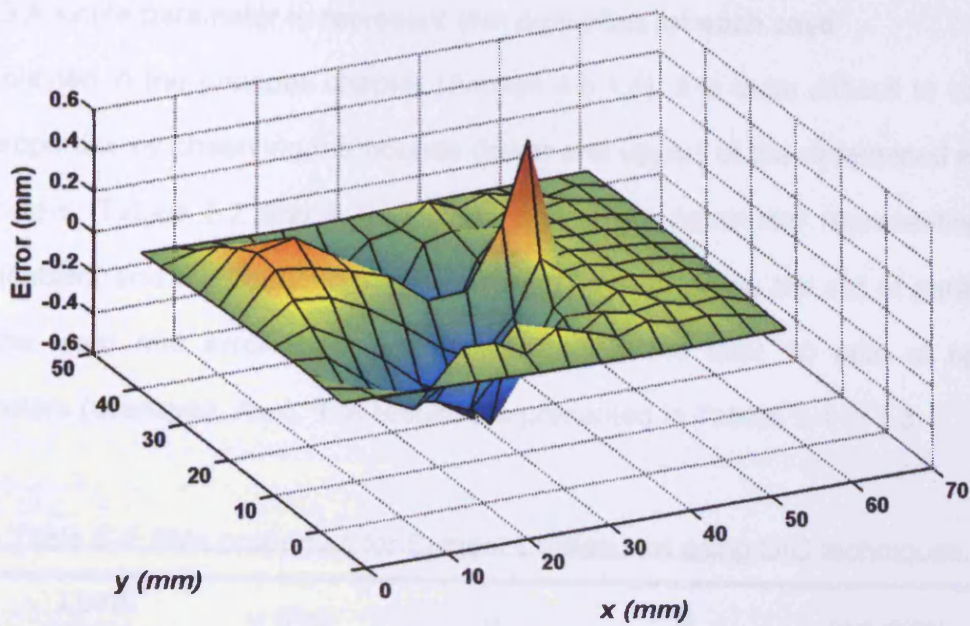
(a)
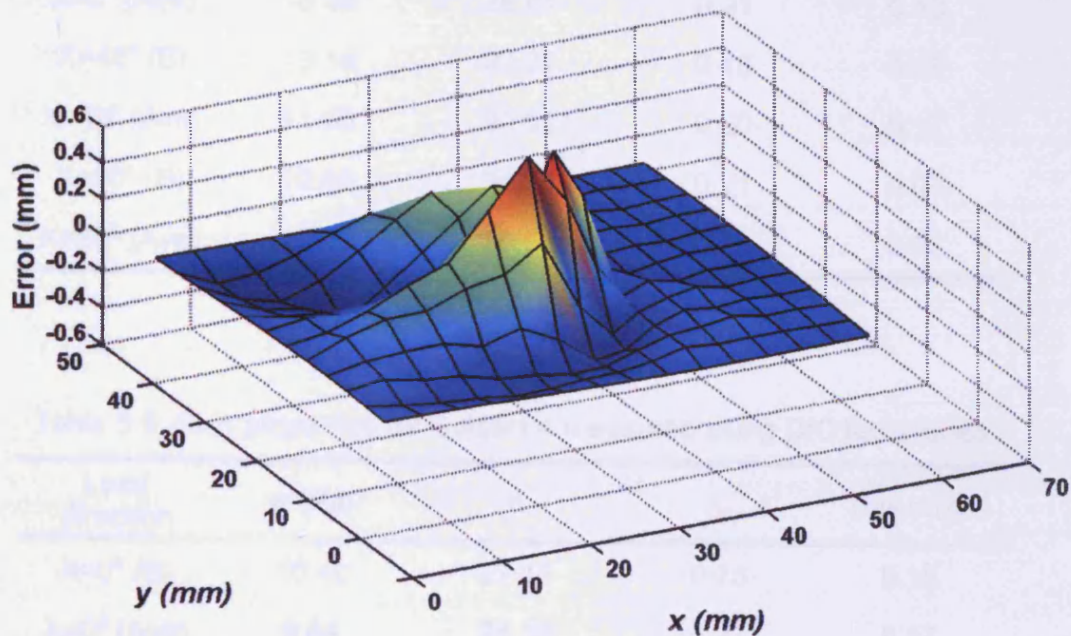
(b)

Figure 5.9: Difference between the finite element model and the experimental measurement (error), for the (a) axial displacement and (b) lateral displacement (Subject 2, X=0°, 0.63 N). The rms error was found to be less than 0.17 mm. It could be observed that the largest error occur at the surrounding area of the loading point.

5.6.1.3 A single parameter to represent skin properties for each case

As explained in the previous chapter (Section 4.5.1.5), it is quite difficult to compare skin properties by observing the bounds (lower and upper) of the determined material parameters (Tables 5.2 and 5.3). Therefore, a single parameter representing each case (subject and load direction) is determined by expressing the set of parameters with the least rms error (best, B) and averaging the best 10 sets of optimum parameters (averaged, Ave). The results are presented in Tables 5.4 to 5.5.

Table 5.4: Skin properties for Subject 2 measured using DIC techniques.

Load direction	μ (Pa)	α	λ_p	rms error
X=0° (B)	11.69	28.06	0.18	0.10
X=0° (Ave)	10.39	26.61	0.21	0.10
X=45° (B)	13.18	32.27	0.18	0.16
X=45° (Ave)	11.36	30.52	0.20	0.17
X=90° (B)	10.83	31.11	0.21	0.06
X=90° (Ave)	10.88	30.52	0.22	0.07

Table 5.5: Skin properties for Subject 4 measured using DIC techniques.

Load direction	μ (Pa)	α	λ_p	rms error
X=0° (B)	10.40	27.11	0.28	0.15
X=0° (Ave)	9.64	28.18	0.27	0.17
X=90° (B)	10.36	32.09	0.15	0.15
X=90° (Ave)	10.43	31.96	0.15	0.16

Up to this stage, the aim to determine the mechanical properties of human skin using DIC techniques has been successfully achieved for two subjects. Unlike when using the MA techniques, all current results produced an rms error <0.2 mm.

5.6.2 *Stage 2*: The parametric study

The result showing the sensitivity of Equation 5.1 to the variations in μ, α and λ_p is presented in Figure 5.10. The current study included the prestretch term, which has been omitted in the previous chapter (Section 4.5.2). Therefore, three sets of curves are plotted to observe the three boundaries. The first set aimed to observe the effect of variations in μ. Therefore, while keeping α and λ_p constant ($\alpha = 26$, $\lambda_p = 0.2$), μ was varied from 5 to 15 Pa ($\Delta\mu = 10$ Pa). The second set aimed to observe the effect of variations in α. Therefore, while keeping μ and λ_p constant ($\mu = 10$ Pa, $\lambda_p = 0.2$), α was varied from 20 to 30 ($\Delta\alpha = 10$). The third set aimed to observe the effect of variations in λ_p. Therefore, while keeping μ and α constant ($\mu = 10$ Pa, $\alpha = 26$), λ_p was varied from 0.15 to 0.25 ($\Delta\lambda_p = 0.1$). Evans and Holt (2009) parameter ($\mu = 10$ Pa, $\alpha = 26$, $\lambda_p = 0.2$) is included as a reference.

It is observed that a 0.1 unit difference in λ_p ($\Delta\lambda_p = 0.1$) produced a larger boundaries than a 10 unit difference in μ ($\Delta\mu = 10$ Pa). A 10 unit difference in α ($\Delta\alpha = 10$) produced a twice significant effect (twice larger boundary) than a 10 Pa difference in μ ($\Delta\mu = 10$ Pa). This shows that Equation 5.1 is very sensitive to a change in λ_p and α and its effect is significant when comparing skin properties for among subjects or loading directions.
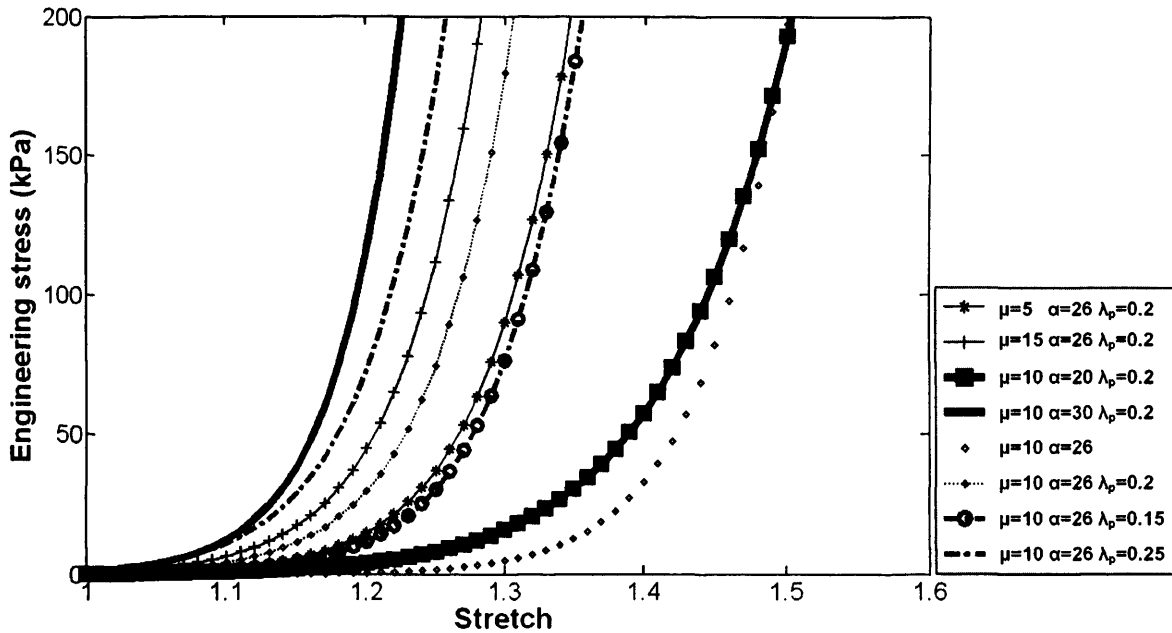
Figure 5.10: The bounds for variations in μ (Δμ = 10 Pa, thin solid lines), α (Δα = 10, thick solid lines) and $λ_p$ (Δ$λ_p$ = 0.1, dotted lines)

A parametric study was also carried out to prove that the optimisation process did not produce a unique solution. This has been described in the previous chapter and the current study enhanced the previous analysis (Section 4.5.2) to include the prestretch term. To demonstrate this, several material parameters were investigated and the result is shown in Table 5.6 and Figure 5.11. It is observed that the curves for several material parameters (Table 5.6) could match one another (Figure 5.11).

The findings deduced from the current parametric study provided a better understanding in interpreting the results from the stress-stretch diagrams with an inclusion of the prestretch effect. The knowledge is used to compare and discuss the current results with the previous study (MA, Chapter 4).

Table 5.6: An example of five sets of material parameters producing a similar graph

Set	Material parameters		
Set 1	μ = 0.8 Pa,	α = 28,	λ_p = 0.30
Set 2	μ = 3 Pa,	α = 27,	λ_p = 0.25
Set 3	μ = 10 Pa,	α = 26,	λ_p = 0.20
Set 4	μ = 35 Pa,	α = 25,	λ_p = 0.15
Set 5	μ = 110 Pa,	α = 24,	λ_p = 0.10
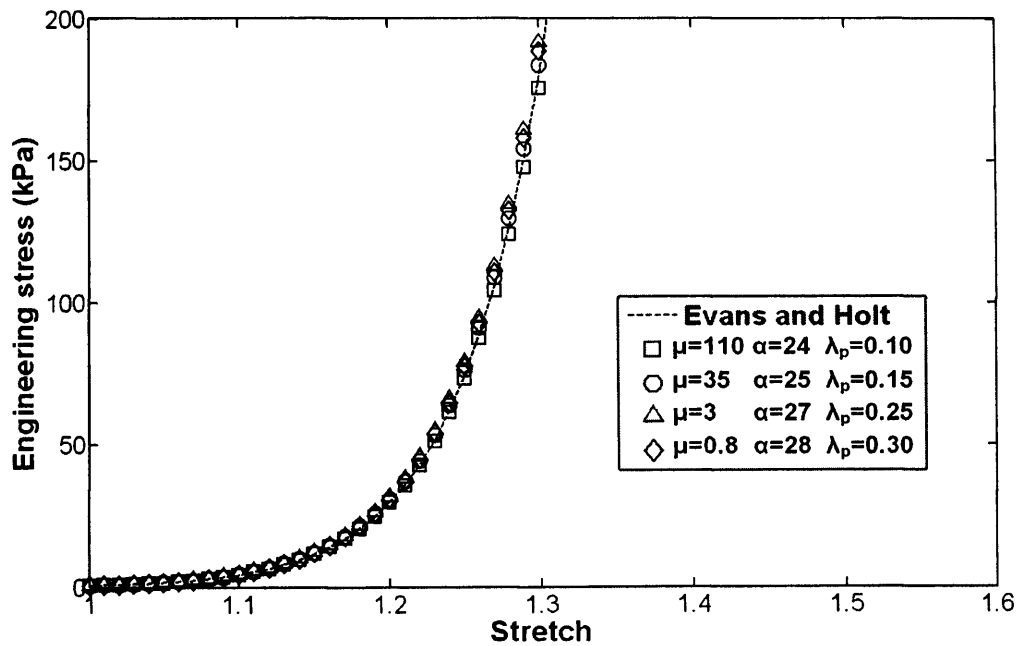
Figure 5.11: The curves for a few sets of material parameters which fit into one another. Evans and Holt (2009) data (μ = 10 Pa, α = 26, λ_p = 0.20, dotted line) is used as a reference.

5.6.3 Stage 3: comparing current results (DIC) to the previous approach (MA).

Skin deformation behaviour is presented using the stress-stretch diagram with a prestretch term (Equation 5.1) for the two subjects (Subject 2 and 4). Before it is compared to the previous approach, the results obtained from the current approach (DIC) are analysed.

5.6.3.1 Stress-stretch diagram for Subject 2

A stress-stretch diagram is shown (Figures 5.12) to observe the results for Subject 2 at different direction (X=0°, 45° and 90°). For each direction, two sets of graph are presented. The black and blue markers represent the averaged and best parameters respectively. The averaged and best parameters for each direction are very close to each other indicating that the solution converged very well and consistent. Moreover, all markers are highlighted to show that its rms error is small (< 0.3 mm). It is observed that the results for different direction are very close to each other and therefore no significant trend of skin behaviour in different directions can be deduced from this. In general, it is observed that the skin property for Subject 2 is close to the skin property determined by Evans and Holt (2009, μ = 10 Pa, α = 26, λ_p = 0.20).
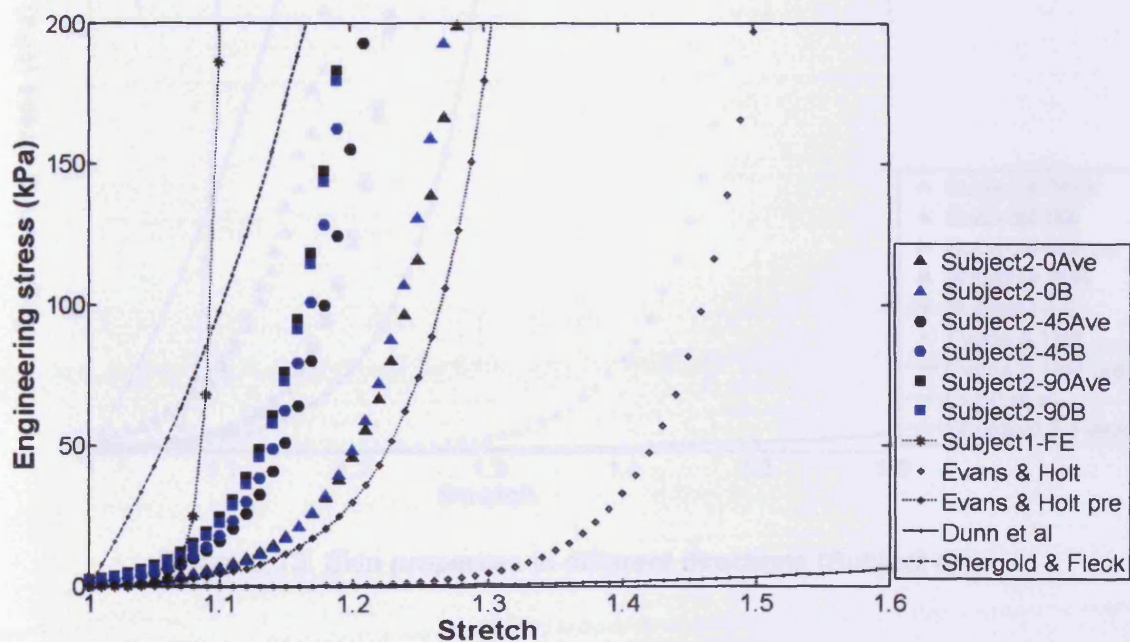
Figure 5.12: Skin properties in different directions (Subject 2).

5.6.3.2 Stress-stretch diagram for Subject 4

A stress-stretch diagram is shown (Figures 5.13) to observe the results for Subject 4 at different direction (X=0° and 90°). In general, it is observed that the skin property for Subject 4 is also close to the skin property determined by Evans and Holt (2009). Similar to Subject 2, the averaged and best parameters for each direction are very close to each other indicating that the solution converged very well and consistent. Moreover, all markers are highlighted to show that its rms error is small (< 0.3 mm). It is observed that the results for different direction are very close to each other and therefore no significant trend of skin behaviour in different directions can be deduced from this.
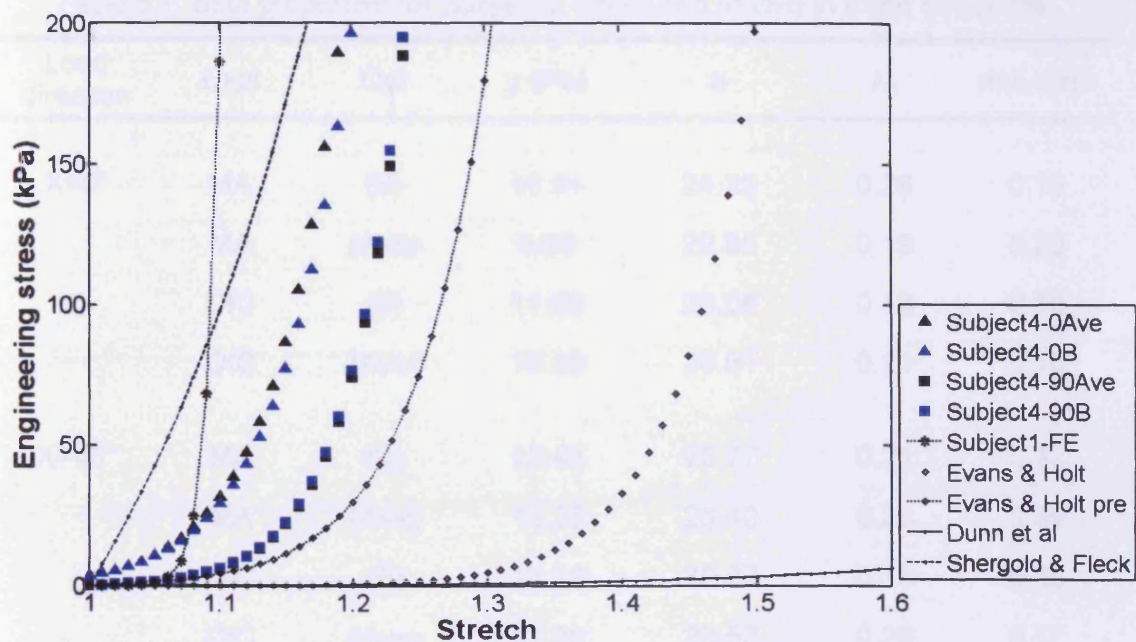
Figure 5.13: Skin properties in different directions (Subject 4).

5.6.3.3 Comparing results between the two approaches (DIC versus MA)

Tables 5.7 and 5.8 present the optimum hyperelastic parameters determined from both approaches for Subject 2 and 4 respectively. The title 'Load direction' refers to the loading directions; 'Expt' refers to the experimental techniques used to measure skin deformation (either MA or DIC) and 'Opt' refers to the type of optimum parameters (either best, B or Averaged, Ave). The corresponding stress-stretch diagrams are shown in Figures 5.14 to 5.17. In general, it could be observed the results in Table 5.7 (Subject 2) are close to each other, indicating its consistency. Except for X=45° (MA), all the errors are small ($\leq$ 0.2 mm) which indicate the optimisation solution converged very well.

Table 5.7: Skin properties for Subject 2 measured *in vivo* in three directions.

Load direction	Expt	Opt	μ (Pa)	α	λ_p	rms error
X=0°	MA	(B)	10.84	24.25	0.26	0.19
	MA	(Ave)	9.68	29.65	0.19	0.20
	DIC	(B)	11.69	28.06	0.18	0.10
	DIC	(Ave)	10.39	26.61	0.21	0.10
X=45°	MA	(B)	13.46	25.77	0.21	0.33
	MA	(Ave)	13.36	25.40	0.23	0.35
	DIC	(B)	13.18	32.27	0.18	0.16
	DIC	(Ave)	11.36	30.52	0.20	0.17
X=90°	MA	(B)	4.57	26.91	0.21	0.17
	MA	(Ave)	5.41	26.16	0.22	0.18
	DIC	(B)	10.83	31.11	0.21	0.06
	DIC	(Ave)	10.88	30.52	0.22	0.07

Table 5.8 shows that in general, except for X=90° (MA) the results for Subject 4 are close to each other. The divergence of the results for X=90° (MA) is self-explanatory by its large error (>0.3 mm) and prestretch (>0.88). The determined prestretch for this specific case is too large, which indicate that the optimisation process failed to converge even after running for 22 hours. One possible cause is the FE model failed to deform according the measured data and the optimisation search path deviated to the closest parameters that could produce the minimum error. Therefore, the solution probably drifted from the correct solution.

Table 5.8: Skin properties for Subject 4 measured *in vivo* in two directions.

Load direction	Expt	Opt	μ (Pa)	α	λ_p	rms error
X=0°	MA	(B)	13.81	29.54	0.16	0.18
	MA	(Ave)	11.13	29.41	0.19	0.20
	DIC	(B)	10.40	27.11	0.28	0.15
	DIC	(Ave)	9.64	28.18	0.27	0.17
X=90°	MA	(B)	10.81	12.44	0.88	0.32
	MA	(Ave)	11.22	12.18	0.92	0.33
	DIC	(B)	10.36	32.09	0.15	0.15
	DIC	(Ave)	10.43	31.96	0.15	0.16

The data in Tables 5.7 and 5.8 are used to construct the stress-stretch diagrams for the two subjects. For each subject, two sets of graphs are plotted, which compare the results for the best, B and averaged, Ave, material parameters respectively. Only the graphs for result producing a small rms error (< 0.3); are highlighted.
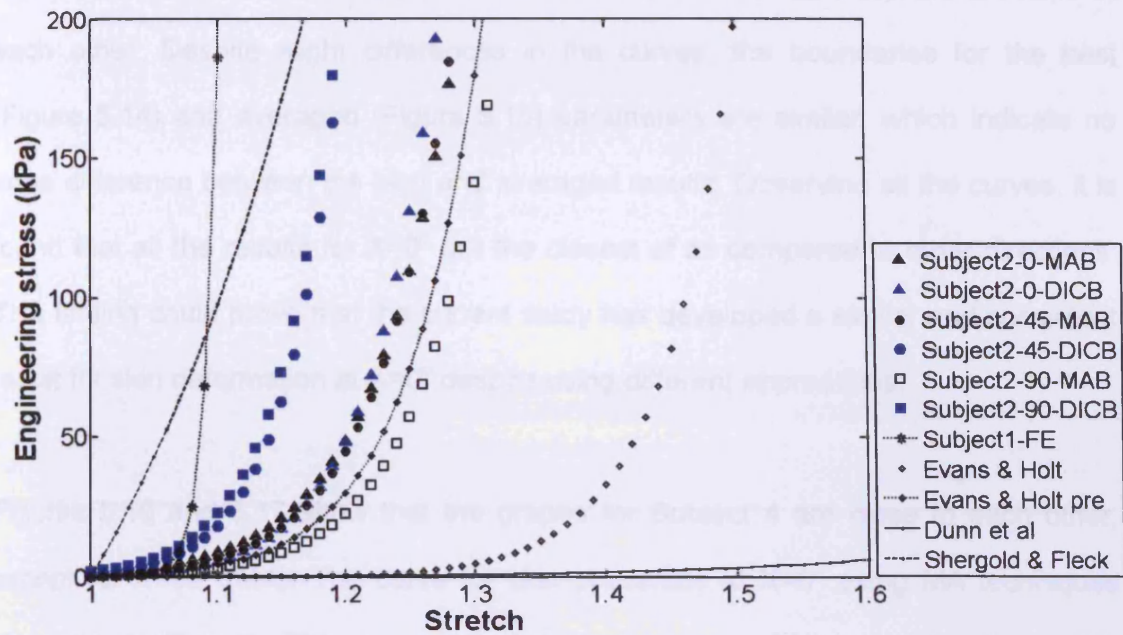
Figure 5.14: Comparison of skin properties for Subject 2 using different techniques (Best parameter set).
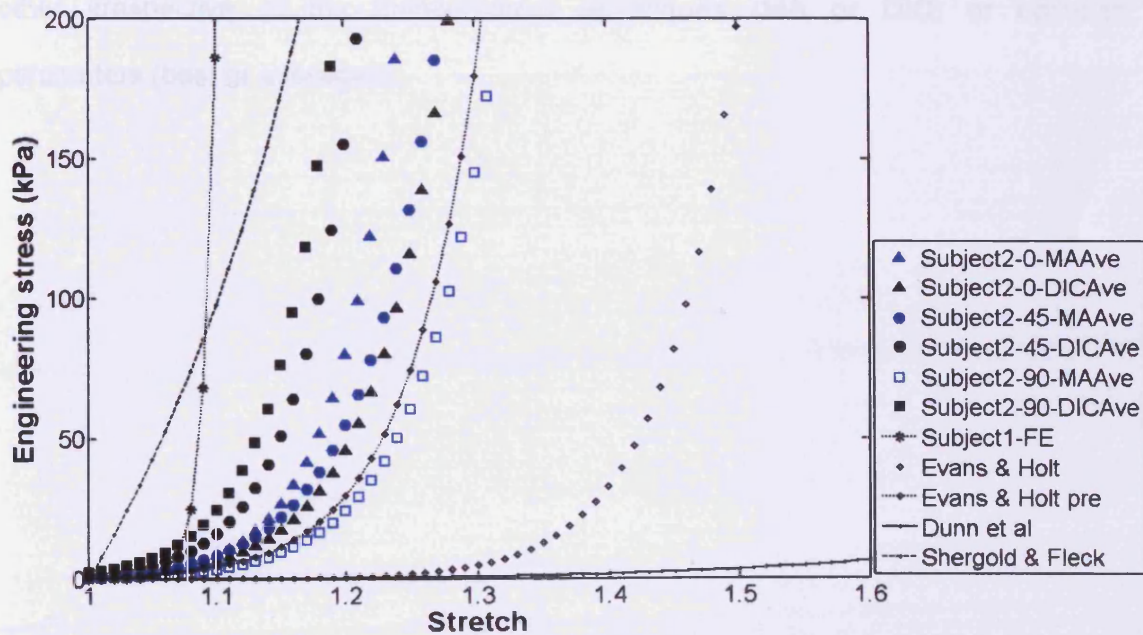
Figure 5.15: Comparison of skin properties for Subject 2 using different techniques (Averaged parameter set).

Figures 5.14 and 5.15 show that all the stress-stretch curves for Subject 2 are close to each other. Despite slight differences in the curves, the boundaries for the best (Figure 5.14) and averaged (Figure 5.15) parameters are similar, which indicate no large difference between the best and averaged results. Observing all the curves, it is found that all the results for X=0° are the closest of all compared to other directions. This finding could prove that the current study has developed a similar and consistent result for skin deformation at X=0° despite using different approaches.

Figures 5.16 and 5.17 show that the graphs for Subject 4 are close to each other, except for X=90° (MA). The curve for skin properties at X=0° using MA techniques diverged significantly. This exaggerated its large error and large prestretch possibly and therefore, not representing the skin properties for Subject 4. Both graphs also reveal that the results for skin deformation at X=0° for Subject 4 are very close to each other irrespective of the measurement techniques (MA or DIC) or optimum parameters (best or averaged).
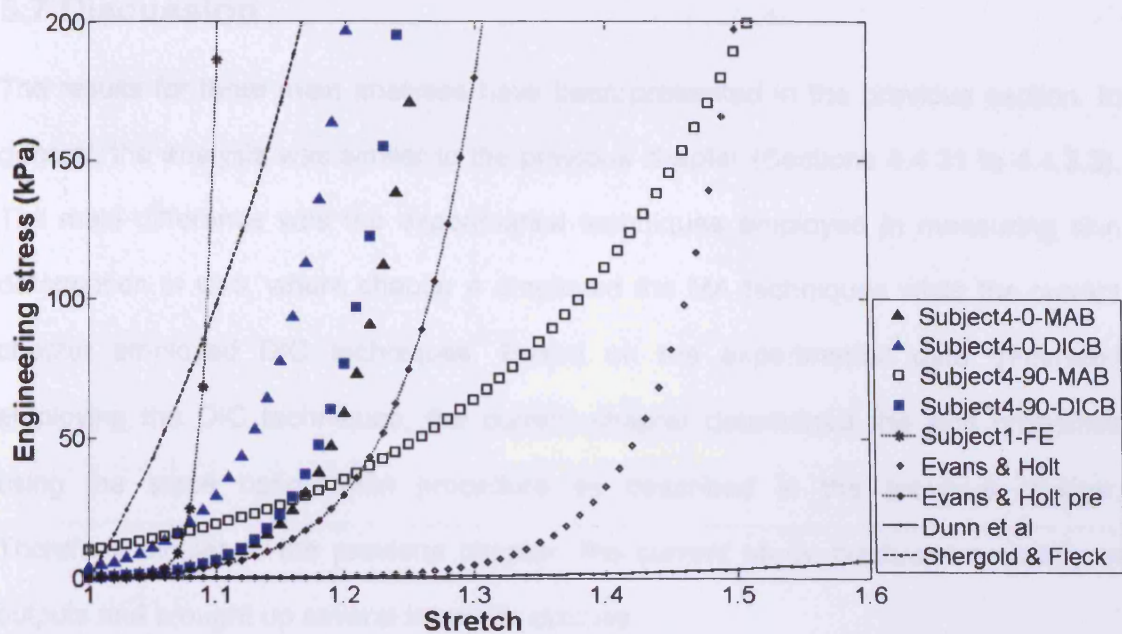
Figure 5.16: Comparison of skin properties for Subject 4 using different techniques (Best parameter set).
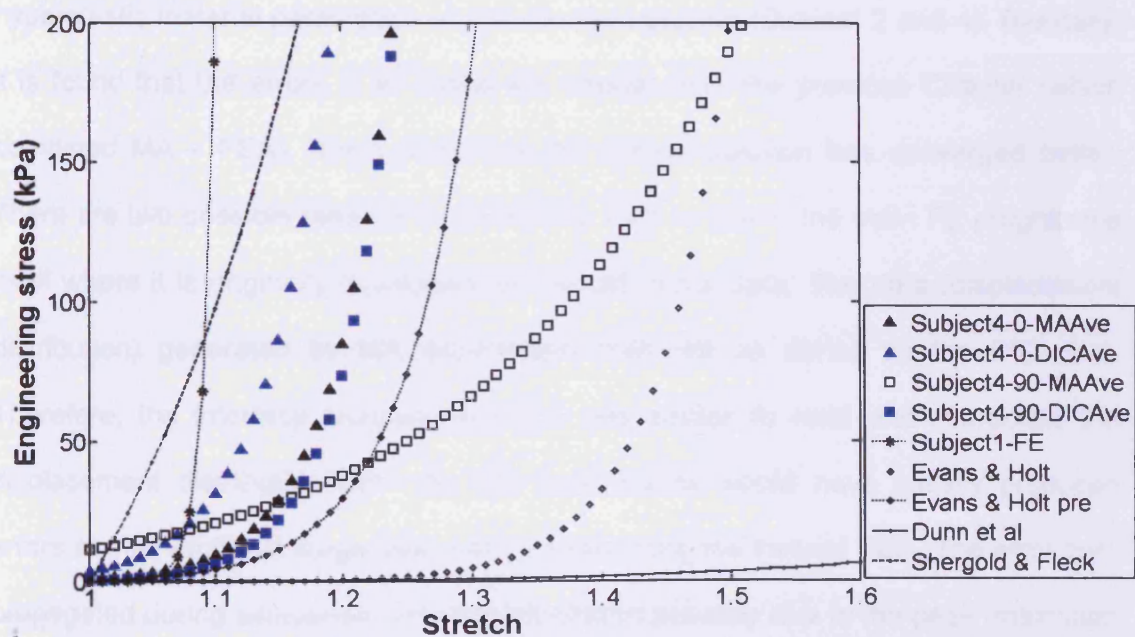
Figure 5.17: Comparison of skin properties for Subject 4 using different techniques (Averaged parameter set).

5.7 Discussion

The results for three main analyses have been presented in the previous section. In general, the analysis was similar to the previous chapter (Sections 4.4.31 to 4.4.3.3). The main difference was the experimental techniques employed in measuring skin deformation *in vivo*, where chapter 4 employed the MA techniques while the current chapter employed DIC techniques. Based on the experimental data generated employing the DIC techniques, the current chapter determined the skin properties using the same optimisation procedure as described in the previous chapter. Therefore, similar to the previous chapter, the current study produced a variety of outputs and brought up several issues to discuss.

The results presented in Tables 5.1 to 5.5 proves that the current study has successfully adapted the DIC techniques and inverse FEA to determine the hyperelastic material parameters of skin for two subjects (Subject 2 and 4). Basically, it is found that the errors in all cases are smaller than the previous Chapter (which combined MA – FEA), which show that the current solution has converged better. There are two possible reasons to cause this. One is due to the main FE programme itself where it is originally developed for the DIC input data. The data (displacement distribution) generated by MA experiments was not as dense as the DIC data. Therefore, the interface programme which was written to read and interpolate the displacement distribution from the MA experiments would have initially produced errors at interventional stage even before conducting the inverse FEA. The error then propagated during simulation. The second reason possibly due to the peak (maximum displacements at the load point) of the contour generated by the MA was higher than the DIC experiments. The original data (displacement contour) generated by the DIC experiments (Figures 5.4 to 5.6) clearly shows that the data surrounding the load point

could not be traced. This loss affected the calculation (interpolation) of displacement at the affected area (load point) and thus producing a lower value than expected. This can be visualised clearly in Figure 5.8 where the simulated peak of the deformation contour is lower than the measured data.

Despite the results converged better, Figure 5.8 shows a similar shape of displacements distribution (measured and simulated) compared to the previous chapter (MA experiments). A similar shape of simulated skin deformation is observed for both experimental techniques (DIC and MA) and thus confirming the consistency of the inverse FEA output. The slope of the deformed shape (simulation) at the midline is found in a more linearly shape than the measured data, which as described in Section 4.5.13 (Chapter 4) was due to the FE model itself as it considered only the first order of Ogden's constitutive equation ($N=1$).

The main achievement in the current study is to come up with a single parameter set that could describe skin properties of the two subjects. Unlike in the previous chapter, the proposed best and averaged parameters in the current chapter are very close to each other (Figure 5.12 and 5.13). Again, this is caused by the better convergence of the current solution compared to the previous chapter and thus confirming that the current work has produced more consistent results.

As an additional analysis, the current chapter introduces a stress-stretch relation (Equation 5.1) that includes a prestretch term. The result of the parametric study is presented in Figure 5.11. By adding the prestretch term, the curves shifted to the left compared to the previous chapter. This reveals that prestretch increases skin stiffness. Therefore, it is found that prestretch is a significant parameter in defining skin properties and should not be ignored when plotting the stress-stretch diagram.

Moreover, as shown in Figure 5.11, the stress-stretch diagram is very sensitive to the change of prestretch value. As described in Section 5.6.2, a 0.1 unit difference in λ_p ($\Delta\lambda_p = 0.1$) produced a larger effect than a 10 unit difference in μ ($\Delta\mu = 10$ Pa) and 4 unit difference in α ($\Delta\alpha = 4$).

However, including the prestretch effect increases the complexity in the analysis. By adding the prestretch term, the non-uniqueness of the current optimisation solution becomes more significant as now it needs to consider three parameters for optimal solution. Figure 5.11 reveals that the solution that can fit into one stress-strain curve is not unique. Compared to the previous chapter, the current study; which included an additional parameter (prestretch), produced a more variety of parameter sets that could match the experimental data. Moreover, skin prestretch is a measured quantity and its actual value is always not easy to measure using *in vivo* experiments. Therefore, it proves that the current study is useful and significant in determining skin properties as it includes the prestretch effect.

Finally, the current chapter compared the optimised hyperelastic material parameters of skin for two subjects determined from MA and DIC techniques. As discussed in Section 5.6.3.3 (Figures 5.14 to 4.17), the results show that the optimum parameters determined for Subject 2 in all directions (X=0°, 45° and X=90°) using both techniques (MA and DIC) are close to each other. However, for Subject 4, the results are only similar in the X=0° direction. At X=90°, the optimum parameter set determined from the MA experiments deviates from others. The skin deformation at X=45° was not measured.

It is interesting to find that the results for both subjects at X=0° are very similar to the skin parameter determined by Evans and Holt (2009) thus confirming that the current

approach has produced very reliable results when load was applied in the X=0° (along crease-to-crease) direction.

5.8 Conclusion

The objective to determine the mechanical properties of human skin by employing the DIC techniques combined with an inverse FEA with an optimisation procedure has been achieved successfully for two subjects (Subject 2 and Subject 4). Based on the results, the hyperelastic material parameters for Subject 2 were approximated to be μ = 10.39 Pa, α = 26.61, λ_p = 0.21; μ = 11.36 Pa, α = 30.52, λ_p = 0.20 and μ = 10.88 Pa, α = 30.52, λ_p = 0.22 at X = 0, 45° and X=90° respectively. The hyperelastic material parameters for Subject 4 were approximated to be μ = 9.64 Pa, α = 28.18, λ_p = 0.27and μ = 10.43 Pa, α = 31.96, λ_p = 0.15 at X=0° and X=90° respectively. The current study also found out that skin stretch is an important parameter in describing skin properties. Finally, the results prove that the current approach has provided a reliable results especially when measuring skin properties in the X=0° direction.

The outcome of the current study highlights the success of replicating the experimental protocol described in Section 2.5 (Chapter 2) and producing outputs comparable to Section 4.5 (Chapter 4). The success of the work conducted in attempt to compare results for the same subjects utilising the combination of MA-FEA and DIC-FEA provides a significant contribution towards demonstrating a powerful integration of experiment-computational approach. Moreover, the results from both techniques are close to each other which indicate the success of this study in determining the mechanical properties of human skin *in vivo*.

The subsequent chapter provides the overall discussions on the work conducted throughout this thesis. It reviews all the experimental techniques employed and the computational work carried out in this study. Finally, it highlights the all the major findings deduced from each chapter.

CHAPTER 6

DISCUSSION

6.1 Introduction

Chapters 2 to 5 have described the work carried out in determining the mechanical properties of human skin using two experimental techniques and two computational applications. Skin deformation for human subjects has been measured *in vivo* using MA (Chapter 2) and DIC techniques (Chapter 5). The data generated by the MA experiments was used to determine skin properties using Abaqus (Chapter 3) and also a FE programme with an optimisation procedure (Chapter 4). The FE programme was once again used to determine skin properties from the experimental data generated by the DIC experiments (Chapter 5).

This chapter attempts to provide an overall discussion of the work conducted throughout this study and reported in this thesis. It reviews the experimental techniques employed and the computational (FE modelling and simulation) work carried out for this study. It highlights the major findings and scientific achievements of the study. It is hoped that this chapter will provide sufficient information for others who wish to adapt and apply these techniques to their research work.

6.2 Experimental techniques

The ultimate aim of this thesis and study has been to determine the mechanical properties of human skin. To achieve this, a protocol was defined to measure human skin deformation accurately, *in vivo*. The outcome of this was the development of a

novel experimental protocol employing the MA techniques (Chapter 2). As an alternative, the DIC technique was adapted to replicate the same protocol (Chapter 5). Table 6.1 provides brief information about the system set up for both experimental techniques employed in this study.

Table 6.1: Equipment and system set up

Technique	MA	DIC
Camera type	Infra red camera	Digital camera
No. of camera	3	2
Calibration tool	Calibration frame	Calibration target
Marker	Reflective stickers	Speckles
No. of markers	41	Thousands
System software	QTM	VicSnap and Vic3D

Table 6.1 shows that the MA system required more cameras than the DIC system to capture the same field of view for this study. However, using many cameras (as commonly practised in a human gait analysis) makes MA techniques more versatile in capturing 3D motions.

6.2.1 System set up and preparation

During implementing the current experimental protocol, setting up the MA system was found to be more time consuming and tedious than the DIC system. Using more cameras means more time was taken for setting up the camera system e.g. connecting cables; and adjusting its aperture and focus. The main challenge was to speed up the process of placing 41 reflective small diamond markers onto the subjects' forearm. Moreover, they should be placed in a consistent pattern (optimum configuration). In contrast, the DIC speckles were easier to apply onto the forearm.

Furthermore, they are applied in a random pattern, which need no careful attention. By using a sponge and a toothbrush, the speckles can be applied with the black theatrical face paint within 3-8 minutes. To clean them, it needs just a simple wash using soap and water. For the MA system, originally, it took more than a half hour to place all the 41 markers onto the subjects' skin. However, using the designed template (patch), the duration was reduced to 10 minutes. Despite that, the preparation of the patch itself took about 20 minutes.

6.2.2 System Calibration

Another significant procedure prior to conducting the *in vivo* tests on subjects was its system calibration. For every test sessions, when the cameras have been placed according to their optimum angle and position, the system must be calibrated. The static calibration procedure for the MA system was found easier than the DIC system. By positioning statically a calibration frame in the field of view (target), a capture of images for 10 seconds would produce the calibration result and define its 3D space. If the result was found to be unsatisfactory, a minor adjustment to the cameras' aperture and focus usually would improve the calibration results. Sometimes, a minor adjustment of calibration frame adjustment would solve the problem. In contrast, for DIC system, a capture of 12 to 16 images of a calibration target was recommended for its system calibration. Then, each image needs to be adjusted until it produces a very good contrast so that the system could extract the positions of the target. From this information, the system will define its 3D space. Even though there was an option for importing calibration information from previous analysis, it was not recommended to do so. In term of duration (in average), the calibration procedure took 10 and 20 minutes for MA and DIC systems respectively. It could be claimed that the calibration procedure for the DIC system requires more skill than the MA system.

6.2.3 Ambience effect

Both systems are made of optical small scale measurement tools and therefore, their performance was very much based on the quality of the images they produced. Therefore, the ambience and background colour of the venue were controlled during tests. For DIC systems, the background was ensured contrast (light coloured and no dot patterns) compared to the speckles (black). Additional lighting was used to illuminate up the calibration space. For the MA system, a reflective background was avoided as the system would register any reflective surfaces as a marker.

6.2.4 Data processing

Another important feature to compare between these two techniques is the processing of images to produce output. Each system provides its own software in producing the outputs. MA system provides a software (QTM) that is used to track the trajectories of markers in the defined 3D space. This has been described in Chapter 2. The output would be the 3D coordinates of each marker (42) for a sequence of image capture and written into a text file. The DIC system provides a software (Vic3D) that is used to calculate 3D displacements (and/or strains) using its correlation algorithm for a selection of surface area. In the current study, the distribution of displacements was recorded for about 10,000 data points (min: 7,600 and max: 13,500 data points). For one image, this information is written into one text file. Therefore, a capture consisting 50 images will produced a set of 50 text files. This has made the analysis of the images to be very slow compared to the current MA system.

6.3 Finite Element Simulations

To determine the mechanical properties from the data generated from the experiments, the current study has conducted FE simulations using two different applications that are Abaqus and Matlab. In this study, the process of modelling skin using a FE software (Abaqus) was found to be very much easier than writing a FE programme to model skin using Matlab. This was because the software provides a menu for a choice of geometry, element types, material, load types and boundary applications. Moreover, the user interface provides graphics to visualise the model and outputs instantly. In most cases, heavy mathematical formulation could be avoided and the computational procedure could be ignored. However, for a complicated model such as a hyperelastic material which demonstrates highly nonlinear deformation, the solution would be very difficult to control without knowing clearly all the computation parameters. The other setback found in this study was the unavailability of an optimisation procedure in the software that can automatically optimise the material parameters to match with the deformation data. Therefore, the FE programme developed by Evans (2009) has been adapted in this study to overcome these limitations. The optimisation procedure was found very useful and in some cases has successfully generated results with a very good accuracy.

6.4 The outputs

This section presents the sample outputs from each chapter to highlight the success of the current study in producing comparable results via integrating experiments (MA and DIC) and computational applications (Abaqus and Matlab). The outputs (Figures 6.1 to 6.4) could reveal the capabilities of each technique. The current study therefore, for the first time, compares side-by-side the outputs and assesses the capabilities of the (i) MA technique, (ii) DIC technique, (iii) FE simulation using Abaqus; and (iv) FE

simulation using Matlab in the attempt to determine the mechanical properties of human skin *in vivo*.

Figure 6.1 shows the preset test area of skin at the forearm and the outputs representing its deformation (axial displacement) using the various techniques. QTM software provides the information by showing the 3D movement of the markers, while Vic3D shows the axial displacements in a 2D and 3D contour. The test area was modelled in 3D (and 2D) using Abaqus and similar to Vic3D, it shows the axial displacements in a 3D (and 2D) contour. A programme was written using Matlab to import the raw experimental data (3D markers coordinate) from QTM and could be visualised as shown in Figures 6.1d and 6.1h. It could be observed that the MA techniques provide less data poins, however, the location of each data point is very clear. In contrary, the DIC techniques provide a full field displacement data; however, loss of data occurred at the area around the loading tab and wrinkle. Moreover, some data may also lose along the load direction where the nylon filament shadowed the speckles beneath it. This might effects the accuracy of the information at the related area. Abaqus offers the facility to probe a value (displacement data) at nodal points; however, this deformation is dependant on the correct material parameters and accurate modelling. This justifies the need to use a FE programme. Moreover, the Matlab output (Figures 6.1d and 6.1h) proves that the data is ready for further analysis and/or inverse FEA.

Initial state	Displacement data
MA Technique (Chapter 2)	QTM output
(a) Initial position of markers	(e) Displaced markers
DIC Technique (Chapter 5)	Vic3D output
(b) Initial speckle pattern	(f) Skin displacement (axial) contour (2D)
Abaqus (Chapter 3)	Abaqus output
(c) Skin Model (3D FE)	(g) Skin displacement (axial) contour (2D)
Matlab (Chapter 4)	Matlab output
(d) Initial position of markers (as in (a))	(h) Displaced markers (as in (e))

Figure 6.1: The comparison of outputs representing skin deformation (axial displacement) for various techniques.
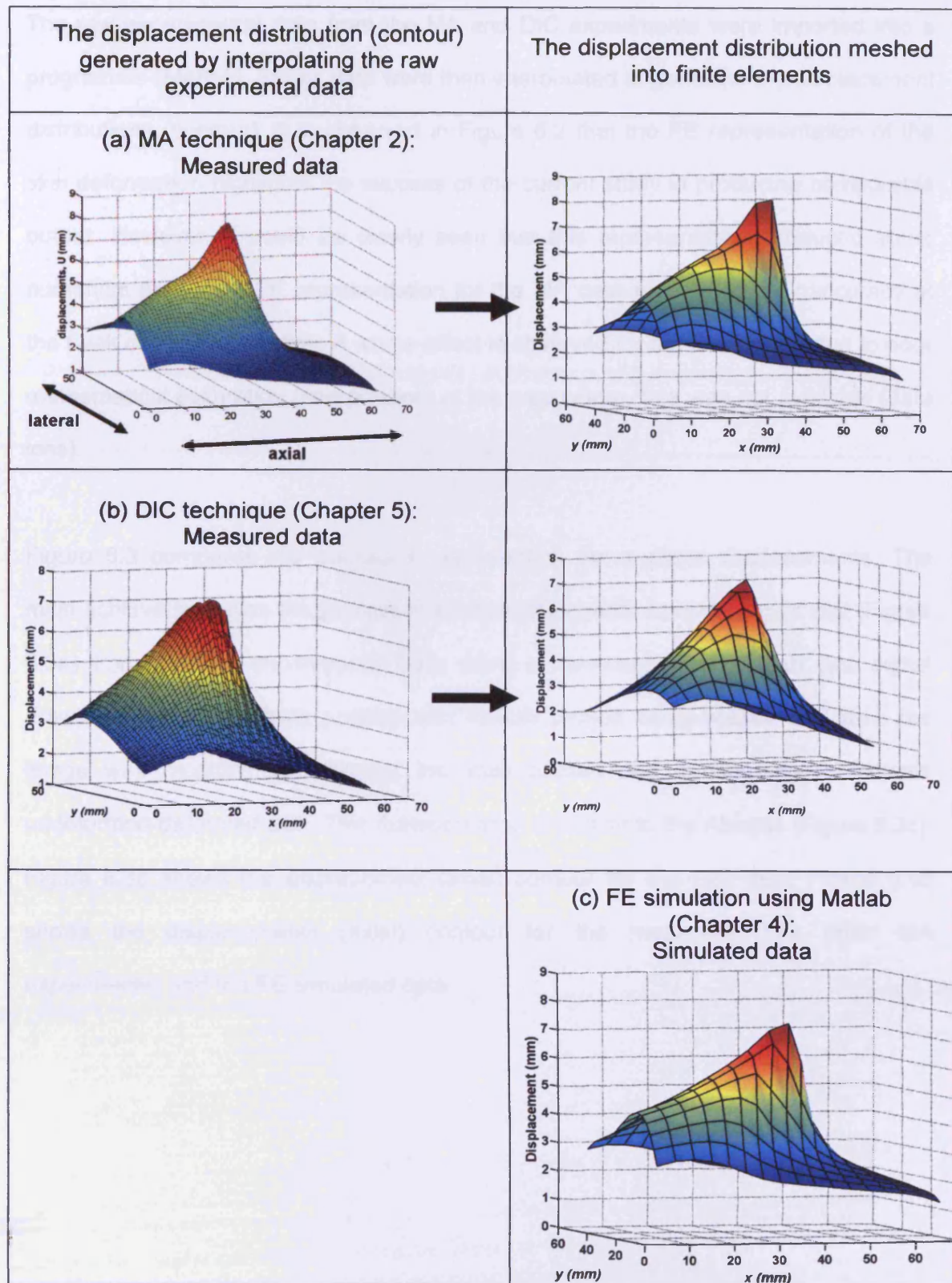
Figure 6.2: The comparison of outputs representing the measured data using finite elements for (a) MA techniques, (b) DIC techniques and (c) simulated data using the inverse FEA (Matlab).

The raw experimental data from the MA and DIC experiments were imported into a programme (Matlab). These data were then interpolated to generate the displacement distributions (contour). It is observed in Figure 6.2 that the FE representation of the skin deformation highlights the success of the current study in producing comparable output. However, it could be clearly seen that this representation produced some numerical area. The FE representation for the MA data reveals some inaccuracy at the peak of the deformation. A worse effect is observed for the DIC output due to poor mathematical estimation (interpolation) at the area where data was not available (data loss).

Figure 6.3 compares the outputs in representing the in-plane displacements. The main achievement was the success to produce the undeformed-deformed plot (Figure 6.3a) from the MA experimental data using a combination of Matlab and digital drawing. The 2D markers position was initially plotted using Matlab and then the image was modified by inserting the lines (dotted and continuous) to indicate undeformed-deformed skin. This representation is similar to the Abaqus (Figure 6.3c). Figure 6.3b shows the displacement (axial) contour for the DIC data. Figure 6.4b shows the displacements (axial) contour for the measured data (from MA experiments) and the FE simulated data.

(a) The markers displacement data imported from QTM and its 2D visualisation (Matlab + digital drawing) and interpolated into 2D contour (Matlab)

(b) The displacement (axial) 2D contour (Vic3D)

(c) The in-plane displacement (Abaqus)

(d) The measured and simulated displacements 2D contour (Matlab)
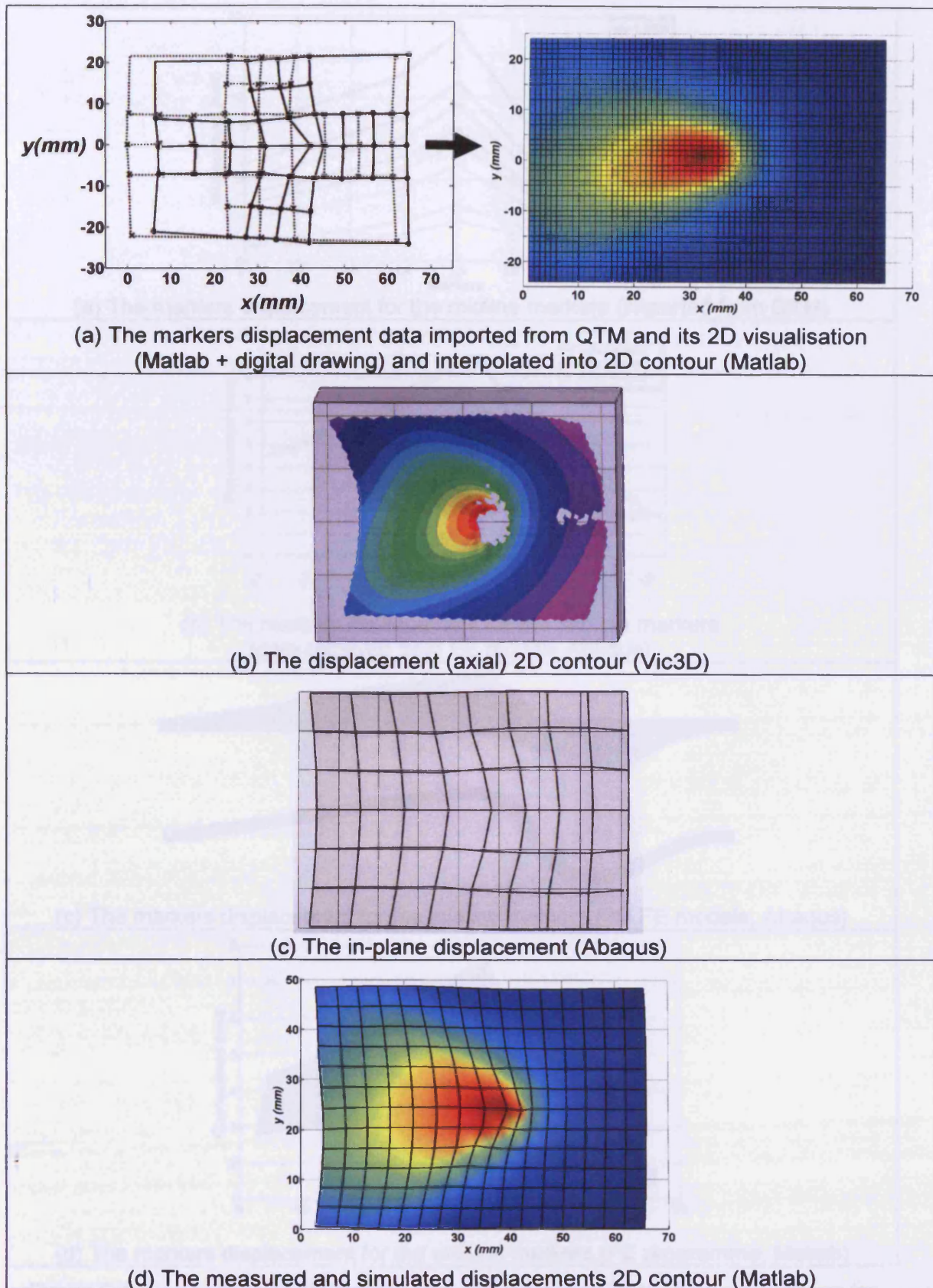
Figure 6.3: Comparison of 2D outputs representing the in-plane displacement (axial) for various techniques.
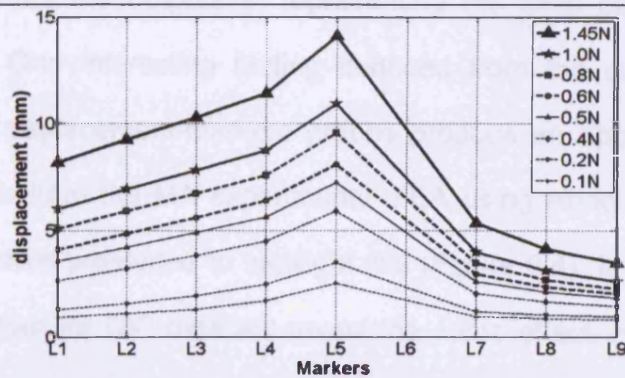
(a) The markers displacement for the midline markers (imported from QTM)
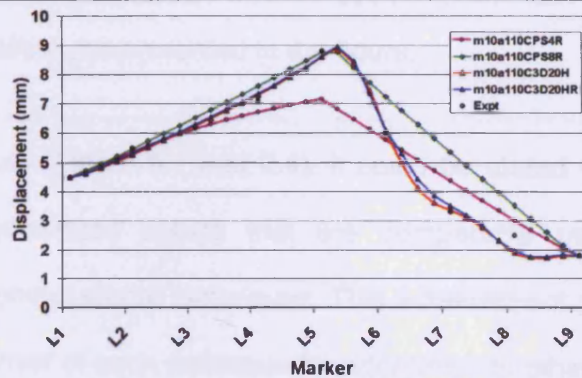
(b) The markers displacement for the midline markers
(data retrieved from FE models Abaqus)
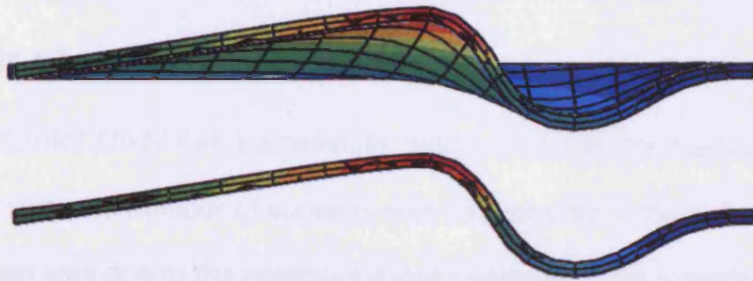
(c) The markers displacement for the midline markers (3D FE models, Abaqus)
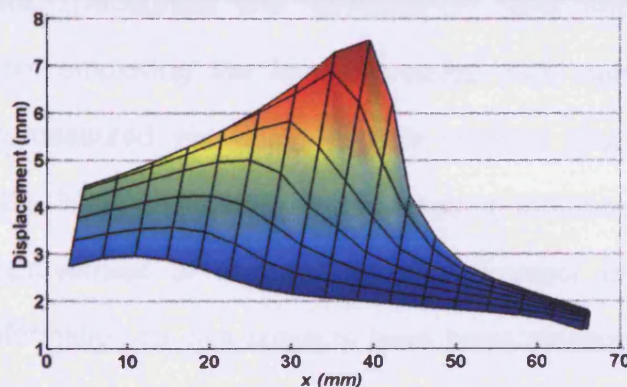
(d) The markers displacement for the midline markers (FE programme, Matlab)

Figure 6.4: Comparison of 2D outputs showing the approximate *bow wave* shape for various techniques.

Figure 6.3 compares the outputs in representing the axial displacements for the midline markers. One interesting finding deduced from the current study was to observe that the displacement-markers graphs produce an approximate *bow wave* shape. The results from the MA experiments, FEA using Abaqus (2D and 3D) and Matlab were therefore presented to highlight this (Figure 6.4). It is predicted that the displacement contour for DIC data will reveal the same effect. However, the loss of data at the loading tab and along the loading direction would surely provide a poor estimation and therefore not presented in the figure.

Based on the outputs (Figure 6.1 and 6.4), it could be stated that the current study has successfully generated results that are comparable using combinations of experimental and computational techniques. This achievement provides an easy way to evaluate the potential of each technique for adaptation to other applications.

6.5 Number of subjects

Although the current study has successfully determined the mechanical properties of human skin *in vivo*, the number of subjects was not consistent throughout the studies. The main reason was due to the continuous improvement of the experimental protocol and time constraint. Throughout the development and improvement of the experimental protocol employing the MA techniques, skin deformation for eight subjects have been measured. However, only five subjects (Subjects 1 to 5) have been tested using the final configuration for the loading direction at $X=0°$ and $90°$. Throughout the improvement of the experimental protocol employing the DIC techniques, skin deformation for five subjects have been measured. However, only two subjects (Subjects 2 and 4) were the same subjects which have been tested using the MA techniques. This was due to time constraint and the availability of the same subjects (Subjects 1, 3 and 5).

It should be reminded that the study currently focused on developing a novel experimental protocol to determine skin properties rather than investigating skin properties for a large sample. However, since the current study has successfully developed a practical and useful tool, it is recommended for others to use the tool for measuring and investigating skin properties for a larger sample (different ages and gender) in the future.

6.6 Applications

A novel technique has been developed to measure skin deformation employing the MA techniques. Combining it with inverse FEA (Abaqus and Matlab), the mechanical properties of skin have been determined. The current study has also adapted and demonstrated the success of combining DIC techniques and inverse FEA to replicate the similar experimental procedure. All this has highlighted the capability of combining experimental and computational approaches to become a powerful research tool.

Apart from measuring skin deformation and properties, the achievement of the current study will open up many possibilities in a wide area of research and provides a valuable tool to measure the deformation of biological and engineering structures. Its combination with the inverse FEA could be explored further to be used in determining the mechanical properties of other biological system or engineering materials.

6.7 Scientific achievements

1. A novel technique to measure human skin deformation *in vivo* has been developed employing the MA techniques. In addition, two calibration frames have constructed and currently being used for small scale measurement. A marker patch has been designed and found helpful for placing the markers onto human skin.

2. The mechanical properties of human skin have been determined and they were found close to skin properties determined by Evans and Holt (2009). This was achieved by adapting a FE programme developed by Evans (2009) into this study.

3. DIC technique has been employed as an alternative approach to replicate the experimental procedure and determine skin deformation.

4. 2D and 3D FE models have been developed using Abaqus to simulate skin deformation according to the experimental procedure.

5. A parametric study has been conducted to observe the effect of the hyperelastic material parameters and the results reveal that prestretch is an important parameter in portraying skin behaviour.

6. The development and outcomes of this study have been presented at several conferences and generated five publications.

   - A paper has been accepted for publication in the Journal of Biomechanics (Mahmud et al 2009a).

   - A journal paper has been revised and resubmitted to the Computer Methods in Biomechanics and Biomedical Engineering for review (Mahmud et al 2009b).

- A paper has been published in the proceedings of the 8th International Symposium on Computer Methods in Biomechanics and Biomedical Engineering, CMBBE2008, Porto, Portugal, ISBN:978-0-9562121-0-8 (Mahmud et al 2009c).

- Four papers have been presented in difference conference proceedings. They were: IMechE Medicine and Health Division Meeting, 15 October 2009 (Invited paper, Mahmud et al 2009d), 10th International Sysmposium on 3D analysis of human movement, (ISB-3DMA2008), Santpoort-Amsterdam, The Netherlands, October 2008 (Mahmud et al 2008, Lovern et al 2008), 2nd International Conference on Mechanics of Biomaterials and Tissues, Hawaii 2007 (Evans et al 2007).

- Two papers have been accepted and will be presented in different conferences. They are: 3rd International Conference on Mechanics of Biomaterials and Tissues, Florida USA December 2009 (Mahmud et al 2009e) and the 9th International Symposium on Computer Methods in Biomechanics and Biomedical Engineering, CMBBE2010, Valencia Spain, Portugal, February 2010 (Mahmud et al 2009f).

7. The tools and techniques developed in and experience gain from the current study has a direct contribution to other work, such as:

  - measuring the deformation of an artificial spider web (MA techniques)

  - analysing facial expressions (MA techniques)

  - measuring tooth movement (MA techniques, Delobelle 2008)

  - measuring scapula movement during shoulder motion (DIC techniques, Lovern et al 2008)

CHAPTER 7

CONCLUSIONS AND FURTHER WORK

7.1 Conclusions

The ultimate aim of the current study and thesis has been to determine the mechanical properties of human skin. The studies described in this thesis have contributed towards fulfilling this aim. Undoubtedly, the complex behaviour of skin has made this study a very challenging one. However, the journey to complete it has been very exciting.

Throughout the studies, two experimental techniques have been employed to measure skin deformation *in vivo* and the inverse FEA have been applied using two different applications (Abaqus and Matlab) in attempt to determine the skin properties from the experimental data. These techniques and applications together with their outcomes have been discussed in detail in the previous chapter. This chapter discusses the conclusions specific to each of the key objectives outlined in Chapter 1.

Objective 1: Development of a novel technique in measuring skin deformation *in vivo* employing MA

As highlighted in Chapter 2, this objective has been achieved successfully. A novel experimental protocol employing the MA techniques has been developed to measure human skin deformation *in vivo*. The experimental set up was confirmed optimum and calibration results proved that the measurement system was accurate. The results

proved that the experimental protocol was practical, reliable, repeatable and non-invasive (Mahmud et al 2009a). Throughout the study, two new useful calibration frames have been constructed and now being used for small scale calibration using motion capture system. In addition, the study has also led to the design and fabrication of an innovative template (patch) used to place reflective markers efficiently and consistently onto human skin.

The outputs from the experiments have been demonstrated (in Chapter 4) to be useful and input-ready for an inverse FEA in determining the hyperelastic material parameters of human skin. Furthermore, the experiments also demonstrated skin viscoelasticity and anisotropy that has produced significant data which could be used to further investigate these characteristics in the future.

As traditionally, motion analysis techniques have been used to study the kinematics of a moving body/system, the success of the current work has highlighted the potential to use them as a full-field small scale deformation measurement tool. This achievement would be the major contribution for the current study and has certainly enhanced the knowledge on measuring human skin *in vivo*.

Objective 2: Development of FE models to simulate skin deformation

A basic approach to determine the mechanical properties of skin is by developing its FE model and simulating its deformation using a FE software. The material parameters used to simulate skin deformation that match to the measured data (Chapter 2) constitute the skin properties. However, simulating a hyperelastic material is always challenging as the finite elements will distort excessively and therefore, the solution will unlikely converge.

The current study has successfully developed FE models and simulated skin deformation according to the experimental procedure (Chapter 2). This has been achieved by conducting systematically 9 case studies to produce a variety of FE models using different element types, mesh sizes, load types and Ogden's parameters.

The result was not in good agreement with other approaches (Chapters 4 and 5). Nevertheless, the thorough study conducted and work reported in this thesis (Chapter 3) would be a significant contribution to the engineering community in simulating a nonlinear hyperelasticity, which the problem has always been very challenging. The tediousness of the methodology has been addressed and recommendation was made to use an inverse FE programme with an optimisation procedure.

Objective 3: Adaptation of a FE programme with an optimisation procedure to determine skin material parameters

An FE programme with an optimisation procedure has been developed by Evans (2009) to determine skin material parameters for experimentation employing a DIC technique. The current study has successfully adapted this programme to determine skin properties from the data generated using the MA techniques. The skin hyperelastic material parameters (mean ± SD) for five subjects have been presented in Chapter 4 and several results were found to be close to skin properties determined by Evans and Holt (2009). The results that produced large error have been discussed and a few recommendations are suggested for future work (Chapter 4). In addition, a programme to read and input the measured data (from the MA experiments) into the main FE programme has successfully been developed.

This study highlights for the first time the success of combining MA experiments and inverse FEA in determining the hyperelastic material parameters for human subjects *in vivo*. This combination produces a powerful tool and has a great potential which can be developed further for other applications; from measuring small scale motion of biological systems till determining the associated mechanical properties.

Therefore, the objective to adapt an FE programme with an optimisation procedure to determine skin material parameters has been achieved. Moreover, this achievement has fulfilled the ultimate aim of this study to determine the mechanical properties of human skin. It significantly contributed to enhancing the knowledge about skin behaviour.

Objective 4: Using the DIC techniques to measure skin deformation *in vivo*

Employing the DIC techniques (Chapter 5) combined with an inverse FEA (Chapter 4), the mechanical properties for two subjects have been determined. The results were found very close to the results obtained using MA experiments. This highlights the success of replicating the experimental protocol employing the MA techniques as described in Section 2.5 (Chapter 2); and producing comparable outputs to the Section 4.5 (MA-FEA, Chapter 4). Therefore, the objective to develop a similar experimental procedure as described in Chapter 2 employing the DIC techniques has been fulfilled successfully. In addition, the study has also included the prestretch term into the relation of stress and stretch. The results of the parametric study prove that skin prestretch is an important parameter to consider when studying skin behaviour.

Replicating the experimental procedure as described in Chapter 2 is a success and the work reported provides a significant contribution to adding knowledge on measuring skin deformation *in vivo*.

Objective 5:   Investigation of skin deformation and properties for all subjects

Using load-displacement diagrams, the skin deformation for five subjects has been compared in Chapter 2. In addition, the displacements ratio has been measured for each subject to investigate skin behaviour at different load directions. This achievement fulfils the objective to investigate skin deformation.

Using stress-stretch diagrams, Chapter 4 has compared the skin properties for five subjects determined from the MA experiments. Chapter 5 compared the skin properties for two subjects determined from the DIC experiments using the stress-stretch diagrams that included the prestretch term. These achievements fulfil the objective to investigate the skin properties for all tested subjects.

However, due to the limited number of subjects, a significant trend of skin behaviour could not be found clearly. Despite that, the results show prestretch increases skin stiffness. This study produced the initial findings of skin behaviour for five subjects with different age and gender. The variations in results for each subject suggested the effect of skin anisotropy and further study is recommended to better understand this behaviour.

Objective 6: Comparison of experimental and computational techniques employed in the current study

The final achievement of this study is the success in combining experimental techniques (MA and DIC) with computational applications (Abaqus and Matlab), which in all cases have produced outputs that could be compared directly. Moreover, several results were found supporting each other. It highlights the success in determining the hyperelastic material properties for human skin in the $X=0°$ direction using both combinations (MA-FEA and DIC-FEA). It demonstrated the novelty of the

current study in integrating the experiment-computational approaches to produce a powerful tool in measuring skin properties.

The comparison and discussion on the experimental and computational techniques employed in the current study could provide a variety of choices in employing those techniques for other applications. The current study intends to provide useful information for other researchers who keen to adapt relevant technique for their research work. This would be a significant contribution to the research community.

7.2 Further Work

This study has highlighted and provoked several potential areas for improvement and further investigations that could be carried out in the future.

1. Although the MA experiments have produced sufficiently accurate results for this study, it set up could be improved by minimising the system residual further. Furthermore, the marker configuration was optimum for the current study. However, it could be improved further for other applications. By putting more markers, it could increase the system's resolution.

2. As demonstrated by the DIC experiments, data loss occurred at the loading tab, its surrounding area and at the wrinkles. Further studies could be carried out to investigate and overcome this phenomenon.

3. The current experimental protocol has been demonstrated to be useful for a clinical setting. Further studies could be carried out to develop a more comfortable seat for the subjects during testing. The posture during

experiments could also be investigated. An attachment could also be developed and constructed to avoid unnecessary arm movement during testing. Other than that, a proper loading method and device that could control the loading rate and direction should also be developed. This is important to produce results with higher reliability.

4. This study has demonstrated the ability of the current approach in determining the skin properties for a few subjects. It would be interesting and useful to investigate the trend of skin behaviour between gender (male and female subjects) and age (young and old subjects). This can be achieved by increasing the number of subjects/cohort from various age and different gender. The preliminary result shown in Table 2.5 (Section 2.7.1.3, Chapter 2) suggests that this study could be used to investigate the underlying tissue of skin (muscle/fat ratio).

5. This study has determined skin properties at the subjects' forearm. A similar approach can be used to determine skin properties at different part of human body, e.g. face, abdomen, thigh and feet. The information might be useful for cosmetologist and surgeons.

6. Apart from that, the current approach could also be used to investigate and compare abnormal to normal skin. The presence of scars on the skin would change the properties of skin. Therefore, a study to investigate its mechanical properties would explain the behaviour of the scar itself or the skin surrounding it.

7. During experiments, although the wrinkling effect could be seen clearly, the current study did not investigate this phenomenon. Therefore, it would be useful to carry out an investigation on skin wrinkling and it effects to the skin properties, or vice versa. The knowledge of this might be useful to prevent wrinkles.

8. The work on skin modelling could also be improved further. As the current study highlights, the use of a 3D skin model would be more accurate and consistent. Therefore, further work could be done to establish an accurate 3D skin model. The output would be useful in simulating skin deformation during surgery.

9. In this study, skin was model as a hyperelastic material based on the first order (N=1) Ogden's strain energy potential. It would be interesting to consider a higher term (N>1) in the future work. The model could also be improved by modelling skin as a multiple layer.

10. Apart from using Ogden's model, several other hyperelastic models could also be used. Therefore, it would be interesting to determine skin properties using different hyperelastic model, e.g. Mooney-Rivlin for comparison.

11. Moreover, the data generated from the MA experiments shows that it could be used to investigate the viscoelastic and anisotropic behaviour of human skin. Therefore, a further study could be conducted by modelling skin as a viscoelastic or anisotropic material, which would be much more complicated than the current model.

This thesis has described studies which determine the mechanical properties of human skin *in vivo*. This has led to several avenues of further investigation and recommendations for its development, so that in future it may be used for other applications (surgery, product design, clinical) and understanding better the behaviour of skin.

Finally, since there is still no constitutive equation specifically developed for human skin, the knowledge and data contributed by this study will be used to develop a constitutive equation that could describe skin viscoelastic and anisotropic behaviour accurately.

REFERENCES

Agache PG, Monneur C, Leveque JL, de Rigal J. 1980. Mechanical properties and young's modulus of human skin *in vivo*. Arc Dermatological Research. 269(3):221-232.

Alexander H, Cook TH. 1977. Accounting for natural tension in the mechanical testing of human skin. Journal of Investigative Dermatology. 69(3):310-314.

Andriacchi TP, Alexander EJ. 2000. Studies of human locomotion: past, present and future. Journal of Biomechanics. 33(10): 1217-1224.

Arruda EM, Boyce MC. 1993. A three-dimensional constitutive model for the large stretch behavior of rubber elastic materials," Journal of the Mechanics and Physics of Solids. 41(2):389–412.

Bader DL, Bowker P. 1983. Mechanical characteristics of skin and underlying tissues *in vivo*. Biomaterials. 4(4):305-308.

Basar, Y. and Itskov, M. 1998. Finite element formulation of Ogden material model with application to rubber-like shells. International Journal for Numerical Methods in Engineering. 42:1279-1305.

Bathe K-J. 1996. Finite Element Procedures. Prentice-Hall, Inc. USA.

Bischoff JE, Arruda EM, Grosh K. 2000. Finite element modelling of human skin using an isotropic, nonlinear elastic constitutive model. Journal of Biomechanics. 33(6): 645-791.

Bischoff JE, Arruda EM, Grosh K. 2002. A microstructurally based orthotropic hyperelastic constitutive law. Transaction of ASME. 69:570-579.

Bosboom EMH, Hesselink MKC, Oomens CWJ, Bouten CVC, Drost MR, Baaijens FPT. 2001. Passive transverse mechanical properties of skeletal muscle under *in vivo* compression. Journal of Biomechanics. 34:1365-1368.

Brown CP, Nguyen TC, Moody HR, Crawford RW, Oloyede A. 2009. Assessment of common hyperelastic constitutive equations for describing normal and osteoarthritic articular cartilage. Proceedings of IMechE Part H: Engineering in Medicine 223:643-651.

Burlin TE, Hutton WC, Ranu, HS. 1977. A method of *in vivo* measurement of the elastic properties of skin in radiotherapy patients. Journal of Investigative Dermatology. 69(3): 321-323.

Cappozzo A, Catani F, Della Croce U, Leardini A. 1995. Position and orientation in space of bones during movement: anatomical frame definition and determination. Clinical Biomechanics. 10(4):171-178.

Carola R, Harley JP, Noback CR, 1992, Human Anatomy, McGraw-Hill Inc., USA.

Chapuis JF, Agache P, 1992. A new technique to study the mechanical properties of collagen lattices. Journal of Biomechanics. 25(1):115-120.

Christensen MS, Hargens CW, Nacht S, Gans EH. 1977. Viscoelastic properties of intact human skin: instrumentation, hydration effects and the contribution of the stratum corneum. Journal of Investigative Dermatology. 69(3):282-286.

Cook T, Alexander H, Cohen M. 1977. Experimental method for determining the 2-dimensional mechanical properties of living human skin. Medical and Biological Engineering and Computing. 159(4):381-390.

Danielson DA. 1973. Human skin as an elastic membrane. Journal of Biomechanics. 6:539-546.

Delalleau A, Josse G, Lagarde JM, Zahouani H, Bergheau JM. 2008. A nonlinear elastic behavior to identify the mechanical properties of human skin *in vivo*. Skin Research and Technology. 14:152-164.

Delobelle V. 2008. Measurement of Tooth Movement. Final Year Project Dissertation. ISIFC, Universite de Franche Comte, France.

Diridollou S, Berson M, Vabre V, Black D, Karlsson B, Auriol F, Gregoire JM, Yvon C, Vaillant L, Gall Y, Patat F. 1998. An *in vivo* method for measuring the mechanical properties of the skin using ultrasound. Ultrasound in Medicine & Biology. 24(2): 215-224.

Dobrev H. 2002. A study of human skin mechanical properties by means of cutometer. Folia Med XILV. Bulgaria. 44:5-10.

Dobrev H. 2005. Application of cutometer area parameters for the study of human skin fatigue. Skin Research and Technology. 11(2):120-122.

Dunn MG, Silver FH, Swann D. 1985. Mechanical analysis of hypertrophic scar tissue:structural basis for apparent increased rigidity. Journal of investigative dermatology. 84(1):9-13.

Dyer R, Zhang H, Moller T. 2007. Delaunay mesh construction. Proceedings of the Eurographics symposium on geometry processing. July 4-6. Barcelona Spain.

Edwards C, Marks R. 1995. Evaluation of biomechanical properties of human skin. Clinics in Dermatology 13: 375-380.

Enderle J, Blanchard S, Bronzino J. 2005, Introduction to Medical Engineering, 2nd edition, Elsevier Academic Press, USA.

Evans SL. 2009. On the implementation of a wrinkling hyperelastic membrane model for skin and other materials. Computer Methods on Biomechanics and Biomedical Engineering 12(3):319-332.

Evans SL, Holt CA. 2009. Measuring the mechanical properties of human skin *in vivo* using digital image correlation and finite element modelling. Journal of Strain Analysis for Engineering Design 44(5):337-345.

Evans SL, Holt CA, Mahmud J, Ozturk H, Saidi K, Shrive NG. 2007. Measuring the mechanical properties of skin using digital image correlation and nonlinear finite element analysis. Proceedings of the 2nd International Conference on Mechanics of Biomaterials and Tissues. December 9th-13th. Hawaii.

Evans SL, Holt CA, Ozturk H, Saidi K, Shrive NG. 2007. Measuring soft tissue properties using DIC and FEM. Proceedings of the 13th International Conference on Experimental Mechanics. 1-6th July. Greece.

Fung YC. 1993. Biomechanics: mechanical properties of living tissue. 2nd ed. Springer-Verlag New York, Inc.

Green M and Nokes L.D.M, 1988, Engineering Theory in Orthopaedics: an introduction', Ellis Horwood Limited, West Sussex, England.

Gruttmann F, Taylor RL. 1992. Theory and finite element formulation of rubberlike membrane shells using principal stretches. International Journal for Numerical Methods in Engineering. 35: 1111-1126.

Guan, E., Smilow, S., Rafailovich, M., and Sokolov, J., 2004. Determining the Mechanical Properties of Rat Skin with Digital Image Speckle Correlation. Dermatology. 208: 112-119.

Guiz MJG, Gonzales LYS. 2006. Comparison of hyperelastic material models in the analysis of fabrics. International Journal of Clothing Science and Technology. 18(5):314-325.

Hager WW, Zhang H. 2005. A new conjugate gradient method with guaranteed descent and an efficient line search. SIAM Review. 16(1):170-192.

Hendriks FM, Brokken D, Van Eemeren JTWM, Oomens CWJ, Baaijens FPT, Horsten JBAM. 2003. A numerical-experimental method to characterize the non-linear behaviour of human skin. Skin Research and Technology. 9(3): 274-283.

Hendriks FM, Brokken D, Oomens CWJ, Baaijens FPT. 2004. Influence of hydration and experimental length scale on the mechanical response of human skin *in vivo*, using optical coherence tomography. Skin Research and Technology. 10:231-241.

Hendriks FM, Brokken D, Oomens CWJ, Bader DL, Baaijens FPT. 2006. The relative contributions of different skin layers to the mechanical behavior of human skin *in vivo* using suction experiments. Medical Engineering and Physics. 28:259–266.

Hibbit, Karlson & Sorenson, Inc. 2000. Getting Started with ABAQUS/Standard. USA.

Highley DR, Coomey M, Denbeste M, Wolfram LJ. 1977. Frictional properties of skin. Journal of Investigative dermatology. 69(3):303-305.

Holzapfel GA. 2000. Nonlinear Solid Mechanics: a continuum approach for engineering. John Wiley and Sons Ltd.

Jacobi U, Chen M, Frankowski, G, Sinkgraven R, Hund M, Rzany B, Sterry W, Lademann J. 2004. *In vivo* determination of skin surface topography using an optical 3D device. Skin Research and Technology. 10(4):207-214.

Jachowicz J, McMullen R, PreetyPaul D. 2007. Indentometric analysis of *in vivo* skin and comparison with artificial skin models. Skin Research and Technology. 13(3):299-309.

Jansen LH, Rottier PB. 1958. Some mechanical properties of human abdominal skin measured on excised strips: a study of their dependence on age and how they are influence by the presence of striae. Dermatologica. 117:65-183.

Jemec GBE, Selvaag E, Ågren M, Wulf HC. 2001. Measurement of the mechanical properties of skin with ballistometer and suction cup. Skin Research and Technology. 7(2):122-126.

Jones L, Holt CA. 2008. An objective tool for assessing the outcome of total knee replacement surgery. Proceedings of Inst Mech Eng [H]. 222(5):647-655.

Khatyr F, Imberdis C, Varchon D, Lagarde J-M, Josse G, 2006. Measurement of the mechanical properties of the skin using the suction test. Skin Research and Technology. 12(1):24-31.

Khatyr F, Imberdis C, Vescovo P, Varchon D, Lagarde J-M. 2004. Model of the viscoelastic behaviour of skin *in vivo* and study of anisotropy. Skin Research and Technology. 10(2):96-103.

Kedgley AE, Birmingham T, Jenkyn TR. 2009. Comparative accuracy of radiostereometric and optical tracking systems. Journal of biomechanics. 42(9): 1350-1354.

Lafrance H, Yahia LH, Germain L, Auger FA. 1998. Mechanical properties of human skin equivalents submitted to cyclic tensile forces. Skin Research and Technology. 4(4):228-236.

Langer K. 1978. On the anatomy and physiology of the skin. II. Skin tension. British Journal of Plastic Surgery. 31: 93–106.

Lanir Y. 1983. Constitutive Equations for Fibrous Connective Tissues. Journal of Biomechanics. 16: 1-12.

Lanir Y, Fung YC. 1974. Two-dimensional mechanical properties of rabbit skin – II. experimental results. Journal of Biomechanics. 7:171-182.

Leveque JL, de Rigal J, Agache PG, Monneur C. 1980. Influence of ageing on the in-vivo extensibility of human skin at a low stress. Archives of Dermatological Research. 269(2):127-135.

Lim KH, Chew CM, Chen PYC, Jeyapalina S, Ho HN, Rappel JK, Lim BH. 2008. New extensometer to measure *in vivo* uniaxial mechanical properties of human skin. Journal of Biomechanics. 41:931-936.

Liu H. 2006. Development of a Novel System to Measure and Calculate Tooth Movements for Studying the Properties of the Periodontal Ligament. PhD thesis, Cardiff University, UK.

Liu H, Holt CA, Evans SL. 2007. Accuracy and repeatability of an optical motion analysis system for measuring small deformations of biological tissues, Journal of Biomechanics. 40(1):210-214.

Lovern B, Stroud L, Mahmud J, Marsden SP, Kontaxis A, Johnson GR, Evans RO, Holt CA, Evans SL. 2008. Using digital image correlation to measure scapula movement during shoulder motion. Proceedings of 3D Motion Analysis Meeting, International Society of Biomechanics (3DMA2008). October. Santpoort-Amsterdam.

Mahmud J, Holt CA, Evans SL. 2008. Small-scale motion analysis techniques for measuring skin deformation properties. Proceedings of 3D Motion Analysis Meeting, International Society of Biomechanics (3DMA2008). October. Santpoort-Amsterdam.

Mahmud J, Holt CA, Evans SL. 2009a. An innovative application of a small scale motion analysis technique to quantify human skin deformation *in vivo*. Journal of Biomechanics. (In press. DOI: 10.1016/j.jbiomech.2009.11.009).

Mahmud J, Evans SL and Holt CA. 2009b. Measuring the strain and mechanical properties of human skin *in vivo* using a motion analysis technique and finite element modelling. Computer Methods on Biomechanics and Biomedical Engineering (Submitted).

Mahmud J, Holt CA, Evans SL. 2009c. A parametric study of the suction test applied to human skin. Proceedings of the 8th Computer Methods in Biomechanics and Biomedical Engineering (CMBBE 2008) Symposium, Porto, Portugal. Arup and Meditech. (ISBN: 978-0-9562121-0-8).

Mahmud J, Evans SL and Holt CA. 2009d. Using Motion Capture and Analysis to Explore the Mechanical Properties of Human Skin In-Vivo. Invited Paper: Measurement and Sensing in Medicine and Health: Capturing Motion and Musculoskeletal Dynamics. IMechE Medicine and Health Division Meeting, 15 October 2009. pp. 43-48.

Mahmud J, Evans SL and Holt CA. 2009e. Measuring skin deformation *in vivo* using a motion capture system. 3rd International Conference on Mechanics of Biomaterials and Tissues, Florida USA, December 2009 (Accepted for poster presentation).

Mahmud J, Holt CA, Evans SL. 2009f. Measuring skin strain distribution *in vivo* using motion capture and finite elements. 9th International Symposium on Computer Methods in Biomechanics and Biomedical Engineering, CMBBE2010, Valencia Spain, Portugal, February 2010. (Accepted for poster presentation).

Moerman KM, Holt CA, Evans SL, Simms CK. 2009. Digital image correlation and finite element modelling as a method to determine mechanical properties of human soft tisuue *in vivo*. Journal of Biomechanics. 42: 1150-1153.

Molinari E, Fato M, Leo GD, Riccardo D, Beltrame F. 2005. Simulation of the biomechanical behavior of the skin in virtual surgical applications by finite element method. IEEE Transactions on Biomedical Engineering 52, 1514-1521.

Nicosia MA. 2007. A theoretical framework to analyze bend testing of soft tissue. Journal of Biomechanical Engineering. 129(1):117-120.

Ogden RW. 1972. Large deformation isotropic elasticity: on the correlation of theory and experiment for incompressible rubberlike solids. Proceedings of Royal Soc London. 326:565-584.

Ogden RW. 1984. Non-linear Elastic Deformation, Ellis Horwood.

Oomens CWJ, Campen DHV, Grootenboer HJ. 1987. A mixture approach to the mechanics of skin. Journal of Biomechanics 20, 877-885.

Payne PA. 1991. Measurement of properties and function of skin. Clinical Physics & Physiological Measurement. 12(2):105-129.

Pierard-Franchimont C, Henry F, Pierard GE. 1997. Mechanical properties of primary anetoderma in a child. Skin Research and Technology. 3(1):81-83.

Prete ZD, Antoniucci S, Hoffman AH, Grigg P, 2004. Viscoelastic properties of skin in Mov-13 and Tsk mice. Journal of Biomechanics. 37(1):1491-1497.

Raposio E, Nordstrom REA, 1998, Biomechanical properties of scalp flaps and their correlations to reconstructive and aesthetic surgery procedures, Skin research and technology 4: 94-98.

Reddy JN, Pandey AK. 1987. A first-ply failure analysis of composite laminates. Computers and Structures 25: 371-393.

Rees D. 2006. Basic Engineering Plasticity - An introduction with engineering and manufacturing applications. Butterworth-Heinemann.

Retel V, Vescovo P, Jacquet E, Trivaudey F, Varchon D, Burtheret A. 2001. Nonlinear model of skin mechanical behaviour analysis with finite element method. Skin Research and Technology. 7(3):152-158.

Ridge MD, Wright V. 1966. Mechanical properties of skin: a bioengineering study of skin structure. Journal of Applied Physiology. 21:1602-1606.

Sanders JE, Garbini JL, Leschen JM, Allen MS, Jorgensen JE. 1997. A bidirectional load applicator for the investigation of skin response to mechanical stress. IEEE Transactions on Biomedical Engineering. 44(4):290-296.

Scanlon VC, Sanders T. 1997. Understanding Human Structure and Function, F.A. Davies Co, USA.

Schlangen LJM, Brokken D, Kemenade PMV. 2003. Correlations between small aperture skin suction parameters: statistical analysis and mechanical model. Skin Research and Technology. 9(2):122-130.

Screen HRC, Evans SL. 2009. Measuring strain distribution in the tendon using confocal microscopy and finite elements. Journal of strain analysis. 44(5):327-335.

Shoemaker PA, Schneider D, Lee MC, Fung YC. 1986. A constitutive model for two-dimensional soft tissues and its application to experimental data. Journal of Biomechanics. 19(9):695-702.

Shergold OA, Fleck NA. 2004. Mechanisms of deep penetration of soft solids, with the application to the injection and wounding of skin. Proc Roy Soc London A. 460(2050):3037-3058.

Shergold OA, Fleck NA. 2005. Experimental investigation into the deep penetration of soft solids by sharp and blunt punches, with application to the piercing of skin. Transaction of ASME. 127:838-848.

Smalls LK, Wickett RR, Visscher MO. 2006. Effect of dermal thickness, tissue composition, and body site on skin biomechanical properties. Skin Research and Technology. 12(1): 43-49.

Taylor DC, Dalton JD, Seaber AV, Garrett WE. 1990. Viscoelastic properties of muscle-tendon units. The biomechanical effects of stretching. The American Journal of Sports Medicine. 18(3):300-309.

Tham LM, Lee HP, Lu C. 2006. Cupping: from a biomechanical perspective. Journal of Biomechanics. 39: 2183-2193.

Tong P, Fung YC. 1976. The stress-strain relationship for the skin. Journal of Biomechanics 9(10), 649-657.

Topliss C, Jackson M, Atkins RM. 2005. Dermal traction on the Ilizarov frame. Injury 36, 194-198.

Tran HV, Charleux F, Rachik M, Ehrlacher A, Ho Ba Tho MC. 2007. *In vivo* characterization of the mechanical properties of human skin derived from MRI and indentation techniques. Computer Methods in Biomechanics and Biomedical Engineering. 10(6): 401-407.

Tsap LV, Goldgof DB, Sarkar S. 1997. Human skin and hand motion analysis from range image sequences using nonlinear FEM. IEEE Nonrigid and Articulated Motion Workshop (in conjunction with IEEE Conference on Computer Vision and Pattern Recognition CVPR'97), San Juan, Puerto Rico.

Tsap LV, Goldgof DB, Sarkar S. 2000. Nonrigid motion analysis based on dynamic refinement of finite element models. IEEE Transactions on Pattern Analysis and Machine Intelligence 22, 526-543.

Wan Abas WAB. 1994. Biaxial tension test of human skin *in vivo*. Bio-Medical Materials and Engineering 4(7): 473-486.

Wan Abas WAB, Barbenel JC. 1982. Uniaxial tension test of human skin *in vivo*. Journal of Biomedical Engineering 4(1): 65-71.

Whatling GM, Dabke HV, Holt CA, Jones L, Madete J, Alderman PM, Roberts P. 2008. Objective functional assessment of total hip arthroplasty following two common surgical approaches: the posterior and direct lateral approaches. Proceedings of Inst Mech Eng [H]. 222(6):897-905.

Websites:

[www] URL: www.correlatedsolutions.com [19:11:09]

[www] URL: http://en.wikipedia.org/wiki/Main_Page [19:11:09]

[www] URL: www.limess.com [21:11:08]

[www] URL: www.mitutoyo.co.uk [19:11:09]

[www] URL: www.qualisys.com [19:11:09]

[www] URL: www.simulia.com [19:11:09]

A-1

APPENDIX A

GLOSSARY

3D tracking	Tracker that uses the 2D data of all cameras in the system to calculate marker positions in three dimensions.
Accuracy	The closeness of an indication or reading of a measurement device to the actual value of the quantity being measured. Usually expressed as ± percent of full scale output or reading.
Anisotropic	Having different physical properties at different levels of measurement.
Anisotropy	The opposite of isotropy (refer isotropy).
Aperture	The size of the opening in the camera's lens. This opening can be adjusted with the adjustment ring.
Bone	Visible connection between two trajectories in the 3D view.
Calibration	Process that defines the position of the cameras in the 3D space. The calibration is used for the 3D reconstruction.
Calibration kit	Equipment that is needed for a wand calibration, e.g wand.
Camera unit	Unit of the data from the camera.
Capture	Measurement which collects several frames at a fixed frame rate.
Capture file	A qtm-file with motion capture data (.qtm).
Capture rate	Frame rate in Hz that is used for the motion capture.
Capture view	View that is used during motion capture.
CCD (Charged Coupled Device)	Device that converts light into an electrical signal. This can be compared to the film of an ordinary camera.
Coordinate system	A system of axes which describes the position of a point. In QTM all of the 3D coordinate systems are orthogonal, right hand systems.

Coordinate system of the motion capture	The coordinate system which is defined with the calibration process.
Deformation	Change in shape due to an applied force.
Field of view (FOV)	The MCU's view, vertical and horizontal on a specific distance from the camera.
Focus	Changes the focal length of the camera to achieve a clear image.
Frame	Single exposure of the camera system.
Frame calibration	Calibration method which uses a rigid structure with markers to calibrate the volume. It is only accurate within the volume of that frame
Frame rate	Frequency of the motion capture.
Gap fill	Function that calculates a probable path between trajectory parts to associate them.
Hertz (Hz)	Units in which frequency is expressed. Synonymous with cycles per second.
Hyperelasticity	The capability of a material to undergo large elastic strain due to small forces, without losing its original properties.
Isotropic	Having the same properties or characteristics along all axes.
Isotropy	The property of being independent of direction.
Label	Name of a trajectory in the identification windows.
Labelled trajectories window	Window with identified trajectories.
Linearity	The closeness of a calibration curve to a specified straight line. Linearity is expressed as the maximum deviation of any calibration point on a specified straight line during any one calibration cycle.
Linearization	Correction data which is needed for each camera to make the capture as good as possible.
Marker	Item that is attached to the moving object to measure its position.
Marker – Passive	Marker with reflective material.
Marker (3D view)	Sphere that represents a trajectory in 3D views.

Max residual	Maximum distance for a 2D ray to be included in a 3D point during tracking.
MCU	Motion Capture Unit (camera).
Modulus of Elasticity, E (Young's Modulus)	The ratio of stress to strain when deformation is totally elastic; also a measure of the stiffness of a material.
Motion capture	Measurement which records a motion.
Plane stress	In real engineering components, stress (and strain) are 3-D tensors, however when one of the dimensions of the material is much smaller than the other two, it can be neglected and the resulting state of stress becomes bidimensional. This state is known as plane stress because the normal and shear stresses with respect to the thin surface are zero.
Poisson's ratio	The ratio between the strain of expansion in the direction of force and the strain of contraction perpendicular to that force.
Pixel	Picture element. Definable locations on a display screen that are used to form images on the screen. For graphic displays, screens with more pixels provide higher resolution.
Residual	In most cases in QTM this is the minimum distance between a 2D marker ray and its corresponding 3D point or an average of this measure.
Residual (3D)	The average of the different residuals of the 2D marker rays that belongs to the same 3D point.
Residual (calibration):	The Average residual in the Calibration results dialog is the average of the 3D residuals of all the points measured by the camera during the calibration.
Stiffness	The resistance of an elastic body to deformation by an applied force. It is an extensive material property.
Strain	Deformation of a physical body under the action of applied forces.
Stress	A measure of force per unit area within a body. It is a body's internal distribution of force per area that reacts to external applied loads.
Tensor	A generalization of the concept of a vector.
Tracking	Process that calculates 3D data or 6DOF data.
Trajectory:	3D data of a marker in a series of frames.

Trajectory info windows: Windows with trajectories and 3D data.

Viscoelasticity   The property of materials that exhibit both viscous and elastic characteristics when undergoing deformation.

Young's Modulus, E (Modulus of Elasticity)   The ratio of stress to strain when deformation is totally elastic; also a measure of the stiffness of a material.

APPENDIX B

QTM 2008 v2.0 (Qualisys AB, Sweden)

B1: CALIBRATION RESULT
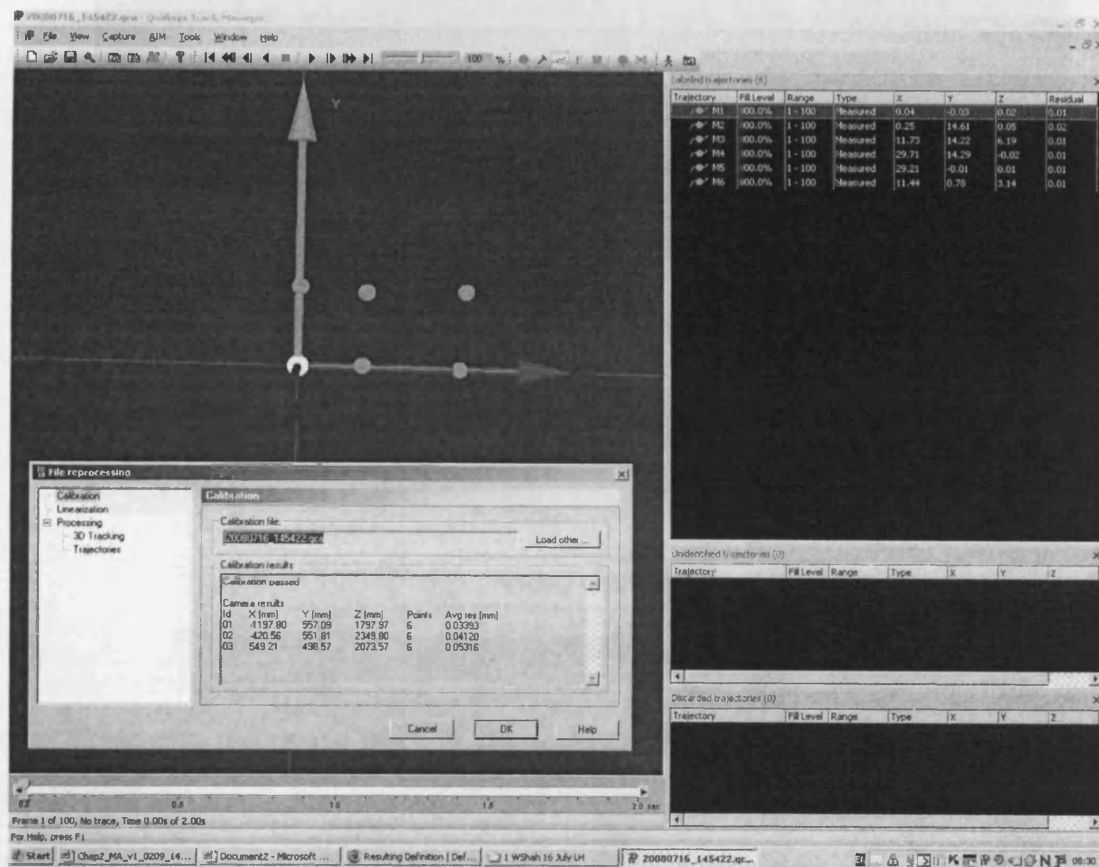
Figure B1: Calibration result for diamond marker
(QTM 2008 v2.0, Qualisys AB, Sweden)

B2: CALIBRATION RESULT
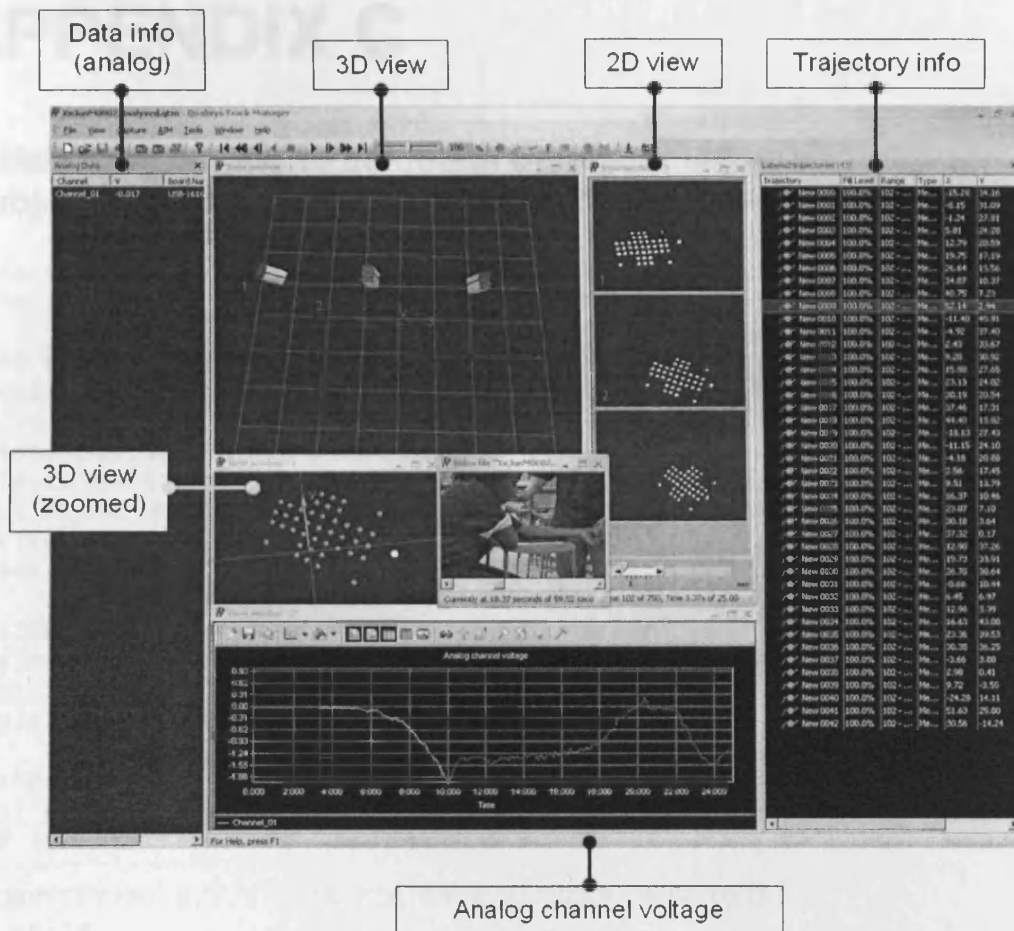
Figure B2: QTM user interface (file mode) view windows.

Figure B2 exhibits the typical windows (file mode) of the QTM user interface for a sample (tracked markers) output from the experiments. From it, the trajectory and the markers in 2D and 3D view could be visualised. In addition, the windows for a video playback and a plot of analog voltage from a specified channel could also be selected and analysed. The trajectory data info window displays all the markers information. In 2D view windows the motion capture data is shown with a 2D view for each camera of the measurement set up. The number in the camera view indicates the camera id. 3D view window shows the motion capture data in 3D space where the 2D data from each camera was converted (tracked) into 3D data. The arrangement of the cameras could also be observed. A small window was added to show the marker in a zoomed view. View windows provide a timeline control bar for user to playback or view the data throughout the captured duration (from the first till the last frame/image).

APPENDIX C

Matlab programme to calculate displacements (Subject 1, X=0)

```
%THIS PROGRAM IS WRITTEN TO READ RAWDATA
%from a *.tsv file. (Succeeded 11 Jan 09 11:30)
%
%READ RAW DATA FROM A FILE
rawdata=dlmread('D:\JMD\PhD\Motion
Analysis\MatlabvsQualysis\JunMLH\JunMLHXx07a.tsv');
rawload=dlmread('D:\JMD\PhD\Motion
Analysis\MatlabvsQualysis\JunMLH\JunMLHXx07a_a.tsv',',');
disp('Frame JunMLHXx07a');
plot(rawload);
pause;
%
%ASSIGN & DISPLAY DATA SIZE,
[x,y]=size(rawdata); %x= no. of frames, y= markers
x1,y1,z1,x2,y2,z2...
disp(size(rawdata));
%
nmarker=y/3; %Calculating no. of markers
disp('no. of markers = ');
disp (nmarker);
%
% IDENTIFYING X,Y,Z DATA FOR EACH MARKERS (RAW DATA)
for i=1:x
    for j=1:nmarker
    xraw(i,j)=rawdata(i,j*3-2);
    yraw(i,j)=rawdata(i,j*3-1);
    zraw(i,j)=rawdata(i,j*3);
    end
end
% PLOT 3D
figure(5);
plot3(xraw(10,:),yraw(10,:),zraw(10,:),'r.','MarkerSize',30);
%
% TRUNCATE DATA where necessary
data=rawdata(1:414,:);
load=rawload(1:414);
[x,y]=size(data);
disp(size(data));
figure(3);
plot(load); % PLOT LOAD
title('Load JunMLHXx07a','FontWeight','bold');
nmarker=y/3; %Calculating no. of markers
disp('no. of markers = ');
disp (nmarker);pause;
%
% RE-IDENTIFYING X,Y,Z DATA FOR EACH MARKERS (TRUNCATED DATA)
for i=1:x
    for j=1:nmarker
```

```
        xdata(i,j)=data(i,j*3-2);
        ydata(i,j)=data(i,j*3-1);
        zdata(i,j)=data(i,j*3);
    end
end
%
%figure(10); % ANIMATE IF NECESSARY
%for k=1:x
%
plot3(xdata(k,:),ydata(k,:),zdata(k,:),'r.','MarkerSize',30);
%        axis([-80 40 -30 70 30 60]); %set axis
%        view([-5 -15 30]);%set viewpoint
%    M(k) = getframe;
%end
%
%TRANSLATE AND ROTATE (2D x-y) PLANE IF NECESSARY
%
%    Translate to set the origin
%
xdataT(1:x,1:nmarker)=xdata(1:x,1:nmarker)-data(1,1);
ydataT(1:x,1:nmarker)=ydata(1:x,1:nmarker)-data(1,2);
%
figure(11);
plot(xdata(1,1:nmarker),ydata(1,1:nmarker),'r*');
axis ([-60 80 -60 80]);
hold on;
plot(xdataT(1,1:nmarker),ydataT(1,1:nmarker),'g+');
hold on;
%
%    FIND THETA TO ROTATE
yy=ydataT(1,8)-ydataT(1,1); % y2-y1 of 2 parallel markers
xx=xdataT(1,8)-xdataT(1,1); % x2-x1
theta=atand(yy/xx)% calculate theta using arc tangent
%
% THE TRANSFORMATION MATRIX
Tdeg=[cosd(theta) sind(theta);-sind(theta) cosd(theta)];
%
% new data = [Tdeg]*[x,y]
for i=1:x
    for j=1:nmarker
    xnew(i,j)=Tdeg(1,1)*xdataT(i,j)+Tdeg(1,2)*ydataT(i,j);
    ynew(i,j)=Tdeg(2,1)*xdataT(i,j)+Tdeg(2,2)*ydataT(i,j);
    end
end
znew=zdata;
%
% FROM HERE WE ARE DEALING WITH NEW x,y,z DATA
% WHICH HAS BEEN TRANSLATED (SET ORIGIN) AND ROTATED
%
plot(xnew(1,1:nmarker),ynew(1,1:nmarker),'bo');
.hold on;
plot(xnew(1,1),ynew(1,1),'b+','MarkerSize',16,'Linewidth',2);
hold off;
% CHECK!!!
figure(12);
plot3(xnew(1,:),ynew(1,:),znew(1,:),'r.','MarkerSize',16);
axis([-10 90 -50 50 30 60]); %set axis
view([5 2 40]);%set viewpoint
%
```

```
%figure(11); % ANIMATE IF NECESSARY
%for k=1:x
%          plot3(xnew(k,:),ynew(k,:),znew(k,:),'r.','MarkerSize',30);
%          axis([-10 90 -50 50 30 60]); %set axis
%          view([-5 -15 30]);%set viewpoint
%       M(k) = getframe;
%end
figure(12); % ANIMATE 2-DIF NECESSARY
%for k=1:x
%          plot(xnew(k,35),ynew(k,35),'m.','MarkerSize',10);
%          hold on;
%          plot(xnew(k,:),ynew(k,:),'r.','MarkerSize',10);
%          hold on;
%          axis([-10 90 -50 50]); %set axis
%             view([-5 -15 30]);%set viewpoint
%       M(k) = getframe;
%end
plot (xnew(1,:),ynew(1,:),'bo','MarkerSize',5,'LineWidth',2);
hold on;
plot (xnew(x,:),ynew(x,:),'g+','MarkerSize',4,'LineWidth',2);
hold on;
%
dlmwrite('xnewJMLHXx07a.csv',xnew,'\t');
dlmwrite('ynewJMLHXx07a.csv',ynew,'\t');
%
% 2D TRANSLATE & ROTATE ALL MARKERS TO NEW ORIGIN
%
%newdata=Tdeg*
%for i=1:x
%    for j=1:nmarker
%    newdata(i,j)=xdata(i,j);
%    new(i,j)=ydata(i,j);
%    end
%end
% ASSIGNING A INITIAL / PIVOT IMAGE
% STILL
xfix=xnew(1:10,:);
yfix=ynew(1:10,:);
zfix=znew(1:10,:);
xstill=mean(xfix);
ystill=mean(yfix);
plot (xstill,ystill,'bo','MarkerSize',4,'LineWidth',2);
hold off;
disp ('stop 1');
pause;
%
%PLOT STILL IF NECESSARY
%figure(15);
%plot(xstill,ystill,'r.','MarkerSize',15);
%pause;
%figure(16);
%plot3(xstill,ystill,zstill,'r.','MarkerSize',15);
%
%DISCRETISE & DIGITISE
dig=x/5;
coun=1
%
for i=1:dig
    digload(i)=mean(load(i*5-4:i*5));
```

```
        coun=coun+1;
end
disp(coun);

%
% MIDLINE & MID-POINTS
%
for j=1:x
    for k=1:42
    xmidpoin(j,k)=xnew(j,k);
    ymidpoin(j,k)=ynew(j,k);
    end
%      xmidpoin(j,9)=xnew(j,39);
%      ymidpoin(j,9)=ynew(j,39);
end
%
%
coum=1
for i=1:dig
    for k=1:42
    digxmid(i,k)=mean(xmidpoin((i*5-4:i*5),k));
    digymid(i,k)=mean(ymidpoin((i*5-4:i*5),k));
    end
    coum=coum+1;
end
disp(coum);
%
% CALCULATE DISTANCE or TOTAL DISPLACEMENT
%
%xstill(9)=xstill(39);
%ystill(9)=ystill(39);
for i=1:dig
    for j=1:42
        xx(i,j)=digxmid(i,j)-xstill(j);% absolute?
        yy(i,j)=digymid(i,j)-ystill(j);% absolute value?
        xx2(i,j)=(xx(i,j))^2;
        yy2(i,j)=(yy(i,j))^2;
        dist(i,j)=sqrt(xx2(i,j)+yy2(i,j));
    end
end
% FILTER Y
for i=1:dig
    for j=1:42
    yyf(i,j)=yy(i,j)-yy(i,9); % filtered
    end
end
%
figure(20); % PLOT DEFORMATIONS FOR ALL MARKERS
plot(dist(:,1:9));
title('deformation');xlabel('no');ylabel('(mm)(mV)');
.hold on;
plot(digload);
hold off;
disp ('stop 3');
pause;
%
% MERGE LOAD:DISTANCE (To print in xls)
%
abload(1:dig)=abs(digload(1:dig));
```

```
loadist(:,1)=abload(1:dig)/1.948;
loadist(:,2:9)=dist(:,1:8);
%
% TRUNCATE IF NECESSARY or use command axis([xmin xmax ymin ymax])
%
figure(25);
abload2(1:dig)=abload(1:dig)/1.948-(abload(1)/1.948);
abload3(1:dig)=abload(1:dig)/1.948;
dist2(1:dig,:)=dist(1:dig,:);
subplot(2,1,1);
plot(abload2,dist2(:,5),'ro');
title('Truncated Graph');xlabel('Load (N)');ylabel('Total Disp(mm)');
hold on;
plot(abload2,dist2(:,1),'b+');
hold off;
subplot(2,1,2);
plot(abload3,dist(:,5),'ro');
hold on;
plot(abload3,dist(:,1),'b+');
title('Original');xlabel('Load (N)');ylabel('Total Disp(mm)');
hold off;
%
% PLOT X-DISPLACEMENT
figure(26);
plot(abload3,xx(:,5),'ro');
hold on;
plot(abload3,xx(:,1),'b+');
title('Original');xlabel('Load (N)');ylabel('x-Disp(mm)');
hold off;
%
% PLOT Y-DISPLACEMENT
figure(27);
plot(abload3,yy(:,5),'r');
title('Original');xlabel('Load (N)');ylabel('y-Disp(mm)')
hold on;
plot(abload3,yy(:,1),'g');
%hold on;
plot(abload3,yyf(:,1),'b+');
hold off;
%
% PLOT LOAD-DISPLACEMENT CURVE L1,L5,L8 --XX
%
figure(28);
plot(xx(:,5),abload2,'k^','MarkerSize',4,'LineStyle','-
','LineWidth',2);
hold on;
plot(xx(:,6),abload2,'m+');
hold on;
plot(xx(:,8),abload2,'bo','MarkerSize',4,'LineStyle','-
','LineWidth',2);
hold on;
plot(xx(:,1),abload2,'r*','MarkerSize',4,'LineStyle','-
','LineWidth',2);
hold on;
plot(xx(:,3),abload2,'c*');
hold off;
%axis([0 12 0 1]);
title('Load-DispX JunMLHXx07a','FontWeight','bold');
% Uncomment the following line to preserve the X-limits of the axes
```

C-5

```
%xlim([0 12]);
% Uncomment the following line to preserve the Y-limits of the axes
%ylim([0 1]);
grid on;
xlabel('x-Displacement(mm)','FontWeight','bold');ylabel('Load
(N)','FontWeight','bold');
legend ('L5','L6','L8','L1','L3');
%
dlmwrite('JMLxx07a.tsv',xx,'\t');
dlmwrite('JMLxx07aload.tsv',abload2,'\t');
%
% PLOT LOAD-DISPLACEMENT CURVE L5,L8,L1 --YY
%
figure(29);
plot(yy(:,5),abload2,'k^','MarkerSize',4,'LineStyle','-
','LineWidth',2);
hold on;
plot(yy(:,6),abload2,'m+');
hold on;
plot(yy(:,8),abload2,'bo','MarkerSize',4,'LineStyle','-
','LineWidth',2);
hold on;
plot(yy(:,1),abload2,'r*','MarkerSize',4,'LineStyle','-
','LineWidth',2);
hold on;
plot(yy(:,3),abload2,'c*');
%axis([0 12 0 1]);
hold off;
title('Load-DispY JunMLHXx07a','FontWeight','bold');
% Uncomment the following line to preserve the X-limits of the axes
%xlim([0 12]);
% Uncomment the following line to preserve the Y-limits of the axes
%ylim([0 1]);
grid on;
xlabel('y-Displacement(mm)','FontWeight','bold');ylabel('Load
(N)','FontWeight','bold');
legend ('L5','L6','L8','L1','L3');
%
%
% PLOT LOAD-DISPLACEMENT CURVE L5,L35,L38 --XX
%
figure(30);
plot(xx(:,5),abload2,'k^','MarkerSize',4,'LineStyle','-
','LineWidth',2);
hold on;
plot(xx(:,35),abload2,'bo','MarkerSize',4,'LineStyle','-
','LineWidth',2);
hold on;
plot(xx(:,38),abload2,'r*','MarkerSize',4,'LineStyle','-
','LineWidth',2);
hold on;
plot(xx(:,14),abload2,'m+');
hold on;
plot(xx(:,23),abload2,'c+');
%axis([0 12 0 1]);
hold off;
title('Load-DispX JunMLHXx07a','FontWeight','bold');
% Uncomment the following line to preserve the X-limits of the axes
%xlim([0 12]);
```

```
% Uncomment the following line to preserve the Y-limits of the axes
%ylim([0 1]);
grid on;
xlabel('x-Displacement(mm)','FontWeight','bold');ylabel('Load
(N)','FontWeight','bold');
legend ('L5','L35','L38','L14','L23');
%
% PLOT LOAD-DISPLACEMENT CURVE L5,L35,L38 --YY
%
figure(31);
plot(yy(:,5),abload2,'k^','MarkerSize',4,'LineStyle','-
','LineWidth',2);
hold on;
plot(yy(:,35),abload2,'bo','MarkerSize',4,'LineStyle','-
','LineWidth',2);
hold on;
plot(yy(:,38),abload2,'r*','MarkerSize',4,'LineStyle','-
','LineWidth',2);
hold on;
plot(yy(:,14),abload2,'m+');
hold on;
plot(yy(:,23),abload2,'c+');
%axis([0 12 0 1]);
hold off;
title('Load-DispY JunMLHXx07a','FontWeight','bold');
% Uncomment the following line to preserve the X-limits of the axes
%xlim([0 12]);
% Uncomment the following line to preserve the Y-limits of the axes
%ylim([0 1]);
grid on;
xlabel('y-Displacement(mm)','FontWeight','bold');ylabel('Load
(N)','FontWeight','bold');
legend ('L5','L35','L38','L14','L23');
%
%
figure(35);
xxta(:,1:8)=xx(:,1:8);
bot=[1 2 3 4 5 7 8 9];
plot(bot,xxta(82,1:8),'k^','LineStyle','-
','MarkerSize',4,'LineStyle','-','LineWidth',3);
disp (abload2(82));
hold on;
plot(bot,xxta(58,1:8),'ko','LineStyle','-
','MarkerSize',4,'LineStyle','-','LineWidth',2);
hold on;
plot(bot,xxta(53,1:8),'b+','LineStyle','-
','MarkerSize',4,'LineStyle','-','LineWidth',2);
hold on;
plot(bot,xxta(48,1:8),'mv','LineStyle','-
','MarkerSize',4,'LineStyle','-','LineWidth',2);
.hold on;
plot(bot,xxta(44,1:8),'k^','LineStyle','-
','MarkerSize',4,'LineStyle','--','LineWidth',2);
hold on;
plot(bot,xxta(40,1:8),'bs','LineStyle','-
','MarkerSize',4,'LineStyle','--','LineWidth',2);
hold on;
plot(bot,xxta(33,1:8),'rv','LineStyle','--');
hold on;
```

```
plot(bot,xxta(31,1:8),'ko','LineStyle','--');
xlabel('Markers','FontWeight','bold','Fontsize',12);
ylabel('x-Displacement (mm)','FontWeight','bold','Fontsize',12)
legend ('1.5N','1.0N','0.8N','0.6N','0.5N','0.4N','0.2N','0.1N');
hold off;
title('Load-DispX JunMLHXx07a','FontWeight','bold');
grid on;
box('on');
%
yyd(:,1)=yy(:,38);
yyd(:,2)=yy(:,32);
yyd(:,3)=yy(:,23);
yyd(:,4)=yy(:,5);
yyd(:,5)=yy(:,14);
yyd(:,6)=yy(:,29);
yyd(:,7)=yy(:,35);
%
figure(37);
%bot=[38 32 23 5 14 29 35];
bot=[1 2 3 4 5 6 7];
plot(bot,yyd(82,1:7),'k^','LineStyle','-
','MarkerSize',4,'LineStyle','-','LineWidth',2);
hold on;
plot(bot,yyd(58,1:7),'b*','LineStyle','-
','MarkerSize',4,'LineStyle','-','LineWidth',2);
hold on;
plot(bot,yyd(53,1:7),'c+','LineStyle','-
','MarkerSize',4,'LineStyle','-','LineWidth',2);
hold on;
plot(bot,yyd(48,1:7),'rv','LineStyle','-
','MarkerSize',4,'LineStyle','-','LineWidth',2);
hold on;
plot(bot,yyd(44,1:7),'k^','LineStyle','-
','MarkerSize',4,'LineStyle','--','LineWidth',2);
hold on;
plot(bot,yyd(40,1:7),'m+','LineStyle','-');
hold on;
plot(bot,yyd(33,1:7),'yo','LineStyle','-');
hold on;
plot(bot,yyd(31,1:7),'yo','LineStyle','-');
hold off;
xlabel('Markers','FontWeight','bold');ylabel('y-Disp
(mm)','FontWeight','bold');
set(gca,'XTickLabel',{'L38';'L32';'L23';'L5';'L14';'L29';'L35'});
legend ('1.45','1.0','0.814','0.6','0.5','0.4','0.2','0.12');
title('Load-DispY Tranv JunMLHXx07a','FontWeight','bold');
box('on');
%
xxd(:,1)=xx(:,38);
xxd(:,2)=xx(:,32);
xxd(:,3)=xx(:,23);
xxd(:,4)=xx(:,5);
xxd(:,5)=xx(:,14);
xxd(:,6)=xx(:,29);
xxd(:,7)=xx(:,35);
%
figure(38);
bot=[1 2 3 4 5 6 7];
```

```
plot(bot,xxd(82,1:7),'k^','LineStyle','-
','MarkerSize',4,'LineStyle','-','LineWidth',2);
hold on;
plot(bot,xxd(58,1:7),'b*','LineStyle','-
','MarkerSize',4,'LineStyle','-','LineWidth',2);
hold on;
plot(bot,xxd(53,1:7),'c+','LineStyle','-
','MarkerSize',4,'LineStyle','-','LineWidth',2);
hold on;
plot(bot,xxd(48,1:7),'rv','LineStyle','-
','MarkerSize',4,'LineStyle','-','LineWidth',2);
hold on;
plot(bot,xxd(44,1:7),'k^','LineStyle','-
','MarkerSize',4,'LineStyle','--','LineWidth',2);
hold on;
plot(bot,xxd(40,1:7),'y+','LineStyle','-');
hold on;
plot(bot,xxd(33,1:7),'mo','LineStyle','-');
hold on;
plot(bot,xxd(31,1:7),'m+','LineStyle','-');
hold off;
xlabel('Markers','FontWeight','bold');ylabel('x-Disp
(mm)','FontWeight','bold');
set(gca,'XTickLabel',{'L38';'L32';'L23';'L5';'L14';'L29';'L35'});
legend ('1.45','1.0','0.814','0.6','0.5','0.4','0.2','0.12');
title('Load-DispX Tranv JunMLHXx07a','FontWeight','bold');
box('on');
%
figure(39);
bot=[1 2 3 4 5 7 8 9];
plot(bot,yy(52,1:8),'k^','LineStyle','-
','MarkerSize',4,'LineStyle','-','LineWidth',2);
disp (abload2(82));
hold on;
plot(bot,yy(58,1:8),'bo','LineStyle','-
','MarkerSize',4,'LineStyle','-','LineWidth',2);
hold on;
plot(bot,yy(53,1:8),'c*','LineStyle','-
','MarkerSize',4,'LineStyle','-','LineWidth',2);
hold on;
plot(bot,yy(48,1:8),'mv','LineStyle','-
','MarkerSize',4,'LineStyle','-','LineWidth',2);
hold on;
plot(bot,yy(44,1:8),'k^','LineStyle','-
','MarkerSize',4,'LineStyle','--','LineWidth',2);
hold on;
plot(bot,yy(40,1:8),'y+','LineStyle','-');
hold on;
plot(bot,yy(33,1:8),'mo','LineStyle','-');
hold on;
plot(bot,yy(31,1:8),'yo','LineStyle','-');
hold off;
xlabel('Markers','FontWeight','bold');ylabel('y-Disp
(mm)','FontWeight','bold')
legend ('1.45','1.0','0.814','0.6','0.5','0.4','0.2','0.12');
title('Load-DispY JunMLHXx07a','FontWeight','bold');
box('on');
%
-------------------- END OF PROGRAMME ------------------------
```

APPENDIX D (from Section 3.3.1, Chapter 3)

COMPARISON OF THE FINITE ELEMENT SOLUTION WITH AN EXACT SOLUTION

Initial study involved testing the FE procedure and solver of Abaqus (Dassault Systemes Simulia Corp, Providence, RI, USA). Therefore, a case study where the results can be compared and validated was designed. For this purpose, an engineering problem with known analytical solutions (Reddy and Pandey 1987) was considered. In this study, an FE composite plate model was developed and for several lamination schemes, its deformation was investigated. The composite plate was made of T300/5208 graphite epoxy and its material property is shown in Table D1.1.

The plate was subjected to uniformly distributed load on the top surface in the z-direction. A quarter of the plate was modelled because of the biaxial symmetry, lamination and boundary conditions. The number of the elements was modelled as shown in Figure D1.1. The boundary conditions used for simply supported cross-ply and anti-symmetric angle-ply are shown in Figure D1.2. A sample result showing the deformed plate is shown in Figure D1.3. The FE solutions for the displacement of the centre point of various cross-ply and angle ply laminates are compared with the exact solution in and the results are shown Table D1.2. The FE solutions are in excellent agreement with the exact solutions.

Table D1.1: Material properties of graphite epoxy (Reddy and Pandey 1987)

Properties	Values
E_1	19.2×10^6 psi
E_2	1.56×10^6 psi
E_3	1.56×10^6 psi
$G_{12} = G_{13}$	0.82×10^6 psi
G_{23}	0.49×10^6 psi
$v_{12} = v_{13}$	0.24
v_{23}	0.49
Ply thickness, h_i	0.005 in./ply
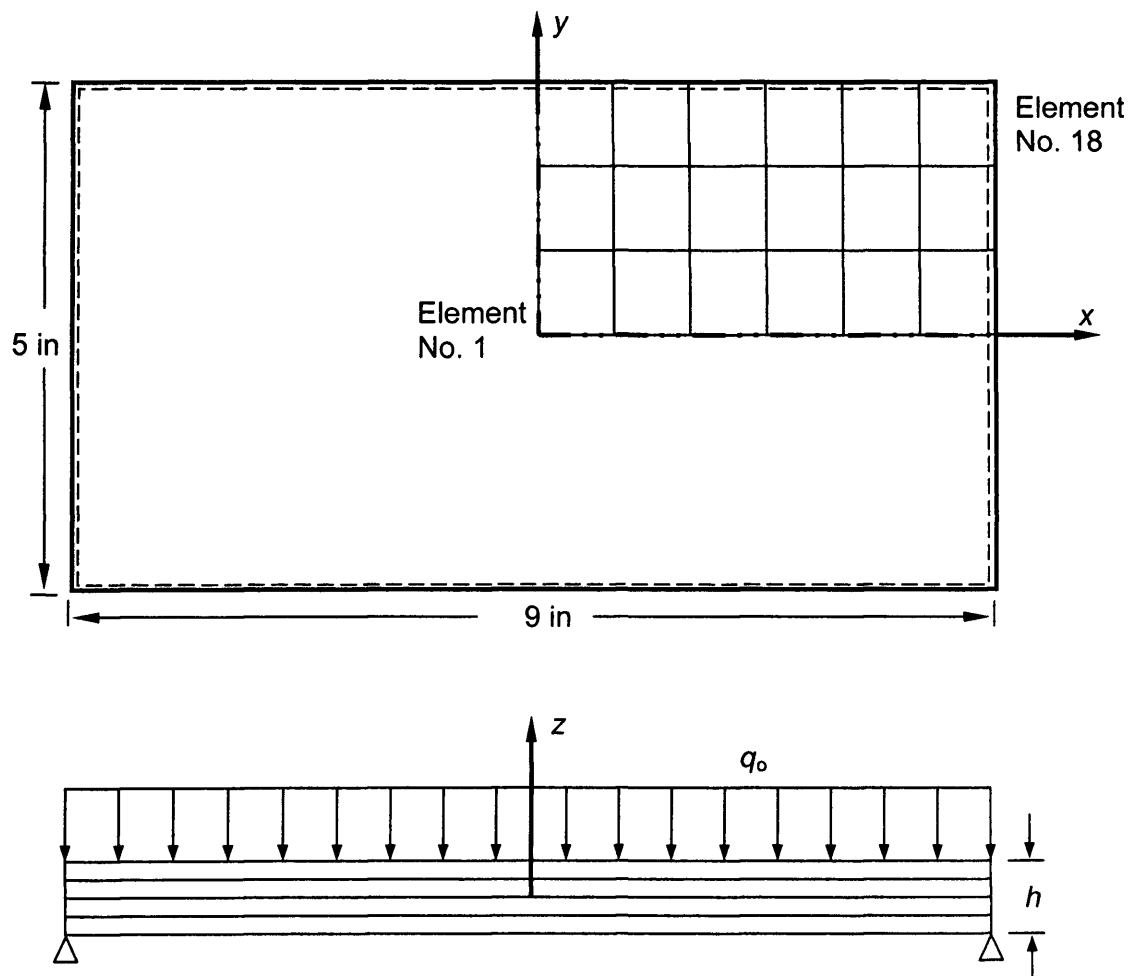
Figure D1.1: Geometry and computational domain for the composite laminate under transverse load.

$u = w = \theta_x = 0$

$v = 0$
$w = 0$
$\theta_y = 0$

$u = 0$
$\theta_x = 0$

$v = 0$
$w = 0$
$\theta_y = 0$

$v = \theta_y = 0$

$u = w = \theta_x = 0$

(a) Cross-ply laminates

$v = w = \theta_x = 0$

$u = 0$
$w = 0$
$\theta_y = 0$

$v = 0$
$\theta_x = 0$

$u = 0$
$w = 0$
$\theta_y = 0$

$u = \theta_y = 0$

$v = w = \theta_x = 0$
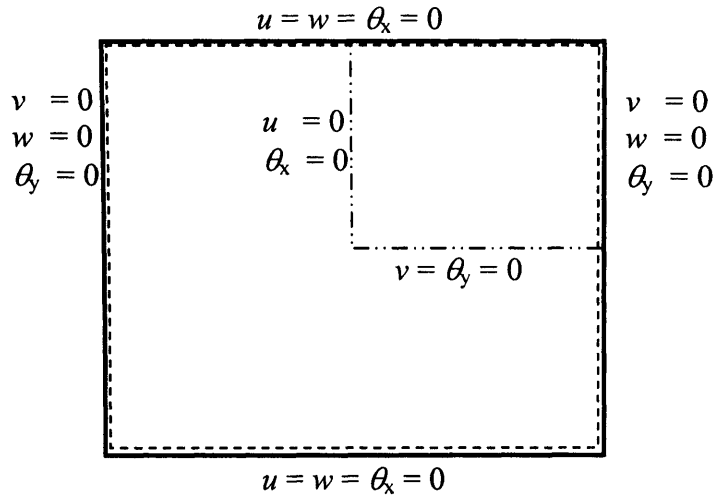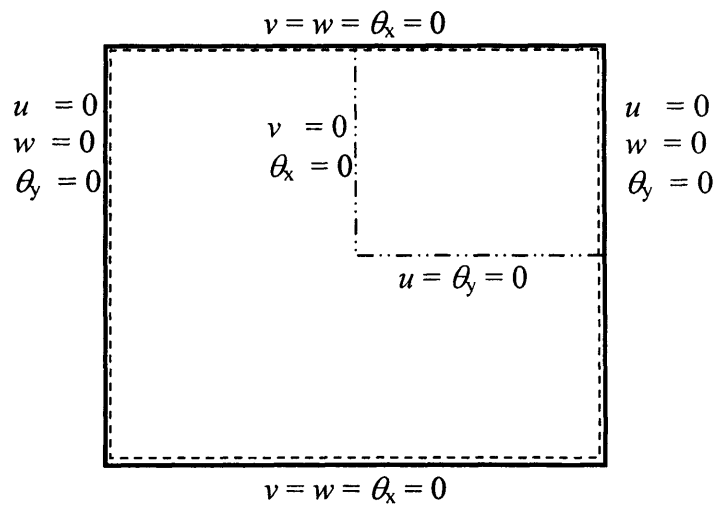
(b) Anti-symmetric angle ply

Figure D1.2: The simply supported boundary conditions for the full-plate and quarter-plate model of cross-ply and anti-symmetric angle-ply laminates.
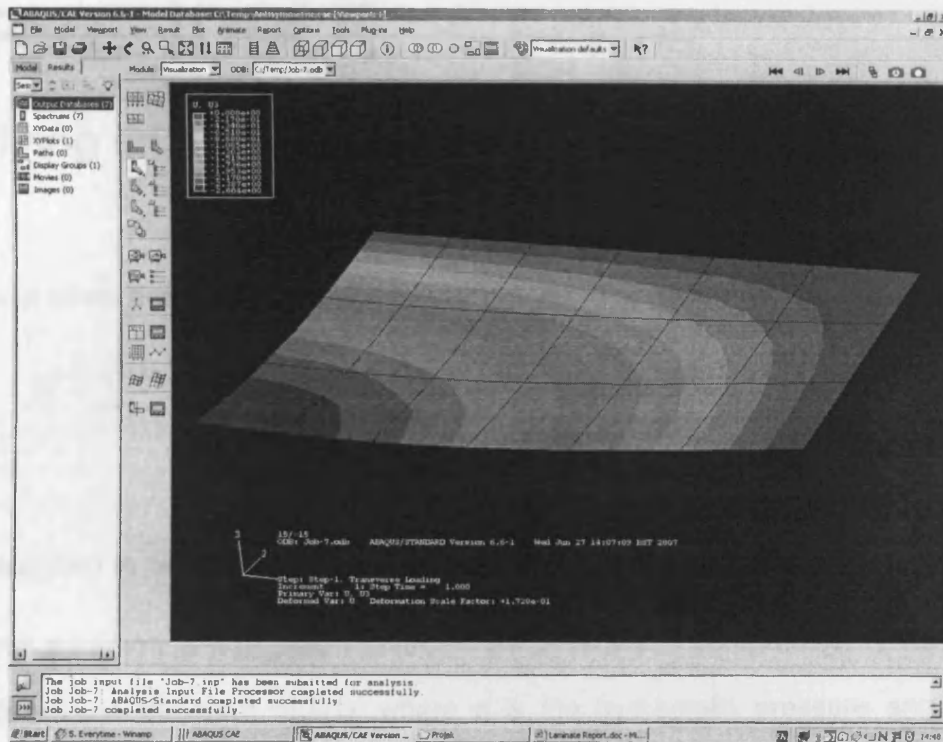
Figure D1.3: The deformed composite plate showing displacements in *z*-direction (Abaqus v6.6-1, Dassault Systemes Simulia Corp, Providence, RI, USA).

Table D1.2: Comparison of exact and finite-element solution, *z*-displacement (in) for laminated   composite plate (9 by 5 in).

Lamination scheme	Type of Laminate	UDL (p.s.i)	Maximum Displacement (*z*-direction in inches)	
			*Exact Solution	Finite-Element Solution using Abaqus/CAE v6.6-1
[0 / 90]$_T$	cross-ply	0.1	1.884	**1.884**
[0/ 90/ 0/ 90]$_T$		0.1	0.134	**0.1349**
[0/ 90/ 90/ 0]$_T$		0.1	0.229	**0.2299**
[45/-45/45/-45]$_T$	anti-symmetric angle ply	0.1	0.1086	**0.1087**
[15/-15/15/-15]$_T$		0.1	0.2515	**0.2515**
[45 / -45]$_T$		0.1	1.6006	**1.601**
[15 / -15]$_T$		0.1	2.6039	**2.604**

Note*:

Source of Exact Solution: *Reddy, J.N. and Pandey, A.K. 1987. A First-Ply Failure Analysis of Composite Laminates. *Computers and Structures* 25: 371-393.

APPENDIX E

Deriving engineering stress

Ogden's strain energy function, W, in its general form (Ogden 1972):-

$$W = \sum_{i=1}^{N} \frac{\mu_i}{\alpha_i}\left(\lambda_1^{\alpha_i} + \lambda_2^{\alpha_i} + \lambda_3^{\alpha_i} - 3\right) - p(J - 1) \tag{E.1}$$

As described in Section 4.4.1.4, λ_i are the principal stretches; and μ_i and α_i are the material parameters with the function's order of N. The incompressibility constraint is introduced via the term $p(J-1)$, where p is the hydrostatic pressure and J is the volume ratio $\lambda_1\lambda_2\lambda_3$.

For incompressible isotropic hyperelastic material, the second Piola-Kirchoff stress, S_a, in terms of the Cauchy stress, σ_a, is (Holzapfel 2000):

$$S_a = \lambda_a^{-2}\sigma_a \qquad , a = 1, 2, 3 \tag{E.2}$$

Re-arranging (E.2);

$$\sigma_a = \lambda_a^2 S_a \tag{E.3}$$

Considering an incompressible material under uniaxial tension (with single pair of Ogden parameter, $N=1$), the second Piola-Kirchoff stress (Evans 2009):

$$S_1 = \mu\left(-\lambda_1^{-2-\frac{\alpha}{2}} + \lambda_1^{\alpha-2}\right) \tag{E.4}$$

Substituting (E.4) into (E.3) and generalising the equation, the Cauchy stress, σ:

$$\sigma = \lambda^2\mu\left(-\lambda^{-2-\frac{\alpha}{2}} + \lambda^{\alpha-2}\right) \quad \text{or} \quad \sigma = \mu\left(\lambda^\alpha - \lambda^{-\frac{\alpha}{2}}\right) \qquad \text{(E.5)}$$

Cauchy (or true) stress is represented by force, F, measured per unit surface area, A_i, defined in the current configuration (Holzapfel 2000):

$$\sigma = \frac{F}{A_i} \qquad \text{(E.6)}$$

The engineering (or nominal) stress, σ_E, is represented by force measured per unit surface area, A_o, defined in the reference configuration:

$$\sigma_E = \frac{F}{A_o} \qquad \text{(E.7)}$$

The relation between the current and reference configurations relate the areas to be:

$$A_i = \frac{1}{\lambda}A_o \qquad \text{(E.8)}$$

Substituting (E.8) into (E.7) yields:

$$\sigma_E = \frac{F}{\lambda A_i} \qquad \text{(E.9)}$$

Therefore, the relation of Cauchy and engineering stresses becomes:

$$\sigma_E = \frac{1}{\lambda}\sigma \qquad \text{(E.10)}$$

Substituting (E.5) into (E.10) yields:

$$\sigma_E = \frac{\mu}{\lambda}\left(\lambda^\alpha - \lambda^{-\frac{\alpha}{2}}\right) \qquad \text{(E.11)}$$

APPENDIX F

Tables of optimum parameters for all subjects (MA)

Table F.1: The best 20 sets of material parameters
(Subject 1, X=0, 0.7N, MA, initial guess values: μ=11, α=25 and λ_p=0.24)

μ (Pa)	α	λ_p	rms error
11.1881	24.1344	0.2834	0.1578
12.5497	21.8875	0.3272	0.1647
9.5866	28.7934	0.2124	0.1653
10.7613	24.9642	0.2665	0.1657
10.9056	25.1671	0.2660	0.1657
10.2341	24.0189	0.2885	0.1662
11.0177	24.1048	0.2818	0.1693
11.7263	22.2255	0.3235	0.1694
9.4121	27.8135	0.2241	0.1696
10.2413	24.1855	0.2888	0.1699
9.5848	24.0210	0.2926	0.1700
10.5816	25.2334	0.2706	0.1705
12.2535	23.9371	0.2697	0.1713
9.4933	27.7201	0.2290	0.1713
10.7455	28.4961	0.2095	0.1716
10.4870	26.2363	0.2454	0.1717
9.4946	27.0425	0.2371	0.1719
12.4148	28.2321	0.2068	0.1721
11.7692	23.4086	0.3041	0.1721
11.6577	26.3559	0.2396	0.1723

Best results:
11.1881   24.1344   0.283436

Minimum rms error (m): 0.00015775

Bounds:9.41207   21.8875   0.2068
Bounds:12.5497   28.7934   0.327244

Elapsed time is 35648.874873 seconds.

Table F.2: The best 20 sets of material parameters
(Subject 1, X=45, 0.7N, MA, initial guess values: µ=11, α=25 and λ_p=0.24)

µ (Pa)	α	λ_p	rms error
10.9323	25.2045	0.2590	0.3059
10.9334	27.6451	0.2146	0.3253
10.9819	25.0085	0.2610	0.3281
12.2173	26.8049	0.2264	0.3330
10.2476	25.6319	0.2600	0.3333
9.7041	29.0357	0.2038	0.3422
12.4733	26.6625	0.2281	0.3429
9.7534	28.0349	0.2188	0.3458
10.0136	26.4537	0.2474	0.3463
9.6920	26.4699	0.2478	0.3482
13.7875	28.3599	0.1965	0.3491
13.1228	26.0640	0.2336	0.3501
10.6505	26.4780	0.2422	0.3506
10.5099	26.7466	0.2358	0.3511
9.7603	29.2645	0.1972	0.3522
13.7241	27.2785	0.2102	0.3525
9.2313	27.6441	0.2228	0.3545
12.5551	27.5544	0.2080	0.3550
10.1097	26.1456	0.2508	0.3561
10.3597	28.3144	0.2092	0.3561

Best results:
10.9323   25.2045   0.259007

Minimum rms error (m): 0.00030595

Bounds: 9.23128   25.0085   0.196511
Bounds: 13.7875   29.2645   0.260979

Elapsed time is 81217.016137 seconds.

Table F.3: The best 20 sets of material parameters
(Subject 1, X=90, 0.7N, MA, initial guess values: μ=11, α=25 and λ_p=0.24)

μ (Pa)	α	λ_p	rms error
10.6154	31.6775	0.1751	0.3536
10.2845	32.4769	0.1626	0.3592
9.8571	31.2617	0.1801	0.3647
9.6635	29.5151	0.1918	0.3659
9.5707	23.0160	0.3231	0.3662
10.4129	22.4693	0.3330	0.3670
10.2544	32.2236	0.1608	0.3683
10.3659	23.1336	0.3232	0.3707
9.2969	31.7871	0.1707	0.3769
9.3114	32.2827	0.1662	0.3784
9.3030	31.6379	0.1735	0.3798
9.0959	29.7779	0.2002	0.3822
9.9343	32.6357	0.1627	0.3826
10.2889	29.0820	0.2133	0.3828
9.8757	31.3216	0.1799	0.3830
9.5985	30.7256	0.1881	0.3857
9.2900	32.3825	0.1636	0.3858
10.3666	31.8078	0.1665	0.3860
9.4693	32.0980	0.1683	0.3863
10.4369	31.4254	0.1774	0.3883

Best results:
10.6154   31.6775   0.1751

Minimum rms error (m): 0.0003536

Bounds: 9.0959   22.4693   0.1608
Bounds: 10.6154   32.6357   0.3330

Elapsed time is 23.4 hours.

Table F.4: The best 20 sets of material parameters
(Subject 2, X=0, 0.7N, MA, initial guess values: μ=11, α=25 and λ_p=0.24)

μ (Pa)	α	λ_p	rms error
10.8394	24.2548	0.2600	0.1918
8.6298	30.3778	0.1802	0.1918
8.5785	30.1100	0.1810	0.1965
9.8764	33.4446	0.1390	0.1969
7.8369	32.0860	0.1557	0.2006
10.7867	24.1355	0.2638	0.2020
9.4919	33.4016	0.1368	0.2039
10.4389	32.3348	0.1450	0.2049
9.4788	32.2464	0.1506	0.2063
10.8814	24.0804	0.2631	0.2092
9.8962	31.6864	0.1604	0.2095
10.4507	24.1005	0.2701	0.2099
8.2756	25.0120	0.2648	0.2127
8.6954	32.3165	0.1534	0.2156
9.0457	32.9833	0.1470	0.2157
9.9669	33.7409	0.1312	0.2160
8.6285	32.8354	0.1490	0.2164
10.7466	24.4926	0.2591	0.2166
9.3105	26.2301	0.2347	0.2177
8.2811	24.3601	0.2767	0.2194

Best results:
10.8394   24.2548   0.259987

Minimum rms error (m): 0.0001918

Bounds: 7.83688   24.0804   0.131205
Bounds: 10.8814   33.7409   0.276694

Elapsed time is 102741.293377 seconds.

Table F.5: The best 20 sets of material parameters
(Subject 2, X=45, 0.7N, MA, initial guess values: μ=11, α=25 and λ_p=0.24)

μ (Pa)	α	λ_p	rms error
13.4597	25.7732	0.2139	0.3290
13.7932	25.7182	0.2190	0.3455
13.5311	26.1257	0.2162	0.3471
13.7244	25.8860	0.2192	0.3491
11.1242	23.3135	0.2801	0.3518
13.5287	23.0621	0.2678	0.3525
13.7362	25.8569	0.2184	0.3537
13.5861	26.1456	0.2139	0.3539
13.6126	26.2848	0.2163	0.3559
13.4958	25.8692	0.2251	0.3560
13.4582	26.0954	0.2161	0.3569
13.6751	25.9704	0.2183	0.3596
13.6355	26.2073	0.2174	0.3598
13.5063	26.1714	0.2155	0.3602
13.3851	25.9670	0.2246	0.3602
11.8158	25.0394	0.2458	0.3604
13.4631	26.4735	0.2149	0.3617
12.3852	25.6552	0.2340	0.3619
14.5624	25.7044	0.2258	0.3619
11.9040	25.7782	0.2322	0.3621

Best results:
13.4597   25.7732   0.213898

Minimum rms error (m): 0.00032899

Bounds: 11.1242   23.0621   0.213878
Bounds: 14.5624   26.4735   0.280084

Elapsed time is 26401.419743 seconds.

Table F.6: The best 20 sets of material parameters
(Subject 2, X=90, 0.7N, MA, initial guess values: μ=11, α=25 and λ_p=0.24)

μ (Pa)	α	λ_p	rms error
4.5684	26.9054	0.2104	0.1655
6.1852	26.1591	0.2057	0.1682
5.1282	26.6089	0.2098	0.1692
5.9181	26.8847	0.1913	0.1737
5.2835	26.5936	0.2041	0.1776
4.8494	24.6085	0.2572	0.1801
6.0164	26.3855	0.2012	0.1803
4.2465	26.9013	0.2206	0.1809
6.0556	23.9529	0.2538	0.1809
5.8121	26.5930	0.2018	0.1812
4.7806	25.1959	0.2521	0.1815
5.4023	26.3367	0.2179	0.1826
6.1362	25.1641	0.2279	0.1826
6.0919	24.2130	0.2513	0.1870
4.4714	22.9694	0.3108	0.1881
5.8543	26.4266	0.2074	0.1881
4.2133	26.5942	0.2294	0.1891
4.1492	27.4653	0.2149	0.1893
4.6244	26.7326	0.2154	0.1899
6.3151	25.3769	0.2260	0.1908

Best results:
4.56843   26.9054   0.21039

Minimum rms error (m): 0.00016555

Bounds: 4.14922   22.9694   0.191282
Bounds: 6.31509   27.4653   0.310761

Elapsed time is 43799.9976 seconds.

Table F.7: The best 20 sets of material parameters
(Subject 3, X=0, 0.7N, MA, initial guess values: μ=11, α=25 and λ_p=0.24)

μ (Pa)	α	λ_p	rms error
6.7994	20.9159	0.4027	0.3273
5.0410	21.8863	0.3953	0.3289
5.3814	20.3489	0.4504	0.3293
5.7157	21.2721	0.4020	0.3296
5.4331	22.3974	0.3786	0.3297
6.5960	19.9856	0.4442	0.3299
5.0077	21.1010	0.4250	0.3299
5.8362	20.9403	0.4168	0.3299
5.7598	21.2488	0.4051	0.3304
5.1765	20.6230	0.4425	0.3305
5.3577	21.6472	0.4033	0.3307
6.0514	20.3743	0.4315	0.3307
4.9704	19.8362	0.4728	0.3308
4.9350	20.4435	0.4509	0.3310
6.4403	22.7058	0.3557	0.3317
6.7979	22.0083	0.3698	0.3320
5.9542	20.8633	0.4229	0.3320
5.6447	23.0121	0.3510	0.3320
6.5224	22.2965	0.3627	0.3320
6.4732	22.3683	0.3670	0.3321

Best results:
6.79935   20.9159   0.402658

Minimum rms error (m): 0.00032734

Bounds: 4.93502   19.8362   0.350973
Bounds: 6.79935   23.0121   0.472827

Elapsed time is 27557.191510 seconds.

Table F.8: The best 20 sets of material parameters
(Subject 3, X=45, 0.7N, MA, initial guess values: μ=11, α=25 and λ_p=0.24)

μ (Pa)	α	λ_p	rms error
22.3649	32.5327	0.1742	0.7841
20.1165	31.1664	0.1904	0.7930
20.8084	21.8494	0.3336	0.8064
16.6618	21.1988	0.3724	0.8088
23.1593	27.4088	0.2108	0.8102
22.7463	30.2036	0.2016	0.8286
22.1896	32.8835	0.1764	0.8368
15.0775	20.7854	0.3854	0.8474
20.0946	21.4716	0.3497	0.8487
23.1217	30.6961	0.1955	0.8498
20.0455	21.4888	0.3517	0.8525
19.8080	28.7885	0.2270	0.8550
22.1314	30.0462	0.2082	0.8597
14.8749	29.7395	0.2402	0.8601
16.4554	29.0025	0.2340	0.8614
19.8070	21.5508	0.3562	0.8643
16.0474	22.5058	0.3362	0.8749
22.5565	24.5767	0.2878	0.8756
20.5897	21.1043	0.3605	0.8771
17.8432	24.0079	0.3157	0.8804

Best results:
22.3649   32.5327   0.174195

Minimum rms error (m): 0.0007841

Bounds: 14.8749   20.7854   0.174195
Bounds: 23.1593   32.8835   0.385384

Elapsed time is 2244.905345 seconds.

Table F.9: The best 20 sets of material parameters
(Subject 3, X=90, 0.7N, MA, initial guess values: μ=11, α=25 and λ_p=0.24)

μ (Pa)	α	λ_p	rms error
9.8527	14.3369	0.5801	0.4940
8.6104	14.1643	0.6067	0.4960
10.0005	15.3739	0.5077	0.4966
9.7945	15.0102	0.5238	0.4973
8.9958	15.9334	0.4831	0.4974
8.6425	15.4656	0.5200	0.4987
10.1487	14.2019	0.5808	0.4996
10.1624	15.5927	0.4866	0.4997
9.7600	15.1229	0.5108	0.4998
9.7454	14.1776	0.5866	0.5002
9.7726	15.1282	0.5215	0.5002
10.7052	15.0625	0.5026	0.5004
8.5481	15.4433	0.5165	0.5004
8.4103	14.8514	0.5743	0.5005
9.3437	15.6376	0.5044	0.5009
10.4433	14.2898	0.5645	0.5012
10.2078	14.3203	0.5767	0.5024
8.6546	15.6515	0.5031	0.5027
9.9511	14.5889	0.5559	0.5028
8.5394	15.4595	0.5084	0.5028

Best results:
9.85269   14.3369   0.580139

Minimum rms error (m): :0.00049401

Bounds: 8.41027   14.1643   0.483145
Bounds: 10.7052   15.9334   0.606686

Elapsed time is 16040.582324 seconds.

Table F.10: The best 20 sets of material parameters
(Subject 4, X=0, 0.7N, MA, initial guess values: μ=11, α=25 and λ_p=0.24)

μ (Pa)	α	λ_p	rms error
3.8122	29.5372	0.1626	0.1821
11.4308	29.3670	0.1826	0.1898
8.2644	31.2692	0.1742	0.1904
13.8761	30.9406	0.1568	0.1946
12.1345	30.4303	0.1656	0.1964
8.9179	31.0470	0.1734	0.1975
12.4122	30.9197	0.1617	0.2042
11.2274	21.9816	0.3203	0.2045
9.8296	28.3352	0.2088	0.2050
9.3956	30.2974	0.1775	0.2052
11.3014	30.9273	0.1671	0.2067
8.6121	30.7657	0.1766	0.2071
9.5645	23.8815	0.2838	0.2077
10.9534	29.9583	0.1780	0.2077
8.3072	29.2982	0.2005	0.2084
9.4784	23.0742	0.3015	0.2086
12.4463	23.0293	0.2856	0.2089
12.3630	22.7336	0.2888	0.2096
11.0750	31.0718	0.1597	0.2107
13.1673	30.4044	0.1624	0.2110

Best results:
13.8122   29.5372   0.162648

Minimum rms error (m): 0.00018207

Bounds: 8.26444   21.9816   0.156773
Bounds: 13.8761   31.2692   0.320317

Elapsed time is 32257.492598 seconds.

Table F.11: The best 20 sets of material parameters
(Subject 4, X=90, 0.7N, MA, initial guess values: μ=11, α=25 and λ_p=0.24)

μ (Pa)	α	λ_p	rms error
10.8050	12.4444	0.8817	0.3189
9.9763	12.0458	0.9666	0.3228
12.5295	12.3250	0.8693	0.3243
11.9860	12.1148	0.9134	0.3250
10.1694	12.4580	0.8883	0.3254
11.1364	12.1755	0.9234	0.3261
12.0684	11.8729	0.9445	0.3271
10.1967	11.8094	1.0053	0.3276
11.5406	12.7144	0.8304	0.3280
11.8359	11.8378	0.9662	0.3280
10.9157	12.5392	0.8711	0.3282
10.4135	13.1149	0.7967	0.3286
10.9409	11.7098	1.0192	0.3289
11.3895	11.6121	1.0150	0.3294
10.6960	12.4936	0.8881	0.3300
10.4106	12.8532	0.8198	0.3302
12.2494	11.6709	0.9976	0.3303
11.7618	11.9890	0.9484	0.3304
10.0011	12.5182	0.8797	0.3306
11.4328	12.6406	0.8490	0.3308

Best results:
10.805   12.4444   0.881708

Minimum rms error (m): 0.00031891

Bounds: 9.97634   11.6121   0.796727
Bounds: 12.5295   13.1149   1.01919

Elapsed time is 78853.545632 seconds.

Table F.12: The best 20 sets of material parameters
(Subject 5, X=0, 0.7N, MA, initial guess values: μ=11, α=25 and λ_p=0.24)

μ (Pa)	α	λ_p	rms error
12.3889	25.1343	0.2673	0.1221
12.1607	25.7960	0.2516	0.1227
11.5706	30.4643	0.1882	0.1237
9.2999	25.0537	0.2711	0.1245
12.1705	24.4511	0.2760	0.1253
12.0811	30.1189	0.1895	0.1256
12.3061	24.8133	0.2684	0.1279
12.0484	24.8064	0.2720	0.1284
13.6432	32.0154	0.1656	0.1295
11.6769	31.2103	0.1803	0.1297
13.4367	29.9387	0.1896	0.1300
13.3943	27.1681	0.2200	0.1302
11.8846	23.8762	0.2867	0.1314
13.4838	31.9520	0.1672	0.1329
13.6307	31.9357	0.1641	0.1333
10.1765	28.2083	0.2225	0.1335
13.5903	31.6165	0.1663	0.1343
10.5143	26.5984	0.2541	0.1347
9.9913	30.0698	0.1970	0.1347
8.6315	30.8884	0.1960	0.1348

Best results:
12.3889   25.1343   0.267291

Minimum rms error (m): 0.00012214

Bounds: 8.63154   23.8762   0.164084
Bounds: 13.6432   32.0154   0.286713

Elapsed time is 26939.99998 seconds.

Table F.13: The best 20 sets of material parameters
(Subject 5, X=90, 0.7N, MA, initial guess values: μ=11, α=25 and Λ_p=0.24)

μ (Pa)	α	Λ_p	rms error
11.8855	28.5974	0.1741	0.1048
12.0126	31.0033	0.1392	0.1055
10.2125	26.8110	0.2037	0.1058
10.9727	30.8820	0.1442	0.1063
11.1255	30.3514	0.1529	0.1076
13.2437	28.3385	0.1746	0.1077
11.3944	31.9639	0.1338	0.1080
11.8254	27.1454	0.1947	0.1082
10.7316	29.1902	0.1686	0.1082
13.2319	27.9196	0.1748	0.1084
10.9702	26.0975	0.2074	0.1084
9.4977	30.5471	0.1555	0.1087
11.4745	31.6464	0.1356	0.1088
12.1511	24.6766	0.2343	0.1089
10.8485	30.0978	0.1562	0.1091
10.6134	31.6119	0.1380	0.1091
9.0849	26.2823	0.2195	0.1093
10.6686	30.8035	0.1475	0.1094
10.5138	29.5121	0.1668	0.1095
9.8772	31.1221	0.1498	0.1095

Best results:
11.8855   28.5974   0.174063

Minimum rms error (m): :0.00010482

Bounds: 9.08492   24.6766   0.133775
Bounds: 13.2437   31.9639   0.234335

Elapsed time is 10787.188240 seconds.

G-1

APPENDIX G

Matlab programme to calculate strain (Subject 1, X=0)

```
%THIS PROGRAM IS WRITTEN TO CALCULATE STRAIN
%FROM NEWDATA ReadMA
%
function x=skin1JMLHXx07a(npts)
% fit a Delaunay mesh to the Qualisys data and calculate the strain
distribution
% read in qualisys data
xdata=dlmread('xnewJMLHXx07a.csv','\t');
ydata=dlmread('ynewJMLHXx07a.csv','\t');
[x,y]=size(xdata);
disp(size(xdata));
points(1:8,1)=xdata(70,1:8)';
points(1:8,2)=ydata(70,1:8)';
points(9:41,1)=xdata(70,10:42)';
points(9:41,2)=ydata(70,10:42)';
% 1N at row 289; 0.8N at Frame 261
% 0.7N = Frame 251/250; 0.6N= Frame 238
newpoints(1:8,1)=xdata(250,1:8)';
newpoints(1:8,2)=ydata(250,1:8)';
newpoints(9:41,1)=xdata(250,10:42)';
newpoints(9:41,2)=ydata(250,10:42)';
%
% add dummy point to replace the missing corner
points(42,:)=points(39,:);
points(42,2)=-points(42,2);
newpoints(42,:)=newpoints(39,:);
newpoints(42,2)=-newpoints(42,2);
%
figure(10);
x=251
for k=1:x
        plot(xdata(250,:),ydata(250,:),'m.','MarkerSize',10);
        hold on;
        plot(xdata(k,:),ydata(k,:),'r.','MarkerSize',10);
        hold on;
        axis([-10 90 -60 60]); %set axis
%            view([-5 -15 30]); %set viewpoint
        M(k) = getframe;
end
plot
(newpoints(:,1),newpoints(:,2),'ko','MarkerSize',4,'LineWidth',2);
hold on;
plot (points(:,1),points(:,2),'bo','MarkerSize',4,'LineWidth',2);
hold off;
title('1N JMLHXx07a','FontWeight','bold');
xlabel('x (mm)','FontWeight','bold');ylabel('y
(mm)','FontWeight','bold');
pause;
```

```
% calculate displacements of points
disps=abs(newpoints-points);%abs
figure(2);
[X,Y]=meshgrid(0:1:64,-24:1:24);%4.2 for model
U=griddata(points(:,1),points(:,2),disps(:,1),X,Y,'v4');
subplot(1,1,1);surf(U);disp(size(U));
%colorbar;
%title('1N CahRHXx07 v4','FontWeight','bold');
xlabel('x','FontWeight','bold');
ylabel('y','FontWeight','bold');
zlabel('U (mm)','FontWeight','bold');
pause;
figure(3);
V=griddata(points(:,1),points(:,2),disps(:,2),X,Y,'v4');
subplot(1,1,1);surf(V),'Color',[1 1 1];
%title('1N CahRHXx07','FontWeight','bold');
xlabel('x','FontWeight','bold');
ylabel('y','FontWeight','bold');
zlabel('V (mm)','FontWeight','bold');
%colorbar;
pause;
dlmwrite('UJMLHXx07a.tsv',U,'\t');
dlmwrite('VJMLHXx07a.tsv',V,'\t');
%
% put it in points and newpoints; points is the original coordinates
and
% newpoints is the current coordinates of each marker
[x1,y1;x2,y2;...]
%
% plot strains using plotstr function
plotstr(points,newpoints);


function flag=plotstr(points,newpoints);
% takes two sets of point coordinates (points and newpoints)
% meshes with a Delaunay mesh and calculates and plots strains
%
% how big is the list of points?
sizep=size(points);
npts=sizep(1,1);
% mesh
tris=delaunay(points(:,1),points(:,2));
% how many triangles have been returned?
sizet=size(tris);
ntris=sizet(1,1);
% for each element, calculate b matrix and strains
strains=zeros(npts,3);
counts=zeros(npts,3);
nels=0;
for i=1:ntris
    for j=1:3
        c(j,:)=points(tris(i,j),:); % coordinates of
        d(j,:)=newpoints(tris(i,j),:)-c(j,:);
    end
    delta=c(1,1)*(c(2,2)-c(3,2))+c(2,1)*(c(3,2)-
c(1,2))+c(3,1)*(c(1,2)-c(2,2));
    ar=norm(c(1,:)-c(2,:))*norm(c(1,:)-c(3,:))/delta; % aspect ratio
of triangle
    if abs(ar)<4 % the triangle has a reasonable aspect ratio
```

```
    b=(1/delta)*[c(2,2)-c(3,2),c(3,2)-c(1,2),c(1,2)-c(2,2);c(3,1)-
c(2,1),c(1,1)-c(3,1),c(2,1)-c(1,1)];
    str=b*d; % strain in tensor (2x2) form
    strv=[str(1,1),str(2,2),str(1,2)+str(2,1)]; % strain in Voigt
(3x1) notation
    for j=1:3 % average strains at each node
        strains(tris(i,j),:)=strains(tris(i,j),:)+strv;
        counts(tris(i,j),:)=counts(tris(i,j),:)+1;
    end
    nels=nels+3; % and construct a new data set where each triangle
appears independently
    newx(nels-
2:nels,1)=[points(tris(i,1),1);points(tris(i,2),1);points(tris(i,3),1
)];
    newy(nels-
2:nels,1)=[points(tris(i,1),2);points(tris(i,2),2);points(tris(i,3),2
)];
    newstr(nels-2:nels,:)=[strv;strv;strv];
    newtris(nels/3,:)=[nels-2,nels-1,nels];
  end
end
% plot the displacements
figure(5);
displ=newpoints-points;
clf;subplot(2,1,1);trisurf(tris,points(:,1),points(:,2),displ(:,1));
axis tight;axis off;
shading interp;set(findobj('Type','patch'),'EdgeColor','Black');
set(gcf,'Color','w');% white background
set(gca,'CameraPosition',[100,100,1000],'CameraUpVector',[0,1,0]);
colorbar;title('X displacement');%pause;
subplot(2,1,2);trisurf(tris,points(:,1),points(:,2),displ(:,2));
axis tight;axis off;
shading interp;set(findobj('Type','patch'),'EdgeColor','Black');
set(gca,'CameraPosition',[100,100,1000],'CameraUpVector',[0,1,0]);
colorbar;title('Y displacement -JMLHXx07');
pause;
% divide the total for each node by the number of elements that are
being averaged
strains=strains./counts;
% and plot the strains
figure(6);
caxis([-0.1,0.1]);
subplot(3,1,1);trisurf(tris,points(:,1),points(:,2),strains(:,1));
axis tight;axis off;
shading
interp;set(findobj('Type','patch'),'EdgeColor','Black');caxis([-
0.1,0.1]);
set(gca,'CameraPosition',[100,100,1000],'CameraUpVector',[0,1,0]);
colorbar;title('X strain, averaged at nodes');%pause;
subplot(3,1,2);trisurf(tris,points(:,1),points(:,2),strains(:,2));
axis tight;axis off;
shading
interp;set(findobj('Type','patch'),'EdgeColor','Black');caxis([-
0.1,0.1]);
set(gca,'CameraPosition',[100,100,1000],'CameraUpVector',[0,1,0]);
colorbar;title('Y strain, averaged at nodes');%pause;
subplot(3,1,3);trisurf(tris,points(:,1),points(:,2),strains(:,3));
axis tight;axis off;
```

```
shading
interp;set(findobj('Type','patch'),'EdgeColor','Black');caxis([-
0.1,0.1]);
set(gca,'CameraPosition',[100,100,1000],'CameraUpVector',[0,1,0]);
colorbar;title('XY strain, averaged at nodes');pause;
%trisurf(tris,points(:,1),points(:,2),counts(:,1));
%disp('counts');pause;
%disp(newstr);disp(newtris);
figure(7);
subplot(3,1,1);trisurf(newtris,newx,newy,newstr(:,1));
axis tight;axis off;
shading
flat;set(findobj('Type','patch'),'EdgeColor','Black');caxis([-
0.15,0.15]);
set(gca,'CameraPosition',[100,100,1000],'CameraUpVector',[0,1,0]);
colorbar;title('X strain');%pause;
subplot(3,1,2);trisurf(newtris,newx,newy,newstr(:,2));
axis tight;axis off;
shading
flat;set(findobj('Type','patch'),'EdgeColor','Black');caxis([-
0.15,0.15]);
set(gca,'CameraPosition',[100,100,1000],'CameraUpVector',[0,1,0]);
colorbar;title('Y strain');%pause;
subplot(3,1,3);trisurf(newtris,newx,newy,newstr(:,3));
axis tight;axis off;
shading
flat;set(findobj('Type','patch'),'EdgeColor','Black');caxis([-
0.15,0.15]);
set(gca,'CameraPosition',[100,100,1000],'CameraUpVector',[0,1,0]);
colorbar;title('XY strain -JMLHXx07');pause;
disp('Mean strains:-');
disp(mean(strains));
figure(8);
hist=histc(newstr(:,1),-0.2:0.01:0.2);
subplot(3,1,1);bar(-0.2:0.01:0.2,hist,'histc');
title('X strains'); %pause;
hist=histc(newstr(:,2),-0.2:0.01:0.2);
subplot(3,1,2);bar(-0.2:0.01:0.2,hist,'histc');
title('Y strains');%pause;
hist=histc(newstr(:,3),-0.2:0.01:0.2);
subplot(3,1,3);bar(-0.2:0.01:0.2,hist,'histc');
title('XY strains -JMLHXx07');
```

---------------------- END OF PROGRAMME --------------

APPENDIX H

LIST OF PUBLICATIONS AND CONFERENCES

Journals:

Mahmud J, Holt CA, Evans SL. 2009. An innovative application of a small scale motion analysis technique to quantify human skin deformation *in vivo*. Journal of Biomechanics. (In press. DOI: 10.1016/j.jbiomech.2009.11.009).

Mahmud J, Evans SL and Holt CA. 2009. Measuring the strain and mechanical properties of human skin *in vivo* using a motion analysis technique and finite element modelling. Computer Methods on Biomechanics and Biomedical Engineering (Submitted).

Conferences:

Mahmud J, Holt CA, Evans SL. 2008. Small-scale motion analysis techniques for measuring skin deformation properties. Proceedings of 3D Motion Analysis Meeting, International Society of Biomechanics (3DMA2008). October. Santpoort-Amsterdam.

Mahmud J, Holt CA, Evans SL. 2009. A parametric study of the suction test applied to human skin. Proceedings of the 8th Computer Methods in Biomechanics and Biomedical Engineering (CMBBE 2008) Symposium, Porto, Portugal. Arup and Meditech. (ISBN: 978-0-9562121-0-8).

Mahmud J, Evans SL and Holt CA. 2009. Using motion capture and analysis to explore the mechanical properties of human skin *in vivo*. Invited Paper: Measurement and Sensing in Medicine and Health: Capturing Motion and Musculoskeletal Dynamics. IMechE Medicine and Health Division Meeting, 15 October 2009. pp. 43-48.

Mahmud J, Evans SL and Holt CA. 2009. Measuring skin deformation *in vivo* using a motion capture system. 3rd International Conference on Mechanics of Biomaterials and Tissues, Florida USA, December 2009.

Mahmud J, Holt CA, Evans SL. 2009. Measuring skin strain distribution *in vivo* using motion capture and finite elements. 9th International Symposium on Computer Methods in Biomechanics and Biomedical Engineering, CMBBE2010, Valencia Spain, Portugal, February 2010. (Accepted for poster presentation).